JAEA-Conf
2011-002

Proceedings of the 2010 Symposium on Nuclear Data

**November 25-26, 2010, C-CUBE, Chikushi Campus,
Kyushu University, Kasuga, Japan**

(Eds.) Yukinobu WATANABE, Hiroyuki KOURA and Satoshi CHIBA

Advanced Science Research Center

JAEA-Conf

September 2011

Japan Atomic Energy Agency

日本原子力研究開発機構

独立行政法人日本原子力研究開発機構　研究技術情報部　研究技術情報課
〒319-1195　茨城県那珂郡東海村白方白根 2 番地 4
電話 029-282-6387, Fax 029-282-5920, E-mail:ird-support@jaea.go.jp

2-4 Shirakata Shirane, Tokai-mura, Naka-gun, Ibaraki-ken 319-1195 Japan
Tel +81-29-282-6387, Fax +81-29-282-5920, E-mail:ird-support@jaea.go.jp

Proceedings of the 2010 Symposium on Nuclear Data
November 25-26, 2010, C-CUBE, Chikushi Campus, Kyushu University, Kasuga, Japan

(Eds.) Yukinobu WATANABE * , Hiroyuki KOURA and Satoshi CHIBA

Advanced Science Research Center
Japan Atomic Energy Agency
Tokai-mura, Naka-gun, Ibaraki-ken

(Received July 6, 2011)

The 2010 symposium on nuclear data organized by the Nuclear Data Division of Atomic Energy Society of Japan (AESJ) was held at C-CUBE, Chikushi Campus, Kyushu University, on November 25 and 26, 2010, with approximately 60 domestic and foreign participants, in cooperation with Advanced Science Research Center of JAEA and under financial support from the Kyushu Branch of AESJ. The symposium was devoted to presentations and discussions about recent research results in a wide variety of fields associated with nuclear data, such as JENDL-4 related evaluation and benchmark tests, nuclear data measurements and facilities, theoretical model calculations, applications, and so on. A tutorial on nuclear data evaluation for actinide nuclides was given in the symposium. This report consists of total 40 papers including 15 oral presentations and 25 poster presentations.

Keywords: Nuclear Data, Symposium, Proceedings, JENDL-4, Benchmark Test, Measurement, Experimental Facilities, Theoretical Model, Recent Topics

---

* Kyushu University
Organizers: Y. Watanabe (Kyushu Univ., Chair), H. Harada (JAEA, Vice-Chair), N. Iwamoto (JAEA), K. Kato (Hokkaido Univ.), H. Koura (JAEA), S. Chiba (JAEA), I. Murata (Osaka Univ.), G. Hirano (TEPSYS), J. Hori (Kyoto Univ.), S. Matsufuji (NIRS), K. Yokoyama (JAEA)

2010年度核データ研究会報告集
2010年11月25日〜11月26日、総合研究棟C-CUBE、
九州大学　筑紫キャンパス、春日市

日本原子力研究開発機構 先端基礎研究センター
(編) 渡辺　幸信* 、小浦　寛之、千葉　敏

(2011 年 7 月 6 日受理)

2010年度核データ研究会は、2010年11月25日と26日の両日、九州大学筑紫キャンパスの総合研究棟C-CUBEにおいて開催され、約60名の国内外の研究者や学生が参加した。本研究会は日本原子力学会核データ部会の主催、日本原子力研究開発機構先端基礎研究センターの共催、及び日本原子力学会九州支部の後援の下、核データ分野における最新の情報交換と議論の場として行われた。発表内容は、JENDL-4関連の評価やベンチマークテスト、核データ測定や実験施設、理論計算、国内外の関連トピックス等と多岐に亘り、アクチニド核種の核データ評価に関するチュートリアルも実施された。本報文集は口頭発表15件とポスター発表25件の全論文を纏めたものである。

原子力科学研究所（駐在） :〒319-1195 茨城県那珂郡東海村白方白根2-4
* 九州大学

2010年核データ研究会実行委員会：渡辺　幸信（委員長、九大)、原田　秀郎（副委員長、原子力機構）岩本　信之 (原子力機構)、加藤　幾芳（北大)、小浦　寛之（原子力機構)、千葉　敏（原子力機構)、村田　勲（阪大)、平野　豪（テプコシステムズ)、堀　順一（京大)、松藤　成弘（放医研)、横山　賢治（原子力機構）

Contents

目 次

1. Program of 2010 Symposium on Nuclear Data

November 25, 26, 2010
C-CUBE, Chikushi Campus, Kyushu University
Host： Nuclear Data Division, Atomic Energy Society of Japan
Co-host: Advanced Science Research Center, Japan Atomic Energy Agency
Support: Kyushu Branch of Atomic Energy Society of Japan

Nov. 25 (Thur.)
13:40 – 13:45
1. Opening address — K. Ishibashi (Kyushu Univ.)

13:45 – 15:15
2. Status of Evaluated Nuclear Data Library and Benchmark 【Chair: N. Yamano (Fukui Univ.)】
  2.1 Personal Perspective of Strategy on Nuclear Data Activities at JAEA [25+5] — T. Fukahori (JAEA)
  2.2 JENDL-4 benchmark for high temperature gas-cooled reactor, HTTR [25+5] — M. Goto (JAEA)
  2.3 Isotope Concentration Prediction Besed on the Latest Nuclear Data Files, for the High Burn-up BWR fuel pellets. [25+5] — T. Ito (NFI)

15:15 - 15:40 Photo & Coffee Break

15:40 - 17:30
3. Status of Nuclear Data Measurement Activities and Accelerator facility 【Chair: M. Baba (Tohoku Univ.)】
  3.1 Measurements of Neutron-Capture Cross Sections at J-PARC/MLF/ANNRI (1) Measurements of Neutron-Capture Cross Sections of Minor Actinides using a high intensity pulsed neutron source [25+5] — A. Kimura (JAEA)
  3.2 Measurements of Neutron-Capture Cross Sections at J-PARC/MLF/ANNRI (2) Measurements of Neutron-Capture Cross Sections of Long-Lived Fission Products using a high intensity pulsed neutron source [25+5] — J. Hori (Kyoto Univ.)
  3.3 Research in Surrogate Method at JAEA [25+5] — S. Chiba (JAEA)
  3.4 The present status of the IFMIF/EVEDA accelerator development [15+5] — S. Maebara (JAEA)

Nov. 26 (Fri.)
9:00 - 10:10
4. Tutorial 【Chair: Y. Watanabe (Kyushu Univ.)】
  Evaluation of actinide nuclear data [60+10] — O. Iwamoto (JAEA)

10:20 - 12:00
5. Poster presentation 【Chair: N. Shigyo (Kyushu Univ.)】

12:00 - 13:00 Lunch

13:00 - 14:45
6. Study of charged particle production from nucleon-induced reactions 【Chair: I. Murata (Osaka Univ.)】
  6.1 Nuclear data and materials irradiation effects - Analysis of irradiation damage structures and multiscale modeling - [25+5] — T. Yoshiie (Kyoto Univ.)

6.2 Measurement of neutron-induced light-ion production at 175 MeV quasi mon-energetic neutrons [20+5] R. Bevilacqua (Uppsala Univ., Sweden)
6.3 Experimental studies of light fragment production cross section for nucleon induced reaction at intermediate energies [20+5] T. Sanami (KEK)
6.4 Intranuclear cascade model for cluster production reaction [20+5] Y. Uozumi (Kyushu Univ.)

14:45 - 15:00 Coffee Break

15:00 - 16:30

7. Latest Topics in International and Domestic Nuclear Data Activities 【Chair: S. Chiba (JAEA)】
7.1 Nuclear Data Activities in Korea [25+5] Y.O. Lee (KAERI, Korea)
7.2 INRNE-BAS: Present Status and Future Prospects [25+5] M.K. Gaidarov (INRNE, Bulgaria)
7.3 Use of γ-ray-generating reactions for diagnostics of energetic particles in burning plasma and relevant nuclear data [25+5] Y. Nakao (Kyushu Univ.)
7.4 Studies on Reaction Mechanisms of Unstable Nuclei [25+5] K. Ogata (Kyushu Univ.)

17:00 - 17:10

8. Poster Award and Closing Address T. Fukahori (JAEA)

Poster Presentation

1. Thermal / epi-thermal neutron spectrometer with a ^{3}Heposition sensitive proportional counter
Masao ITO (Osaka Univ.)
2. Measurement of ^{151,153}Eu Neutron Capture Cross-Sections using a pair of C_6D_6 Detectors
JaeHong LEE (Kyoto Univ.)
3. Resonance Parameter Measurements and Analysis of ^{155,156,157,158,160}Gd From 10 eV to 1 keV at the RPI LINAC
Yeong-Rok KANG (KAERI)
4. Measurement of Deuteron Induced Thick Target Neutron Yields at 5 MeV and 9 MeV
Keiichi HIRABAYASHI (Kyushu Univ.)
5. Systematic Measurement of Neutron and Gamma-ray Yields on Thick Targets Bombarded with 18 MeV Protons
Masayuki HAGIWARA (KEK)
6. Production of light charged particles from silicon bombarded by 175 MeV quasi mono-energetic neutrons
Shusuke HIRAYAMA (Kyushu Univ.)
7. Measurement of deuteron-production double differential cross sections by 290 MeV/u oxygen beams on C, Al and Cu targets at forward angles
Kazuya TAHARA (Kyushu Univ.)
8. Study of the BGO detector for the measurement of the double differential cross sections of cluster production reactions
Aleksandre MZHAVIA (Kyushu Univ.)
9. Measurement of Neutron-Production Double-Differential Cross Sections for 290 MeV/u Oxygen Ion Incidence
Daisuke MORIGUCHI (Kyushu Univ.)
10. Neutron and proton yields for reaction induced by 120 GeV proton on thick copper target
Tsuyoshi KAJIMOTO (Kyushu Univ.)
11. Comparison of Neutron Production from Heavy-ion Reaction using PHITS and FLUKA
Cheol-Woo LEE (KAERI)
12. DPA calculations for heavy-ion and proton incident reactions using the PHITS code
Yosuke IWAMOTO (JAEA)
13. Developments in INC model for extension for low energy region and cluster-induced reactions
Masakatsu YOSHIOKA (Kyushu Univ.)

14. A Study of Pre-equilibrium Reaction Induced by Neutron for Nickel — Myeong-Hwan MUN (KAERI)
15. Preliminary evaluations and covariances of neutron-induced reactions for ^{237}Np and ^{240}Pu above resonance region — Hyeong-Il KIM (KAERI)
16. Effect of Newly-Measured Cross Sections of ^{157}Gd on Burnup Characteristics of High Burnup BWR UO_2 and MOX assemblies — Yoshihira ANDO (JNES)
17. Improvement of FP Decay Heat Calcutation by Introducing TAGS Data I. Beta and Gamma Spectra — Hideo TAJIMA (Tokyo City Univ.)
18. Improvement of FP Decay Heat Calculation by Introducing TAGS Data II. Priority Proposal for Future — Takayuki ARAI (Tokyo City Univ.)
19. Activation analysis by the beam loss in the IFMIF/EVEDA accelerator — Sunao MAEBARA (JAEA)
20. Evaluation of gamma-ray and neutron energy in the IFMIF/EVEDA accelerator building — Hiroki TAKAHASHI (JAEA)
21. Sensitivity analysis for curium isotope concentrations of light water reactor mixed-oxide burned fuel — Go CHIBA (JAEA)
22. Sensitivity analysis for higher order Legendre coefficients of elastic scattering matrices — Go CHIBA (JAEA)
23. Detailed Evaluation Criticality Change of MOX Cores Based on Sensitivity Analysis — Masahiro KIMURA (Osaka Univ.)

24 Analysis of Sample Worth for Dy_2O_3, Ho_2O_3, Er_2O_3 and Tm_2O_3 Measured at KUCA by MVP with Recent Version of JENDL, ENDF and JEFF — Koichi IEYAMA (Osaka Univ.)

25 Renewal of JENDL photonuclear data file 2004 (I) Elements of atomic number below 20 MeV — Toru MURATA (former NAIG)

2. Personal Perspective of Strategy on Nuclear Data Activities at JAEA

Tokio FUKAHORI
Nuclear Data Center, Nuclear Science and Engineering Directorate,
Japan Atomic Energy Agency
Tokai-mura, Naka-gun, Ibaraki-ken, 319-1195 Japan
fukahori.tokio@jaea.go.jp

1. Introduction

The latest general purpose file of Japanese Evaluated Nuclear Data Library (JENDL) has been released as JENDL-4 in 2010. The statistics of JENDL-4 is illustrated in **Table 1** comparing with the latest versions of the major general purpose evaluated nuclear data files, ENDF/B-VII.0 and JEFF-3.1.1. JENDL-4 was the one of the goals of the first period mid-term research plan for Japan Atomic Energy Agency (JAEA) and the main target of JENDL revision in this time was minor actinide (MA) and fission product (FP) nuclides. The second period of mid-term research plan has started since 2010FY. In the plan, the objective is “incident energy expansion of JENDL”.

The above objective can be achieved by producing special purpose files (JENDL Intermediate Energy Nuclear Data Files) as JENDL High Energy File (JENDL/HE), JENDL Photonuclear Data File (JENDL/PD), JENDL PKA/KERMA File (JENDL/PK), and so on. Those files are applicable for accelerator related applications such as an accelerator-driven nuclear waste transmutation system (ADS), International Fusion Material Irradiation Facility (IFMIF), radiation therapies, and accelerator-driven BNCT. For this purpose, the nuclear model code, CCONE which has been mainly used in the JENDL-4 evaluation, is planned to be improved by adding some models to expand the incident energy region.

On the other hand, we never forget that the main user of nuclear data is nuclear energy application, such as the fast breeder reactors (FBR, ex. “*Monju*”), the next generation light water reactors (NGLWR), and the innovative reactors (ex. Generation IV). Recently the importance is reported for the safety research of down-stream applications, which are related to the (spent) fuel transportation, reprocessing, waste management, etc. Nuclear security and nuclear forensics for nuclear non-proliferations are also new topics.

In this paper, personal perspective according to the assumption described above is reported. Nuclear data needs and future nuclear data activities not only for JAEA and also the others are considered.

2. Nuclear Data Needs

2.1 Fission and Fusion Reactor Developments

The main user of nuclear data is the energy applications, such as research and developments for FBR, NGLWR, Innovative Reactors and Fusion Reactors. The NGLWR concept is summarized in **Table 2**. For these requirements, higher burn-up calculation and material science investigation are needed. For these applications, rather common nuclear data are necessary for the burn-up calculations for inventory estimation as reactor physics, PKA and/or DPA calculation for material science with radiation damage, and activation library for clearances. Those nuclear data should be produced and merged into JENDL general purpose file as the next version or revision of JENDL-4.

Table 1 Comparison of Three Major Libraries

Library	**ENDF/B-VII.0**	**JEFF-3.1.1**	**JENDL-4.0**
Developed by	US	EU	Japan
Released Year	2006	2009	2010
No. of Nuclides	393	381	406
No. of Nuclides with Gamma-ray Data	206	139	354
No. of Nuclides with Neutron DDX	171	83	318
No. of Nuclides with Covariances	26	37	95
Main Evaluation Code(s)	GNASH EMPIRE	TALYS	CCONE POD
Purity*	60%	20%	96%

*: "Purity" is defined as the ratio of the number of nuclides originally evaluated (not adopted from other file) to total number.

Table 2 The Main Concept* of Next Generation Light Water Reactor in Japan

Item	Feature
Electric Power Output	1.7-1.8 GW (1.0-1.4 GW optionally)
Fuel	Over 5% Enriched U
Plant Life Time	80 year
Others	Shorter Construction Period
(Balanced with Economy)	Higher Rate of Operation
	Top Level Passive and Active Safety Equipments
	Earthquake-proof Construction

*Japan Atomic Energy Commission, for example, (in Japanese);
(http://www.aec.go.jp/jicst/NC/iinkai/teirei/siryo2010/siryo43/siryo3-2.pdf)

The most urgent item is "covariance business" and this must be solved at least its direction of preparation in near future. The covariances in JENDL-4.0 have been mainly evaluated with the CCONE+KALMAN Method. The covariance data for 110 nuclides of ENDF/B-VII.1 will be provided for the Advanced Fuel Cycle Initiative (AFCI) project (BNL, LANL). The motto for covariance is "*Might not be perfect but must be sensible*". The JEFF covariance data is being prepared by using "*Total Monte-Carlo Method*". It must be stressed that covariance data and nuclear data qualities are the different items.

2.2 Medical, Space and Accelerator Related Applications

For medical applications (radiation therapy, medical RI production, accelerator-driven BNCT, etc.) and space engineering (error of semi-conductor, dose estimation from cosmic-ray, etc.), nuclear data for particle transport calculation, energy deposition, RI production rate and so on are necessary. Those are the neutron and charged particle spectra and activation cross sections below 250 MeV.

JENDL Intermediate Files are also useful for accelerator related applications such as accelerator driven system (ADS) for nuclear waste transmutation, International Fusion Material Irradiation Facility (IFMIF). The neutron production cross section and neutron spectrum are important.

2.3 Safety Researches

The safety researches can be categorized into "*frontend*" (Nuclear Fuel Supply), "*reactor*" (Core Characteristics and Operation), "*down-stream*" of nuclear fuel cycle (Spent Fuel Treatment) and "*backend*" (Nuclear Waste Management). At the frontend stage, criticality safety for handling of processing, storage and transport of fuel should be considered. If fail to control, critical accident, ex. the JCO Accident (1999.9.30), is happened. For the reactor safety, the operation by grasping power distribution, control rod worth, reactivity coefficients, etc. is important (ex. Chernobyl (1986.4.26), and TMI Accident (1979.3.28)). For this purpose, the prediction of burn-up characteristics and evaluation of delayed neutron effects should also be considered. At the down-stream stage of nuclear fuel cycle, the criticality safety for storage, transport and reprocessing, shielding and decay heat is important. At the backend stage, the waste management such as the long-term radio-toxicity (HLW) and clearance level (LLW) should be considered.

The "Criticality Safety" is one of the key items for safety researches and well established. Though recent experiments are getting more expensive relatively than before, some databases have been prepared, ex. the OECE/NEA International Criticality Safety Benchmark Evaluation Project (ICSBEP), the Criticality Safety Handbook (JAEA-Data/Code 2009-010) with the critical limits for minimum mass, size, concentration, etc. at k_{eff} = 0.98. For the criticality safety research, nuclear data such as fission and capture cross sections, fission product yields (FPY) are the most important.

Safety researches at the down-stream and backend stages are getting more important from my point of view, since the replacement period of current nuclear power plants is coming near future and competition of international sales of power reactors by developed countries is harder so as to reduce CO_2 emission. The critical safety is still important for spent fuel storage and cask design; keeping "Subcritical when immersed in water" and "Subcritical when piled up in numbers". For this purpose, neutron absorbers, B-SUS, B-Al, B-Resin, Cd-Alloy etc. are considered to keep $k_{eff} < 0.95$ even for unirradiated fuel with initial ^{235}U enrichment. The "Burn-up Credit" is also considered to estimate the reactivity loss and the nuclide concentrations. The Post Irradiation Experiments (PIE) is one of the good benchmark tests for analyzing accuracy of calculations and data (FPY, capture cross section and decay data). Important nuclides are, for example, 12FPs (^{95}Mo, ^{99}Tc, ^{103}Rh, ^{133}Cs, ^{143,145}Nd, ^{147,149,150,152}Sm, ^{153}Eu, ^{155}Gd) by JAERI-Tech 2001-055, 15FPs (^{95}Mo, ^{99}Tc, ^{101}Ru, ^{103}Rh, ^{109}Ag, ^{133}Cs, ^{143,145}Nd, ^{147,149,150,151,152}Sm, ^{153}Eu, ^{155}Gd) by OECD BUC WG and 13FPs (^{99}Tc, ^{103}Rh, ^{131}Xe, ^{133}Cs, ^{143,145}Nd, ^{147}Pm, ^{147,149,151,152}Sm, ^{153}Eu, ^{155}Gd) by SAND87-0151 for casks.

The clearance (= radioactive nuclide productions) level estimation is needed for dispose waste, especially at the reactor replacement period. For this purpose, radioactive isotope (RI) production should be estimated as accurate as possible and activation cross sections and decay data are necessary. The nuclide list included in the IAEA Safety Guideline for the clearance level estimation is shown in **Table 3** as an example. The similar list is also enacted in Japan and is given in Table 3. Other long-lived RIs, for example ^{182}Hf

($T_{1/2}$=8,900,000 year) and ^{60}Fe ($T_{1/2}$=1,500,000 year) might be considered, even though not included in Table 3. The Hf is used for control rods of BWR as a strong neutron absorber and the ^{182}Hf is produced by two step neutron capture reaction as ^{180}Hf (n,g) ^{181}Hf (n,g) ^{182}Hf. The ^{60}Fe is created by also two step capture reaction and decays to ^{60}Co! It should be also noted it is difficult to measure half-lives for these RIs accurately.

Table 3 Nuclides Listed in Table 2 of IAEA Safety Guideline RS-G-1.7

$\underline{^{3}\mathrm{H}}$, $\underline{^{7}\mathrm{Be}}$, $\underline{^{14}\mathrm{C}}$, $\underline{^{18}\mathrm{F}}$, $^{\underline{22},24}$Na, ^{31}Si, $\underline{^{32,33}\mathrm{P}}$, $\underline{^{35}\mathrm{S}}$, $\underline{^{36,38}\mathrm{Cl}}$, ^{42,43}K, $^{\underline{45},47}$Ca, $^{\underline{46},47,48}$Sc, ^{48}V, $\underline{^{51}\mathrm{Cr}}$,
$^{51,52,52m,53,\underline{54},56}$Mn, $^{52,\underline{55,59}}$Fe, $^{55,\underline{56,57,58},58m,\underline{60},60m,61,62m}$Co, $^{\underline{59,63},65}$Ni, ^{64}Cu, $^{\underline{65},69,69m}$Zn, ^{72}Ga, ^{71}Ge,
^{73,74,76,77}As, $\underline{^{75}\mathrm{Se}}$, ^{82}Br, $\underline{^{86}\mathrm{Rb}}$, $^{\underline{85},85m,87m,\underline{89,90},91,92}$Sr, $^{\underline{90},91,91m,92,93}$Y, ^{93,95,97}Zr, $^{\underline{93m,94},95,97,98}$Nb,
$^{90,93,\underline{99},101}$Mo, $^{96,96m,97,97\underline{m,99,99m}}\underline{\mathrm{Tc}}$, ^{97,103,105,106}Ru, ^{103m,105}Rh, ^{103,109}Pd, $^{105,\underline{110m},111}$Ag,
$^{\underline{109},115,115m}$Cd, $^{\underline{111},113m,114m,115m}$In, $^{\underline{113},125}$Sn, $^{122,124,\underline{125}}\underline{\mathrm{Sb}}$,
$^{\underline{123m},125m,127,127m,129,129m,131,131m,132,133,133m,134}$Te, $^{\underline{123,125},126,129,130,\underline{131},132,133,134,135}$I,
$^{129,131,132,\underline{134},134m,135,136,\underline{137},138}$Cs, ^{131,140}Ba, ^{140}La, $^{\underline{139,141},143,144}$Ce, ^{142,143}Pr, ^{147,149}Nd, $^{\underline{147},149}$Pm,
^{151,153}Sm, $^{\underline{152},152m,\underline{154},155}$Eu, $^{\underline{153},159}$Gd, $\underline{^{160}\mathrm{Tb}}$, ^{165,166}Dy, ^{166}Ho, ^{169,171}Er, ^{170,171}Tm, ^{175}Yb, ^{177}Lu,
^{181}Hf, $\underline{^{182}\mathrm{Ta}}$, ^{181,185,187}W, $^{\underline{186},188}$Re, ^{185,191,191m,193}Os, $^{190,\underline{192},194}$Ir, ^{191,193m,197,197m}Pt, $^{\underline{198},199}$Au,
$^{197,197m,\underline{203}}$Hg, $^{200,\underline{201},202,\underline{204}}$Tl, ^{203}Pb, ^{206,207}Bi, ^{203,205,207}Po, ^{211}At, ^{225,227}Ra, ^{226,229}Th, ^{230,233}Pa,
^{230,231,232,233,236,237,239,240}U, ^{237,239,240}Np, ^{234,235,236,237,238,239,240,241,242,243,244}Pu, $^{\underline{241},242,242m,243}$Am,
$^{242,243,\underline{244},245,246,247,248}$Cm, ^{249}Bk, ^{246,248,249,250,251,252,253,254}Cf, ^{253,254,254m}Es, ^{254,255}Fm

Under Line: Nuclides considered in the Japanese Clearance Regulation (+^{41}Ca, ^{44}Ti, ^{49}V, ^{67}Ga, ^{68}Ge, ^{81}Rb, ^{108m}Ag, ^{133}Ba, ^{169}Yb, ^{188}W, ^{195}Au)

Shielding calculation (radiation transport and deep penetration) is also needed for the human radiation protection. For this purpose, elastic scattering cross section and angular distribution, neutron disappearance cross section, nuclear structure and decay data are required. And also PKA and KERMA data with charged-particle spectra is needed for the dose evaluation as the Linear Energy Transfer (LET).

2.4 Nuclear Security and Forensics for Nuclear Non-proliferation

The nuclear forensics and nuclear detection are necessary for the nuclear non-proliferation. The nuclear forensics is to determine the origin of fissionable materials, by analyzing isotope abundances, impurities, etc. with irradiation and/or mining histories. Nuclear data are needed for this irradiation history by estimating isotope productions.

For nuclear detection, candidate techniques such as the Neutron Interrogation Method (NIM) and Laser-Induced Breakdown Plasma (LIBP) + Resonance Absorption Spectroscopy (RAS) are being developed. For these, neutron and photo fission cross sections, FPY, decay data and photonuclear reaction data are requested.

The objective mentioned in this chapter can be achieved by producing JENDL General Purpose File, JENDL/HE, JENDL/PD and JENDL/PK. Furthermore, JENDL Activation File including RI production cross sections and FPY is required for the down-stream applications near future.

3. Perspective of Future Nuclear Data Activities

The 2nd Period Mid-term Plan of JAEA (2010-2014) is “incident energy expansion of JENDL” for nuclear data to produce Intermediate Energy Files (JENDL/HE, JENDL/PD, etc.). For update of the general purpose file of JENDL (JENDL-4.1?), covariance data and quality assurance are also important. Furthermore, JENDL Activation File (JENDL/A) with error data is also mentioned above.

To prepare and update nuclear data files, the development of original nuclear reaction model code is necessary for easily and timely nuclear data evaluation and/or improvement to meet user requirements. For this purpose, the code CCONE is the strong candidate. In the short period, the CCONE is planned to be improved by adding some models, such as multiple nucleon and light charged particle emissions from pre-equilibrium stage, to expand the incident energy region, and for unknown (at this moment) user needs. This improvement is also useful to prepare for the next generation.

As the preparation for the next generation, some items related to nuclear data activities not only in Japan and also in the world stand on the edge of precipice. They are crisis of the human resources for nuclear data evaluation (especially for decay and nuclear structure data), the budget (especially for nuclear data measurements), and presence (appearing) to the stake-holders. Those should be considered as soon as possible so that nuclear data activity level is kept for next generations.

To avoid the crisis of human resources, the urgent fostering talents (tutorials, production of textbook, etc.) are required for nuclear data producers, especially for the items of “*Endangered Species*” such as ENSDF evaluators, resonance analyzers, producers of the thermal scattering law, etc. And the next generation evaluators for fission reaction (neutron spectra, delayed neutron, FPY, etc.), light-mass nuclides and evaluation tool makers should also be considered. Collaborations with the people of nuclear physics fields such as fundamental theories, microscopic approaches are getting more important. To produce evaluated nuclear data file, the international collaborations and considering TENDL-like approaches might be necessary.

Though the certain level budget is desired to keep measurement facilities for nuclear data, recently if faces to some difficulty. It is true that nuclear data is an item like air, however, producers cannot live on air. Here international collaborations to share the experiments into the several facilities like European example should be convinced urgently. For obtaining the budget, it is also important to show the presence of nuclear data with the impact to the stake-holders such as the government (both nuclear power developments and regulation sides), industry users and plant makers.

4. Summary

The JENDL-4 has been released in 2010 as one of goals of the first period mid-term research plan for JAEA. In the plan for the second period, the objective is “incident energy expansion of JENDL”. The objective can be achieved by producing JENDL/HE, JENDL/PD, and JENDL/PK. For this purpose, CCONE is planned to be improved by adding some models. The nuclear data for the burn-up, activation, and PKA/DPA calculations will be prepared for the applications of reactors, safety research, material science, nuclear forensics, etc. The urgent problems for human resources, presence to the stake-holders, and budget should be solved for example, by efforts of the international collaborations, etc.

Though words too many, however, what I have often heard is "*Nuclear data are an important database for research and developments of nuclear applications. Target materials and kinds of nuclear data are different application by application. The new nuclear data are needed to be produced. Is it necessary to be done by Japan?*" It is necessary for proper usage of nuclear data to know about the origin and background. In the case of nuclear data being produced in abroad, it has some difficulty to see it. And I also hear "*Why do not consider the world-unified nuclear data file?*" Since nuclear data are a kind of physical quantities, it must converge into certain values. However, it needs much more time to be fixed. Before it is achieved, it is necessary to produce country by country, or area by area, so that they can choose their own purpose of developing nuclear data and keep competition opportunity to upgrade nuclear data quality

3. JENDL-4.0 benchmark for high temperature gas-cooled reactor, HTTR

Minoru GOTO[1], Satoshi SHIMAKAWA[1] and Takashi YASUMOTO[2]
1. *Japan Atomic Energy Agency, 4002, Oarai-machi, Higashi-ibaraki-gun, Ibaraki 311-1393, Japan*
2. *Kyushu University, 744, Motooka, Nishi-ku, Fukuoka-city 819-0395, Japan*
e-mail: goto.minoru@jaea.go.jp

In the past, benchmark calculations of criticality approach for the HTTR, which is a Japanese HTGR, were performed by research institutes in several countries, and almost all of the calculations overestimated the excess reactivity. In Japan, the benchmark calculations performed by JAEA also resulted in overestimation. JAEA improved the calculations by revising the geometric model and replacing the nuclear data library with JENDL-3.3, which was the latest JENDL at that time. However, the overestimation remained and this problem has not been resolved until today. We performed calculations of the HTTR criticality approach with several nuclear data libraries, and found that slight difference in the capture cross section of carbon at thermal energy among the libraries causes significant difference in the k_{eff} values. The cross section value of carbon was not concerned in reactor neutronics calculation because of its small value of the order of 10^{-3} burn, and consequently the cross section value was not revised for a long time even in the major nuclear data libraries: JENDL, ENDF and JEFF. We thought that the cross section value should be revised based on the latest measurement data in order to improve the accuracy of the neutronics calculations of the HTTR. In May 2010, the latest JENDL: JENDL-4.0 was released by JAEA, and the capture cross section of carbon was revised. Consequently, JENDL-4.0 yielded 0.4-0.9%Δk smaller k_{eff} values than JENDL-3.3 in the calculation of the HTTR critical approach, and then the problem of the overestimation of the excess reactivity in the HTTR benchmark calculation was resolved.

1. Introduction

In the past, the neutronics calculations for the HTTR critical approach were performed with the three major nuclear data libraries, which are JENDL-3.3 (Japan), ENDF/B-VI.8 (U.S.A) and JEFF-3.0 (Europe)[1]. As a result, JENDL-3.3 yielded the k_{eff} values which were in better agreement with the experimental results than the other libraries. Additionally, it was found that the discrepancies of the k_{eff} values between JENDL-3.3 and the other libraries are mainly caused by the slight difference of the neutron capture cross section of carbon at 0.0253eV among the libraries, and we had been focusing on the accuracy of this cross section as one of the important subjects for the improvement of the neutronics calculations for the HTGRs.

JENDL-3.3 showed better applicability to the HTTR criticality calculations than the other libraries as mentioned above, but still overestimated the k_{eff} values by 0.5-1.1%Δk. Overestimating the k_{eff} values, the calculation result of the loaded number of the fuel columns achieving the first criticality did not agree with the experimental results. These problems has not been resolved until today, despite our efforts of the refinement such as the description of the core geometry and the concentration of the components. Meanwhile, the neutron capture cross section of carbon at 0.0253eV stored in each nuclear data library had not been revised for a long time. Thus we proposed this cross section should be revised based on the latest measurement data, and also predicted that the problem of overestimating the k_{eff} values will be resolved by revising the cross section to be about 10% larger than that of JENDL-3.3.

In May 2010, the latest JENDL: JENDL-4.0[2], was released by JAEA. In JENDL-4.0, our proposal and prediction were applied, and the neutron capture cross section of carbon at 0.0253eV was revised based on the latest measurement data[3]. Accordingly the problem of overestimating the k_{eff} values in the HTTR criticality calculations was expected to be improved. This paper describes the investigation of the applicability of JENDL-4.0 to the HTTR criticality calculations.

2. Calculations for HTTR critical approach with JENDL-4.0

2.1 Objective and method

The objective of this study is to investigate the applicability of JENDL-4.0 to the HTTR criticality calculations. The investigation was performed by comparing (a)The loaded number of fuel columns achieving the first criticality, and (b)Excess reactivity of the fully loaded core, between the experimental results and the calculation results with several nuclear data libraries, which are JENDL-4.0, previous JENDL: JENDL-3.3, the latest ENDF: ENDF/B-VII.0, and the latest JEFF: JEFF-3.1. Additionally, identification of nuclides which have large effects on the difference of the following issues among the libraries was studied.

2.2 HTTR critical approach

(1) HTTR

The HTTR is a graphite-moderated and helium gas-cooled block-type HTGR, situated at JAEA-Oarai Resarch and Development Center. It has 30MW thermal power and its outlet coolant temperature, which can be used for nuclear heat utilization, is 850°C in rated power operation. Additionally, the HTTR can also be operated in high temperature test operation mode, with which its outlet coolant temperature is 950°C.

Figure 1 shows radial and bird-eye views of the HTTR core. The core is constructed by stacking four kinds of hexagonal blocks, which are fuel blocks, control rod guide blocks, replaceable reflector blocks and irradiation blocks (for irradiation test), and is surrounded by permanent reflectors made of graphite. All these hexagonal blocks are made of high-purity graphite, and are the same in across flats (36cm) and height (58cm). Fuel region in the core is composed of 30 fuel columns, in which five fuel blocks are stacked.

(2) Critical approach

The critical approach of the HTTR was carried out by the fuel addition method at room temperature. In the critical approach, dummy graphite blocks previously placed in the core were replaced with fresh fuel blocks from the outer core region in the form of fuel columns as shown in Fig. 2. The first criticality was achieved by an annular form core comprising 19 fuel columns. After the first criticality, the fuel loading was carried out additionally to construct the fully loaded core at room temperature. The fully loaded core was constructed by a cylindrical form core comprising 30 fuel columns.

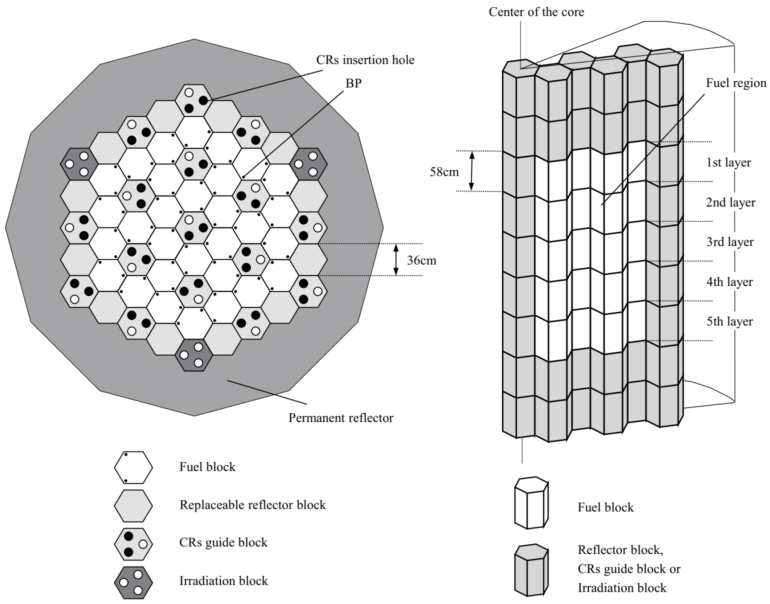

Fig. 1 Schematic diagram of HTTR core

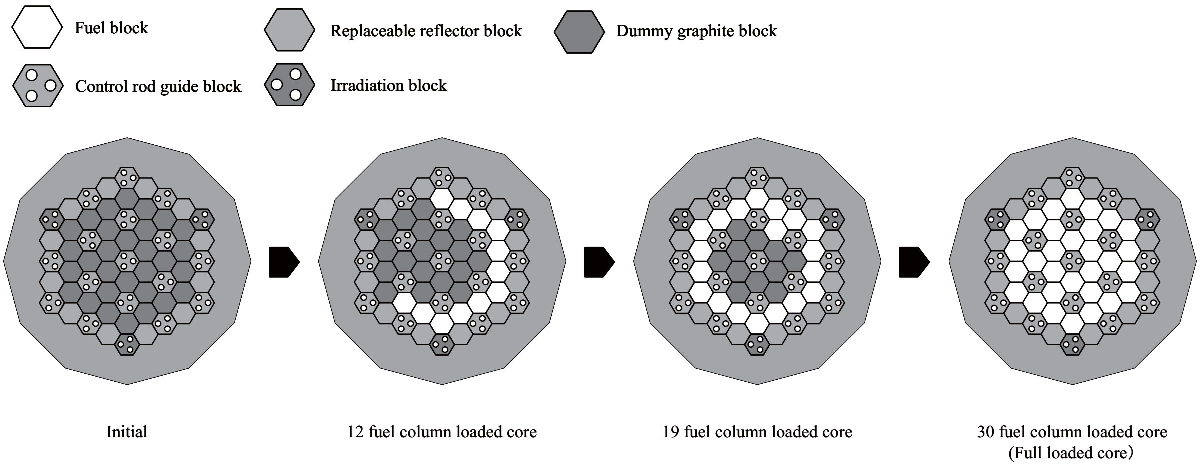

Fig. 2 Procedure of HTTR critical approach

2.3 Neutron capture cross section of carbon at 0.0253eV stored in each libraries

Table 1 shows the neutron capture cross section of carbon at 0.0253eV stored in the each libraries. In JENDL-4.0, the cross section was revised to 3.85mb, which is 9% larger than JENDL-3.3 and is 15% larger than ENDF/B-VII.0 and JEFF-3.1.

The neutron capture cross section of carbon at 0.0253eV of JENDL-3.3 was taken from JENDL-3[4], which was released in 1989, and therefore this cross section stored in JENDL had not been revised for 21 years. Meanwhile the cross section of ENDF/B-VII.0 is taken from ENDF/B-IV[5,6], which was released in 1974, or might be taken from more previous version of

ENDF. Thus this cross section stored in ENDF has not been revised more than 36 years at least. The cross section of JEFF-3.1 was taken from ENDF/B-VI.8[7], and it evaluated based on as old measurement data as ENDF.

Table 1　Neutron capture cross section of carbon at 0.0253eV

JENDL-4.0	JENDL-3.3	ENDF/B-VII.0	JEFF-3.1
3.85mb	3.53mb	3.36mb	3.36mb

2.4 Calculation conditions and method

The criticality calculations for the 12-30 fuel columns loaded core with all control rods withdrawn at room temperature were performed with the continuous energy Monte Carlo code MVP[8] to obtain the k_{eff} value for each core state. The core geometry was treated as much detail as possible, and a heterogeneous effect caused by a coated fuel particle was taken into account by using a Statistical Geometry (STG) model[9]. The history number was defined 8,000,000 for each calculation to reduce the standard deviation (1σ) to about 0.03%.

3. Results and discussion

Figure 3 shows calculated k_{eff} curves for the several HTTR core states, which were configured in the critical approach. JENDL-4.0 yields the k_{eff} values which are smaller than the other libraries for the all core states. Specifically, the k_{eff} values calculated with JENDL-4.0 are 0.5-0.9%Δk smaller than JENDL-3.3, and are 1.0-1.5%Δk smaller than ENDFL/B-VII.0 or JEFF-3.1. The k_{eff} values calculated with ENDF/B-VII.0 and JEFF-3.1 are the same within 2σ for the each core states.

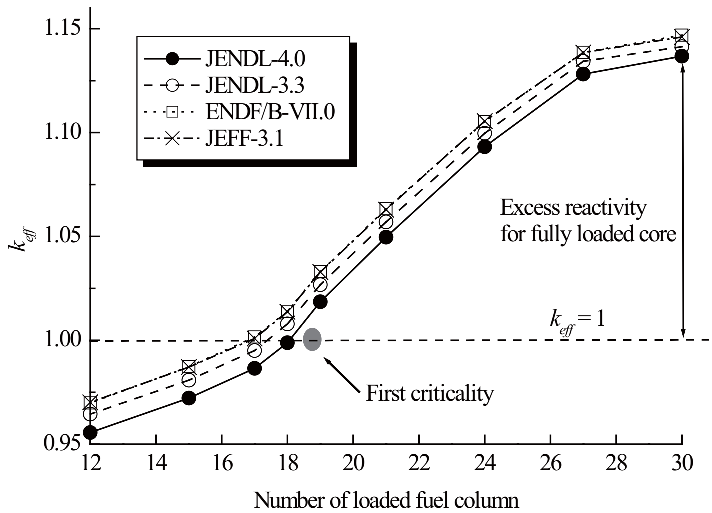

Fig. 3　k_{eff} curves for each core states

3.1 Loaded number of fuel columns achieving first criticality

The loaded number of the fuel columns at the first criticality is determined by identifying the first column with which the k_{eff} value is more than 1.0. Thus, the k_{eff} curve with JENDL-4.0 indicates that the first criticality is achieved by loading 19 fuel columns, which agrees with the experimental result. Meanwhile, the k_{eff} curves with JENDL-3.3, ENDF/B-VII.0 and JEFF-3.1 indicate the first criticality is achieved by loading 18, 17, and 17 fuel columns, respectively. These libraries underestimate the loaded number of the fuel columns by one or two columns, which are caused by the overestimation of the k_{eff} value.

The discrepancy of the loaded number of the fuel columns achieving the first criticality between the experiment and the calculations was resolved by replacing the nuclear data libraries with JENDL-4.0.

3.2 Excess reactivity of fully loaded core

The excess reactivity of the fully loaded core ρ_{ex}, is defined by

$$\rho_{ex} = \frac{k_{eff} - 1}{k_{eff}}. \tag{1}$$

Table 2 shows that JENDL-4.0 yields the excess reactivity of 12.0%Δk/k, which agrees well with the experimental result. Meanwhile, JENDL-3.3, ENDF/B-VII.0 and JEFF-3.1 give the excess reactivity of 12.4, 12.8 and 12.7%Δk/k, and they overestimates by 0.4-0.8%Δk/k.

The problem of overestimating the excess reactivity at the fully loaded core was also resolved by replacing the nuclear data libraries with JENDL-4.0.

Table 2 Comparisons between experimental[10] and calculation results

	Experiment	JENDL-4.0	JENDL-3.3	ENDF/B-VII.0	JEFF-3.1
Number of fuel columns achieving the first criticality	19	19	18	17	17
Excess reactivity of the fully loaded core (%Δk/k)	12.0	12.0	12.4	12.8	12.7

4. Conclusions

The criticality calculations of 12-30 fuel columns loaded core, which were constructed in the critical approach, were performed with JENDL-4.0, JENDL-3.3, ENDF/B-VII.0, and JEFF-3.1. As a result, JENDL-4.0 yields k_{eff} values which are 0.5-0.9%Δk smaller than JENDL-3.3, and 1.0-1.5%Δk smaller than ENDFL/B-VII.0 or JEFF-3.1. The k_{eff} values calculated with ENDF/B-VII.0 and JEFF-3.1 are the same within 2σ for the all core states.

The discrepancies between the experimental and the calculation results on the following two issues were resolved as expected by replacing the nuclear data libraries with JENDL-4.0. This fact shows that the applicability of JENDL-4.0 to the HTTR criticality calculations is more excellent than the other nuclear data libraries.

(a) The loaded number of fuel columns achieving the first criticality.
(b) Excess reactivity of the fully loaded fuel columns core.

JENDL-4.0 promises to improve the accuracy of the HTGR criticality calculations, which allows the design of the commercial HTGR with lower cost and higher performance.

Acknowledgement

The authors thank K. Okumura of the research group for reactor physics, JAEA, for preparing the neutron cross-section sets for the MVP. The authors also thank Y. Nagaya of the research group for reactor physics, JAEA, for supporting parallel execution of the MVP.

References

[1] M. Goto, N. Nojiri and S. Shimakawa, "Neutronics Calculations of HTTR with Several Nuclear Data Libraries," J. Nucl. Sci. Technol., 43[10], 1237 (2006).

[2] K. Shibata, O. Iwamoto, T. Nakagawa, et al., "JENDL-4.0: A New Library for Innovative Nuclear Energy Systems," Proc. of the Int. Conf. on Nuclear Data for Science and Technology (ND2010), Jeju Island, Korea, April 26-30, 2010.

[3] Firestone R.B., M. Krticka, D.P. McNabbet, et al., " New Methods for the Determination of Total Radiative Thermal Neutron Capture Cross Sections," Proc. of 2007 Int. Workshop on Compound-Nucleus Reactions and Related Topics, Yosemite, U.S.A., Oct. 22-26, 2007.

[4] K. Shibata, Evaluation of neutron nuclear data for ^{12}C, JAERI-M 83-221, Japan Atomic Energy Research Institute (JAERI) (1983).

[5] Los Alamos National Laboratory, T-2 Nuclear Information Service, http://t2.lanl.gov/data/data/ENDFB-VII-neutron/C/nat.

[6] R. Kinsey, ENDF/B Summary documentation, BNL-NCS-17541, Brookhaven National Laboratory (BNL) (1979).

[7] A. Koning, R. Forrest, M. Kellett, et al., The JEFF-3.1 Nuclear Data Library, JEFF Report 21, OECD/NEA (2006).

[8] Y. Nagaya, K. Okumura, T. Mori, et al., MVP/GMVPII: General Purpose Monte Carlo Codes for Neutron and Photon Transport Calculations based on Continuous Energy and Multigroup Methods, JAERI 1348, Japan Atomic Energy Research Institute (JAERI), (2005).

[9] I. Murata, T. Mori, M. Nagaya, et al., Continuous Energy Monte Carlo Calculations for Randomly distributed Spherical Fuels Based on Statistical Geometry Model, JAERI-Research 96-015, Japan Atomic Energy Research Institute (JAERI), (1996), [in Japanese].

[10] N. Nojiri, S. Shimakawa, N. Fujimoto, et al., "Characteristics test of initial HTTR core," Nucl. Eng. Des., 233, 283 (2004).

4. Isotope Concentration Prediction Based on the Latest Nuclear Data Files for the High Burn-up BWR fuel pellets

Takuya Ito, Shogo Matsuoka, Shota Okui
Nuclear Fuel Industries, Ltd. Tokai-works,
Tokai-mura, Naka-gun, Ibaraki, 319-1196, Japan
Email:t-itoh@nfi.co.jp

To understand the characteristics of evaluated nuclear data from a view point of isotope concentration prediction, burnup calculations for high burnup BWR MOX fuels were performed based on several nuclear data libraries, including JENDL-4.0. The calculation results were compared to measurements and each other calculations.

1. Introduction

JENDL/AC-2008[1)] was released in 2008 in Japan. In USA, ENDF/B-VII.0[2)] was released in 2006 and preparation of ENDF/B-VII.1 is progressing. In Europe, JEFF-3.1.1[3)] was released in 2009. JENDL-4.0[4)] was released in May 2010.

In this study, isotope concentration prediction calculations for high burnup BWR MOX fuels with the new several evaluated nuclear data files are performed and compared to reference values.

The result of C/E comparison to the results of radio-chemical analysis of the MALIBU[5,6)] high burn up BWR MOX samples is shown for JENDL-3.2[7)], JENDL/AC-2008, ENDF/B-VII.0, JEFF-3.1 by using MVP-BURN[8)]. MALIBU program is an international PIE program for high burnup fuel which was irradiated in commercial reactors.

As for JENDL-4.0, C/C comparison of isotope concentration against the latest evaluated nuclear data files at high burn up BWR MOX condition is shown.

Continuous energy Monte-Carlo code "MVP-BURN" is employed for burnup calculation to reduce both of geometry approximation and effective cross section approximation. In calculation, fuel assembly geometry is simulated exactly and irradiation data which are provided by MALIBU program are traced.

3. Overview of MALIBU program

MALIBU program[5,6)] is an international PIE program for high burnup MOX and UOX fuels. In this program, various nuclides, 17 heavy metal nuclides and 34 fission products nuclides are subject of analysis. The sample matrix is shown in Table 1.

In the MALIBU program, isotope concentration of one sample was measured by two or three laboratories independently, then, the measured results were checked each other. Finally “recommendation value” for isotope concentration of each nuclide was evaluated for each sample.

Table 1 MALIBU sample matrix

	PWR			BWR		
Sample	GGM1	GGU1	GGU2	GRM1	GRM2	GRM3
Fuel Type	MOX	UOX	UOX	MOX	MOX	MOX
Assembly	GOESGEN 15×15			GUNDREMMINGEN-C 9×9		
U235 [wt%] Puf [wt%]	DU 5.5	4.3 —	4.3 —	DU 5.5	DU 5.5	DU 5.5
Burnup [GWd/t]	- 70	- 70	- 50	- 80	- 75	- 50
Histrical Void Frac.	-	-	-	- 20%	- 50%	- 70%
Labo.	SCK·CEN, PSI, CEA	PSI, CEA	SCK·CEN, PSI	SCK·CEN, PSI	SCK·CEN, PSI	SCK·CEN, PSI

*GRM1 is focused on the following discussion.

2. Analysis

Isotope concentration Prediction

A continuous energy Monte-Carlo code "MVP-BURN" is employed for isotope concentration prediction to reduce both of geometry approximation and effective cross section approximation. 104 fp chain model which includes 21 heavy metals and 104 fission products was applied. Neutron history was 0.5 million per each burnup step with Predictor-Corrector method. Fuel assembly geometry was simulated without any approximation. Irradiation history of the sample, which was evaluated in the In Core Fuel Management, ICFM, was provided in MALIBU program. It was used for the isotope concentration prediction calculation. Spectrum interference is large because MOX fuel assembly is adjacent to UOX fuel assemblies. Spectrum interference was taken into account for the Pu isotopes concentration prediction.

Four neutron cross section libraries, JENDL-3.2, JENDL/AC-2008, ENDF/B-VII.0 and JEFF-3.1[9], are used for the calculation. JNDC v2[10] was used as the FP yield.

Sample burnup

"Calculated burnup" which is evaluated in ICFM and "Measured burnup" which is evaluated by radio-chemical analysis can be different naturally. This sample burnup difference must be considered appropriately. An example of difference between the "Calculated burnup" and "Measured burnup" is shown schematically in Fig.1. Our approach to take the burnup difference into account is followings.

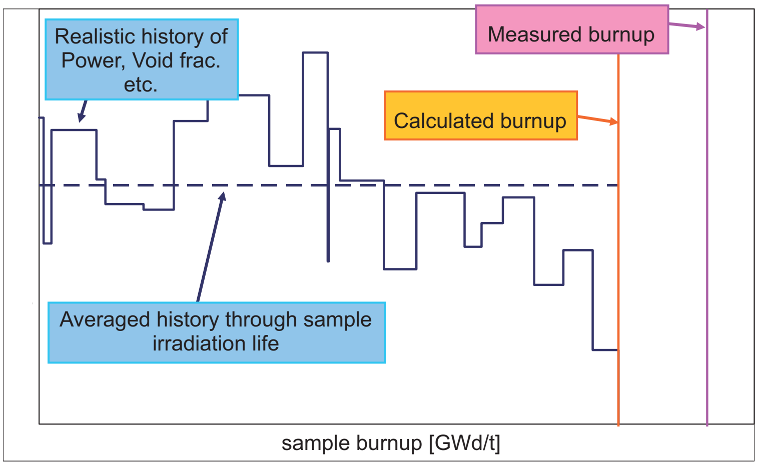

Fig. 1. Schematic explanation of irradiation history

- **Realistic burnup history calculation**

  The time dependent irradiation conditions from the beginning of sample life, BOL, to the end of sample life, EOL, which is given in the irradiation report supplied from ICFM, linear power rate, etc. are considered in burnup calculation directly.

- **Averaged burnup history calculation**

  All irradiation conditions are averaged through BOL to EOL, and then burnup calculation is performed with the averaged irradiation condition.

- **Irradiation history coefficient evaluation**[11)]

  The irradiation history effect coefficient is a ratio of each isotope concentration in fuel calculated with averaged burnup history calculation over the concentration evaluated with realistic burnup history calculation at the EOL given in the report.

- **Evaluation of C/E for all measured isotopes**

  Once the irradiation history coefficient was obtained, the effect of the change of the irradiation condition through the sample irradiation can be reflected to the isotope concentration evaluated for the arbitrary sample burnup with averaged burnup history calculation. Therefore the isotope concentration at the burnup evaluated by radiochemical analysis, "Measured burnup", can be obtained with consideration of the change of the irradiation condition correctly. Finally the calculated isotope concentration can be compared with measured isotope concentration to obtain the C/E value.

3. Results

C/E Comparison

For highest burnup BWR MOX sample of MALIBU, C/E values for heavy metals are shown below. Calculation results with all libraries are agreed to measurements within about 5% for most major actinides. On the other hand, difference between calculation and measurements are over 10% for some minor actinides.

For major actinides, the impact by difference of nuclear data is relatively large about ^{234}U and ^{238}Pu. For minor actinides, the impact by difference of nuclear data is larger than for major actinides and is large about ^{237}Np, ^{241}Am, ^{243}Cm, ^{244}Cm and ^{245}Cm, as shown in Fig. 2.

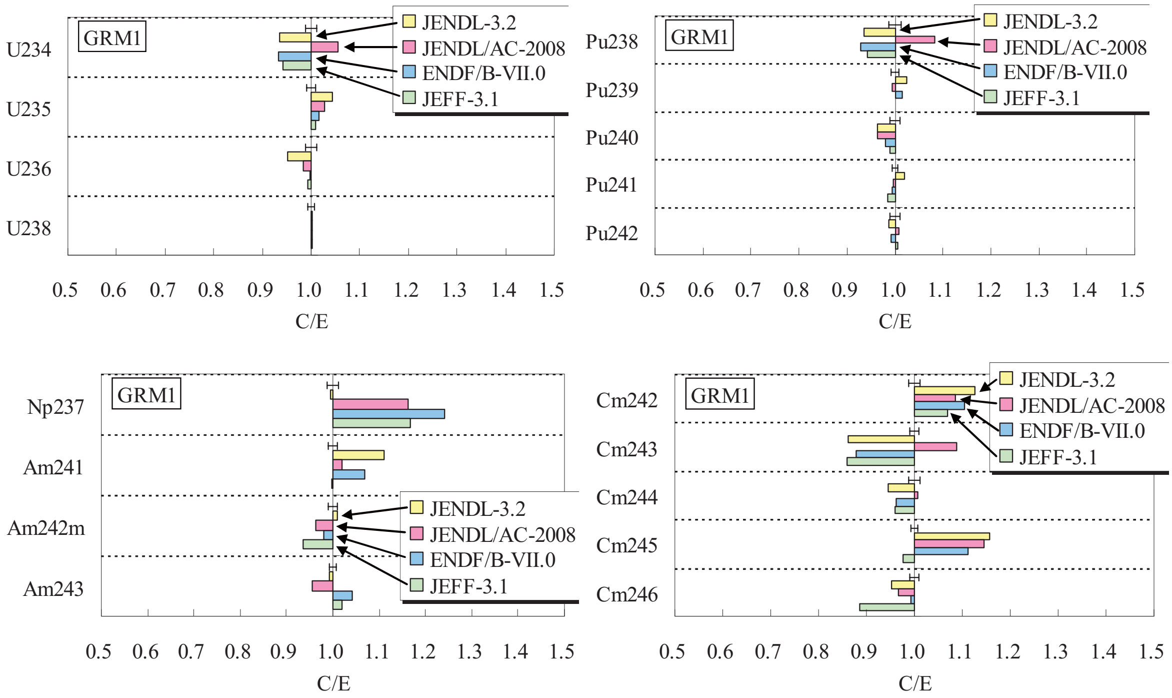

Fig. 2 C/E Comparison of 4 major evaluated nuclear data file with MALIBU GRM1.

C/C Comparison

To measure the characteristics of JENDL-4.0 from a viewpoint of isotope concentration, C/C comparison was performed. The latest 4 evaluated nuclear data files, including JENDL-4 for isotope concentration at high burn up BWR MOX condition were compared with JENDL-3.2.

JENDL-4.0, JENDL/AC-2008, JEFF-3.1 and ENDF/B-VII.0 are subject for comparison. JENDL/AC-2008 was used with combination of JENDL-3.2.

C/C comparison of major and minor actinides is shown in Fig. 3. Isotope concentration evaluated by JENDL-4.0 is very close to JENDL/AC-2008 result. Remarkable characteristic of JENDL-4.0 are that isotope concentration of ^{234}U, ^{238}Pu and ^{243}Cm is 10% or more higher than other libraries results.

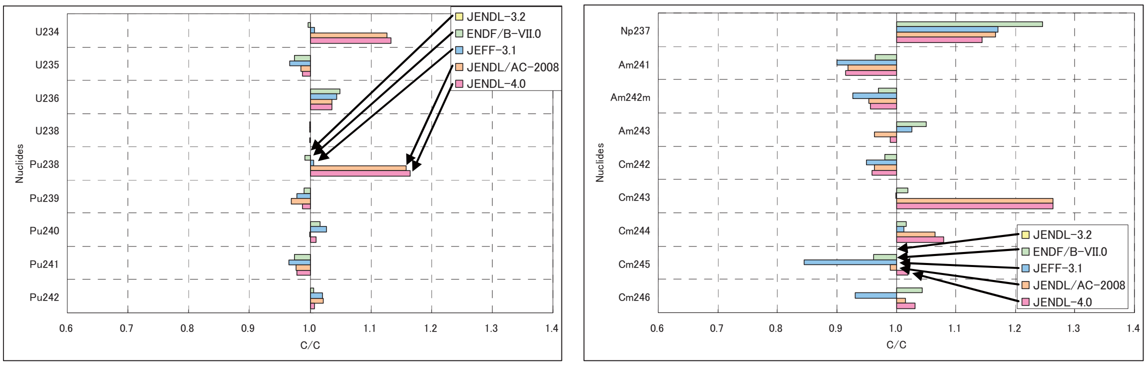

Fig. 3 C/C Comparison of 4 major evaluated nuclear data file with JENDL-3.2

4. Conclusion

The characteristics of the latest evaluated nuclear data were measured from a view point of isotope concentration prediction. For major heavy metal isotopes, their performances are excellent. For minor heavy metal isotopes, their performances are good, but some remarkable differences are observed. An analysis of performance of JENDL-4.0 is evaluated by C/C comparison. Its characteristic is similar to JENDL/AC-2008 for major and minor actinides.

References

1) O. Iwamoto, T. Nakagawa, N. Otuka et al., "JENDL actinoid file 2008," *J. Nucl. Sci. Technol.,* **46**[5], 510 (2009).

2) M. B. Chadwick, P. Oblozˇinsky´, M. Herman et al., "ENDF/B-VII.0: Next generation evaluated nuclear data library for nuclear science and technology," *Nucl. Data Sheets*, **107**, 2931 (2006).

3) A. Santamarina, D. Bernard, Y. Rugama (Eds.), *The JEFF-3.1.1 Nuclear Data Library,* JEFF Report 22, OECD/NEA (2009).

4) K. Shibata, O. Iwamoto, T. Nakagawa et al., "JENDL-4.0: A new library for nuclear science and engineering," *J. Nucl. Sci. Technol.*, **48**[1], 1 (2011).

5) D. Boulanger, M. Lippens, J. Basselier, "High burnup PWR and BWR MOX fuel performance: A review of BELGONUCLEAIRE recent experimental programs," *Proc. Int. Mtg. on LWR Fuel Performance*, Orland, Florida, Sept. 19-22, paper1109 (2004).

6) S. Matsuoka, T. Ito, "Impact of difference of neutron cross section libraries to isotopic concentration of actinides," *Proc. Int. Conf. on Advances in Reactor Physics to Power the Nuclear Renaissance (PHYSOR 2010)*, Pittsburgh, Pennsylvania, USA, May 9-14 (2010).

7) T. Nakagawa, K. Shibata, S. Chiba, et al., "Japanese evaluated nuclear data library version-3 revision 2: JENDL-3.2," *J. Nucl. Sci. Tchnol.*, **32**, 1259 (1995).

8) K. Okumura, T. Mori, M. Nakagawa, et al., "Validation of a continuous-energy monte carlo burn-up

code MVP-BURN and its application to analysis of post irradiation experiment," *J. Nucl. Sci. Technol.*, **37**, 128 (2000).

9) A. Koning, R. Forrest, M. Kellett et al. (Eds.), *The JEFF-3.1 Nuclear Data Library,* JEFF Report 21, OECD/NEA (2006).

10) K. Tasaka, J. Katakura, H. Ihara et al., *JNDC Nuclear Data Library of Fission Products−Second Version−,* JAERI 1320, Japan Atomic Energy Research Institute (JAERI) (1990).

11) T. Ito, Y. Kanayama, S. Matsuoka, "Burnup determination by using Multiple Burnup Indicators for MALIBU high burnup samples," *Proc. of Int. Conf. on the Physics of Reactors "Nuclear Power: A sustainable Resource" (PHYSOR 2008)*, Interlaken, Switzerland, Sept. 14-19 (2008).

5. Measurements of Neutron-Capture Cross Sections at J-PARC/MLF/ANNRI (1)

Measurements of Neutron-Capture Cross Sections of
Minor Actinides using a high intensity pulsed neutron source

A. KIMURA*, T. FUJII[1], S. FUKUTANI[1], K. FURUTAKA, S. GOKO* , H. HARADA, J. HORI[1], M. IGASHIRA[2], T. KAMIYAMA[3], T. KATABUCHI[2], T. KIN, K. KINO[3]** , F. KITATANI, Y. KIYANAGI[3], M. KOIZUMI, M. MIZUMOTO[2], S. NAKAMURA, M. OHTA*** , M. OSHIMA, K. TAKAMIYA[1], and Y. TOH
Nuclear Science and Engineering Directorate, Japan Atomic Energy Agency
2-4 Shirakata Shirane, Tokai, Naka, Ibaraki 319-1195, Japan
[1]Research Reactor Institute, Kyoto University
[2]Research Laboratory for Nuclear Reactors, Tokyo Institute of Technology
[3]Graduate School of Engineering, Hokkaido University
* Present address: Graduate School of Engineering, Hokkaido University
** Present address: High Energy Accelerator Research Organization
*** Present address: Center of Atomic and Molecular Technology, Osaka University
Email: Kimura.atsushi04@jaea.go.jp

In order to improve data accuracy of neutron-capture cross sections of minor actinides (MAs) and long-lived fission products (LLFPs), a new experimental instrument named "Accurate Neutron-Nucleus Reaction measurement Instrument (ANNRI)" has been constructed in the Materials and Life science experimental Facility at the Japan Proton Accelerator Research Complex, and measurements of neutron-capture cross sections of MAs and LLFPs with high intensity pulsed neutrons have been started. Together with a brief view of ANNRI, preliminary neutron-capture cross sections of ^{244}Cm and ^{246}Cm are reported as examples of the measurements of the MAs.

1. Introduction

Accurate data of neutron-capture cross sections of minor actinides (MAs) and long-lived fission products (LLFPs) are being required to estimate the production and the transmutation rates in the field of nuclear systems such as transmutation of radioactive waste and various innovative reactor systems[1-2]. However, accurate measurements of these cross sections are very difficult due to high radioactivity of these samples.

To satisfy these demands, Accurate Neutron-Nucleus Reaction measurement Instrument (ANNRI) has been developed by the collaboration of Hokkaido University, Tokyo Institute of Technology and JAEA. ANNRI is located on the Beam Line No. 04 of the Materials and Life science experimental Facility (MLF) at the Japan Proton Accelerator Research Complex (J-PARC).

[3] Measurements of neutron-capture cross sections of MAs and LLFPs have been started. Some very preliminary neutron-capture cross sections were reported in the 2010 International Conference on Nuclear Data for Science and Technology (ND2010) and a rapid communication. [4-7] In this part (1), a brief view of ANNRI and, as examples of the measurements of the MAs, preliminary neutron-capture cross sections of ^{244}Cm and ^{246}Cm were reported.

2. A brief view of ANNRI

2.1 ANNRI Beam Line

A new experimental apparatus, ANNRI, is located on the Beam Line No. 04 of the MLF in the J-PARC. Fig. 1 shows a photo of ANNRI and Fig. 2 shows a schematic view of ANNRI. The neutron beam goes through a T0 chopper, a neutron filter, a double disk chopper, and a rotary collimator and two experimental areas, and then is dumped into a beam stopper. There are two detector systems in ANNRI. One is a large germanium (Ge)-detectors array named "4π Ge spectrometer". The "4π Ge spectrometer" is the main detector of ANNRI and located at a flight-length of 21.5 m. The other one is a NaI spectrometer located at a flight-length of 27.9 m. Using the NaI spectrometer, a reliable analysis is possible by the established pulse-height weighting technique.[8] The most downstream collimator, "rotary collimator", defines the spatial

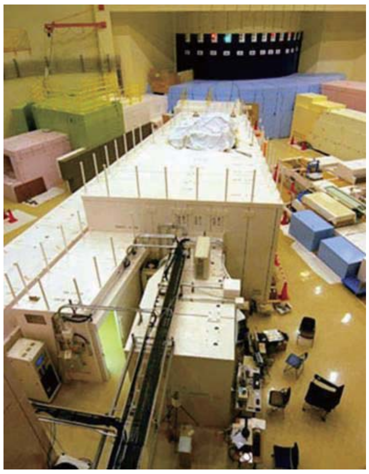

Fig.1. An outward appearance of ANNRI

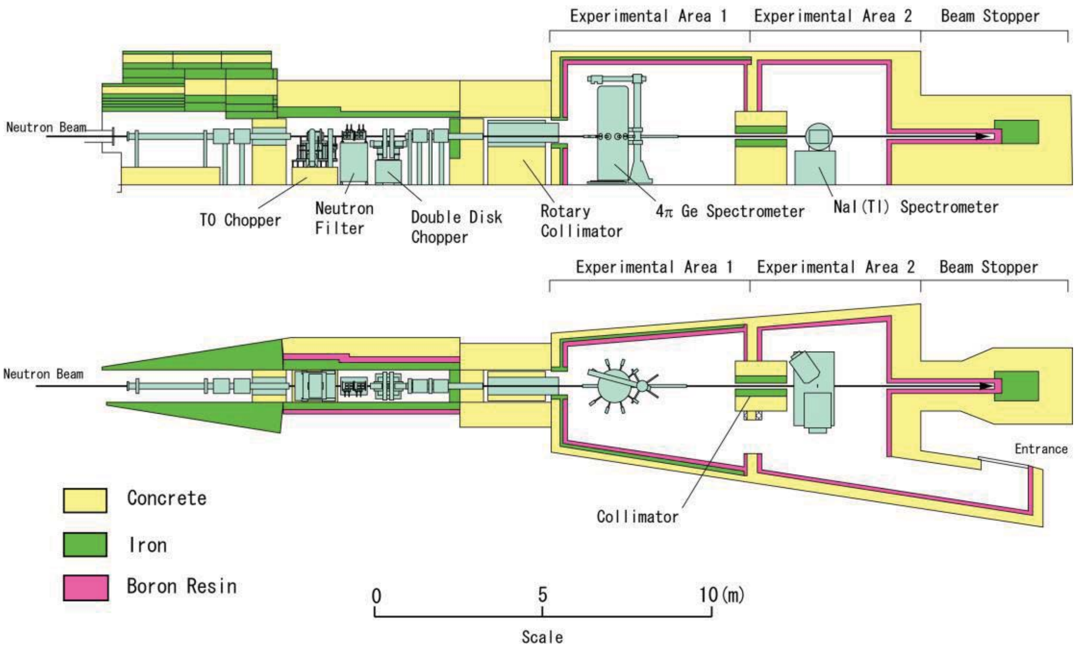

Fig. 2. A schematic view of ANNRI. There are two detector systems in ANNRI. "4π Ge spectrometer" is the main detector of ANNRI and located at a flight-length of 21.5 m. A NaI spectrometer located at a flight-length of 27.9 m.

distribution of the neutron beam at the 21.5-m sample position. Using the rotary collimator, neutron beams with diameters of 22, 7, and 3 mm to suit samples of different sizes are provided at the 21.5-m sample position.

2.2 Characteristics of the neutron beam at ANNRI

The energy resolution of the neutron beam at the 21.5-m sample position depends on the moderator system and the proton-beam operation of MLF. The proton beam usually consists of two bunches with a distance of 600 ns. The width of each bunch increases up to 185 ns depending on an incident proton beam power to MLF. [9] In the case of two bunches in the proton beam, the resolution deteriorates gradually above 10 eV as the energy increases and reaches to about 10% at 10 keV. 9) The energy-integrated neutron intensities under 120 kW operation are 4.5×10^6 n/s/cm^2 in the neutron energy range of 1.5-25 meV, and 6.6×10^5 n/s/cm^2 in 0.9-1.1 keV at the 21.5-m sample position. Under the future 1-MW operation, these intensities are expected to increase to 4.3×10^7, and 6.3×10^6 n/s/cm^2. [10] The proton intensity of shots was stable within 1% in FWHM.

2.3 The "4π Ge spectrometer"

The "4π Ge spectrometer" is composed of two cluster-Ge detectors and eight coaxial-shaped Ge detectors as seen in Fig. 3. The Ge detectors were covered with BGO Compton suppression detectors, which eliminated background Compton events. The peak efficiency of the "4π Ge spectrometer" is 3.64 ± 0.11 % for 1.33-MeV γ rays. A typical energy resolution is 9.8-keV (on beam) and 2.4keV (off beam) in FWHM for 1.33-MeV γ rays. [11]

Fig.3. An outward appearance of the"4π Ge spectrometer"

2.4 Data Acquisition System

A data acquisition system (DAQ) for the "4π Ge spectrometer" is required to deal with a large amount of signals from the spectrometer. Since MA samples are highly radioactive and the DAQ has to handle high event rates, a high performance DAQ system based on a digital data processing technique is developed. [12] The time resolution of the DAQ is 10 ns. The dead time of this system is only 3.3 μs per event at 50k events/s and the maximum event rate is more than 200k events/s.

3. Measurements of Neutron-Capture Cross Sections of ^{244}Cm and ^{246}Cm

^{244}Cm and ^{246}Cm are the most important nuclei in MAs. However, only one neutron-capture cross-section data was made in the past. [13] Furthermore, this previous measurement was performed by the neutron time-of-flight (TOF) method using the nuclear explosion "Physics 8" as a pulsed neutron source in 1969. The accuracy in this neutron-capture cross-section measurement is not enough for these demands of 10%. [1] In the ND2010, very preliminary neutron-capture cross sections of ^{244}Cm and ^{246}Cm were reported. [4] In this paper, having additional measurements and analyses, preliminary but more accurate neutron-capture cross sections of ^{244}Cm and ^{246}Cm are reported.

3.1 Experimental Set up

A target in a ^{244}Cm sample was 0.6-mg curium oxide, its activity was 1.8GBq and isotopic abundance was 89.6%. That in ^{246}Cm sample was 2.1-mg curium oxide with a 27.5% contamination of ^{244}Cm and its activity was 12.1 MBq from ^{246}Cm and 1.7 GBq from ^{244}Cm. [14] The samples were sealed in aluminum capsules 9 mm in diameter and 0.5 mm thick walls. Using the “4π Ge spectrometer” with a neutron time-of-flight method, both energy of neutrons and prompt-γ rays from the samples were measured at the same time. The measurement time for the ^{244}Cm sample was about 80 hours and that for the ^{246}Cm sample was about 100 hours. For the background estimation, a measurement with a dummy sample of the aluminum case without curium oxide powder was done for 40 hours and a measurement with neither of a sample material nor the sample case (only with a sample holder) was done for 32 hours. In the measurements, MLF was operated at an average beam power of 120 kW, and a repetition rate of 25 Hz. For dead-time correction, pulses from a random-pulse generator (Berkeley Nucleonics : DB-2) were input through the “test input” of the pre-amplifier of every Ge crystal.

3.2 Data Processing and Analysis

Fig. 4 shows neutron-capture γ-ray yields of the ^{244}Cm, the ^{246}Cm sample, and the dummy case. In these experiments, neutron energies were calibrated with resonances in ^{197}Au(n, γ) reaction. Resonance peaks of ^{244}Cm, ^{246}Cm, and ^{248}Cm are clearly observed.

In the experiments, pulses from the random-pulse generator were input and measured with the DAQ. The stored counts were used for the dead time correction by comparing the counts of input pulses with actually stored pulses. Time dependent dead time was obtained from this method. [15]

Neutron-energy dependent backgrounds were mainly caused by prompt γ rays from the Al case and scattered neutrons by the Al case and the helium in the beam duct. The backgrounds were derived from the neutron-capture γ-ray yields of the Al case and the blank measurement using the full-energy peaks of 7724-keV prompt γ rays from ^{27}Al(n, γ) reactions.

The effect from the decay γ rays from ^{244}Cm, ^{28}Al, and the other activated nuclides was also deduced from the counts in the TOF time range after 30 ms by extrapolation with exponential and constant function.

Self-shielding and multi-scattering factors of the Cm samples and the Al case were calculated with the MCNP code. The incident neutron flux shape was deduced from neutron-capture γ-ray yields of the 478-keV γ ray from ^{10}B(n,αγ) reactions. [16]

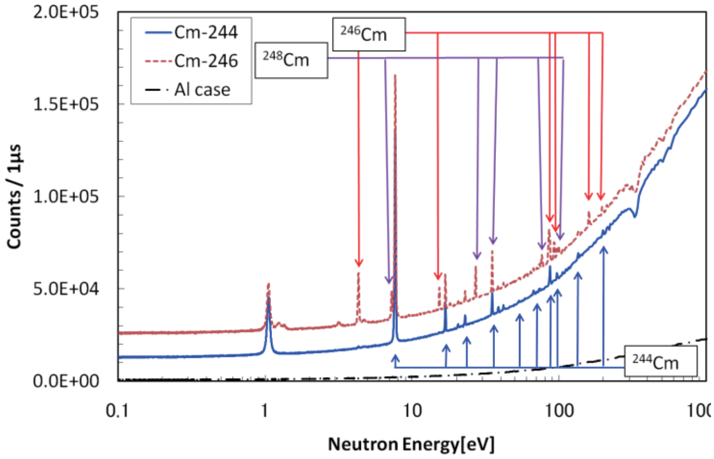

Fig. 4. Neutron-capture γ-ray yields of the ^{244}Cm sample (dashed line), the ^{246}Cm sample (solid line), and the dummy Al case (dashed-dotted line).

3.3 Preliminary Results

Relative cross sections were deduced with these corrections and the incident neutron flux. Absolute values were normalized to the values of those in JENDL 4.0 at the 1st resonances. Fig. 5 (a) shows a comparison of our preliminary neutron-capture cross section of ^{244}Cm with the one given by Moore [13], and the evaluated value of JENDL 4.0 [17]; and Fig. 5 (b) shows a comparison for ^{246}Cm.

The results of the 7.67-eV and 16.77-eV resonance peaks of ^{244}Cm and the 4.32-eV and 15.30-eV resonance peaks of ^{246}Cm are the first experimental results in the world. The results show that neutron-capture cross section can be obtained using a small amount (less than 1 mg) of a high radioactive sample in ANNRI.

4. Summary

Neutron-capture cross section measurements of MAs and LLFPs using a new experimental apparatus, ANNRI, have been started. Results of these measurements show that neutron-capture cross sections can be obtained using a small amount (less than 1 mg) of a high radioactive sample in ANNRI. In near future, ANNRI will be used not only for nuclear data but also nuclear astrophysics and quantitative analysis.

Acknowledgments

Present study includes the result of "Study on nuclear data by using a high intensity pulsed neutron source for advanced nuclear system" entrusted to Hokkaido University by the Ministry of Education, Culture, Sports, Science and Technology of Japan (MEXT). This work is supported by JSPS KAKENHI (22226016 and 22760675).

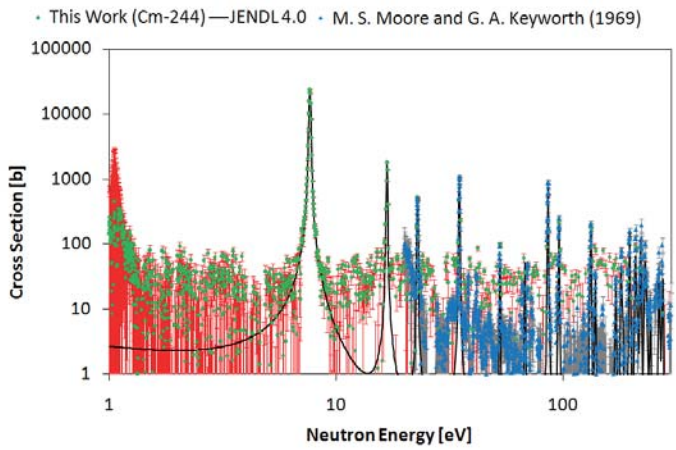

(a) Preliminary results of ^{244}Cm.

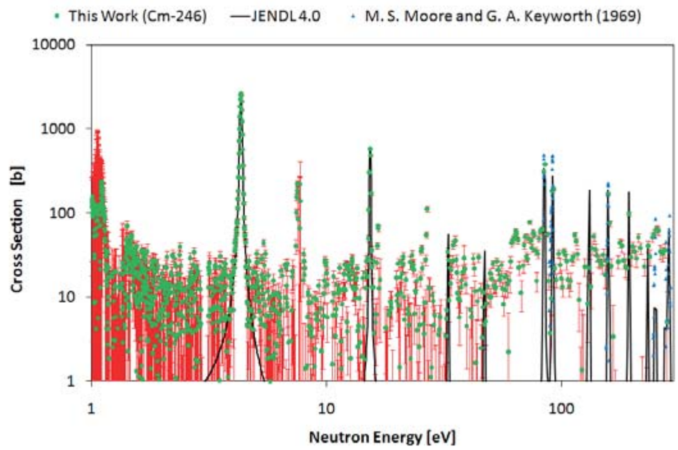

(b) Preliminary results of ^{246}Cm.

Fig.5 Preliminary results of neutron capture cross-sections of ^{244}Cm and ^{246}Cm (circles with error bars) and comparison to the one measured by Moore [13](triangles with error bars) and JENDL 4.0 [17](solid line). The experimental values were normalized at 1st resonances with the data in JENDL 4.0.

References

[1] NEA/WPEC-26, Uncertainty and target accuracy assessment for innovative systems using recent covariance data evaluations, ISBN 978-92-64-99053-1, 2008.
[2] M. Mizumoto, et al. "Neutron capture cross section measurements on 237Np with a 4π Ge spectrometer", *Proc. Int. Conf. on ND 2007*, 591 (2008).
[3] M. Oshima et. al., "Performance of a 4 π Ge spectrometer for neutron capture cross section measurements," *Proc. Int. Conf. on ND 2007*, 603(2007).
[4] A. Kimura, et al. "Measurements of neutron-capture cross sections of ^{244}Cm and ^{246}Cm at J-PARC/MLF/ANNRI", *Proc. Int. Conf. on ND 2010,* #1380 (2010).
[5] S. Nakamura, et al., "Measurements of neutron-capture cross section of palladium isotopes at the J-PARC/MLF/ANNRI", *Proc. Int. Conf. on ND 2010,* #1295 (2010).
[6] J. Hori et al., "Measurements of neutron-capture gamma rays from the resonances of ^{91}Zr and ^{96}Zr at the J-PARC/MLF/ANNRI", *Proc. Int. Conf. on ND 2010*, #1301 (2010).
[7] S. Goko, et al, "Measurement of neutron capture cross section ratios of ^{244}Cm resonances using NNRI"*, J. Nucl. Sci. Technol.* **47** 1097 (2010).
[8] S. Mizuno, et al.," Measurements of keV-Neutron Capture Cross Sections and Capture Gamma-Ray Spectra of 161, 162, 163Dy", *J. Nucl. Sci. Technol.*, **36** 493 (1999).
[9] F. Maekawa, et al., "First Neutron Production Utilizing J-PARC Pulsed Spallation Neutron Source JSNS and Neutronic Performance Demonstrated", *Nucl. Instrum. Methods. Phys. Res. A* **620**, 159 (2010).
[10] K. Kino et al., "Measurement of energy spectra and spatial distributions of neutron beams provided by the ANNRI beamline for capture cross-section measurements at the J-PARC/MLF", Nucl. Instrum. Methods. *Phys. Res. A* **626,** 58 (2011).
[11] T. Kin et. al., "Development of a 4π Germanium Spectrometer for Nuclear Data Measurements at J-PARC," *the 2009 NSS-MIC Conf. Rec.* , N24-2, (2009).
[12] A. Kimura, et. al., "Performance of a high speed and high density data acquisition system for multiple gamma-ray detection", *Conference Record of IEEE NSS/MIC/RTDS 2008,* Article Number: N30-68, (2008).
[13] M. S. Moore and G. A. Keyworth,"Analysis of the Fission and Capture Cross Secssions of the Curium Isotopes", *Physical Review C*, **3**, 1656 (1971).
[14] T. Fujii, et al. "Study on nuclear data by using a high intensity pulsed neutron source for advanced nuclear system (4) Analysis of components of the samples for nuclear data", *Conference record of 2010 Annual Meeting of AESJ*, B42 (2010) [in Japanese].
[15] A. Kimura, et al. "A Dead-Time Correction Method for Multiple Gamma-ray Detection", *Conference Record of IEEE NSS/MIC 2009,* Article Number: N07-03, (2009).
[16] M. Ohta, et al. "Measurement of Neutron Spectrum at BL04 of J-PARC / MLF", *Conference record of 2009 Fall Meeting of AESJ*, J15, (2009) [in Japanese].
[17] K. Shibata, et al., "JENDL-4.0: A New Library for Nuclear Science and Engineering," *J. Nucl. Sci. Technol.* **48**[1], 1-30 (2011).

6. Measurements of Neutron Capture Cross Sections at J-PARC/MLF/ANNRI (2)

Measurements of Neutron Capture Cross Sections of
Long-Lived Fission Products using a high intensity pulsed neutron source

J. HORI[1], T. FUJII[1], S. FUKUTANI[1], M. FURUSAKA[4], K. FURUTAKA[2], S. GOKO[2,a], H. HARADA[2], F. HIRAGA[4], M. IGASHIRA[3], T. KAMIYAMA[4], T. KATABUCHI[3], A. KIMURA[2], T. KIN[2], K. KINO[4,b], F. KITATANI[2], Y. KIYANAGI[4], M. KOIZUMI[2], M. MIZUMOTO[3], S. NAKAMURA[2], M. OHTA[2,c], M. OSHIMA[2], K. TAKAMIYA[1], and Y. TOH[2]

[1]Research Reactor Institute, Kyoto University
[2]Nuclear Science and Engineering Directorate, Japan Atomic Energy Agency
[3]Research Laboratory for Nuclear Reactors, Tokyo Institute of Technology
[4]Graduate School of Engineering, Hokkaido University
Present address : [a]Hokkaido University, [b]High Energy Accelerator Research Organization, [c] Osaka University
e-mail: hori@rri.kyoto-u.ac.jp

The neutron capture cross sections of ^{93}Zr, ^{99}Tc and ^{107}Pd have been measured relative to the ^{10}B(n,αγ) standard cross section by the neutron time-of-flight (TOF) method. Neutron capture γ rays were measured with a 4π Ge spectrometer as a part of the Accurate Neutron-Nucleus Reaction measurement Instrument (ANNRI) installed at the neutron Beam Line No.4 (BL04) of the Material and Life science experimental Facility (MLF) in the Japan Proton Accelerator Research Complex (J-PARC). This paper presents the preliminary results.

1. Introduction

The neutron capture cross sections of long-lived fission products (LLFPs) are of great importance for the research of the nuclear transmutation of radioactive waste. Seven nuclei of ^{79}Se, ^{93}Zr, ^{99}Tc, ^{107}Pd, ^{126}Sn, ^{129}I and ^{135}Cs were selected as the most important LLFPs [1]. At first, the current status of experimental data on neutron capture cross sections of those nuclei is summarized briefly.

There are no experimental data for ^{79}Se. As for the status of ^{126}Sn and ^{135}Cs, there are only available experimental data with the activation method. It is noted that the only experimental result of ^{126}Sn was recently reported at the thermal energy [2]. For ^{93}Zr and ^{107}Pd, the experimental data obtained by the neutron time-of-flight (TOF) method at the Oak Ridge Electron Linear Accelerator (ORELA) are only available in the resonance region [3,4]. Since a pair of C_6D_6 detectors was used as a capture γ-ray detector in the works, the effects due to the isotope impurities contained in a sample were subtracted by using the other experimental data on those isotopes. Therefore, the uncertainty associated with subtraction was large. The activation method is not applicable for thermal neutron capture cross section measurements since the residual nuclei are stable. Recently, Nakamura *et al.* measured the thermal neutron capture cross sections of ^{93}Zr and ^{107}Pd with a prompt γ-ray spectroscopy [5,6] and gave the only available datum for ^{107}Pd. Though Pomerance also measured the thermal capture cross section of ^{93}Zr with a pile oscillator method [7,8], there is a large discrepancy between two data with different methods. For ^{99}Tc and ^{129}I, a number of experimental data with the activation, lead spectrometer, prompt γ-ray and TOF methods were reported. However, the accuracy of experimental data for ^{99}Tc and ^{129}I was not enough since those were considered as the first priority nuclei for a transmutation.

As mentioned above, the current status of experimental data is not sufficient both in quality and in quantity. This is because it is not easy to prepare enough amount of sample with a high purity. To overcome the difficulty, we have started a series of experimental studies for LLFPs using the Accurate Neutron-Nucleus Reaction measurement Instrument (ANNRI) which was installed at the neutron Beam Line No.4 (BL04) of the Material and Life science experimental Facility (MLF) in the Japan Proton Accelerator Research Complex (J-PARC) [9]. Neutron capture γ rays from a sample were measured with a 4π Ge spectrometer using the TOF method. A high intensity pulsed neutron source makes it possible to measure the capture γ rays accurately with a small amount of sample. Moreover, the background due to impurities contained in a sample can be removed from the observed events using Ge detectors with a high energy resolution. In this paper, the preliminary results of ^{93}Zr, ^{99}Tc and ^{107}Pd are reported.

2. Experimental Procedure

The samples of ^{93}Zr, ^{99}Tc and ^{107}Pd were purchased from the Oak Ridge National Laboratory (ORNL) of USA, the Research Institute of Atomic Reactors (RIAR) of Russia and the Nuclear Research and consultancy Group (NRG) of Netherlands, respectively. The metal or oxide powder of ^{93}Zr, ^{99}Tc and ^{107}Pd were encapsulated in aluminum disk-shaped containers. A sintered natural boron sample was used for the measurement of the incident neutron flux on the sample. A crystal of NaCl sample which emits well-known γ rays from the neutron capture of chlorine was also used as a standard γ-ray source. The characteristics of samples and containers are shown in Table 1. Isotopic purities of LLFP samples were determined with a Thermal Ionization Mass Spectrometer (TIMS) as shown in Table 1 except for ^{99}Tc sample which contains no isotopic impurities. The net weight of ^{99}Tc was 78 mg. The net weights of ^{93}Zr and ^{107}Pd were determined as 470 and 20 mg using the weights of powder and the isotopic purities, respectively.

The neutron capture cross section measurements have been performed at the ANNRI. The pulsed-neutron beam was produced by spallation of 3-GeV proton beam at the Japan Spallation Neutron Source (JSNS) [10] of MLF. The accelerator was operated in a double-bunched mode at a power of 120 kW and repetition rate of 25 Hz. The 4π Ge spectrometer composed of two cluster and eight coaxial Ge detectors surrounded by BGO Compton suppression detectors was placed at a distance of 21.5 m from the pulsed neutron source. In this work, we used only two cluster Ge detectors. Each sample was set at the center

Table 1. Characteristics of samples

Sample	Chemical Form	Isotopic Compsition [%]	weight of sample [g]	Diameter of sample [mm]	Outer diameter of container [mm]
^{93}Zr	ZrO_2	18.9	3.31	20.0	30.0
^{99}Tc	Tc	100	0.078	6.3	9.0
^{107}Pd	Pd	15.3	0.137	4.5	9.0
^{10}B	B	19.9	0.083	10.0	---
^{35}Cl	NaCl	75.8	0.500	10.0	---

of the spectrometer and in a neutron beam duct. The neutron beam was collimated to a diameter of 3 or 7 mm at the sample position using a rotary collimator system [11].

The signals from the Ge crystals were stored using a data acquisition (DAQ) system [12,13] with event-by-event mode as three-dimensional data of γ-ray pulse height, TOF, and time-interval between coincidence signals. Random timing pulses were also fed into every pre-amplifier from a random generator for making a dead-time correction [14].

The measurement times for ^{93}Zr, ^{99}Tc and ^{107}Pd samples were about 52, 25 and 31 hours, respectively. In order to estimate the background, a measurement with an empty aluminum container was also done.

3. Data Processing and Analysis

The neutron flux at the sample position was deduced from the TOF spectrum corresponding to the 478-keV γ ray emitted via the ^{10}B(n,$\alpha\gamma$)^{7}Li reaction. The neutron capture cross section data were taken from JENDL-3.3 [15].

For TOF spectrum of ^{99}Tc, the background subtraction was performed using the capture γ-ray yields from an empty aluminum container. The normalization of the background TOF spectrum was performed on the basis of the prompt γ-ray emitted from the neutron capture reaction of ^{27}Al. For ^{93}Zr and ^{107}Pd which contain a large amount of impurities, the events related to an objective nuclide were extracted with a ground-state transition method [16,17]. In the case of ^{93}Zr, five ground-state transitions from the 919-, 1671-, 2846-, 2908-keV states and the capture state were clearly observed in the γ-ray pulse-height spectrum. Especially, the very strong ground-state transition at 919 keV is remarkable and the intensity amounts to about 83 % of the total intensity of five ground-state transitions. We have gated on those γ-ray peaks corresponding to the ground-state transitions and derived the net TOF spectrum for ^{93}Zr. The background component was estimated from the TOF spectra for the continuous region around the γ-ray peaks of ground-state transitions. The absolute neutron capture yields were derived with the full-energy peak efficiency curve for the 4π Ge spectrometer. In the case of ^{107}Pd, it is summarized how to reject the contribution due to impurities. The details of analysis have been described in Ref.[18]. The components due to ^{105}Pd mainly contained in the sample were extracted by gating on the ground-state transition γ ray peak at 512 keV.

The neutron capture cross sections of ^{93}Zr, ^{99}Tc and ^{107}Pd were derived from the neutron flux and the net TOF spectra. The corrections were made for the self-shielding and multiple-scattering of neutron in the sample, dead time, and so on.

4. Results and Discussion

The neutron capture cross sections of ^{93}Zr were derived in the energy range from 0.01 eV to 5 keV as shown in Fig. 1. In the thermal energy region, the present results are close to the previous value by Nakamura *et al.*[5]. However, there is an obvious discrepancy between the values of JENDL-4.0 [19] and the present data. In the keV region, the averaged cross sections by Macklin [3] are in agreement with the present data. Moreover, the resonance at 14 eV was newly found.

The neutron capture cross sections of ^{99}Tc were derived in the energy range from 0.01 eV to 1 keV. The relative cross sections were normalized to the value of JENDL-3.3 at the thermal energy. The comparison of the present results with the previous data by Kobayashi *et al.* [20] and the evaluated data of JENDL-3.3 is shown in Fig. 2. It is found that the signal-to-noise ratio has been improved remarkably compared with the previous data. The evaluated values of JENDL-3.3 are almost consistent with the present results.

The neutron capture cross sections of ^{107}Pd were derived in the energy range from 0.1 eV to 300 eV. The relative cross sections were normalized to the values of JENDL-3.3 at the third resonance peak. The present results are shown in Fig. 3 together with the thermal neutron capture cross section by Nakamura *et al.* [6] and the evaluated values of JENDL-3.3 and 4.0. In the thermal energy region, the present results support the previous value obtained by the prompt γ-ray spectroscopy and indicate that the values of JENDL-3.3 are about five times as small as the present results. However, the modified values of JENDL-4.0 are consistent with the present data.

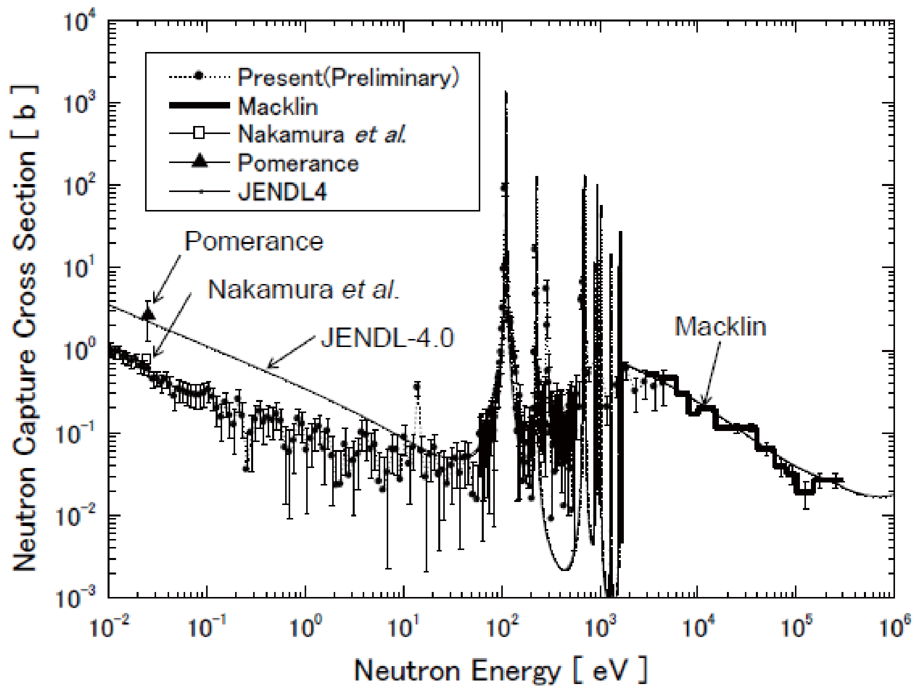

Fig. 1 Preliminary results of neutron capture cross sections of ^{93}Zr.
The previous experimental data by Macklin [3], Nakamura *et al.*[4] and Pomerance [7,8] and the evaluated values of JENDL-4.0 [19] are plotted together.

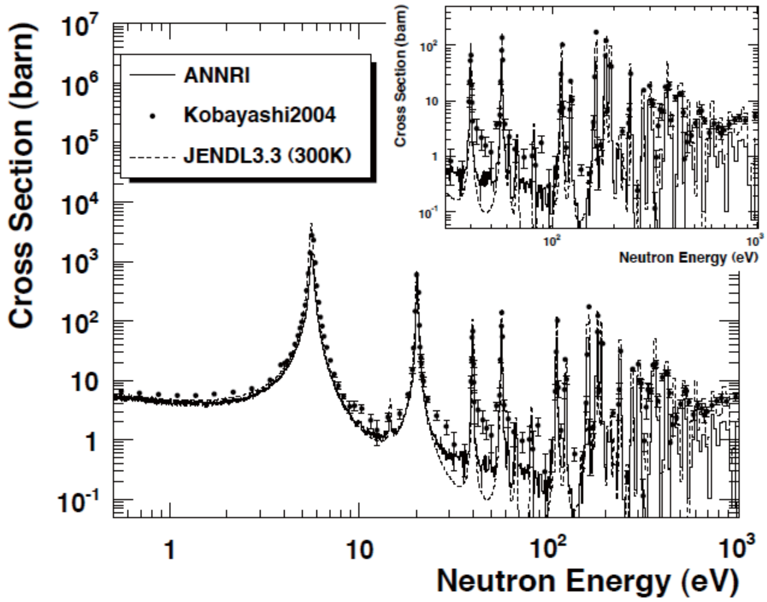

Fig. 2 Preliminary results of neutron capture cross sections of ^{99}Tc.
The previous experimental data by Kobayashi *et al.* [20] and the evaluated values of JENDL-3.3 [15] are plotted together.

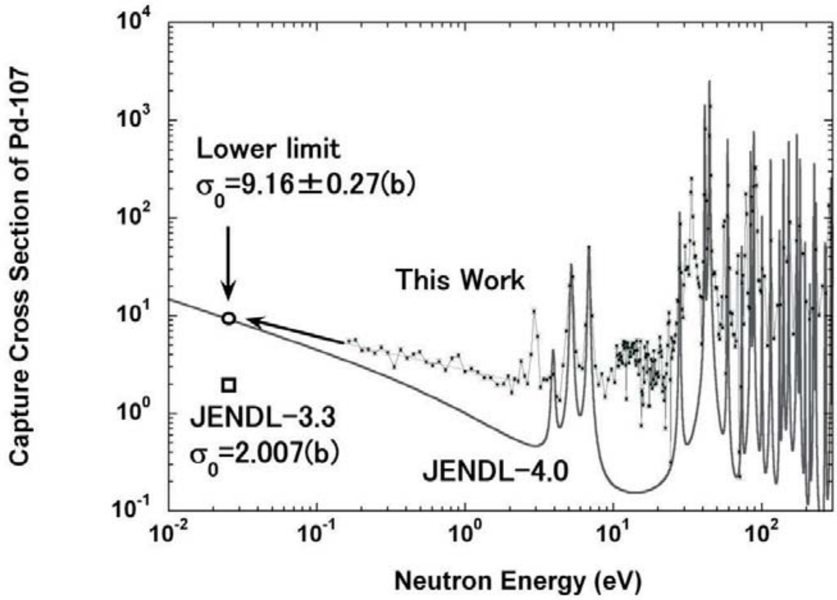

Fig. 3 Preliminary results of neutron capture cross sections of ^{107}Pd.
The previous experimental data by Nakamura *et al.* [6] and the evaluated values of JENDL-3.3 [15] and 4.0[19] are plotted together.

5. Summary

The preliminary neutron capture cross sections of ^{93}Zr, ^{99}Tc and ^{107}Pd were obtained by the TOF method at the ANNRI/MLF/J-PARC. The results of ^{99}Tc show that the signal-to-noise ratio has been improved remarkably compared with the previous experiments. For ^{93}Zr and ^{107}Pd, the background due to impurities contained in the sample was able to be successfully subtracted with the ground-state transition method. In the near future, final results will be published for each nuclide.

Acknowledgments

Present study includes the result of "Study on nuclear data by using a high intensity pulsed neutron source for advanced nuclear system" entrusted to Hokkaido University by the Ministry of Education Culture, Sports, Science and Technology of Japan (MEXT).

References

[1] H. Harada, *et al.*, "Plan of LLFP neutron cross section measurements for nuclear transmutation," *J. Nucl. Sci. Technol.*, Suppl. **2**, 366 (2002).

[2] S. Zhang, *et al.*, "Measurement of thermal neutron cross sections of the reactions ^{126}Sn(n,γ)^{127g,127m}Sn," *Radiochim. Acta*, **94**, 385 (2006).

[3] R. L. Macklin, "Neutron capture measurements on radioactive ^{93}Zr," *Astrophys. Space Sci.*, **115**, 71 (1985).

[4] R. L. Macklin, "Neutron capture and transmission measurements on fission product ^{107}Pd," *Nucl. Sci. Eng.*, **89**, 79 (1985).

[5] S. Nakamura, *et al.*, "Thermal neutron capture cross sections of Zirconium-91 and Zirconium-93 by prompt γ-ray spectroscopy," *J. Nucl. Sci. Technol.*, **44**, 1, 21 (2007).

[6] S. Nakamura, *et al.*, "Thermal neutron capture cross section of Palladium-107," *J. Nucl. Sci. Technol.*, **44**, 2, 103 (2007).

[7] H. Pomerance, "Neutron cross section and fission physics," ORNL-1879, 50 (1955).

[8] H. Pomerance, "Thermal neutron capture cross sections," *Phys. Rev.*, **88**, 412 (1952).

[9] M. Igashira, *et al.*, "Nuclear data study at J-PARC BL04," *Nucl. Instrum. Meth.*, **A 600**, 332 (2009).

[10] Y. Ikeda, "J-PARC status update," *Nucl. Instrum. Meth.* **A 600**, 1 (2009).

[11] K. Kino, *et al.*, "Measurement of energy spectra and special distributions of neutron beams provided by the ANNRI beamline for capture cross-section measurements at the J-PARC/MLF," *Nucl. Instrum. Meth.* , **A 626-627**, 58 (2011).

[12] A. Kimura, *et al.*, "Development of a data acquisition system for a multiple gamma-ray detection method," *AIP Conference Proceedings*, **769**, 784 (2005).

[13] A. Kimura, *et al.*, "Performance of a high speed and high density data acquisition system for multiple gamma-ray detection," *Conference Record of IEEE NSS/MIC/RTDS 2008*, Article Number: N30-68 (2008).

[14] A. Kimura, *et al.*, "A Dead-Time Correction Method for Multiple Gamma-ray Detection," *Conference Record of IEEE MSS/MIC 2009*, Article Number: N07-03 (2009).

[15] K. Shibata, *et al.*, "Japanese Evaluated Nuclear Data Library Version 3 Revision-3: JENDL-3.3," *J. Nucl. Sci. Technol.*, **39**, 1125 (2002).

[16] S. Raman, *et al.*, "Thermal-neutron capture by ^{58}Ni, ^{59}Ni, and ^{60}Ni," *Phys. Rev.*, **C 70**, 044318 (2004).

[17] K. Furutaka, *et al.*, "Prompt gamma rays emitted in thermal-neutron capture reaction by ^{99}Tc and its reaction cross section", *J. Nucl. Sci. Technol.*, **41**, 1033-1046 (2004).

[18] S. Nakamura, *et al.*, "Measurements of neutron-capture cross sections of palladium isotopes at the J-PARC/MLF/ANNRI", Proc. Int. Conf. on Nuclear Data for Science and Technology, April 26-30, 2010, Jeju Island, Korea, #1295 (2010).

[19] K. Shibata, *et al.*, "JENDL-4.0: A New Library for Nuclear Science and Engineering," *J. Nucl. Sci. Technol.*, **48**, 1 (2011).

[20] K. Kobayashi, *et al.*, "Neutron Capture Cross-Section Measurement of ^{99}Tc by Linac Time-of-Flight Method and the Resonance Analysis," *Nucl. Sci. Engin.*, **146**, 209 (2004).

7. Research in Surrogate Reactions at JAEA

Satoshi Chiba
Advanced Science Research Center, Japan Atomic Energy Agency
Tokai-mura, Naka-gun, Ibaraki-ken 319-1195 Japan
e-mail: chiba.satoshi@jaea.go.jp

A novel method to measure neutron cross sections of unstable or rare nuclei, namely, the surrogate reaction method, is becoming a unique tool in the field of nuclear data and nuclear astrophysics. We will describe a status of research in the surrogate method based on heavy-ion as well as light-ion projectiles carried out at JAEA in collaboration with other organizations.

1. Introduction

Accurate nuclear data for rare or unstable nuclei are more and more necessitated in design of next-generation high-burnup reactors and fast reactors acting as transmuters of long-lived radioactive nuclei contained in nuclear wastes. For these nuclei, direct measurements using neutrons are extremely difficult to be carried out. Therefore, a lot of important data still remain unmeasured in the minor-actinide and fission product reagions. Similary, nuclear data for unstable nuclei at branching points of the s-process are necessary to assess astrophysical conditions such as density and temperature of the s-process cite.

Recently, a new method called surrogate method is actively applied to measure neutron cross section indirectly using available targets. This method utilizes nucleon transfer reactions or inelastic scattering to populate excited nuclei which correspond to compound nuclei in neutron-induced reactions on a target nucleus having one-less neutron. Then, decay branching ratios to fission or capture channel can be determined in principle. A conceptual drawing of the surrogate method is shown in **Fig. 1**. This particular figure explains a way to determine neutron cross sections of ^{239}U which has a half life of only 23.5 min. Obviously, we cannot conduct direct measurements using neutrons on a ^{239}U target. Instead, we will prepare in the surrogate method a target of ^{238}U and use a 2 neutron transfer reacction, ^{238}U(^{18}O,^{16}O)^{240}U* reaction, to populate the same compound nucleus ^{240}U as the desired ^{239}U+n reaction.

Already, US-French collaboration has yielded some interesting results (see, e.g., refs. [1,2] and references therein). However, physical foundation of the surrogate method is not established yet. The problem lies in the fact that the spin and parity distributions of the nuclei populated by the surrogate reactions are not easy to be determined due to the complexity of relevant reaction mechanisms. Furthemore, the spin-distributions are (very probably) different from those of the neutron-induced reactions, while the decay branching ratios are sensitive to the spin-parity values in the energy range of our interest.

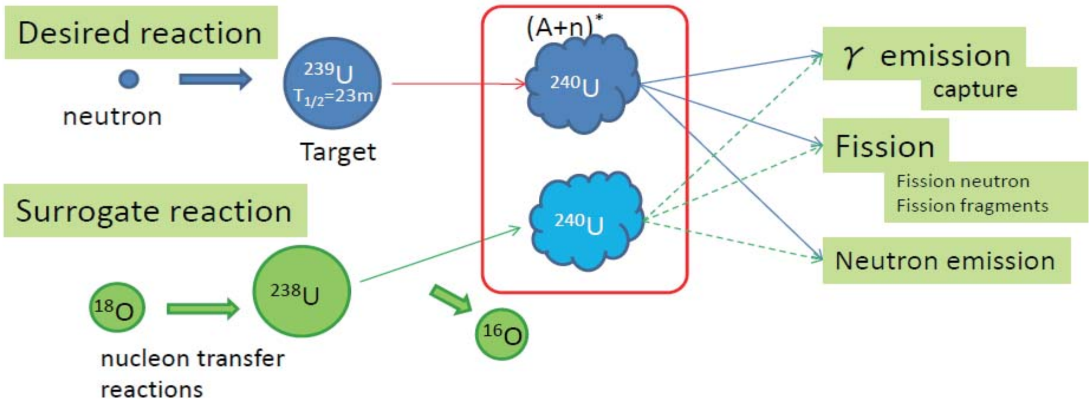

Fig. 1 A conceptual picture of the surrogate reaction. This particular example shows a way to determine neutron cross sections of short-lived nucleus ^{239}U ($T_{1/2}$=23 min.) by populating the same compound nucleus ^{240}U via ^{238}U(^{18}O,^{16}O)^{240}U reaction.

These problems are fundamental in nature, so reseach from the viewpoint of nuclear physics is necessary to understand the underlying physics and to really yield the desired neutron cross section data by the surrogate method.

In this paper, a JAEA-based activity on the installation of equipments for the surrogate method and its physical justification will be explained briefly below.

2. Strategy

By using the surrogate method, we plan to determine primalily 1) fission cross sections, 2) capture cross sections, and subsequently 3) fission-fragment mass distributions and 4) number of prompt neutrons per fission, of minor actinides. Also, capture cross sections of LLFPs and some nuclei relevant to the s-process nucleosynthesis are in our scope. Therefore, our detection system must involve i) charged-particle deterctors to identify the populated nuclear species and their excitation energies, ii) fission fragment detectors, iii) γ-ray detectors and iv) neutron counters. The system is

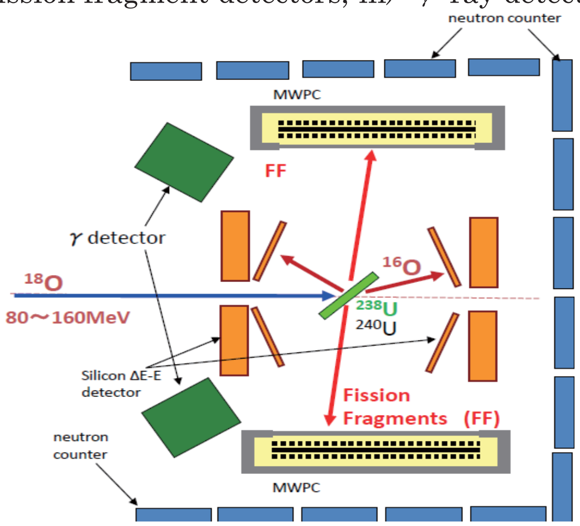

Fig.2 A schematic layout of the surrogate detection system under plan

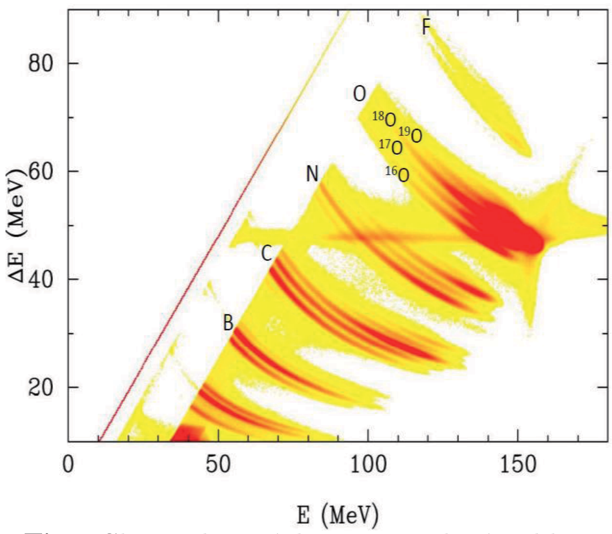

Fig.3 Charged-particle spectra obtained by a silicon ΔE-E deterctor

shown schematically in **Fig. 2**. The charged particles are detected by silicon ΔE and E detectors, which will yield a signal such as shown in **Fig. 3**. This spectrum was taken in a test experiment for the ^{18}O + ^{238}U system as explained below. We can observe various isotopes of O, N and C (although not designated). They correspond to population of a series of U, Np and Pu isotopes as compound nuclei. Therefore, surrogate reactions based on heavy-ion projectiles have a certain advantage that they can populate many compound nuclei cimultaneously, while those based on light ions such as ^{3}He can populate less variety.

3. Test experiment and detector development

We carried out a text experiment to verify that the surrogate method based on heavy-ion projectiles can yield desired fission properties[3]. We have chosen the ^{18}O + ^{238}U system, for which we have enough experience in the in-beam γ-ray spectroscopy. The detecor consists of the silicon ΔE-E counter and the MWPC (multi-wire proportional counter for detection of fission fragments) of **Fig. 2**. **Figure 4** shows the number of coincidence events between ^{16}O ejectile and fission fragments as a function of the excitation energy of residues. We observe a clear threshold of 5.5 MeV, which coincides with the fission barrier of ^{240}U. This result therefore shows population of ^{240}U and decay of it to the fission channel. At the upper horizontal axis, equivalent neutron energy in the n+^{239}U system is indicated. We also observed fission fragment mass distribution (FFMD) from a number of residues. Some examples are shown in **Fig. 5**. All these FFMD data were observed for the first time (still preliminary though). Therfore, it was justified that the surrogate method based on the heavy-ion projectiles can yield a large variety of new data. Based on these experiments, we finalized design of our equipments. We have also prepared an anti-Compton γ-ray detector system. The main detectors of it are two 4"-dia. by 5"-thick LaBr$_3$(Ce) scintillators. The fission neutrons will be measured by an array of NE213 liquid scintillators.

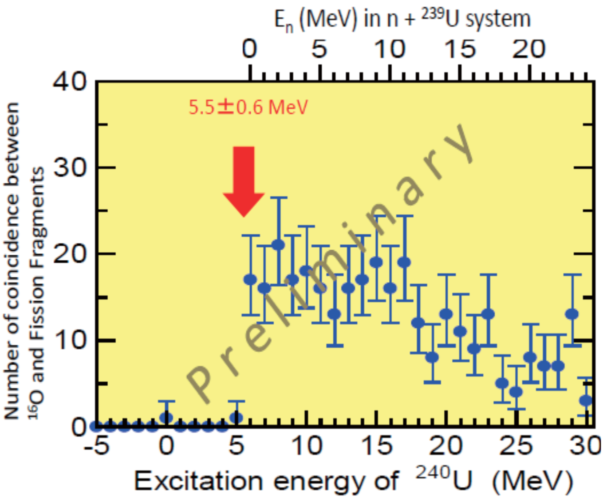

Fig.4 Number of coincidence events between ^{16}O and fission fragments for a $^{238}U(^{18}O,^{16}O)$ reaction[3]

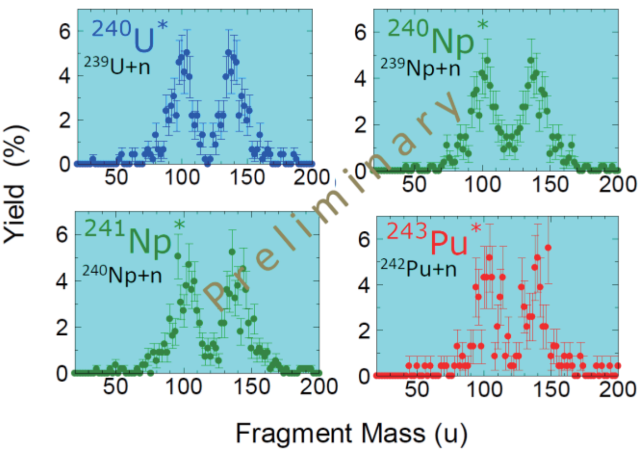

Fig.5 Prelimiary FFMD data from various residues measured by a surrogate reaction ^{238}U+^{18}O[3]. FFMDs from these nuclei were not observed in the past

4. Theoretical studies

Theoretical investigations of the surrogate reactions are important since simple Weisskopf-Ewing approximation is not applicable to low-energy neutron reactions. Therefore we have to find condition under which the surrogate method really yields information which can be converted to desired neutron cross sections. Especially, the capture cross section may deviate by a factor of 5 or more due to the difference of spin distributions between neutron-induced and surogate reactions[2]. Recently, SC and Iwamoto have discoved a condition for the surrogate "ratio" method to work[4]. Surrogate ratio method requirs an existence of 2 pairs of neutron-induced and corresponding surrogate reactions. It was concluded that 1) the weak Weisscopf-Ewing condition defined in ref. [4] should be satisfied, 2) the 2 surrogate reactions should yield equivalent spin-parity distributions, and 3) the maximum spin populated by the surrogate reactions must not be too large (less than 10 hbar) compared to the neutron-induced reactions. It was demonstrated that even the capture cross section can be determined with an accuracy of around 10% if they are fulfilled. In ref. [4], however, the conditions 2) and 3) were simply assumed. Then, we verifed these conditions based on both quantal[5] and semi-classical[6] models in subsequent works.

The quantal model describes the ^{238}U(^{18}O,^{16}O)^{240}U reaction as a one-step transfer of a dineutron from ^{18}O to ^{238}U by a three-body piture[5]. The model is formulated as a Born-approximation with a CDCC (coupled discretized continuum channels) wave function which includes the breakup effects. The calculated angular distributions corresponding to different values of spin transfer are shown in **Fig. 6**. The incident energy was chosen to be 160 MeV which is close to the energy we are planning in actual experiments. We notice that this reaction yields a well-defined peak at the grazing angle, forming a well defined spin distribution. It shows that the whole process proceeds in the semi-classical manner (like Fresnel diffraction). The transferred spin has a maximum at 5, and the spin distribution do not depend much on the angle and target

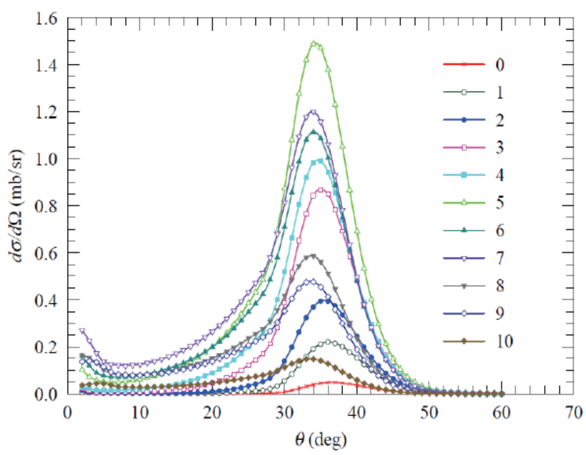

Fig.6 Angular distribution of ^{16}O for different spin-transfer values (denoted by numbers) in the ^{238}U(^{18}O,^{16}O)^{240}U$_{g.s.}$ reaction at incident energy of 160 MeV[5]

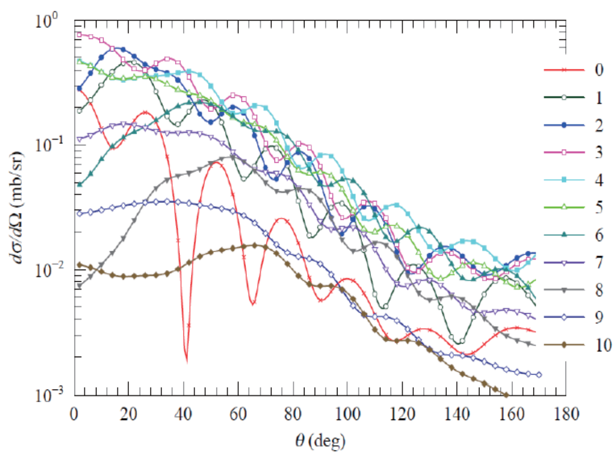

Fig.7 Angular distribution of protons for different spin-transfer values in the ^{238}U(^{3}He,p)^{240}Np$_{g.s.}$ reaction at incident energy of 30 MeV[5]

nucleus[5]. Therefore, the conditions 2) and 3) of SC and Iwamoto paper explained above are shown to be satisfied within this model. Such a feature is in sharp constrast to what we expect for light-ion induced surrogate reactions which exhibit typical quantum-mechanical diffraction patterns (see **Fig. 7**), which makes the spin distribution very sensitive to the detection angle, Q-value and target mass. The quantal model will be used to investigate physics occuring in the initial stage of the reaction.

It was shown above by a quantum-mechanical model that the reaction $^{18}O+^{238}U$ proceeds in a semi-classical manner. Therefore, it makes sense that we construct a semi-classical model which can describe the whole process of surrogate reactions. Such a model is implemented[6] based on the unified model of Zagrevaev and Greiner[7]. In this model, the reaction is assumed to go through initially on a diabatic potential energy surface of the total composite system, ^{256}Fm, and nucleon transfer is described by an inertialess change of asymmetry parameter. Then, we switch to the potential enregy surface of residues, e.g., ^{240}U, and decay of it is considered (**Fig. 8**). Time evolution of the whole process is described by a dissiption-fluctuation theorem in terms of a set of coupled Langevin equations. The potential energy surfaces are calculated by a folding model for initial diabatic phase and by the 2-center shell model otherwise.

This semi-classical model is powerful enough so it can predict almost all of the observables of the surrogate reactions, namely, the angular and energy distribution of the ejectile, the mass, energy and angular distribution of the fission fragments, and angular and energy distribution of emitted neutrons via evaporation, pre-scission emission and emission from fission fragments. These imformation are vital to assess the spin distribution of populated compound nuclei.

An example of the predicted fission fragment mass distribuions from ^{256}Fm and ^{240}U are compared in **Fig. 9** with experimental data obtained in the test experiment (still preliminary). These data can be obtained cimultaneously in the $^{18}O+^{238}U$ reaction system. We notice that the present model can describe both the single-peaked distribution from a highly-excitged ^{256}Fm nucleus and the double-peaked asymmetric

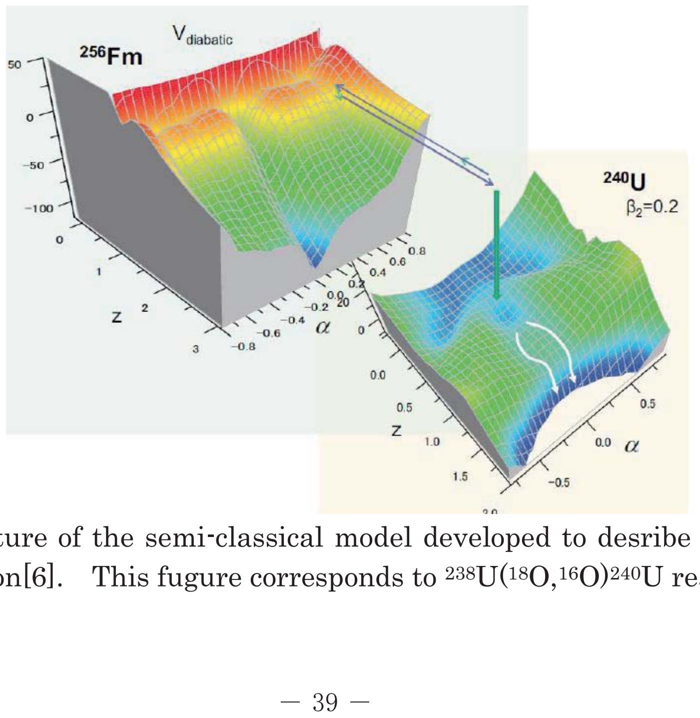

Fig.8 Schematic picture of the semi-classical model developed to desribe whole process of the surrogate reaction[6]. This fugure corresponds to $^{238}U(^{18}O,^{16}O)^{240}U$ reaction

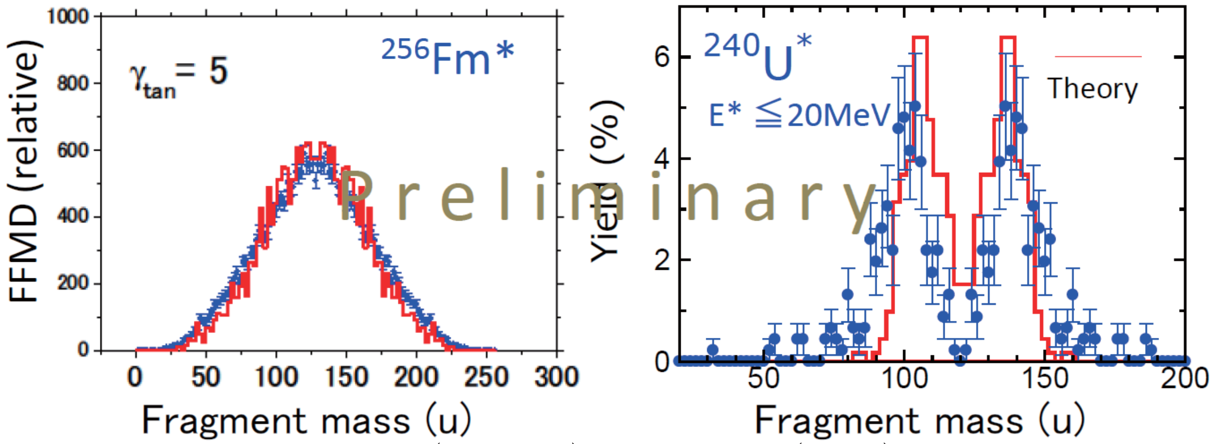

Fig.9 Comparison of predicted (histogram) and observed (circles) mass distribtuion of fission fragments in the ^{18}O+^{238}U reaction. A model parameter ($\gamma_{\rm tan}$) was determined from the data of ^{256}Fm (left panel)[6], and it was used to predict FFMD of ^{240}U (right panel)

mass distribution from ^{240}U in a unified manner, which alone is a great advancement of the nuclear model toward practical calculations of fission-related phenomena.

5. Summary

We have an intensive plan at JAEA to develop experimental and theoretical tools to investigate surrogate reactions to determine neutron cross sections of unstable or rare nuclei. The project started under financial support from MEXT. I wish to comment that some variations of the method, such as the inverse kinematics, projectile fragmentation and even some other methods would be possible as a surrogate method and in some cases they would be very useful. We are wokring on the direction as well.

Acknowledgments

The present paper containes research results obtained by my colleagues. Especially, the author is grateful to Dr. K. Ogata of Kyushu University, Drs. K. Nishio and Y. Aritomo of JAEA for a close collaboration. Present study includes the result of "Development of a Novel Technique for Measurement of Nuclear Data Influencing the Design of Advanced Fast Reactors" entrusted to Japan Atomic Energy Agency (JAEA) by the Ministry of Education, Culture, Sports, Science and Technology of Japan (MEXT).

References

[1] G. Kessedjian et al., Phys. Lett. **B 692**, 297(2010).
[2] N.D. Scielze et al., Phys. Rev. C **81**, 034608(2010).
[3] K. Nishio et al., Fall Meeting of Atomic Energy Society of Japan, Sapporo (2010).
[4] S. Chiba and O. Iwamoto, Phys. Rev. C 81, 044604(2010).
[5] K. Ogata, S. Hashimoto and S. Chiba, arXiv:1101.2732 (2011), submitted to Prog. Theor. Phys.
[6] Y. Aritomo, S. Chiba and K. Nishio, arXiv:1009.5924 (2010), submitted to Phys. Rev. C.
[7] V. Zagrebaev and W. Greiner, J. Phys. G: Nucl. Part. Phys. **31**, 825(2005).

8. The present status of the IFMIF/EVEDA accelerator development

Sunao MAEBARA

IFMIF development group, Directorates of Fusion Energy Research, Tokai-JAEA
Shirakata Shirane 2-4, Tokai-mura, Naka-gun, Ibaraki-ken, 319-1195, Japan
e-mail:maebara.sunao@jaea.go.jp

The International Fusion Materials Irradiation Facility (IFMIF) is an accelerator-based neutron irradiation facility to develop materials for a demonstration fusion reactor next to the International Thermonuclear Reactor (ITER). For providing materials to make a decision of IFMIF construction, Engineering Validation and Engineering Design Activities (EVEDA) under the Broader Approach (BA) agreement have been started. For the prototype accelerator, the acceleration tests up to 9MeV by employing the deuteron beam of 125 mA, are planned in Rokkasho, Aomori, Japan. The present status of the IFMIF/EVEDA accelerator development is presented.

1. Introduction

The IFMIF has been conceived as an intense 14MeV neutron-source for a demonstration fusion reactor materials development to next the ITER [1-3]. The IFMIF provides an irradiation volume of 0.5 liter with a neutron flux of 10^{18} n/m^2/s or more using the neutron-generating D-Li stripping reaction. A damage production rate of 50dpa/y in an irradiation volume of 0.1 liter and a 20 dpa/y in volume of 0.5 liter will be achieved. In the accelerator system, a 40MeV deuteron beam with a current of 250mA has to be injected into liquid lithium flow, being realized by two independent beam lines of 125mA each. Furthermore, accelerator system availability of 88% or more with CW operation mode is required. In order to validate the most critical part of such an accelerator system development, the accelerator prototype up to 9MeV has been developed in the IFMIF/EVEDA project. The outline of the accelerator prototype and the readiness for installation at BA Rokkasyo site are presented.

2. IFMIF/EVEDA prototype accelerator

The prototype accelerator [4] consists of Injector (output energy;100keV), a 175MHz RFQ linac (0.1-5.0MeV), a medium energy beam transport, the first section of Superconducting RF linac (5.0-9.0MeV), a high energy beam transport line and a beam dump (9MeV-125mA CW), as shown in Fig.1.

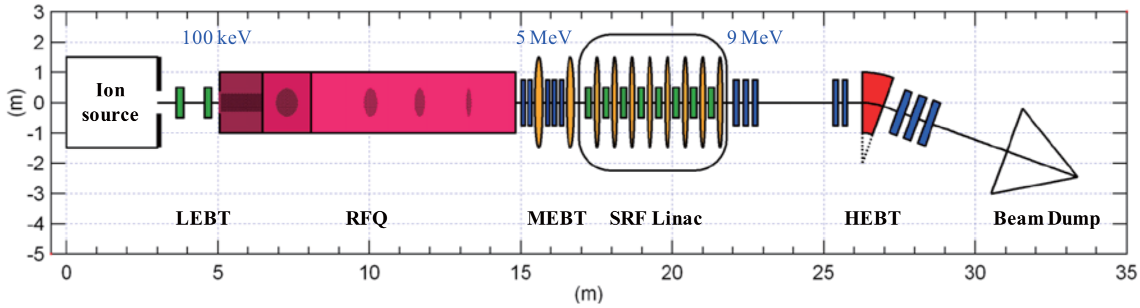

Fig.1 A schematic drawing of the prototype accelerator

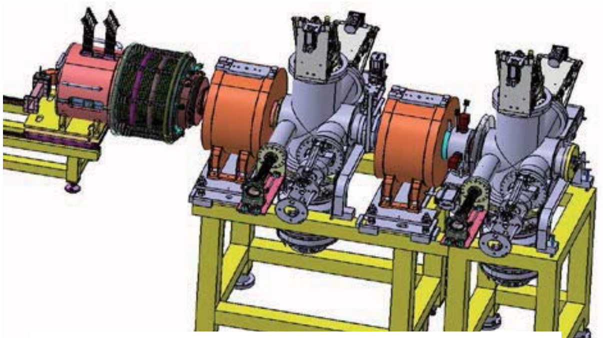

Fig.2 Illustration of the Injector

In the injector design by CEA-Saclay (Fig.2), the output power of 100keV-140mA is generated with CW operation mode, and the deuteron beam emittance of 0.30 π mm mrad or less is required for acceptance criteria to inject to the RFQ [5]. The ECH ion source by a 2.45GHz magnetron is used, and a dual solenoid focusing magnets with a s pace charge neutralization scheme for the Low Energy Beam Transport (LEBT) are designed to restrict the beam emittance growth with a minimal length of a 2m-long.

For the design of prototype RFQ linac by INFN (LNL), a four-vane integrated cavity type of RFQ, which has a longitudinal length of 9.78m (Fig.3), was proposed to accelerate deuteron beam from 0.1 t o 5MeV. The operation frequency of 175MHz was selected to accelerate a l arge current of 125mA in CW mode [6]. The cavity is composed of 18 x 0.55m-long modules. The peak surface electric field of 1.8 Kilpatrick's factor is designed.

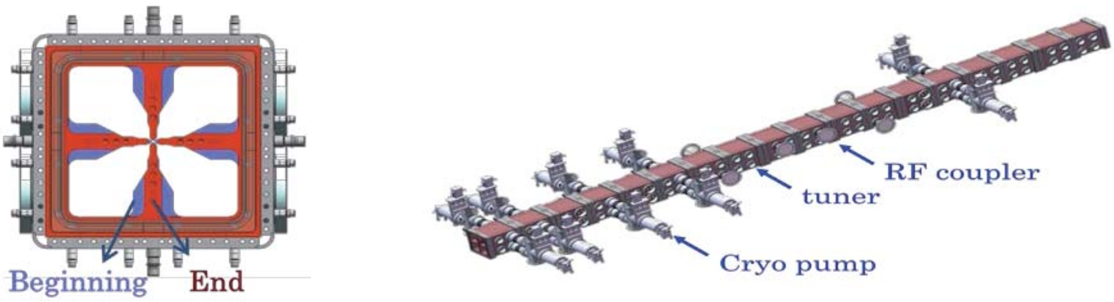

Fig.3 Illustration of Radio Frequency Quadrupole

The driving RF power of 1.28 M W has to be injected to the RFQ cavity for full beam power operation. The 8 couplers are used to share the required driving power and located at 4 different longitudinal positions. Each two couplers are arranged to have the same longitudinal position. For each coupling at different positions, the minimum H fields of 3100, 3400, 3800 and 4100 [A/m] are required by two couplers, respectively. The required coupling values are achieved by the rotation of the loop with respect to the axis normal to beam direction (0 to 90 °) and /or by changing the penetration depth inside the RFQ cavity [7].

In the main accelerator from 5MeV to 9MeV, a superconducting Half Wave Resonator (HWR) (Fig.4 (a)) was proposed by CEA-Saclay, as an alternative to Alvarez-type room temperature Drift Tube Linac (DTL) [8]. For the resonators and focusing coils, moderate accelerating field of 4.5 MV/m or less with beam aperture of 40 mm, and moderate focusing strength by solenoids of ∫Bzdl ~ 1T.m are designed. The cryomodule (Fig.4 (b)) is about 5m-long, and consists of 8 resonators (β=0.094) with a capacitive tuning system (range±50kHz) and 8 solenoid packages including a superconducting magnet field on axis Bz= 6T.

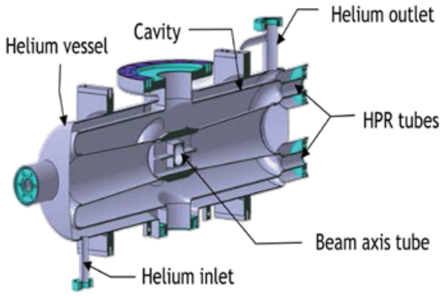

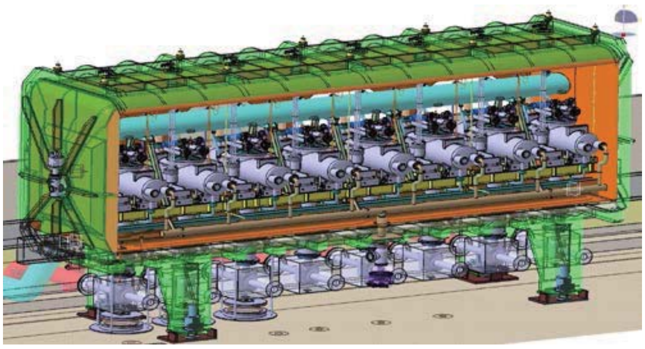

Fig.4 (a) Half Wave Resonator (b) Cryomodule including 8 resonators and 8 solenoids

A beam dump of 9MeV-125mA of CW operation mode is designed by CIMAT, the draft design (Fig.5) is proposed. The whole beam dump size is a 4m-long and a 1.50 m-radius, and a cone-shaped copper, a 2.5m long and a 5 mm-thickness, is used for the beam stopping material. Cooling water is circulated to remove heat generated at the copper cone by beam, and neutron and gamma ray are shielded by surrounding water tank. Gamma-ray is shielded by iron with a 0.25m-thickness, and a backscattering neutron is also suppressed by polyethylene of a 0.3m-thickness.

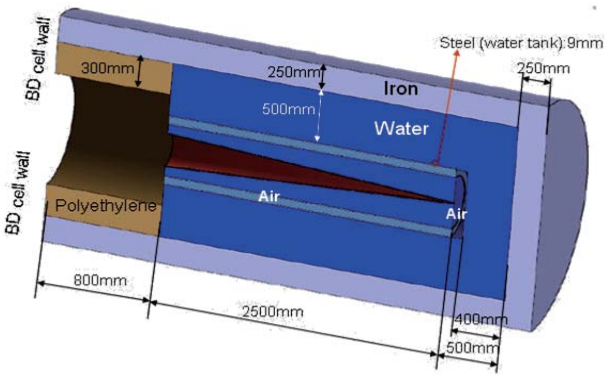

Fig. 5 Monte Carlo calculation model of a beam dump of 9MeV-125mA of CW operation mode by CIEMAT

3. Readiness at BA Rokkasyo site

At the BA Rokkasyo site, the construction of International Fusion Energy Research Center (IFERC) was opened in April 2009, and the IFMIF/EVEDA Accelerator building, the computer simulation & remote experimentation building and the DEMO R&D building were completed in March 2010.

Fig. 5 Photograph of the IFERC at BA Rokkasyo sirte

The IFMIF/EVEDA accelerator building has the total area of 2019.5m^2, and the accelerator vault has the inside area of W: 8.0m x D: 41.5m x H: 7.0m. The building consists of an accelerator vault, a nuclear heating ventilation and air conditioning (HVAC) area, a heat exchange and cooling water area for both radiation controlled and non-controlled areas, an access room, a control room and a large hall for power racks, RF systems(HVPS and RF power chains) and 4K refrigerator. The vault is surrounded by concrete walls of 1.5m thickness. A local concrete shield of 0.5m thickness is also planned to reinforce around the beam dump.

For the accelerator tests at Rokkasyo, domestic safety review is indispensable to obtain the RI license, and the shielding design and the activation analysis are key issues. As shown in Fig. 6(a), there is no experimental data of Cu(d,n) reaction in the range of 5.0-9.0 MeV, deuteron induced thick target neutron yield at 5MeV and 9MeV[9] were measured in collaboration with Kyushu University using Tandem accelerator in 2009FY and 2010FY. Using these experimental data, calculations of the shielding effects and the activation are in progress.

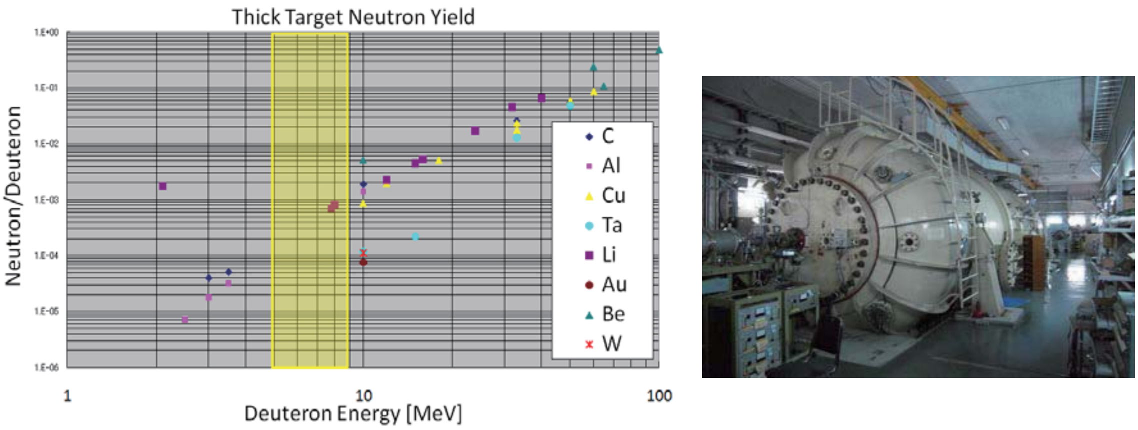

Fig. 6(a) Data of thick target neutron yield vs. deuteron energy, (b) Kyushu University Tandem accelerator

4. Summary

Without changing final objectives of the IFMIF/EVEDA accelerator prototype, the R&D's for each accelerator components are in progress, but the delivery time of some components is delayed at the BA Rokkasyo site. In March, 2010, at the BA Rokkasyo site, the construction of the IFMIF/EVEDA accelerator building was completed. For domestic safety review, experimental data of deuteron induced thick target neutron yield at 5 and 9MeV were obtained in collaboration with Kyushu University, and shielding effects and activation analysis are in progress.

References

[1] IFMIF-CDA Team (Ed.) M. Martone,ENEA Frascati Report, RT/ERG/FUS/96/17 (1996).
[2] T. KONDO, J. of Nucl. Mater. 258-263,47-55(1998)
[3] T. F. Shannon , J.of Nucl. Mater. 258-263,106-112(1998)
[4] MOSNIER, A., et al., Proc. 1st Int. Particle Accelerator Conf., Kyoto, Japan, 588-590(2010)
[5] R. Gobin et al., Rev. of Sci. Instrum., vol.81, 02B301-02B301-3(2010)
[6] A. Palmieri, et al., Proc. 1st Int. Particle Accelerator Conf., Kyoto, Japan, 603-605(2010)
[7] S.Maebara., Proc. 1st Int. Particle Accelerator Conf., Kyoto, Japan, 3720-3722(2010)
[8] F. Orsini, et al., Proc. 1st Int. Particle Accelerator Conf., Kyoto, Japan, 591-593(2010)
[9] N. SHIGYO, et.al., Proc. Int. Conf. on Nuclear Data for Science and Technology 2010 will be published.

9. Nuclear Data and Materials Irradiation Effects
- Analysis of irradiation damage structures and multiscale modeling -

Toshimasa YOSHIIE
Research Reactor Institute, Kyoto University
Kumatori-cho, Sennan-gun, Osaka-fu, 590-0494 Japan
yoshiie@rri.kyoto-u.ac.jp

Nuclear data plays an important role for the study of materials irradiation effects. Displacement per atom (DPA) is a commonly used parameter to estimate the displacement damage by particle irradiation on materials. Recently the primary knock-on atom (PKA) energy spectrum analysis has been proposed to introduce effects of cascade formation. In both cases, accurate nuclear data is required for the analysis of damage structures, especially incident particle energy is high. In this paper, the application of nuclear data for materials irradiation experiments is demonstrated. Then a multiscale modeling of irradiation effect in high energy proton irradiated Ni is shown.

1. Introduction

For the development of nuclear materials which are used under high energy particle irradiation, materials degradation by irradiation damage is the most important factor in determining the lifetime of components in the nuclear system. Irradiation experiments are essential to the development of such structural materials. There are, however, several materials being developed despite the lack of appropriate irradiation test facilities, such as a fusion reactor and an accelerator driven system (ADS). In these cases, there are two ways to investigate materials properties. One is simulation irradiations by using other irradiation facilities. The other is computer simulations. In these studies, the nuclear data plays an important role. In this paper, the role of nuclear data for materials irradiation studies is demonstrated.

2. Simulation irradiation

For simulation irradiations, we use various kinds of irradiation facilities, such as neutron irradiation, ion irradiation and electron irradiation facilities. For these cases, one needs to translate the data to other high energy particle irradiation environment, which requires an understanding of factors that influence generation and accumulation of point defects. Displacement per atom (DPA) is commonly used as a damage parameter to estimate the effect of high energy particle irradiation on materials. The accuracy of DPA strongly depends on the nuclear data when the nuclear reaction is involved in the irradiation. DPA is, however, not sufficient to reflect for the effect of high energy recoils such as cascade formation. The primary knock-on atom (PKA) energy spectrum analysis [1-3] has been proposed to compensate the deficit of DPA. The analysis is based on the fact that a large PKA forms a large cascade and the large cascade separates into several subcascades. In each subcascade, vacancy rich area is surrounded by an interstitial rich area and point defect reactions occur in each subcascade. In the case of fcc metals, stacking fault tetrahedra of vacancy type defects are formed directly from subcascades at lower temperatures such as below 400 K and the PKA energy spectrum analysis is possible.

2.1 PKA energy spectrum analysis

The PKA energy spectrum analysis was made by fitting the observed cascade size distribution to calculated PKA energy spectrum. The population of each size of cascade was assigned to the cross-section of PKA energy from its larger side by larger cascade zones. Fig. 1 is the case of Cu irradiated by 14 MeV neutrons at room temperature. From the relation between the cascade zone size and PKA energy spectrum, the density of energy deposition to cascade zone was estimated. The calculated cross-section (curve in the figure) was adopted from the work by Logan and Russell [4]. From the relationship between the area and deposited energy, it was concluded that in the case of 100keV and 800keV PKA, 0.35 eV and 0.03 eV were given, respectively, in each atom in the cascade.

The analysis was also made by fitting the observed subcascade number distribution to calculated PKA energy spectrum. The groups with higher number of subcascades were assumed to be produced from PKAs with higher energy as shown in Fig. 2. The fitting of subcascade groups to PKA energy spectrum can be converted to the relation between the PKA energy and the number of subcascades as in Fig. 3. If one supposes that each of subcascades comes from the same energy, the subcascade formation energy is about 10 keV.

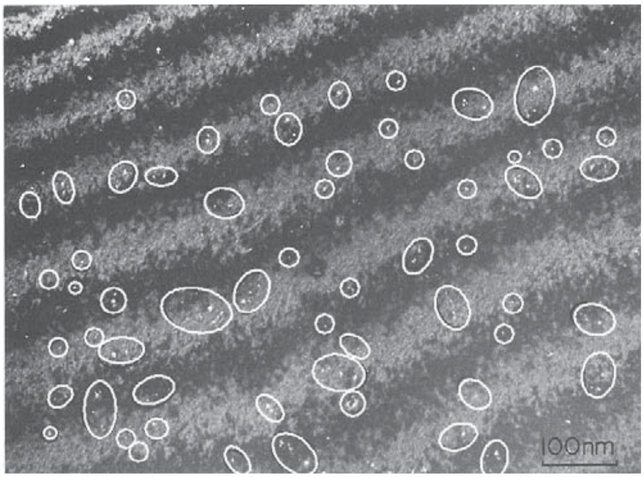

Figure 1. An example of grouped defect clusters in fusion neutron irradiated Cu to $1.2x10^{-4}$dpa. Each circle or oval corresponds to one cascade.

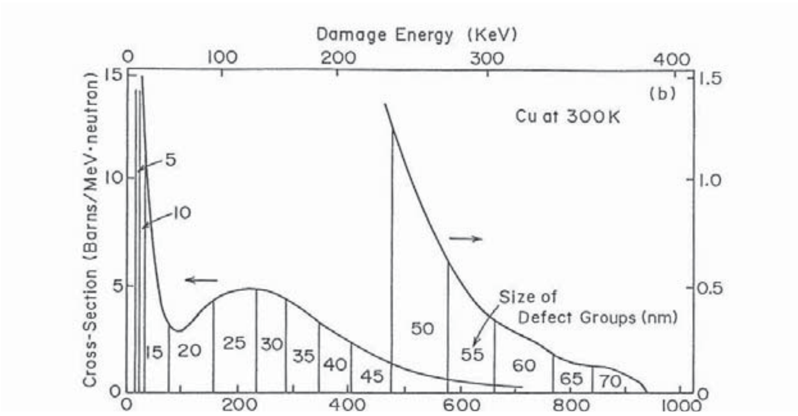

Figure 2. PKA energy spectrum in Cu and its correspondence to the size of cascade zone.

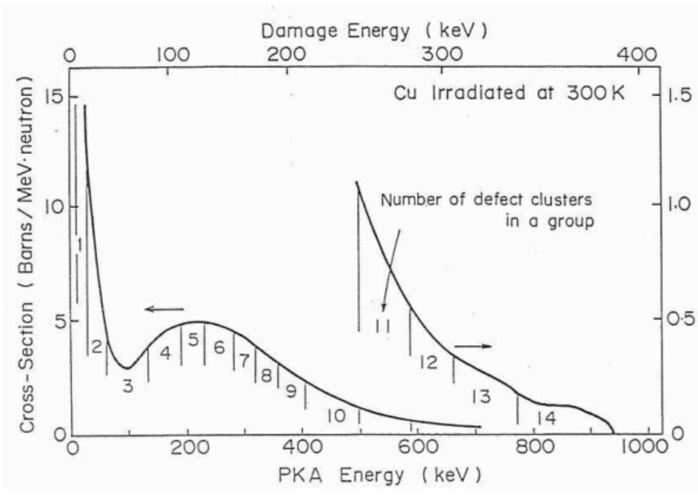

Figure 3. PKA energy spectrum in Cu and its correspondence to the number of produced subcascades from a single PKA.

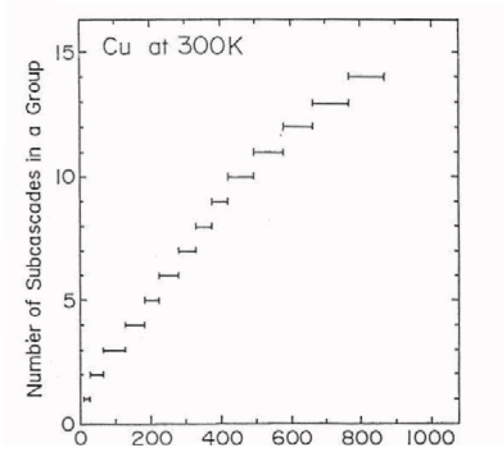

Figure 4. Variation of the number of subcascades in a group with the PKA energy.

2.2 Fission fusion correlation in SFT formation

In the case of most compact cascade such as those produced in Au, with increasing irradiation temperatures, above 473K, well separated subcascades (SFTs) fuse into a large SFT as shown in Fig. 5. Average SFT sizes irradiated at 300K and 473K were 1.6nm and 3.7nm, respectively. Above 623K only few SFTs remained due to their thermal unstableness. The SFT size is larger for larger PKA energy. Figure 6 shows the comparison of defect structures between fusion neutron irradiation (the RTNS-II, 563K, 0.017dpa) and fission neutron irradiation (the JMTR, 573K, 0.044dpa). Though the total displacement damage for the fission neutron irradiation was higher than that of the fusion neutron irradiation, the remaining number of SFTs was higher in the fusion neutron irradiation.

The cross-section for the formation of SFTs was 1.7×10^{-1}barns and 9.4×10^{-4}barns for fusion neutrons and fission neutrons, respectively. The average size of SFTs by fusion neutron irradiation was also larger than that of fission neutron irradiation. If there exists a threshold energy for SFT formation, E_{SFT}, it is evaluated using the following equation,

$$N_{SFT} = \alpha\phi\int_{E_{SFT}}^{E_{MAX}} \frac{d\sigma(E_p)}{dE_p} dE_p \,, \tag{1}$$

where N_{SFT} is the concentration of SFTs observed, α is the SFT formation efficiency. We adopted the cross section calculated by the SPECTER code [5] using the neutron spectrum of the JMTR and RTNS-II as shown in Fig. 7. α and E_{SFT} were obtained to be 0.05 and 80keV, respectively, using the number density of SFTs formed by fission neutron irradiation and fusion neutron irradiation. It is concluded that SFTs are formed for PKA energies larger than 80keV with a cascade efficiency of 0.05 at 563-573K. Actually α depends on the PKA energy, so the value is an average one above 80keV.

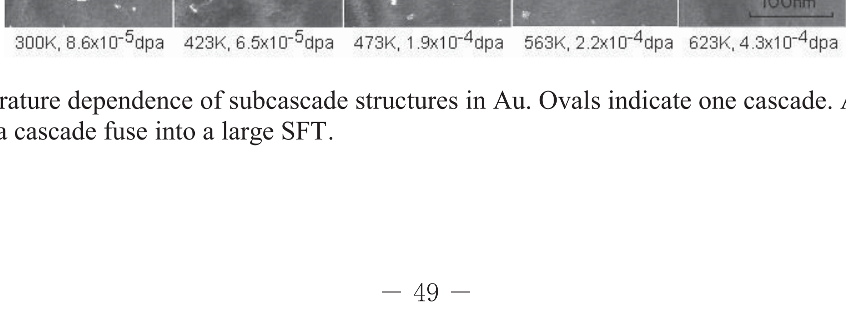

Figure 5. Temperature dependence of subcascade structures in Au. Ovals indicate one cascade. Above 473 K SFTs formed in a cascade fuse into a large SFT.

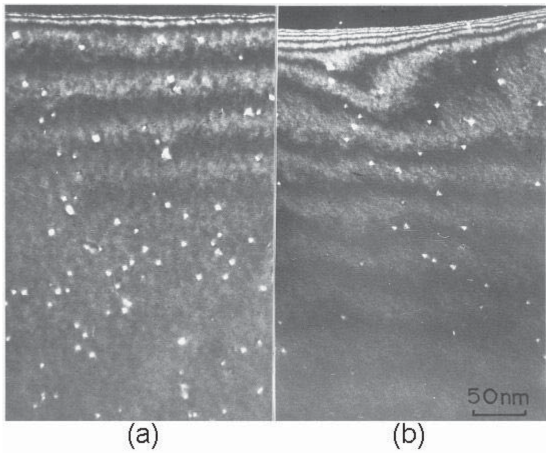

Figure 6. Comparison of damage structures in thin foil irradiated Au between (a) fusion neutron irradiation to 0.017 dpa at 563 K and (b) fission neuron irradiation to 0.044 dpa at 573 K.

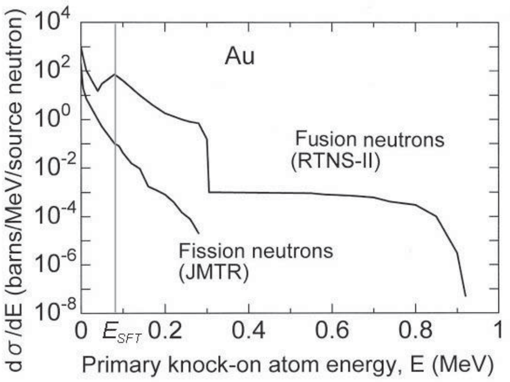

Figure 7. Comparison of PKA energy spectra between fusion neutrons and fission neutrons in Au.

3. Computer simulation

3.1. Multiscale modeling

A spallation neutron source is a coupling between a target and a proton accelerator. High energy proton (GeV) irradiation produces a large number of neutrons in the target. The beam window and the target materials are thus subjected to a very high irradiation load by source protons and generated spallation neutrons. At present, there are no window materials that can operate for the desired period of time without deterioration of mechanical properties.

Irradiation experiments are essential to the development of such structural materials. Recently, strong spallation neutron sources, SNS in the United States and J-PARC in Japan have been completed. These facilities, however, are not designed for materials irradiation experiments. Therefore computer simulations play an important role in predicting the behavior of materials.

In this section, changes in mechanical property of Ni after irradiation with 3 GeV protons were calculated using multi-scale modeling [6]. A proton energy of 3GeV was chosen to simulate the J-PARC spallation neutron source. Ni is the simplest model material of austenitic stainless steels, which are currently used as the proton beam window. The multi-scale modeling code consisted of four parts.

The first part covered nuclear reactions based on the PHITS code [7]. This part calculated the interactions between high energy protons and nuclei in the target from 10^{-22} s and estimated secondary particles and PKAs. The second part simulated atomic collisions between particles without nuclear reactions. Because the energy of particles was high, the PKA energy spectrum analysis was employed according to the procedure by Satoh *et al.* [8]. In each subcascade, the direct formation of clusters and the number of mobile defects were estimated using molecular dynamics and kinetic Monte-Carlo methods. The third part considered damage structural evolution, estimated using reaction kinetic analysis. The development of damage structures affects the mechanical properties of target materials. The fourth part estimated mechanical property changes using three-dimensional discrete dislocation dynamics (DDD). Stress-strain curves of high energy proton irradiated Ni were thus obtained.

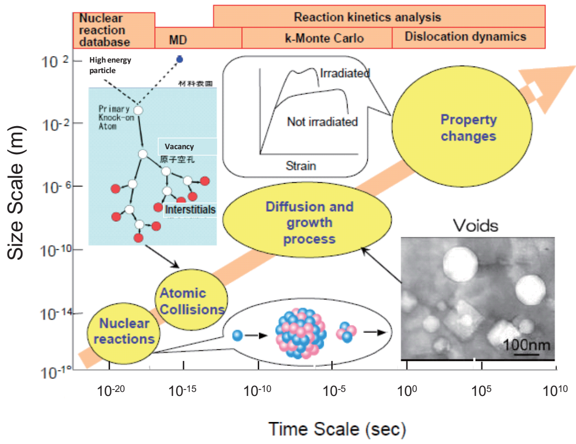

Figure 8. Multiscale modeling of irradiation effects by high energy particles.

3.2. Nuclear reaction

To estimate the PKA energy spectrum under high energy proton irradiation, the PHITS code was used. The code was the first general-purpose heavy ion transport Monte Carlo code covering the incident energies from several MeV/nucleon to several GeV/nucleon. It was developed for general purpose calculations based on the NMTC/JAM code [9], which is widely used for hadron transport calculations. In the PHITS code, the HIC code [10], which is used in the HETC-CYRIC code [11], was revised into the JQMD code [12] for heavy ion nuclear reaction simulation. This is because the JQMD code is based on a more modern nucleus-nucleus reaction model than QMD, while the HIC is based on a traditional intranuclear-cascade-evaporation model. The PKA energy spectrum of 3 mm thick Ni irradiated by 3GeV protons was calculated. The PKA energy dependence of damage energy deposition indicated that the highest energy deposition was caused by 65 keV PKAs.

3.3. Atomic collision

As mentioned in 2.1, a high energy PKA produces a large cascade, which can be divided into subcascades. The subcascade formation energy of Ni was estimated to 10 keV [8]. Therefore we assumed the formation of several 10 keV subcascades for the initial damage structure instead of large cascades. The number of 10 keV subcascades during irradiation was obtained from the PKA energy spectrum calculated by the PHITS and by PKA energy spectrum analysis [1, 2].

Molecular dynamics (MD) was employed to calculate the defect clusters and freely migrating defects from subcascades of 10 keV. The size of the model lattice was 35×35×35 lattice constants. An EAM potential with the parameters proposed by Daw and Baskes [13] was used. A periodic boundary condition in three directions and an NVE ensemble (i.e., fixed number of atoms, cell volume and energy) were used for the simulation. Three MD runs were performed and the results indicated that, on average, seventeen vacancies and seventeen interstitials were formed in each 10 keV subcascade. Using the point defect distribution determined by MD, the kinetic Monte-Carlo simulation was performed and a cluster of three point defects was formed on average. These values were then used in a defect structural evolution.

3.4. Damage structure evolution

The damage structural evolution was estimated using reaction kinetic analysis [14]. The following assumptions were used in the calculation. (1) Mobile defects: interstitials, di-interstitials, tri-interstitials, vacancies and di-vacancies. (2) Point defect clusters of four point defects or more were assumed to be stable clusters. (3) The time dependence of ten variables: concentration of interstitials, di-interstitials, tri-interstitials, interstitial clusters (interstitial type dislocation loops), vacancies, di-vacancies, tri-vacancies, vacancy clusters (voids), the total interstitials in interstitial clusters, and the total vacancies in vacancy clusters. (4) Interstitial clusters (three interstitials) and vacancy clusters (three vacancies) were also formed directly in cascades. The formation rates were obtained by MD simulation. (5) The material temperature was 423 K during irradiation. The result of 10 dpa irradiation was as follows: the void concentration was $5.93\text{x}10^{-4}$/atoms, the void size was four vacancies and the dislocation density was $1.1\text{x}10^{9}\text{cm/cm}^{3}$.

3.5. Mechanical property change

Changes in mechanical property were calculated by three dimensional DDD [15]. In the usual DDD simulation [16], a curved dislocation line was treated as a connection of short straight segments to simplify the calculation of dislocation movements. In the present study, dislocation segments with edge components were employed. Each segment was subjected to forces resulting from another dislocation segment, dislocation line tension and external stress. A lattice constant, a shear modulus and Poisson's ratio of Ni were used. A velocity of the segment was determined by a shear stress [17] which was calculated from the summation of the forces exerted.

During the DDD simulation, the dislocation was pinned at an obstacle on at the slip plane, and then the dislocation line shape became discontinuous at the pinning point because of a bowing of the other movable segments. When the angle between two dislocation segments connected at the pinning point fell below a critical angle, the two segments were released from the pinning point.

To estimate this critical angle, an energy calculation using a model lattice was performed by a static method [18, 19] with an effective medium theory potential for Ni fitted by Jacobsen *et al*. [20]. A vacancy cluster of 4 vacancies was located near an edge dislocation. To move the dislocation, a shear stress was applied in the $[\bar{1}10]$ direction and the critical angle was determined to be 65°. Stress-strain curves obtained from the DDD simulation and the yield strength of the model crystal containing voids was higher than that without voids by a factor of 1.33.

4. Concluding remarks

The PKA energy spectrum analysis to study materials irradiation effects was shown, and as an example of the analysis, the multiscale modeling of the effect of high energy proton irradiation on mechanical property of Ni up to 10 dpa was presented. The result was primitive because many assumptions were made to simplify the calculations. In the Research Reactor Institute, the irradiation experiments with high energy protons by using a fixed filed alternative gradient accelerator are in progress and results to compare with the simulation will be obtained. In these studies, more precise calculation are required as well as an improvement of nuclear data.

Acknowledgment

A part of this study is the result of "Clarification of behaviors of accelerator driven system materials by FFAG accelerator" carried out under the Strategic Promotion Program for Basic Nuclear Research by the Ministry of Education, Culture, Sports, Science and Technology of Japan, and Grant-in-Aid for Science Research (S), Task No. 19106017 by Japan Society for the Promotion of Science.

References

[1] M. Kiritani, T. Yoshiie, S. Kojima, Y. Satoh, Radiation Effect. Defect. Solid., 113, 75-96 (1990).
[2] Y. Satoh, T. Yoshiie, M. Kiritani, 1988 Annual Research report of Japanese Contributions for Japan-US collaboration on RTNS-II Utilization, 48-60 (1989).
[3] T. Yoshiie, X. Xu, Q. Xu, S. Yanagita and Y. Satoh, Reactor Dosimetry: Radiation Metrology and Assessment, ASTM STP 398, 625-632 (2001).
[4] C. M. Logan and E. W. Russel, UCRL-52903, University of Calfornia 1976.
[5] L .R. Greenwood, P. K. Smither, *ANL/FPP/TM-197*, Argonne National Laboratory, 1985.
[6] T. Yoshiie, T. Ito, H. Iwase, Y. Kaneko, M. Kawai, I. Kishida, S. Kunieda, K. Sato, S. Shimakawa, F. Shimizu, S. Hashimoto, N. Hashimoto, T. Fukahori, Y. Watanabe, Q. Xu, S. Ishino, Nucl. Inst. Meth. Phys. Res. B, in press.
[7] H. Iwase, K. Niita and T. Nakamura, J. Nucl. Sci. Tec., 39, 1142 (2002).
[8] Y. Satoh, S. Kojima, T. Yoshiie and M. Kiritani J. Nucl. Mater. ,179-181, 901 (1991).
[9] K. Niita, H. Takada, S. Meigo, Y. Ikeda, Nucl. Instrum. Methods, B184, 406 (2001).
[10] H. W. Bertini, T. A. Gabriel, T. T. Santoro, *et al.*, ORNL-TM-4134, Oak Ridge National Laboratory (1974).
[11] H. Iwase, T. Kurosawa, T. Nakamura, N. Yoshizawa, J. Funabiki, Nucl. Inst. Meth, B183, 374 (2001).
[12] K. Niita, S. Chiba, T. Maruyama, H. Takada, T. Fukahori, Y. Nakahara, A. Iwamoto, Phys. Rev., C52, 2620 (1995).
[13] M. S. Daw, M. I. Baskes, Phys. Rev. B, 29, 6443 (1984).
[14] T. Yoshiie, Q. Xu, K. Sato, K. Kikuchi, M. Kawai, J. Nucl. Mater., 377, 132 (2008).
[15] Y. Kaneko, S. Hirota, S. Hashimoto, Key Eng. Mater., 353-358, 1086 (2007).
[16] H. M. Zbib, T.D. de la Rubia, M. Rhee, J. P. Hirth: J. Nucl. Mater., 276, 154 (2000).
[17] J. P. Hirth, J. Lothe: Theory of Dislocations (A Wiley-Interscience Publication, New York 1982), p.208.
[18] E. Kuramoto, K. Ohsawa, T. Tsutsumi, M. Koyanagi, J. Nucl. Mater. 271-272, 26 (1999).
[19] K. Sato, T. Yoshiie, T. Ishizaki, Q. Xu, Phys. Rev. B 75, 094109 (2007).
[20] K. W. Jacobsen, P. Stoltze, J. K. Norskov, Surf. Sci. 366, 394 (1996).

10. Exciton model and quantum molecular dynamics in inclusive nucleon-induced reactions

Riccardo BEVILACQUA[1,†], Yukinobu WATANABE[2], Stephan POMP[1]

[1] Department of Physics and Astronomy, Uppsala University, P.O. Box 516, 751 21 Uppsala, Sweden
[2] Department of Advanced Energy Engineering Science, Kyushu University, Kasuga, Fukuoka 816-8580, Japan
[†] email: riccardo.bevilacqua@physics.uu.se

We compared inclusive nucleon-induced reactions with two-component exciton model calculations and Kalbach systematics; these successfully describe the production of protons, whereas fail to reproduce the emission of composite particles, generally overestimating it. We show that the Kalbach phenomenological model needs to be revised for energies above 90 MeV; agreement improves introducing a new energy dependence for direct-like mechanisms described by the Kalbach model. Our revised model calculations suggest multiple pre-equilibrium emission of light charged particles. We have also compared recent neutron-induced data with quantum molecular dynamics (QMD) calculations complemented by the surface coalescence model (SCM); we observed that the SCM improves the predictive power of QMD.

1. Introduction

Nuclear power plants for the production of electricity have been in operation since 1954, when the Obninsk facility, in the former Soviet Union, was connected to the grid on the evening of June 26th. Today nuclear energy plays a key role in the global economy. Japan and South Korea have a leading position in the nuclear sector. Third country in the world for nuclear power capacity, Japan is currently operating 55 nuclear reactors; these nuclear reactors generate 30% of the electricity produced in the country. South Korea is producing 40% of its electricity with a network of 20 nuclear reactors. To reduce CO_2 emission and to meet an increasing need for energy, governments of Japan and South Korea are considering an expansion of nuclear power capacity, however the issue of nuclear waste disposal needs to be addressed and solved [1].

A possible approach to the nuclear waste issue follows the idea of Carlo Rubbia and his group at CERN; they proposed in 1990's the concept of Energy Amplifier [2], a device composed by a hadron accelerator coupled to a subcritical reactor. This device would produce energy with a very small production of minor actinides and long-lived fission products. In the same years, Charles D. Bowman and coworkers at Los Alamos National Laboratory proposed a transmutation facility for nuclear waste [3]. Accelerator Driven Systems (ADS) are a direct evolution of these two concepts. The present leading technology in ADS consists in a subcritical core coupled to a proton accelerator and a spallation target. Hence, transmutation techniques in ADS involve high-energy neutrons, with energies up to 2 GeV created in the proton-induced spallation process. Although a large majority of the neutrons will be below 20 MeV, the effects on the system of the relatively small fraction at higher energies has to be characterized. Above 200 MeV theoretical descriptions, like the intranuclear cascade model, work well and can be used to estimate the needed cross sections, whereas experimental data are required in the energy region between 20 and 200 MeV. Since the beginning of the decade, a large set of neutron-induced double differential cross sections (DDX) were measured in this energy range at the quasi-monoenergetic neutron (QMN) beam line of the The Svedberg Laboratory (TSL), Uppsala (Sweden). Data for light-ion production [4,5,6,7] at 96 MeV QMN have been published for several target materials and are available. New measurements at 175 MeV QMN for production of light charged particles from C, O, Si, Fe, Bi and U have been performed since 2007 and are now under analysis. Proton induced data for production of light-ions in the 20 to 200 MeV region were more extensively measured and are available to scientific community. In the present study we focus on the pre-equilibrium emission of light complex particles (deuteron, triton, ^{3}He and α particle) in nucleon-induced reactions. To describe the dynamical processes in these reactions we used both a phase space statistical approach, with the exciton model (EM) [8,9,10] and the Kalbach systematics [11], and a microscopic simulation approach, with the quantum molecular dynamics (QMD) model [12,13,14] complemented by a surface coalescence model (SCM) as described by Watanabe and Kadrev [15]. Neutron experimental data considered in this work are from preliminary results of the measurements conducted at TSL by Bevilacqua *et al.* [16]; proton induced data, retrieved from the EXFOR database, are from Piskor-Ignatowicz [17] and from experiments by Cowley *et al.* [18].

2. Materials and methods

2.1 Exciton model and Kalbach systematics

We focused our study on the dynamical processes in the production of light charged particles (proton, deuteron, triton, ^{3}He and α particle) in nucleon-induced reactions. The two-component EM [8,9,10] describes the time evolution of the nuclear state; this description is given by the total energy of the system and the total number of particles above the Fermi surface and corresponding holes below it. The EM does not include direct-like mechanisms as the nucleon transfer (NT) and the knock-out (KO) of preformed clusters. These mechanisms are playing a relevant role in the production of light complex particles in the pre-equilibrium emission region. To account for these direct-like mechanisms, Kalbach [11] proposes a phenomenological model based on experimental proton and neutron-induced data, with energies respectively up to 90 MeV and up to 63 MeV. TALYS-1.2 [19] is a code developed to analyze and predict nuclear reactions involving neutrons, photons and light charged particles for energies up to 200 MeV. The two component EM complemented by the Kalbach systematics is the default model used by TALYS to calculate nucleon induced DDX for light charged particles production. TALYS allows to scale the contribution to the DDX of the NT and KO direct-like mechanisms described by Kalbach. These are the Cstrip parameter (NT) and the Cknock parameter (KO). Their value can vary between 0 (no contribution) to 10; the default value is 1, corresponding to the original Kalbach prescription.

2.2 Quantum molecular dynamics and surface coalescence model

The QMD model [12,13,14] is a semiclassical simulation method that gives a microscopic description of the time evolution of nucleon many-body system. Each nucleon propagates in the nuclear mean field formed by all other nucleons and interactions among nucleons are described by stochastic two-body collisions. In the original QMD simulation method the nucleon many-body system evolves for a given time, of the order of 10^{-22} s, after the first interaction between the incident neutron and the target nucleus; at the end of this evolution time, emitted single (proton, neutron) and complex particles are identified according to a specified set of rules. However, this method underestimates the pre-equilibrium production of light complex particles. To account for this underestimation Watanabe and Kadrev [15] proposes a modification of the QMD model, including a surface coalescence effect. In this description, they assume that cluster formation occurs in low-density region of the nucleon many-body system, i.e. on the surface of the composite system. Here, when a leading nucleon reaches an *a priori* defined boundary region, the time evolution of the system is suspended and condition for the formation of a cluster in the phase space is checked. If this condition is positively verified, then a kinetic energy condition is checked. If the kinetic energy of the cluster and the Coulomb barrier tunneling allow it, then a cluster particle is emitted; otherwise, only the leading nucleon is emitted as single particle. The simulation then resumes and the system evolves until a next leading nucleon will reach the boundary region or until the given evolution time is completed. The generalized evaporation model is used to describe particle emission when the compound system reaches thermal equilibrium. In our work, we used a modified version of the JQMD [12,15] code. A complete description of the method is given by Watanabe and Kadrev [15].

3. Results and discussion

Bevilacqua *et al.* [16] presented preliminary DDX for the production of light charged particles, at several angles in the laboratory system, in the interaction of 175 MeV QMN with Fe and Bi. Experimental proton production is reproduced by default TALYS calculations with the two-component exciton model, whereas production of light complex particles is largely overestimated by the TALYS code in the pre-equilibrium emission energy region. In Figure 1, DDX for production of deuteron, triton, 3He and α particle from Bi at

175 MeV QMN is compared with default TALYS calculations (solid line). In the pre-equilibrium region the dominant emission mechanism in the TALYS code is the direct pick-up of one or more nucleons; in the case of α particles is also present the concurrent knock-out of preformed clusters. TALYS computes these mechanisms according to the Kalbach systematics [11]. The model proposed by Kalbach is based on proton-induced experimental data with energies up to 90 MeV, and neutron-induced experimental data up to 63 MeV. However TALYS extends tout-court the Kalbach systematics to higher incident energies, up to 200 MeV.

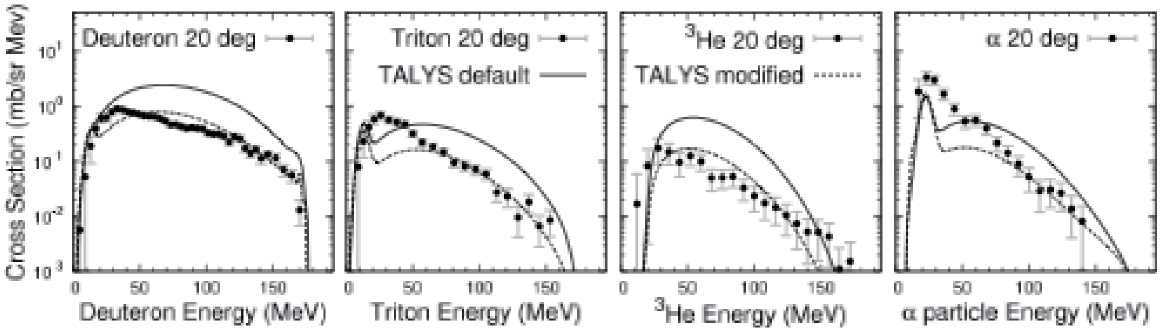

Figure 1. Production of deuteron, triton, ^{3}He and α particle in the interaction of 175 MeV QMN with Bi [16]. Experimental data at 20^o in the laboratory system are compared with default TALYS calculations (solid line) and with TALYS calculations modified reducing the Kalbach contribution to the pre-equilibrium emission (dashed line).

Preliminary data by Bevilacqua *et al.* [16] are the first neutron-induced DDX for production of light complex particles available in the 100 to 200 MeV region, however several proton-induced data are present in literature in this energy interval. We compared TALYS calculations with proton-induced production of light complex particles and we observed the same overestimation seen in the comparison with neutron-induced data. In Figure 2 we present production of light complex particles in the interaction of 175 MeV protons with Ni [17]; default TALYS calculations (solid line) overestimate pre-equilibrium production of all the light complex particles. Calculations without the contribution of the direct-like mechanisms described by Kalbach show large underestimation of the experimental data. Our preliminary results show that the NT and KO mechanisms should be included, but that the energy dependence described by Kalbach needs to be corrected for higher incident energies. We observed that reducing the NT and KO (only α particle) contribution to the pre-equilibrium emission provides a better description of the experimental data for incident energies above 90 MeV. In Figure 2 we present, as an example, TALYS calculations with different values of the Cstrip parameter (overall multiplication factor for the NT mechanism); we observe that scaling the NT contribution down to 25% of its default value improves the fitting of the experimental data at 20^o in the laboratory system.

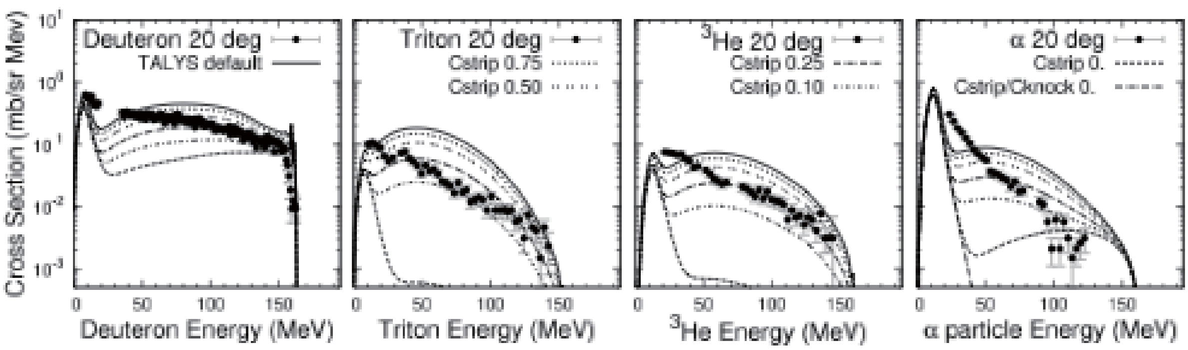

Figure 2. Production of deuteron, triton, ^{3}He and α particle in the interaction of 175 MeV protons with Ni [17]. Experimental data at 20^o in the laboratory system are compared with default TALYS calculations (solid line) and with TALYS calculations modified reducing the Kalbach contribution to the pre-equilibrium emission. The NT contribution (Cstrip parameter) has been scaled by a factor 0.75, 0.50, 0.25 and 0.10. “Cstrip 0.” line represents TALYS calculations without NT contribution. In the case of α particle production, we plotted also TALYS calculations without NT and KO (“Cstrip/Cknock 0.” line).

Cowley *et al*. [18] have measured inclusive (p,^{3}He) reactions on Co and Au at different incident energies in the 120 to 200 MeV region. In Figure 3 we present proton-induced ^{3}He production from Co [18] at 20^o in the laboratory system, at 120, 160 and 200 MeV incident energies, in comparison with default TALYS calculations (solid line). We observe that TALYS overestimates the pre-equilibrium production of ^{3}He. However calculations with TALYS including only the two-component EM contribution and excluding the Kalbach contribution show a large underestimation of the experimental data. Calculations applying different values of the Cstrip parameter suggest an energy dependence for the scaling factor. We observe that for 120 MeV incident-protons, the best fit of the data in the 30 to 90 MeV emission energy region was obtained for 0.5 ≤ Cstrip ≤ 0.75. For 160 MeV incident-protons the best fit of the pre-equilibrium emission energy region is obtained for 0.25 < Cstrip ≤ 0.5, whereas for the 200 MeV incident-protons the best fit is given by Cstrip ≈ 0.25.

The general underestimation of the experimental data for low emission energies in the pre-equilibrium region may be explained as multiple pre-equilibrium emission. After a light charged particles is emitted in the pre-equilibrium phase, the nucleon-target composite system may have enough residual energy to emit a second particle before reaching statistical equilibrium; this process is defined multiple pre-equilibrium emission. TALYS includes this mechanism only for the emission single particles (proton, neutron), whereas does not allow a composite particle to be emitted in the pre-equilibrium phase if another particle has been produced before in the same phase. We can observe this underestimation also in the production of complex particles from Ni at 175 MeV, as presented in Figure 2. This underestimation become more evident, or in same cases appear, when calculations are considered with the reduced Cstrip parameter, to better fit the wide pre-equilibrium emission region. In Figure 4, proton-induced production of ^{3}He from Au [18] at 20^o in the laboratory system, for incident energies of 120, 160 and 200 MeV, is compared with default TALYS calculations, TALYS calculations with only the contribution of the two-component EM to the pre-equilibrium emission and TALYS calculations with varying values of the Cstrip scaling factor. We observe similar results to the emission of ^{3}He from Co presented in Figure 3. When TALYS calculations are fitted to the data in the single-emission pre-equilibrium region, we observe an energy dependence in the value of the Cstrip parameter. Also in the ^{197}Au(p,^{3}He) case, reducing the contribution of the NT mechanism as described by Kalbach enhances the underestimation of ^{3}He production for lower energies in the pre-equilibrium emission region.

We extrapolated a preliminary energy dependence for the scaling factor from the comparison of TALYS calculations with proton data, to apply a reduction of the NT (and eventually KO, for α particles) contribution to calculations for quasi-monoenergetic incident neutrons. Our tentative energy dependence for the Cstrip parameter is given by CStrip = 1.9 – E / 100 MeV, for 90 MeV < E < 180 MeV, while Cstrip = 1 for E < 90 MeV. In Figure 1 we show TALYS calculations with reduced NT contribution (dashed line); these describe the experimental data in the pre-equilibrium region with better agreement than default calculations (solid line).

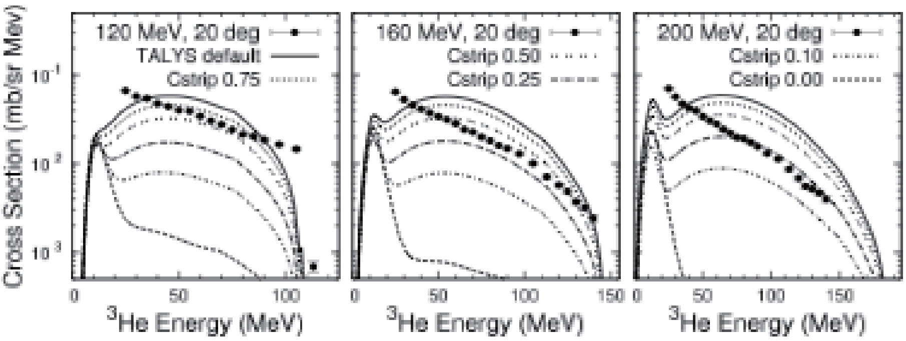

Figure 3. Production of ^{3}He in the interaction of 120, 160 and 200 MeV protons with Co [18]. Experimental data at 20^o in the laboratory system are compared with default TALYS calculations (solid line) and with TALYS calculations modified reducing the Kalbach contribution to the pre-equilibrium emission. The NT contribution (Cstrip parameter) has been scaled by a factor 0.75, 0.50, 0.25 and 0.10. “Cstrip 0.00” line represents TALYS calculations without NT contribution.

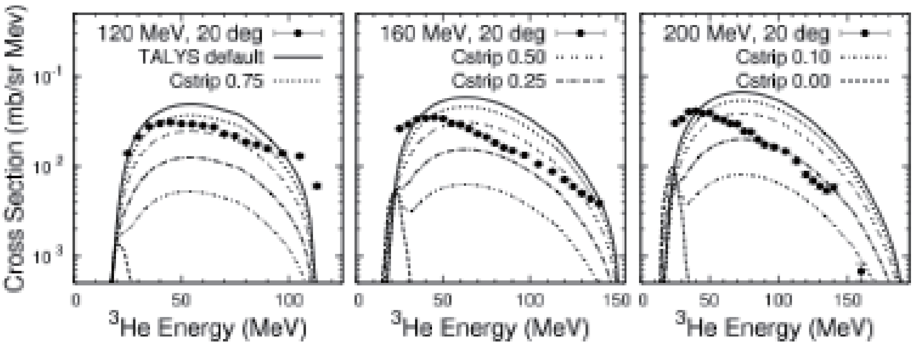

Figure 4. Production of ^{3}He in the interaction of 120, 160 and 200 MeV protons with Au [18]. Experimental data at 20^o in the laboratory system are compared with default TALYS calculations (solid line) and with TALYS calculations modified reducing the Kalbach contribution to the pre-equilibrium emission. The NT contribution (Cstrip parameter) has been scaled by a factor 0.75, 0.50, 0.25 and 0.10. "Cstrip 0." line represents TALYS calculations without NT contribution.

In Figure 5 we show comparison between light complex particles production from Fe at 175 MeV QMN [16] with QMD model calculations (dashed line). Whereas proton production is described by QMD (not shown in the picture), we observe that the calculations generally underestimate the experimental data for composite particles. A similar deficiency is observed by Watanabe and Kadrev [15] in the comparison of QMD calculations with angle-integrated energy-differential cross sections for the production of light complex particles at 96 MeV. To provide a more realistic description of the dynamical processes, we assumed that light charged particles are formed by successive coalescence starting from a leading nucleon, and that this process is occurring on the surface of the pre-equilibrium nucleon-target compound. Watanabe and Kadrev modified the JQMD code to include this surface coalescence model. This model is dependent on three adjustable parameters: a radius defining the internal part of the nucleon-target compound, a distance defining the surface region and a phase-space condition expressed in MeV c^{-1} fm^{-1} to verify is a cluster is formed. We performed our calculations applying to the adjustable parameters the same values chosen by Watanabe and Kadrev as best fit for the 96 MeV data.

Preliminary calculations with the modified JQMD code including the surface coalescence model are presented in Figure 5 (solid). We observe that production of triton, ^{3}He and α particle is described by the modified calculations. Prediction of deuteron production is enhanced, however the calculations still underestimate the data. This deficiency is larger at small emission angles, whereas we did not observe it at larger angles. The underestimation in the production of deuteron with the modified JQMD calculations is also observed by Watanabe and Kadrev at 96 MeV. Other reaction processes as direct pick-up of a proton by an incident neutron may explain this discrepancy.

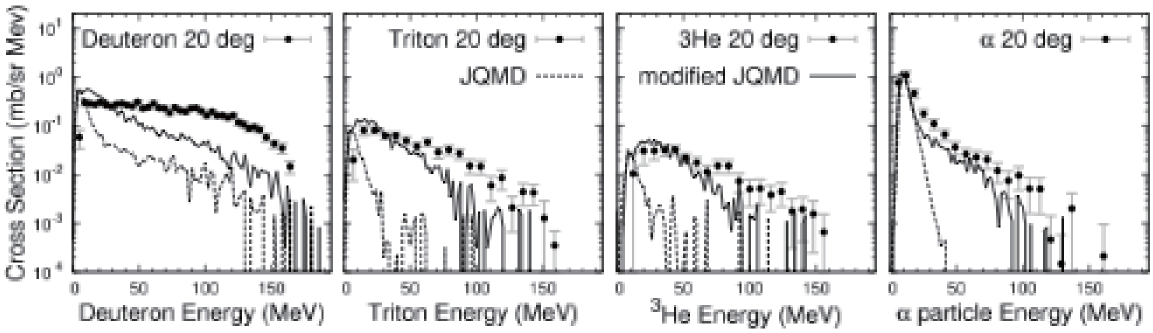

Figure 5. Production of deuteron, triton, ^{3}He and α particle in the interaction of 175 MeV QMN with Fe[16]. Experimental data at 20^o in the laboratory system are compared with default QMD calculations with the JQMD code (dashed line) and with modified QMD calculations where a surface coalescence model was applied (solid line).

4. Conclusions

We have compared nucleon-induced pre-equilibrium production of light complex particles with the two-component EM complemented by the Kalbach systematics. We observed that the large overestimation of the production of composite particles could be reduced introducing a new energy dependence in the NT contribution to the EM. These results are consistent in both proton-induced and neutron-induced data. However, reducing the NT contribution to the pre-equilibrium emission leads to an underestimation of the production of light complex particles in the low energy emission region. We explain this underestimation in terms of multiple pre-equilibrium emission and suggest this mechanism to be included, also for complex particles, in future releases of the TALYS code.

We have also presented the first preliminary results of QMD calculations in comparison with recent neutron induced data at quasi-monoenergetic 175 MeV. QMD underestimation of the production of composite particles was enhanced by the introduction of a SCM, however direct-like mechanisms seem to play a role in the production of deuterons and need to be accounted for.

New neutron-induced data at 175 MeV from C, O, Si and U were also measured at TSL; these data will be soon available and will provide the opportunity to a systematic study of the pre-equilibrium emission of light complex particles.

Acknowledgements

We thank M. Hayashi, S. Hirayama, Y. Naito, S. Abe, U. Tippawan, V.D. Simutkin, P. Andersson, J. Blomgren, M. Österlund, M. Tesinsky, F.-R. Lecolley, N. Marie, A. Hjalmarsson, A. Prokofiev, A. Kolozhvari. We thank the TSL staff for the assistance during the experiments. This work was supported by the Swedish Radiation Safety Authority, the Swedish Nuclear Fuel and Waste Management Company, Ringhals AB and by the European Commission within the Sixth Framework Programme through I3-EFNUDAT (EURATOM contract no. 036434). RB received financial support from the Japan Student Services Organization and from the Stiftelsen Th Nordströms testamentsfond granted by the Royal Swedish Academy of Sciences.

References

[1] S. V. Valentine and B. K. Sovacool, Energy Policy, Volume 38, Issue 12, 7971-7979 (2010)
[2] C. Rubbia *et al.*, CERN, Geneva, CERN-AT-95-44 ET (1995)
[3] C. D. Bowman *et al.*, Nulc. Inst. and Meth. A, 320, 1-2 (1992) 336-367
[4] V. Blideanu *et al.*, (2004) Phys. Rev C 70 014607
[5] U. Tippawan *et al*., (2004) Phys. Rev C 69 064609
[6] U. Tippawan *et al*., (2006) Phys. Rev C 73 034611
[7] U. Tippawan *et al.*, (2009) Phys. Rev C 79 064611
[8] J.J. Griffin, Phys. Rev Lett., 17, 478481 (1966)
[9] J.J. Griffin, Phys. Rev Lett., 19,57 (1967)
[10] A. J. Koning and M.C. Duijvestijn, Nuclear Physics A, 744 1576 (2004)
[11] K. Kalbach, Phys. Rev C, 71, 034606 (2005)
[12] K. Niita *et al.,* Phys. Rev C 52, 2620–2635 (1995)
[13] S. Chiba *et al.* , Phys. Rev C 54, 285–291 (1996)
[14] K. Abdel-Waged, Phys. Rev C 74, 034601 (2006)
[15] Y.Watanabe and D.N. Kadrev, Radiat. Prot. Dosimetry (2007) 126 (1-4): 40-44.
[16] R. Bevilacqua *et al.*, Proceedings of the International Conference on Nuclear Data for Science and Technology, April 26-30, 2010, Jeju, Korea (accepted)
[17] B. Piskor-Ignatowicz, Energy dependence of proton-induced fragmentation of atomic nuclei, PhD Thesis, Jagellonian University, Cracow, Poland (2009)
[18] A.A. Cowley *et al.*, (1997) Phys. Rev C 55 1843-1847
[19] A.J. Koning *et al.*, TALYS-1.0, Proceedings of the International Conference on Nuclear Data for Science and Technology, April 22-27, 2007, Nice, France, EDP Sciences, p. 211-214 (2008)

11. Experimental studies of light fragment production cross section for nucleon induced reaction at intermediate energies

Toshiya SANAMI[1], Masayuki HAGIWARA[1], Hiroshi IWASE[1], Masashi TAKADA[2], Daiki SATOH[3], Hiroshi YASHIMA[4], Tsuyoshi KAJIMOTO[5], Yosuke IWAMOTO[3], So KAMADA[2], Yoshihiro NAKANE[3], Satoshi KUNIEDA[3], Atsushi TAMII[6], Kichiji HATANAKA[6]

[1]*Applied Physics Laboratory, High Energy Accelerator Research Organization*
[2]*National Institute of Radiological Sciences*
[3]*Japan Atomic Energy Agency*
[4]*Kyoto University Research Reactor Institute*
[5]*Kyushu University*
[6]*Research Center for Nuclear Physics, Osaka University*
Email: toshiya.sanami@kek.jp

Energy, angular double differential cross section (DDX) data for fragment production from intermediate energy proton induced reactions were measured using a Bragg Curve Counter (BCC) for light to medium mass target nuclei. Systematic experimental data have been obtained for C, N, O, Al, Ti and Cu targets, incident energies from 40 to 300 MeV, fragments from Li to O with energies down to 0.5 MeV/u, at 30,60,90,120° laboratory angles. Typical examples of results are presented for the Al(p,x) reaction at 200 MeV, 30,60,90,120° and the C(p,xLi) at 40-200 MeV at 30°.

1. Introduction

Energy and angular double differential cross section (DDX) for nucleon-induced charged-particle production reactions are of importance to estimate radiation effects, energy deposition and radionuclide production. For this reason, the DDX of light charged particle (hydrogen and helium isotopes) production have been studied experimentally and theoretically. In addition to light charged particles, nucleon-induced reactions produce fragments (charged particle heavier than helium) in intermediate energy. Since the fragments have large liner energy transfer (LET), considerable amount of energy can be deposited in a μm region even by a single nucleon. The energy deposition causes anomalous effect on materials irradiated by intermediate energy radiation. According to recent studies, for instance, fragment productions show large contribution for irradiation effects of nucleon incidence on micro-electric devices [1]. Thus, precise data of fragment production are required for nucleon induced reaction in particular for tens of MeV and hundreds of MeV region with highest cosmic-ray neutron flux. The data provided from theoretical models, however, are not reliable enough for prediction of fragment production. Therefore, experimental data on nucleon-induced fragment production are required to establish theoretical models and its parameters that can cover various energy, target and products.

Several experimental studies reported DDX data for proton induced fragment production. R.Green et al. gave fragment DDXs of p+Ag reaction for Ep=210, 300 and 480 MeV [2]. S.J.Yennello et al. gave DDXs of p+Ag for Ep=161 MeV [3]. Recently, H.Machner et al. gave DDXs of p+Al, Co, Au for Ep=200 MeV [4]. In addition to these works, K.Katitkowski et al. reported mass distribution and energy spectra of p+Al reaction for Ep=180 MeV [5]. However, it should be noted that there is no data covering the energy range for tens of MeV to hundreds of MeV and target mass range for light to medium. The energy and target mass range are important to study transition of reaction mechanism and applicability statistical methodology for light nuclei. The data for light target nuclei are required to evaluate radiation effects on an organ.

To meet the requirements, we have conducted measurement of DDXs for fragment production in intermediate energy, light target nuclei, proton and neutron incidence [8-15]. We have developed Bragg Curve Counter (BCC) which has large solid angle and particle identification capability without additional detectors. The energy dynamic range, however, was limited in conventional BCC. Therefore, we have developed two new methods [8,9] to extend the energy dynamic range as described in the next section.

In this paper, we report recent fragment DDX measurements using the BCC, for proton-induced reaction on C, N, O, Al, Ti and Cu targets at 40-300 MeV region. The data of the Al(p,x) reaction for 200 MeV at 30,60,90,120° and the C(p,xLi) for 40-200 MeV at 30° are shown as typical examples of results.

2. Experimental

The present experiments were performed using the NIRS 930 cyclotron in National Institute of Radiological Science (NIRS) for 40-80 MeV protons and the ring cyclotron in Research Center for Nuclear Physics (RCNP), Osaka University for 140-300 MeV protons. Details of the BCC and experimental system employing it were described in references [8,9]. In this section, outline of this system is described.

Figure 1 shows plan view of the experimental setup at RCNP. Proton beam was focused to 1 mm diameter spot at the target foil that is mounted on a target

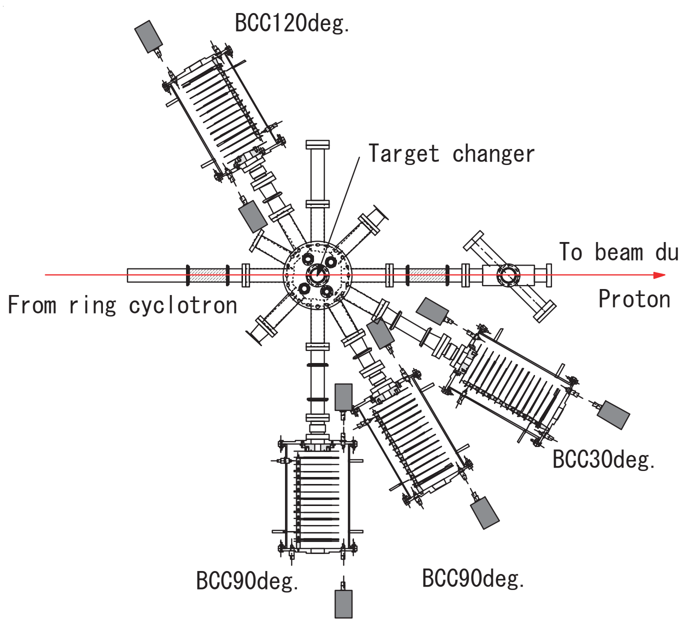

Fig.1 Plan view of experimental setup on ENN beam course in RCNP

changer. The target changer mounts blank, ZnS viewer and ^{241}Am α checking source as well as five targets. **Table 1** shows the list of target foils for the experiments. Al_2O_3 and AlN on Ta foils were for oxygen and nitrogen cross section measurement with subtracting Al and Ta contribution by separate runs. Fragments from the target were measured by the BCCs mounted on the 30, 60, 90 and 120° port of the scattering chamber.

Table 1 List of targets

	Thickness	Physical Form
Graphite	208 μg/cm2	Self support
Al	0.8μm	Self support
Al_2O_3	1.05μm	Sputtering on Ta
AlN	0.91μm	Sputtering on Ta
Ta	10μm	Self support
Ti	1μm	Self support
Cu	1μm	Self support

Figure 2 shows schematic view of the BCC. The BCC has been developed as a detector satisfying requirement for fragment measurement in intermediate energies, large solid angle, small energy loss, low threshold energy, and, insensitivity to protons [8,9].

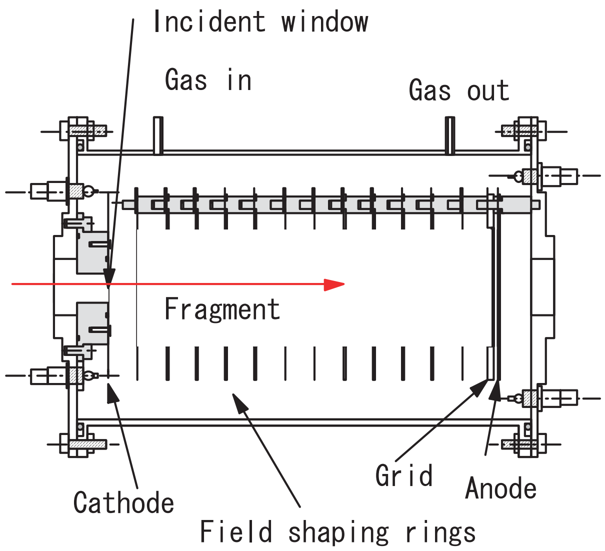

Fig. 2 Schematic view of the BCC

The BCC is a parallel plate ionization chamber with a grid. The structure is contained in a stainless steel cylindrical chamber. The distances between cathode and grid, and, grid and anode are 300 mm and 5 mm, respectively. The field shaping rings maintain uniformity of the electric field. High voltage is applied to the cathode, field shaping rings and grid electrodes to form electric field for electron drift. The cylindrical chamber is sealed using O-rings to keep low-pressure counting gas, 267 kPa (200 Torr) Ar+10% CH_4 gas, inside. The cathode side of the chamber has a hole of 20 mm in diameter covered with a thin entrance window, 0.5 μm thick SiN supported by window frame, to introduce fragments from the target.

Fragments which entered the BCC stops and produces electrons through ionization process. The number of electrons along its trajectory is proportional to the energy loss of the fragment, i.e, Bragg curve. The electrons drift toward to the grid with keeping their distribution along the electric field between the cathode and grid. The grid potential is chosen to allow that all electrons reach to the anode with passing through the grid. Under this condition, time distribution of the anode signal has inverse shape of the original distribution of electrons that equal to Bragg curve. Thus, the energy and atomic number of the fragment can be deduced from integral and peak height of the anode signal.

Two dimensional plots of events at 30° from 80 MeV proton induced reaction on carbon are shown in **Fig 3**. The vertical and horizontal axes correspond to fragment Z and energy. The events within the dotted circle (i) in Fig.3 have too low energy to identify using the Bragg curve vs energy plot. These events can be identified through the range-energy plot method [8]. The range can be determined using the signal from the cathode electrode. On the other hand, the events within the dotted circle (ii) have too high energy to be stopped in BCC and penetrate it. The missed energy can be compensated through off-line analysis [9]. By using these two new methods, the energy spectra can be obtained for each fragment over 0.5 MeV/nucleon to tens of MeV.

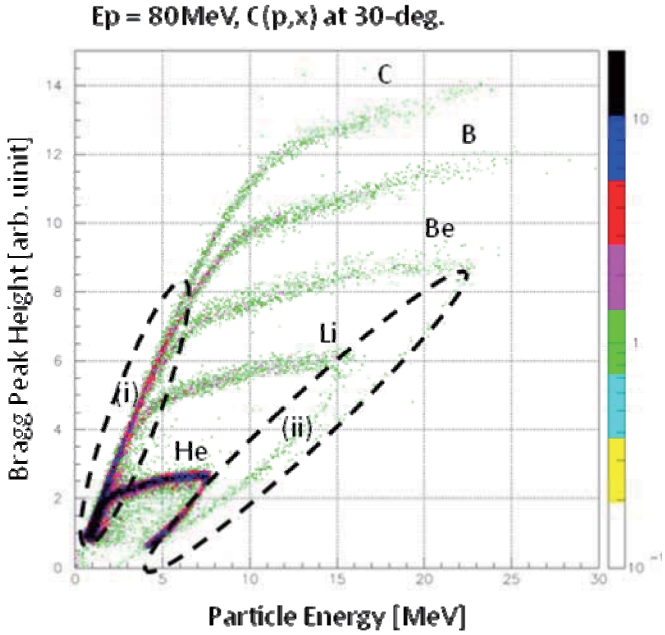

Fig.3 Two dimensional plot of events at 30° from 80 MeV proton induced reaction on carbon

The measured data were analyzed to obtain energy spectra for each fragment with Z, corrected for the effects of energy losses in sample and incident window, and normalized to solid angle, the number of target atoms and the number of incident protons.

3. Results and discussion

From the measurements, we have obtained DDX data of fragments for proton-induced reactions on C, N, O, Al, Ti and Cu at several beam energies between 40 and 300 MeV, and several laboratory angles between 30° and 120°. The spectra were obtained down to 0.5 MeV/u. Here, typical examples are shown as preliminary data. Final results will be reported later.

Figure 4 shows the results of fragment DDX for the Al(p,X) reaction for Ep=200 MeV. The figure shows Li, Be, B and C spectra for 30°, 60°, 90°, 120° emission angles. The experimental results taken by Machner et al. are also plotted for Li and Be emission. It should be noted that their data were obtained using counter telescopes with Si detectors and cover the energy region only above 20 MeV. The present data smoothly connect to their data. The figure clearly shows that two data are consistent with each other. The low cutoff energies of the present data, < 0.5 MeV/u permits to cover the energy region with highest yields. Therefore, the data provides not only spectrum information but also integral cross section, experimentally. In addition, the present result has relatively continuous distribution shows high energy tail that is observed in the other results for Li and Be emission [2-5]. Concerning B and C spectra, the peak yields are comparable to Li and Be. The fact indicates that emission process of B and C are similar to that of Li and Be.

Figure 5 shows the results for the C(p,xLi) reaction at 30° for Ep=40, 50, 70, 80, 140, 200 MeV. A change of spectra shapes is observed with increasing incident proton energy. For relatively low incident energies, 40 and 50 MeV, peak structures are observed around the high energy end above continuum components. The energy differences between peak structures are close to the energy between the ground

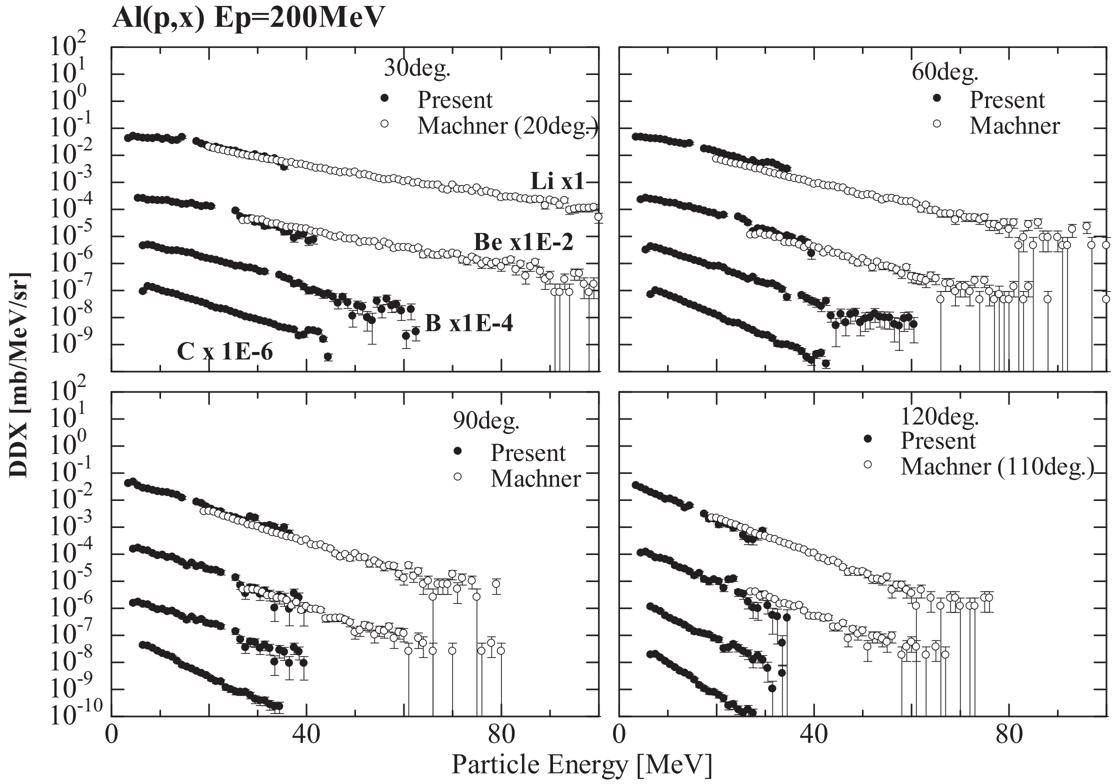

Fig.4 Fragment DDX for Al(p,X) reaction for Ep=200MeV (Preliminary)

and excitation states of ^{7}Be. Thus, the peak will be attributed to the two-body reaction, ^{12}C (p,^{6}Li)^{7}Be. A similar peak structure is also observed for Be spectra for 40 and 50 MeV proton on carbon (not shown here). The peak structure disappears with increasing incident energy. Therefore, the contribution of the cluster structure of target nuclei should be considered to describe fragment emission from light targets in this energy range, as pointed out in former works [6,7].

The present data set covers fragment DDXs for light to medium target nuclei, incident energies from 40 to 300 MeV. With combining the former studies for medium to heavy target nuclei [2-5], systematic, self-consistent experimental data become available to evaluate and improve theoretical

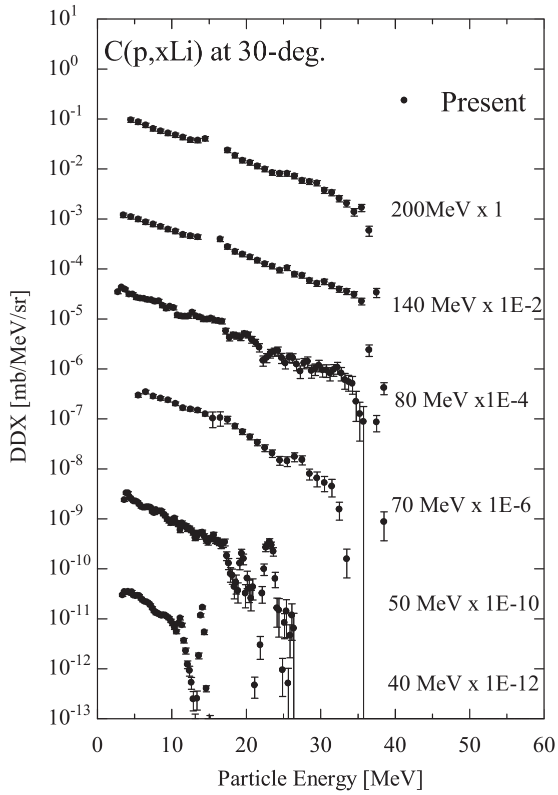

Fig. 5 C(p,xLi) reaction at 30 degrees for Ep=40, 50, 70, 80, 140, 200 MeV (Preliminary)

models and its parameters. Further data analysis is in progress to make clear the dependency of fragment production on energy, mass, and angle.

4. Conclusion

We measured systematic DDX data down to 0.5 MeV/u for proton-induced fragment-production reactions on C, N, O, Al, Ti and Cu. The results were consistent with the other experimental results from comparison of the Al(p,xLi) and Al(p,xBe) results for Ep=200 MeV. From the Al(p,x) data, the amounts of B and C emission are comparable to Li and Be emission. From the C(p,xLi) data for various proton energies, two body reaction process that indicated cluster structure of target nuclei was observed for lower incident proton energy. Further data analysis is undergoing to derive not only systematic data set but also pictures of fragment production reaction. The both results would help to improve treatment of fragment production that is used for energy deposition calculation in a matter.

Acknowledgements

The authors wish to thank operators and supporting crew of NIRS cyclotron and RCNP for their help to perform beam experiment. The BCC was originally developed with support of Grant-in-aid of ministry of education "KAKENHI(15360499, M.Baba, Tohoku University) " . The part of this work is funded by "2009 Genshiryoku-Kiban-Kenkyu-Initiativ" program for young scientist.

References

[1] Y.Watanabe, *"Nuclear Data Relevant to Single Event Upsets in Semiconductor Memories Induced by Cosmic-ray Neutrons and Protons", Proc. 2006 Symp. Nucl. Data (JAEA-Conf 2008-006)*
[2] R.Green et al., *Phys.Rev.***C22** 1594(1980)
[3] S.J.Yennello et al., *Phys.Rev.***C41**, 79(1990)
[4] H.Machner et al., *Phys.Rev.***C73**, 044606(2006)
[5] K.Katitkowski et al. *Phys.Rev.Lett.* **50**,1648 (1983)
[6] G.D'Erasmo et al, *Phys Rev.* **C31** 656 (1985)
[7] S.Kato et al, *Phys Let* **62B** 153, (1976)
[8] T.Sanami et al., *Nucl. Instrm. Meth*. **A Vol 589** 193 (2008)
[9] M. Hagiwara et al., *Nucl. Instrm. Meth.* **A Vol 592** 73 (2008)
[10] T.Sanami et al., *Nucl. Instrm. Meth*. **A Vol 610** 660 (2009)
[11] M.Hagiwara et al., *Radiat Prot Dosimetry* **126** 104 (2007)
[12] M. Hagiwara et al., *"Measurements of Double Differential Fragment Production Cross Sections of Silicon for 70 MeV Protons", Proc. 2005 Symp. Nucl. Data (JAEA-Conf 2006-009)*
[13] T.Sanami et al., *"Recent progress of fragment measurement from tens of MeV proton induced reaction using Bragg Curve Counter", Proc. 2008 Symp. Nucl. Data(JAEA-Conf 2009-004)*
[14] T.Sanami et al., *"Measurement of fragment production DDX of 72 and 144 MeV ^{12}C beam induced reaction on carbon using Bragg Curve Counter", Proc. 2009 Symp. Nucl. Data (JAEA-Conf 2010-005)*
[15] T.Sanami et al, *"Fragment DDX measurement of proton induced reactions on light-medium nuclei for energy range from reaction threshold to a few hundred MeV ", Proc.Int.Conf.Nucl.Data Sci Tech. 2010 JeJu, Korea, in Print*

12. Intranuclear cascade model for cluster production reactions

Yusuke UOZUMI and Yusuke SAWADA
Faculty of Engineering, Kyushu University
Motooka Nishi-ku, Fukuoka 819-0395, Japan
Email:uozumi@nucl.kyushu-u.ac.jp

The intranuclear cascade model is used to describe cluster production in intermediate-energy nucleon-nucleus reactions. Although a great deal of effort has been made toward unraveling the cluster formation mechanism, its dynamical and quantitative aspects are still controversial. The emission of a cluster is governed mainly by the indirect-knockout and indirect-pickup (or coalescence) processes. To describe these two processes, nucleon correlation is introduced into the initial and final state in the model. The resulting double differential cross sections for proton-induced light-cluster (p, d, t, ^{3}He, α) production reactions are demonstrated to be in good agreement with experimental results.

1. Introduction

The intranuclear cascade (INC) model is a powerful method for describing intermediate-energy spallation reactions, and INC code has been incorporated into macroscopic simulation tools such as PHITS and GEANT4. The INC model has been shown to satisfactorily predict nucleon spectra over a wide energy range above the evaporation region. With the rapid development of simulation tools, there is an increasing demand to extend the INC model to cluster-production reactions. Since the model treats the reaction process as a succession of binary hard collisions, it does not consider the formation of clusters. To apply the INC model to cluster production requires a deep understanding of the process to allow generalization of the calculations.

Although the mechanism of cluster production from nucleon-induced reactions has been investigated for many years, important questions still remain [1]. The reaction giving rise to α-cluster emission has attracted particular attention and many theoretical models have been proposed to clarify the mechanism involved. Almost all of these have been based on exciton or hybrid models and have focused on two different mechanisms. The first involves knockout of a preformed cluster, and the second coalescence or pickup, in which a cluster is formed in the course of a reaction. In the higher energy domain, the roles played by these mechanisms can be more easily distinguished. Moreover, the exciton model does not take angular momentum into account, and therefore does not consider angular distributions, which are among the most important physics quantities. It is clear that the classical cluster-knockout picture has difficulty in accounting for the forward peak in experimental angular distributions, but nevertheless this is intuitively expected to influence higher-energy cluster production.

The quantum molecular dynamics (QMD) and antisymmetrized molecular dynamics (AMD) models are also candidates for describing cluster production. Since it lies within the framework of molecular dynamics, cluster production might be considered to be a natural application of such models. Actually, AMD has been reported to reasonably well describe [2] the α-cluster energy distribution resulting from collisions between heavy ions with energies around 30 MeV/u. However, the study was carried out for the case where the nucleon momentum was small relative to the center-of-mass of the system, and in such a scenario cluster formation should be governed by a coalescence-like process. In fact, the coalescence model [3] can reproduce the lower energy part of the spectrum, but fails at higher energies. Meanwhile, there have been no successful attempts to model the high-energy portions of spectra due to heavy-ion collisions and proton-induced reactions. The mechanism involved in high-energy deuteron production has been an open question because of the very small binding energy involved. In these cases, the clustering process must overcome a large momentum difference by quantum mechanisms, and QMD and AMD may lose their predictive power.

In the present work, an attempt is made to apply the INC model to cluster formation reactions. Since INC is a simulation model, it has the great advantage of having high flexibility, allowing it to be extended to include cluster formation. It is essential to consider clustering phenomena in detail and to accurately model the physical processes in order to allow generalization over a range of reactions, targets, ejectile clusters, and energies up to several GeV. In the present study, numerical calculations are carried out to shed light on the influence of the wave nature of nucleons on the combination process. Thus, we extend the INC to include knockout and pickup processes. It should be noted that neither of these processes is a so-called "direct" reaction. Strictly speaking, they should be referred to as "indirect pickup" and "indirect knockout" processes; however, for brevity, we will drop the word "indirect" hereafter. The validity of the proposed model is verified through comparison with experimental data for (p, d*x*), (p, t*x*), (p, ^{3}He*x*) and (p, α*x*) reactions with incident energies ranging from 150 to 400 MeV.

2. Calculation model

2.1 Theoretical background of clustering phenomenon

The mechanism of high-energy cluster formation is not well understood because the momentum difference between nucleons is larger than their binding energy. It is impossible to describe this phenomenon using a classical particle approach since the quantum wave nature of nucleons plays an essential role in the clustering process. In order to investigate this role, numerical calculations are carried out using wave-packet dynamics.

We consider the dynamics of Gaussian wave packets ϕ_i and ϕ_j via a potential *U*. The time development of the system is described by

$$i\hbar\frac{\partial}{\partial t}\psi(x_i,x_j,t) = \left(\hat{T}_i+\hat{T}_j+U(r)\right)\psi(x_i,x_j,t),$$

where T is the kinetic energy. When spin and iso-spin are ignored, the total wave function is in the form of $\psi(x_i,x_j,t) = \phi_i(x_i,t)\phi_j(x_j,t)$. Hence, Eq. (1) can be written as

$$i\hbar\frac{\partial}{\partial t}\phi_i(x_i,t) = \left(\hat{T}_i+V_i(x_i,t)\right)\phi_i(x_i,t),$$

$$V_i(x_i,t) = \int dx_j\phi_j^*(x_j,t)\left(\hat{T}_i - i\hbar\frac{\partial}{\partial t}+U(r)\right)\phi_j(x_j,t).$$

Typical calculation results are shown in Fig. 1, which represents the time development of a two wave packet system through a two-range Yukawa potential U with a short-range repulsive and a long-range attractive force. Panels (C) and (D) show the appearance of quasi-bound states at a positive energy in addition to refraction and penetration of wave packets. It is, of course, impossible to interpret this result in classical terms. In the case of a proton-neutron interaction, a gamma-ray is emitted at this point, and the system enters a true bound state. This process is considered to be especially important in the production of high-energy clusters.

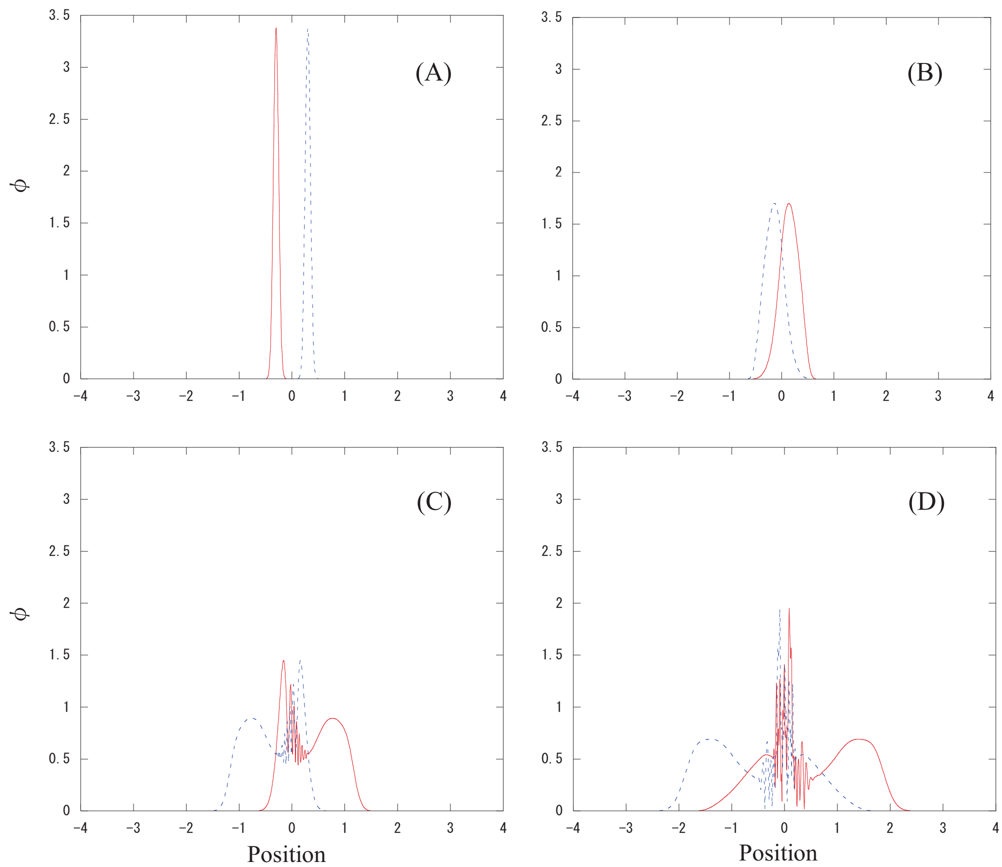

Fig. 1: Time development of two wave packets from panel (A) to (D). Panel (D) shows refraction, penetration and quasi-binding of the wave packets.

2.2 Pickup process

As discussed above, the pickup process is dominant in the low-energy part of the spectrum above the evaporation regime. A cluster is assumed to be formed when nucleons are within a limited phase space in the final state. Non-excited nucleons below the Fermi level can be picked up by a leading particle. This assumption is similar to that involved in the Iwamoto-Harada model [4], but different from coalescence models, which assume an outgoing cluster is formed by nucleons excited above the Fermi level. The clustering criterion for the final state is written in the form

$$r_{ij}\, p_{ij} \leq C_{\mathrm{f}}\,,$$

where r_{ij} and p_{ij} represent the distance between nucleons in phase space. The appropriate value of C_{f} is determined to give the best fit to experimental data for different reactions: C_{f} is 2000 fm MeV/c for deuteron, and 2500 for triton, ^{3}He and α cluster.

2.3 Knockout process

The knockout process is responsible for reproducing the high-energy portion of the spectra. The underlying physics is based on the existence of preformed clusters inside the target nucleus. If we consider a preformed deuteron as a single elementary particle (see Fig. 2), it is impossible to account for the experimentally observed forward-peaked angular distribution resulting from (p, d*x*) reactions.

In the present study, the preformed cluster is considered to be a composite of nucleons. A schematic diagram of the deuteron knockout process is shown in Fig. 3(A) and (B). It should be noted that an exchange process is essential to explain the forward peak in the angular distribution. Since a high-energy cluster is produced via interference, this cannot be interpreted from a classical view point. The criterion for the initial state interaction is defined as

$$r_{ij} \leq C_{\mathrm{i}}.$$

In the present work, we determined C_{i} = 1.0, 1.4 and 1.5 fm for clustering deuteron, triton and ^{3}He, and α respectively, to give the best fit to experimental data.

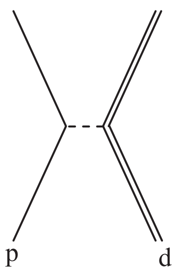

Fig. 2 Scattering p+d, where d is treated as an elementary particle

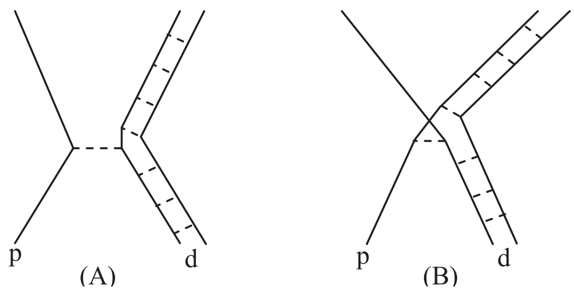

Fig. 3 Scattering p+d, where d is treated as a composite particle.

2.4 Other processes

Direct reaction processes may include the pickup reaction and direct deuteron formation via

$$\mathrm{p} + \langle \mathrm{N} \rangle \rightarrow \mathrm{d} + \pi \text{ or } \gamma.$$

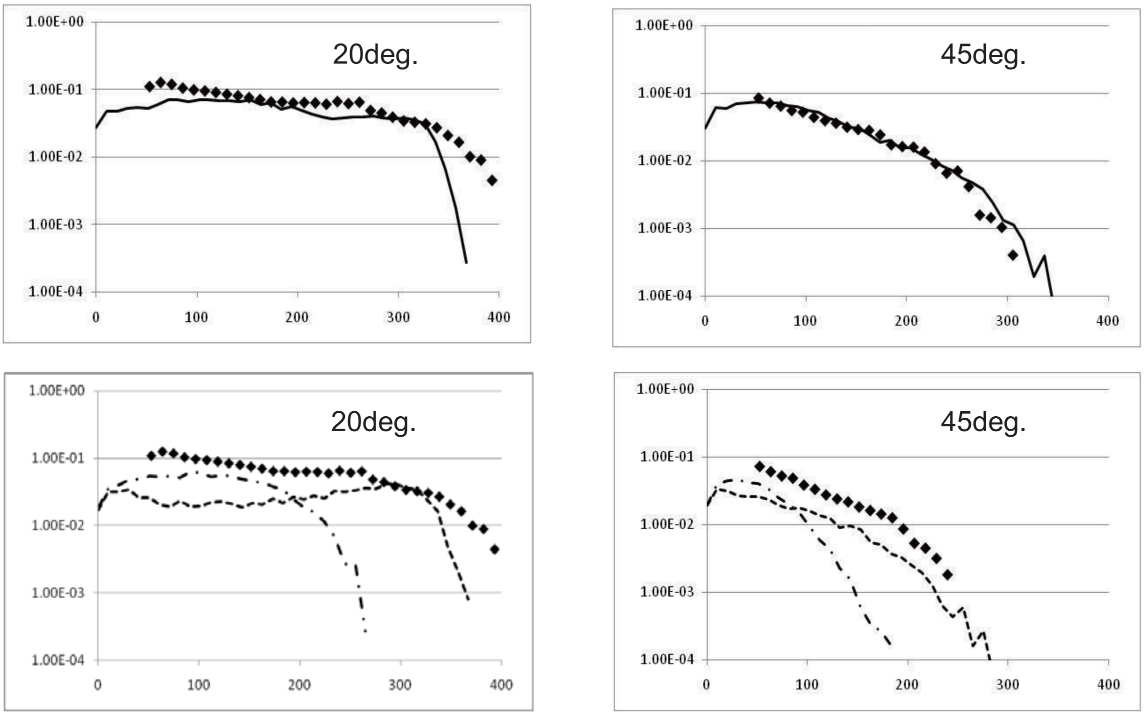

Fig. 4 Deuteron spectral double differential cross sections of V(p, dx) at 392 MeV. Lower panels show contributions from pickup (dash-dotted line) and knockout (broken line).

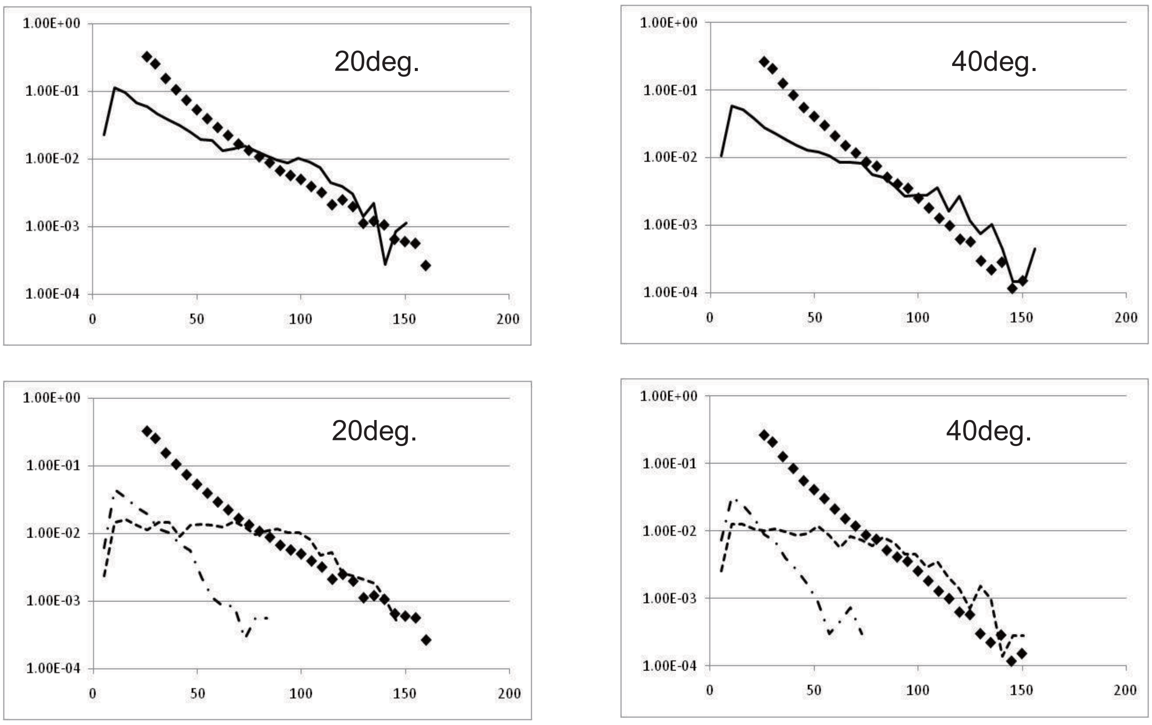

Fig. 5 Alpha spectral double differential cross sections of Co(p, αx) at 200 MeV. Lower panels show contributions from pickup (dash-dotted line) and knockout (broken line).

Since it is difficult to predict the magnitude of the cross sections involved, we ignore these processes at present. Another important process is evaporation, which is treated using a stochastic model.

3. Results and discussion

In the present work, we incorporated the pickup and knockout processes into our INC code [5]. Typical simulation results for energy spectra are shown in the upper panels of Figs. 4 and 5, and are compared with experimental data for 392-MeV (p, d*x*) reaction [6] and 200-MeV (p, α*x*) reaction [7], respectively. Despite slight underestimations, all of the results are in good overall agreement with the experimental data.

The lower panels show the contributions from the pickup and knockout processes. In both of the reactions, the knockout appears in the high-energy range and the pickup the low-energy. In (p, d*x*) reaction case, the influence of direct reaction appears at 20 deg. around the high energy end. In (p, α*x*) reaction, the knockout process dominates over the entire spectral range, and the pickup process has only a weak contribution. The underestimation in the low-energy domain is due to lack of the evaporation process.

4. Conclusion

Light-cluster production from intermediate-energy proton-induced reactions was investigated. Calculations using a modified version of the INC model including indirect cluster knockout and pickup processes exhibited reasonable agreement with experimental data over a wide range of reactions and energies. For proton energies of 200-400 MeV, the results indicate that cluster production is governed mainly by the knockout process. Though ambiguities remain in the parameterization, we believe present one is close to the best in order to explain reactions at above 400 MeV, where the influence of knockout is expected to be significant. Generalization is essential over a range of bombarding energies. To cover a range up to 3 GeV is required by PHITS.

Acknowledgement

This work was performed in collaboration with Mr. Yoshioka, Dr. Iwamoto, and Prof. Nakano. The author deeply appreciates their cooperation.

References

[1] P.E. Hodgson and E. Běták: Phys. Rep. 374, 1 (2003).
[2] A. Ono, H. Horiuchi, T. Maruyama: Phys. Rev. C47, 2652 (1993).
[3] H.H. Gutbrod et al.: Phys. Rev. Lett. 37, 667 (1976).
[4] A. Iwamoto and K. Harada: Phys. Rev. C 26, 1821 (1982): Nucl. Phys. A 419, 472 (1984).
[5] H. Iwamoto, et al.: Phys. Rev. C82, 034604 (2010).
[6] F. Saiho: Doctoral thesis, Kyushu university (2004).
[7] A.A. Cowley et al.: Phys. Rev. C55, 1843 (1997).

13. Nuclear Data Activities in Korea

Young-Ouk Lee
Nuclear Data Evaluation Lab.
Korea Atomic Energy Research Institute
e-mail: yolee@kaeri.re.kr

Mission of Nuclear Data Evaluation Laboratory (NDEL) of Korea Atomic Energy Research (KAERI) includes disseminating outcomes of international network as well as promoting domestic nuclear data activities. Nuclear data needs in Korea are mainly from following major nuclear R&D programs:

- SFR (Sodium-cooled fast reactor) project requires high quality neutron data including uncertainties for actinides, MA and structural materials for fast energy region.
- AFC (Advanced Fuel Cycle) project needs cross sections and covariance for MA as well as fission products for full energy region of neutron.
- Korea, as one of ITER members, requires reliable nuclear data of major ITER components (first wall, tritium breeding module, etc) for their neutronics calculations and analyses.
- Korea Rare Isotope Accelerator (KoRIA) project which has started this year needs more reliable nuclear data of spallation and fragmentation reactions for energies up to a few hundred MeV of charged particles and heavy ions.

KAERI/NDEL is performing nuclear data evaluation, multi-group library processing, and validation which are required by the above mentioned R&D program in Korea. For measurement of nuclear reaction data, KAERI/NDEL is coordinating measurements of Pohang Neutron Facility (PNF) of Pohang Accelerator Laboratory (PAL), Van de Graff laboratory of Korea Institute of Geosciences and Mineral Resources (KIGAM), and MC-50 Cyclotron at Korea Institute of Radiological and Medical Sciences (KIRAMS).

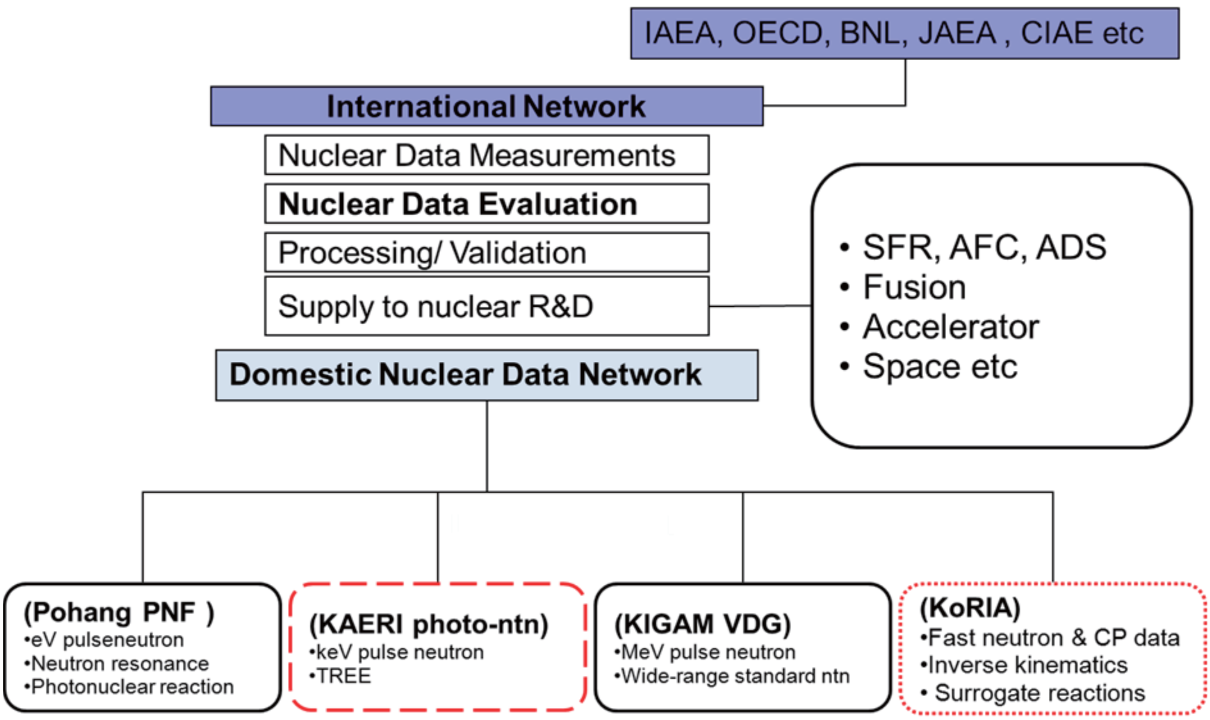

1. The recent activities under the international collaborations

NDEL/KAERI collaborates with the international organizations such as IAEA and OECD/NEA, and the foreign institutes such as ORNL and BNL regarding the evaluation, processing and validation of nuclear data to satisfy present requests and to prepare future latent needs. Below summarizes the recent activities of NDEL/KAERI in collaboration with international organizations and foreign institutes.

- Fusion Evaluated Nuclear Data Library (FENDL) CRP of IAEA
- Participation in IAEA EXFOR compilations since 2009
- Contribution of group constant libraries to OECD/NEA Data Bank.
- Evaluations and uncertainty analysis of Minor actinides with ORNL
- Improvements of resonance module ncluding covariances with BNL
- Evaluation of neutron cross sections for fast energy region with BNL

2. Production and validation of evaluated nuclear data

1) Developments of nuclear data evaluation methodology

Recent evaluations of neutron cross section covariances in the resolved resonance region reveal the need for further research in this area. Major issues include declining uncertainties in multigroup representations and proper treatment of scattering radius uncertainty. A practical method is being investigated for estimating neutron radiative capture and elastic scattering covariances in the resolved resonance region. The method is based on a “kernel approximation” using resonance parameter uncertainties from the Atlas of Neutron Resonances. Suitable analytical expressions were derived from the consideration of cross section sensitivities in order to determine cross section uncertainties. The role of resonance-resonance and bin-bin correlations is specifically studied.

2) New evaluations of charged particle induced nuclear reactions

- The evaluations are performing for reactions induced by charged particles including proton, deuteron, and alpha. The considered nuclides are $^{28\text{-}30}$Si, ^{27}Al, ^{54,56,57,58}Fe, ^{92,94,95,96,97,98,100}Mo, ^{58,60,61,62,64}Ni.
- Evaluations will go through validations and verifications by FENDL CRP.

3) New evaluations of minor actinides for Advanced Fuel Cycle (AFC)

- Producing new evaluations for Advanced Fuel Cycle (AFC) including covariance files. The considered nuclides are ^{237}Np, ^{240}Pu, $^{240\text{-}250}$Cm
- Evaluation, validation and benchmarks are in collaboration with ORNL

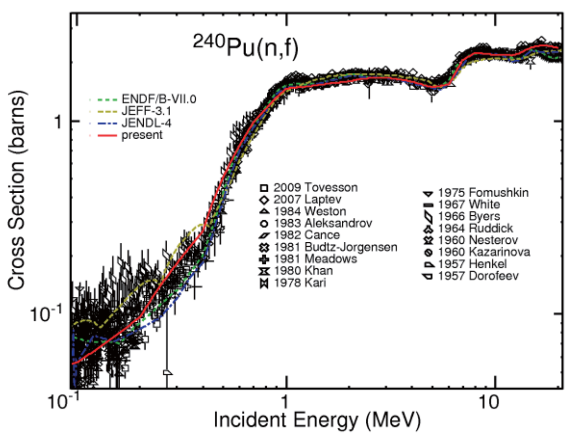

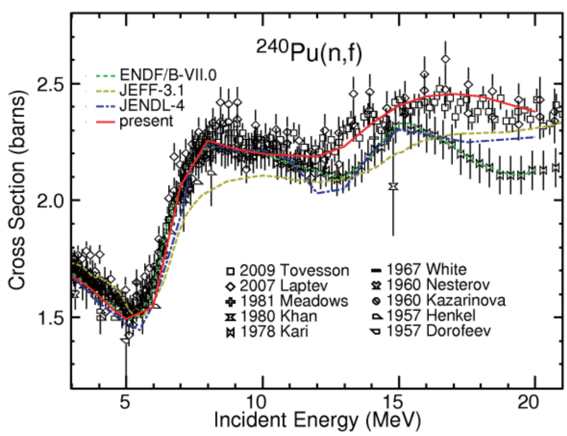

3. Operation of nuclear data measurement facilities

1) Pohang Neutron Facility of PAL
- Specifications: 50- 70 MeV beam energy, 30-70 mA beam current, 10-15Hz, TOF
- Measurements of neutron total cross sections of Fe, Ho, Pd, Ni, Dy.
- The photo-nuclear reaction for Ti, Nb, Mo, Cd, Pd, Ag, Au, Th, Er, W, Cu by using the Bremsstrahlung radiation by the electron beam with energies of 50, 60, and 70 MeV
- BGO detector module was constructed by coupling the BGO crystal and PMT, and tested by using the radiation sources

2) Vand der Graaf of KIGAM
- Monoenergetic pulsed neutron beam for energies 500 keV ~ 2.2 MeV with TOF
- Measurements of total cross sections of Al and W
- Productions of neutron sources with 4 MeV ~ 6.6 MeV using d-d reaction
- Design of neutron sources at 14 MeV using d-T reaction

3) MC-50 of KIRAMS
- Azimuthally-Varying Field-Type MC-50 cyclotron, Ep: 45 MeV, 50 nA beam current
- Measurements of proton c.s. for ^{nat}W, ^{nat}Sn, ^{nat}Cd, ^{27}Al, ^{nat}Zr, ^{nat}Ag, ^{nat}Pd and ^{nat}T

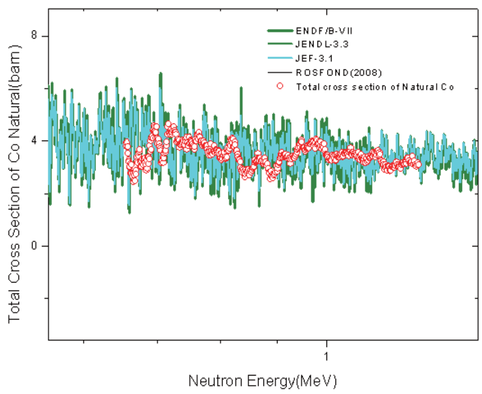

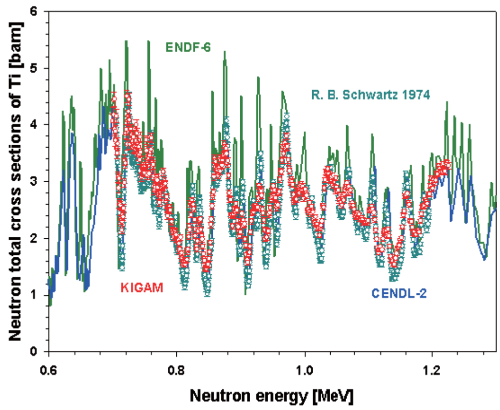

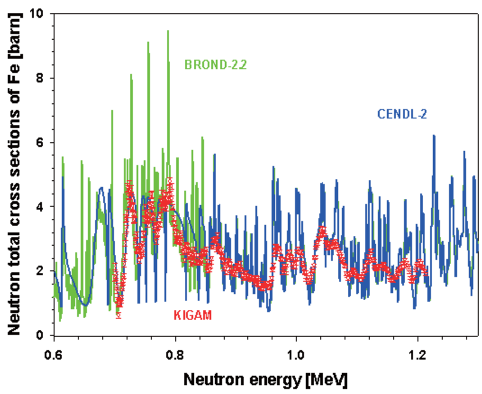

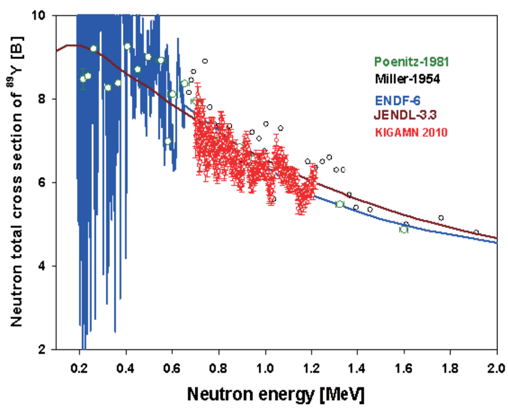

4. Conceptual design of KAERI photo-neutron source

KAERI (Korea Atomic Energy Research Institute) is developing a neutron TOF facility by using KAERIs electron accelerator. KAERI has a superconducting electron accelerator which can produce 17 MeV pulsed electron beams with a pulse width of 20 ps. The pulse current and maximum frequency of the electron accelerator are 20 A and 2 MHz respectively. Fast neutrons with energy of a few hundreds keV and a few MeV can be used for cross-section measurements. A short pulse width can provide a good neutron energy resolution for fast neutrons at relatively short flight lengths. The time resolution related to the neutron source target should be small enough to utilize the short pulse. We adopted the liquid Pb target which was developed by FDZ (Forschungszentrum Dresden-Rossendorf). The first step of the neutron source development is to simulate the neutron production. MCNPX was used to simulate the neutron production when an electron beam irradiates the Pb target. Those simulations were performed by varying the electron beam diameter, beam energy and target size to find out optimal variables related to the beam and target. The dissipated heat information was studied by MCNPX since a proper cooling system should be considered to operate the liquid Pb target safely. The thermal-hydraulic analysis was performed based on the dissipated heat information. The thermal stress calculation of the target wall was also performed from the temperature information obtained by the thermal-hydraulic analysis. The study of the detection system is under progress. The design of experimental hall and collimator is also being progressed with the development of the detection system. We plan to finish the design of the facility by 2011 and start the construction at 2012.

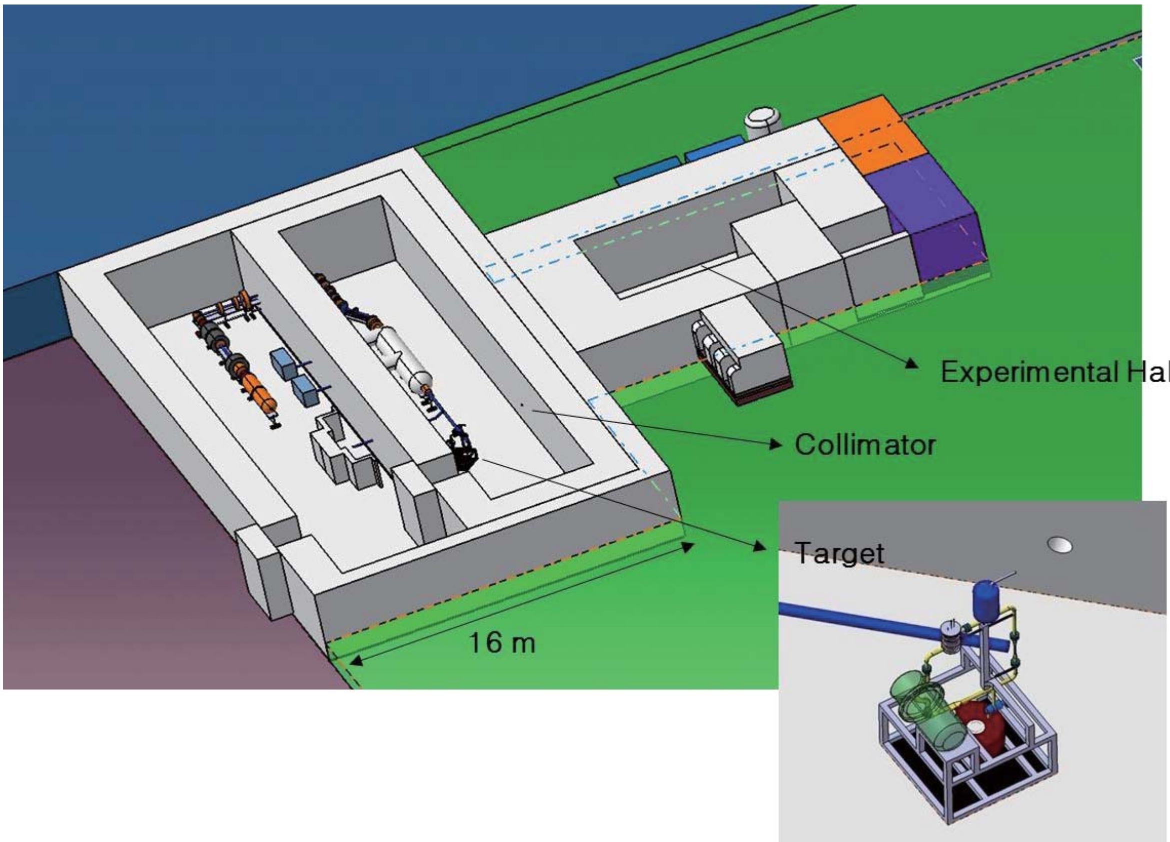

5. Nuclear Data vs. KoRIA

Conceptual design of Korea Rare Isotope Accelerator (KoRIA) project started as of March 2010. Korean Nuclear data network led by NDEL is proposing a utilization plan of KoRIA for the nuclear data production as follows:

-Neutron data for GEN-VI and fusion device using d + light targets and spallation n source,
-Nuclear data for waste transmutation using In-flight and ISOL facilities, and
-Nuclear data from Surrogate reactions using heavy ion sources.

Nuclear data measurements can be performed using beams provided by KoRIA. There are three possible research topics related to the nuclear data measurements at KoRIA. Those three research topics utilize fast neutrons, spallation neutrons and charged particles respectively. Among three research topics, the priority is given to the nuclear data measurements using fast neutrons. Fast neutrons can be produced by proton and deuteron beams coming from the cyclotron of KoRIA. The thin Li target is bombarded by proton beam to produce mono-energy fast neutrons. Fast neutron nuclear data is essential in developing fast reactors, fusion reactors and accelerator-driven systems. At KoRIA, the fast neutron cross sections can be measured for the elements constituting the fuel and structural materials of the above-mentioned systems. The detection system is also being investigated for the measurements of capture, fission, elastic scattering and inelastic scattering cross sections.

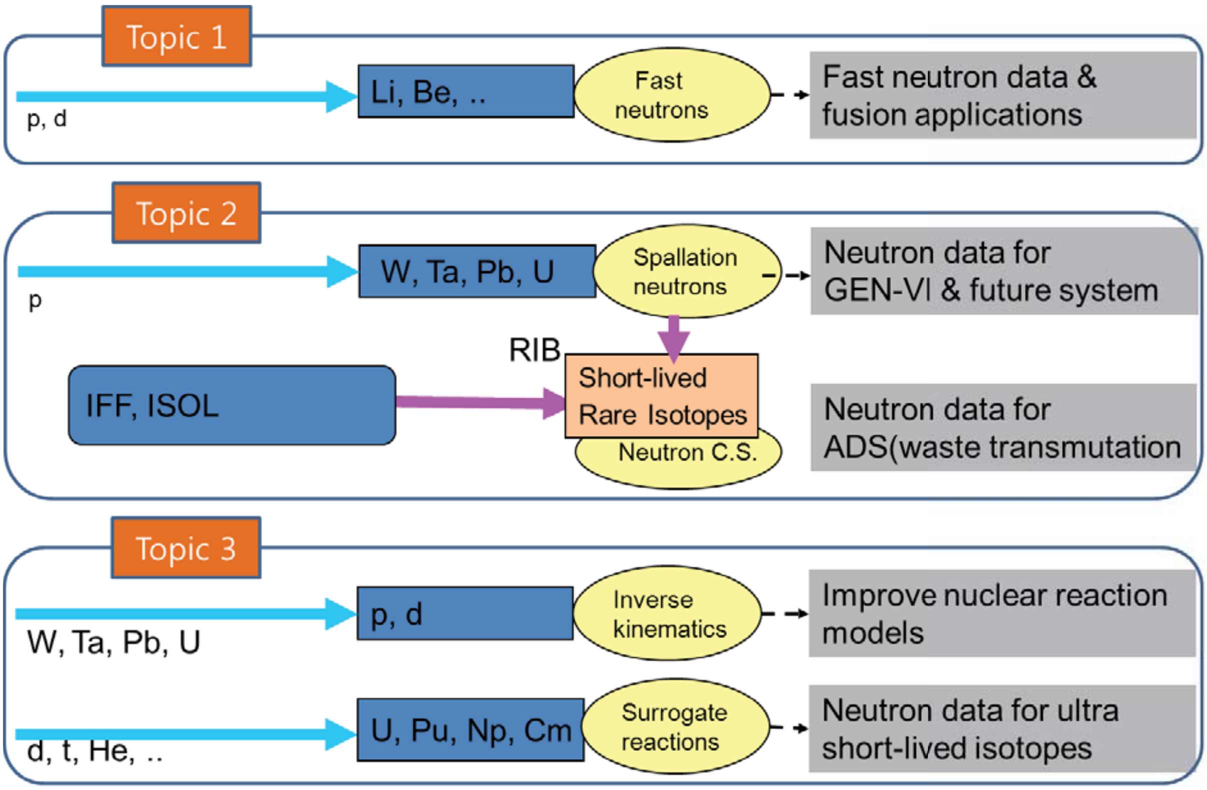

14. INRNE-BAS: Recent State and Future Prospects

Mitko K. Gaidarov
Institute for Nuclear Research and Nuclear Energy,
Bulgarian Academy of Sciences
Blvd. Tzarigradsko chaussee 72, 1784 Sofia, Bulgaria
e-mail: gaidarov@inrne.bas.bg

In this presentation a review of the Institute for Nuclear Research and Nuclear Energy (INRNE) of the Bulgarian Academy of Sciences (BAS) will be done. The main accent is to show the mission and the vision of the Institute, its structure and the general scientific activities. First, a short historical introduction will be made. A special attention will be paid to the international contacts of INRNE (with world-wide organizations, institutions and universities) which are very important for the successful Institute staff's work. As it was concluded by the 2009 Science Review Committee for INRNE from the side of the European Science Foundation (ESF) and the All European Academies (ALLEA) Federation, "INRNE is currently well placed in the national and international context, having gained considerable experience in international collaborations". As a part of the international collaboration, the INRNE participation in the Sixth and Seventh Framework Programs of European Commission (EC) is given. Particularly, the Institute's participation in SPIRAL2 project in GANIL (France) being one of the EC infrastructure projects with a priority will be considered. The two basic experimental facilities of INRNE, namely the Nuclear Scientific and Experimental Centre with Research Reactor and the Basic Environmental Observatory "Moussala" are presented. A specific view on the present state of the Nuclear Theory Laboratory of the INRNE, one of the laboratories in the field of theoretical nuclear and particle physics in Bulgaria, will be done. The publication activity for the last few years, knowledge dissemination and innovation transfer are shown together with the educational activity performed by the scientists of the Institute. Finally, the future plans in developing of INRNE are indicated. For more details, please use the Institute web-site: http://www.inrne.bas.bg/

1. Introduction

The Institute for Nuclear Research and Nuclear Energy is one of the biggest within the Bulgarian Academy of Sciences. It is the leading complex center in Bulgaria for scientific research and applications of the nuclear science and technologies and studies of their interactions with the environment. INRNE guarantees a high quality performance of research and innovation activities, addressed to support important national programs, keeping abreast with the modern scientific achievements. With its longstanding experience and active collaboration with leading European and international institutions, INRNE contributes to the progress of the physical science.

The Physical Institute of BAS was established on July 1 1946 by academician Georgi Nadjakov who became its first director. In 1962 the Physical Institute of BAS was renamed as the Physical Institute with a Nuclear Experimental Facility. A crucial factor for the nuclear research in Bulgaria became its membership at the Joint Institute for Nuclear Research established in Dubna near Moscow in 1956. In 1972 the Institute of Physics split into Institute for Nuclear Research and Nuclear Energy and Institute of Solid State Physics.

The Institute's staff of about 280 (150 of them are scientific researchers) works in 16 laboratories, 2 scientific experimental facilities and 9 departments providing general support activities. Since 2005 nearly half of all laboratories in INRNE qualified for QQS certificate for Quality Management System ISO 9001:2000 and for Environmental Management System ISO 14001:2004. The main topics of activities include:

- Theory of the elementary particles, fields and atomic nuclei
- Nuclear physics and astrophysics
- High energy physics
- Nuclear methods
- Nuclear instrumentation
- Radiochemistry
- Dosimetry and radiation safety
- Neutron physics
- Reactor physics
- Nuclear energy and nuclear safety
- Monitoring and management of environment

The INRNE has a programme accreditation from the National Evaluation and Accreditation Agency for Doctor's degree in six different areas of theoretical and mathematical physics, nuclear physics, physics of elementary particles and high energies, neutron physics and physics of nuclear reactors, radiochemistry and nuclear reactors. The Institute has collaboration agreements with the Faculty of Physics of Sofia University “St. Kliment Ohridski”, South-West University “Neofit Rilski” (Blagoevgrad), American University in Bulgaria (Blagoevgrad), Konstantin Preslavsky University of Shoumen, Technical University (Sofia) and University of Mining and Geology “St. Ivan Rilski” (Sofia).

2. Recent state of INRNE

In 2009 INRNE has undergone an independent, comprehensive and detailed review from the ESF and ALLEA on the base of self-evaluation report provided by the Institute for the period 2004-2008. For the purposes of this evaluation, and given the very wide breadth and heterogeneity of activities carried out at INRNE and the complexity of the institute, it was decided to divide INRNE into the following three units:
Unit 1: Theoretical and experimental nuclear and particle physics and astrophysics, including mathematical theory
Unit 2: Applications
Unit 3: Facilities
The corresponding scores according to three criteria considered by the Science Review Committee are as follow:

	Quality and Productivity	**Relevance: Socio-economic Impact**	**Prospects**
Unit 1	**A**	**A**	**A**
Unit 2	**B**	**A**	**B**
Unit 3	**B**	**A**	**B**

The main conclusion of the group of international experts was: *"The INRNE obtained many important achievements in all its areas of investigations both in pure and applied science. INRNE is currently well placed in the national and international context, having gained considerable experience in international collaborations"*. It was recommended that links with industry need developing and strengthening. Given the number of products already developed by INRNE for practical applications, this should be quite achievable.

In the thematic plan of the Institute for 2009 11 projects were devoted to fundamental problems and 12 projects to nuclear safety, applied and environmental problems. This balance between fundamental and applied research resulted from our strategy, clearly defined several years ago to be in accordance with the national and EC priorities. Almost half of the developments concerns problems related to the scientific background of the national nuclear energy production, radioactive waste treatment monitoring and management of the environment. Of 23 projects 14 are supported by national and 9 additionally by international organizations. The results of our research were published in 432 papers including 4 in scientific books and monographs, 221 journal articles, 201 reports in proceedings of international conferences and symposia, and 6 in popular science articles and books.

Large amount of these results have been obtained in close collaboration with international and foreign centers, universities and other institutions. INRNE is a part of a very large number of national and international collaborations in all its areas of activity. Most of these collaborations are with leading European and international institutes and laboratories like IAEA, JINR, CERN, DESY, CNRS, INFN and others. The reconstruction and modernisation of the storage facility at Novi Han was chosen by IAEA as a model for the reconstruction of all similar facilities in South-East Europe. The Basic Environmental Observatory (BEO) is a Centre of Excellence and is an infrastructure of pan-European importance. The collaborations with 5 from 7 Institutes of the Joint Research Center (JRC) of the EC play extremely important role for the effective participation of INRNE in big EC projects of the 6FP and 7FP. INRNE was awarded 1st prize within FP6 for the most active scientific team. Taking into account the importance of the scientific collaborations in attempt to preserve the high scientific level of the research, in 2009 the staff of INRNE proposed 9 projects in the frame of FP7 of EC–4 of the proposals were accepted (5 under evaluation). The scientific contacts became stronger and more efficient due to 9 international conferences, organized by INRNE during 2009. The membership of Bulgaria in EURATOM fusion program in 2009 is very successful. All projects reached the planned milestones. In 2009 some very significant contracts have been signed: project SPIRAL-2 with National Large Heavy Ion Accelerator (GANIL), with CEA, France and SEVAN with Erevan Physical Institute. The cycle of activities connected with our participation in CMS experiment of the LHC collider is successfully finished and the correspondent part of the detectors and connected electronic channel, designed and produced in Bulgaria were put in operation. Serious scientific results were obtained within the frame of MAGIC collaboration with active participation of scientists from INRNE.

The scientific experimental facilities of INRNE also made essential progress. Environmental Impact Assessment Report for the investment proposal for conversion and reconstruction of the research reactor IRT-2000 was developed and approved by Ministry of Environment and Water of Bulgaria. The whole cycle of planning, execution and assessment of the accomplished work concerning the partial dismantling of the IRT research reactor is completed. All these activities were fulfilled with the expert help by the IAEA, in cooperation with Argonne National Laboratory and with the financial help of the USA Department of Energy. In 2009 BEO "Moussala" has been confirmed as regional station for South-East Europe in Global Atmospheric Watch World program.

3. Nuclear Theory Laboratory

The laboratory is within the Theoretical and Mathematical Physics Division. The main topics of scientific interest of the 15 members of the Nuclear Theory Laboratory include:

- nucleon-nucleon correlation effects on nuclear structure and reactions
- symmetries in nuclear physics
- algebraic methods in nuclear theory
- exotic nuclei and few-body systems
- advanced studies of many-fermion systems.

In the period 2004-2008 the laboratory members have published 65 papers in journals abroad (Physical Review C, Physics Letters B, Journal of Physics G, Physical Review Letters, Physics of Atomic Nuclei, International Journal of Modern Physics E, International Journal of Quantum Chemistry, Progress of Theoretical Chemistry and Physics, European Physical Journal A and others), 9 papers in Bulgarian journals, 26 papers in conference proceedings abroad and 45 papers in conference proceedings in Bulgaria. In the same period the obtained results were partly supported by Contracts Ф-905, Ф-1416, Ф-1501, Ф-1502 and DO 02-285 with the National Science Fund. The laboratory keeps very active international collaborations with GSI (Darmstadt) (Project ELISe), University of Giessen, N.C.S.R. "Demokritos", University of Tübingen, the Royal Society in London, University of Oxford, CSIC and Complutense University of Madrid, University of Seville, Kyushu University, INFN, Italy (Perugia), University of Pavia, University ot Torino, University of Naples, CNRS, Paris, JINR, Dubna, University of Thessaloniki and University of Lousiana.

In the next two figures some results of investigations, namely devoted to neutron skin emergence in exotic nuclei [1] and superscaling phenomenon of inclusive lepton scattering [2] are presented. The differences between the rms of neutrons and protons $\Delta r_{np}=r_n-r_p$ are plotted in Fig. 1. On the left panel our results for Sn isotopes are shown and compared to relativistic mean-field (RMF) results and to experimental data. As it can be seen the experimental data are located between the predictions of both theoretical approaches and in general, there is agreement with experiment within the error bars. On the right panels we see the predictions for Δr_{np} in the cases of Ni and Kr isotopes, where there are no data. As it can be seen, the RMF results for the difference Δr_{np} systematically overestimate the Skyrme HF results. The reason for this is related to the difference in the nuclear symmetry energy and, consequently, to the different neutron equation of state which has been extensively studied in recent years.

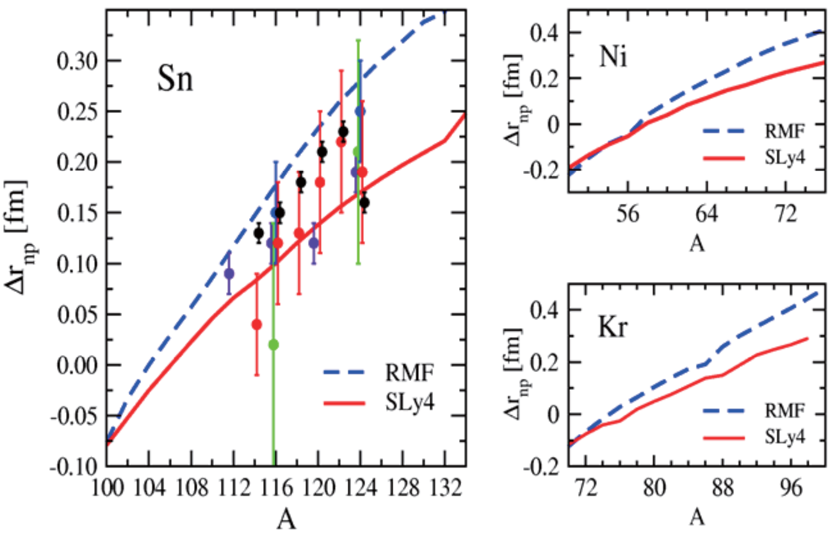

Fig. 1

In Fig. 2 the quasielastic (QE) coherent density fluctuation model (CDFM) scaling function for ^{12}C in comparison with the experimental data, with the relativistic Fermi gas (RFG) model result using the parabolic form and with the superscaling analysis (SuSA) result is presented. The CDFM scaling function is given for two values of the parameter c_1: c_1=0.75 and 0.60. In the case of c_1=0.75 the QE scaling function is symmetric, while in the case with c_1=0.60 it is asymmetric and is in better agreement with the empirical data. This is true even in the interval for values of the scaling variable less than -1, whereas in the RFG model the scaling function is zero in the same region. As a consequence, the asymmetric scaling function with an exponential form leads to a sharper slope of the cross sections, in comparison to that with the parabolic form shown in the figure for the values of the kinetic energy $T_{p(n)}$ of the knocked-out nucleon smaller than those in the maximum of the cross section.

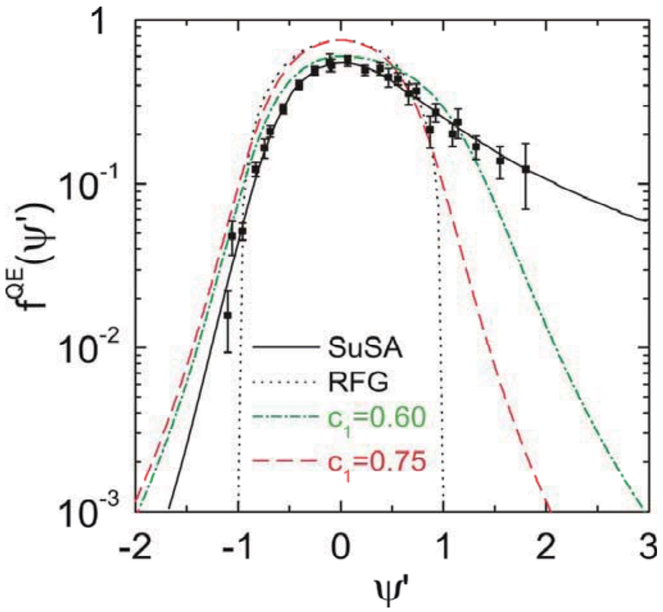

Fig. 2

The laboratory organises annually since 1980 the International Workshop on Nuclear Theory in the Rila Mountains, Bulgaria, which gives the opportunity to discusse new results of nuclear theory and experiment, as well as achievements of fruitful collaborations. By good tradition the Rila meeting is an occasion to initiate new research projects and make future plans. It is a very good opportunity for young scientists and students in friendly and relaxed atmosphere to study physics, to work on their communication skills and to become a part of the nuclear physics community.

4. Conclusion

INRNE has a highly qualified scientific potential, well developed infrastructure, broad international cooperation and longstanding traditions in scientific research and PhD training. Now 30% of the scientists are younger than 40 years which is a promising basis for the future development of INRNE.

Acknowledgements

I am grateful to the JSPS Invitation Fellowship Program for Research in Japan (Short-Term) for conducting research with Professor Yukinobu Watanabe from the Department of Advanced Energy Engineering Science of Kyushu University, Fukuoka.

References
[1] P. Sarriguren, M.K. Gaidarov, E. Moya de Guerra, A.N. Antonov: Phys. Rev., C76, 044322 (2007).
[2] A.N. Antonov, M.V. Ivanov, M.B. Barbaro, J.A. Caballero, E. Moya de Guerra, M.K. Gaidarov: Phys. Rev., C75, 064617 (2007).

15. Use of γ-ray-generating reactions for diagnostics of energetic particles in burning plasma and relevant nuclear data

Y. Nakao[1], **M. Nakamura**[2], **V.T. Voronchev**[3]

[1]*Department of Applied Quantum Physics and Nuclear Engineering, Kyushu University, 744 Motooka, Fukuoka 819- 0395, Japan*

[2]*Department of Advanced Energy, Graduate School of Frontier Sciences, University of Tokyo, Kashiwa, Chiba 277-8561, Japan*

[3] *Institute of Nuclear Physics, Moscow State University, Moscow 119991, Russia*

We discuss from theoretical side the possibility of energetic particle diagnostics based on γ- ray measurement in DT fusion plasma at burning stage. Attention is focused on 0.981-MeV γ- rays emitted in the ^{6}Li (t, p_1) ^{8}Li* reaction governed in the plasma by energetic tritons. It is shown that these γ- rays have an important application for diagnostics of the knock-on tritons and α-particles confined in DT burning plasmas.

1. Introduction

Fusion plasmas at burning stage will contain great variety of energetic particles: products of fusion reactions, injected beam ions, ions accelerated by electromagnetic waves, and knock-on particles scattered by these particles. These particles are indispensable constituents for plasma burning. They heat bulk electron and ion fluids so that high temperature is sustained and fusion reactions continue for a sufficiently long time. On the other hand, high pressure of the energetic particles can trigger many wave-particle interactions and fast particle-driven instabilities. Thus, establishment of confined energetic particle diagnostics is recognized as one of the key issues in nuclear fusion research aiming at ITER.

These energetic particles should be diagnosed while they are in the plasma. Since the measurements inside plasma are hardly possible, it is appropriate to use indirect methods operating with neutral particles or photons freely escaping from plasma core. Gamma-ray spectroscopy is recognized to be a promising tool for such purposes [1-3].

Previously we examined rates of various γ-ray-generating reactions in fusion plasmas, and found that some of them are essentially enhanced by supra-thermal channels induced by energetic knock-on ions [4,5]. The respective γ-ray fluxes carry signature of the knock-on ions and may effectively be used for plasma diagnostics. This especially concerns the threshold ^{6}Li (t, p_1) ^{8}Li* reaction emitting 0.981-MeV γ-quanta and governed by fast tritons. Thus we proposed use of this γ-line for diagnosing knock-on tritons and α-particles confined in burning DT plasmas [6, 7].

In this paper, after describing the outline of the energetic particle diagnostics based on the γ-ray measurement, and we will show that key parameters of the knock-on triton population (T_{eff}, n_{eff}), as well as the confinement property of α-particles can be obtained by comparing experimental data on the 0.981-MeV γ-ray yield and emission spectrum with the theoretical slowing-down calculations.

2. Gamma-Ray-Generating Nuclear Reaction

The basic idea is to use a small amount of ^{6}Li as admixture in DT plasma to induce nuclear reaction capable of providing information on energetic particles. We consider an endotherrmic γ-ray mode of the reaction $^{6}\mathrm{Li} + t \rightarrow {}^{8}\mathrm{Li}^{*}[0.981] + p - 0.18\mathrm{MeV}$; $^{8}\mathrm{Li}^{*} \rightarrow {}^{8}\mathrm{Li}\,[\mathrm{gr.\ st.}] + \gamma$ which proceeds through the excited nucleus ^{8}Li* emitting 0.981-MeV γ-quanta in its decay to the ground state.

As is shown in **Fig.1**, the cross section has very strong energy dependence at sub-MeV energy range. This process is forbidden below the threshold at 181 keV, essentially suppressed at thermal energies, and thus it is induced in plasma predominantly by fast nuclei.

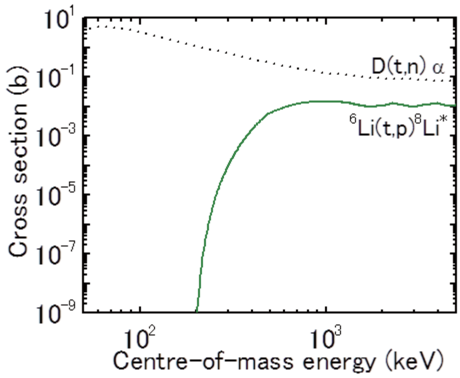

Fig. 1. The cross section of $^{6}\mathrm{Li}(t,p_1)^{8}\mathrm{Li}^{*}$ as a function of energy in the CM frame.

One more important feature is that the excited state of ^{8}Li* has a short life time of 12fs, so one can consider that ^{8}Li* emits γ-rays before slowing-down. Therefore, the broadening of the 0.981-MeV γ- line correlates strongly with the ^{8}Li* emission spectrum which in turn might be solely governed by energetic triton populations.

Experimental data are available at center-of-mass energies above 2 MeV [8] only. So, in Ref. [9] the cross sections below 2 MeV were calculated within a realistic nuclear model.

3. Energetic Triton Population

Energetic particle populations in the plasma are described by the Fokker-Planck equation with an appropriate source term. We solve the Fokker-Planck equation for the populations of fusion-born α-particles, beam-injected deuterons, and also for α knock-on, D-beam knock-on, DD burn-up tritons. **Figure 2** show the energetic triton populations calculated under the conditions typical of ITER. For completeness, the Maxwellian thermal triton population f_{tht} is also shown. We can see, the α knock-on tritons populate up to 3- to 4-MeV energy, and is dominant throughout the suprathermal energy range.

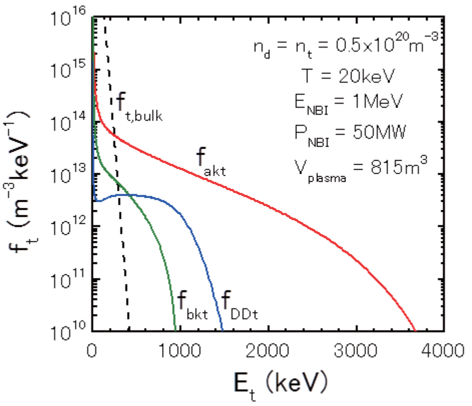

Fig. 2. Energy distribution functions of α knock-on, D-beam knock-on and DD burn-up tritons f_{akt}, f_{bkt} and f_{DDt}.

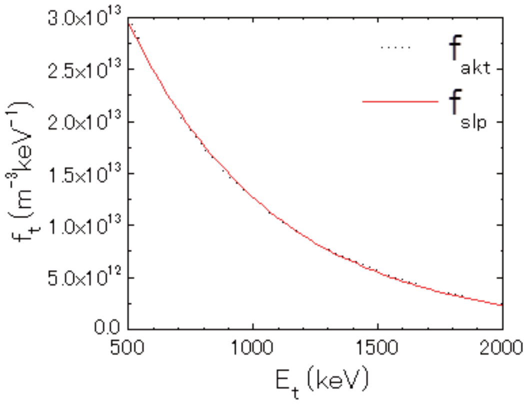

Fig. 3. Distribution of α knock-on tritons, f_{akt}, in the case of T = 20 keV (dotted line), and slope distribution function, f_{slp}, with T_{eff} = 593 keV (solid line).

The distribution function of α knock-on tritons f_{akt} can be well fitted to a slope distribution function defined by

$$f_{slp}(E) = \frac{n_{eff}}{T_{eff}} \exp\left(-\frac{E_t - E_C}{T_{eff}}\right), \tag{1}$$

where T_{eff} and n_{eff} are the effective temperature and concentrations of the α knock-on tritons, respectively, and E_C is a critical energy above which $f_{akt} > f_{tht}$. Although n_{eff} is not the 'real' density of the α knock-on tritons, it conveniently indicates the amplitude of f_{akt}. For example, f_{akt} in Fig. 2 agrees the amplitude of

f_{slp} at T_{eff} = 593 keV and n_{eff} = 2.46 × 10^{16} m^{-3}, especially in the energy range of 0.5- 2 MeV (See **Fig. 3**).

Figure 4 shows a correlation between plasma temperature T and T_{eff}. As T rises, the fraction of α-particles at energy above 3.5 MeV increases, which allows α knock-on tritons to have high energy even above 4 MeV. As a result, when T rises from 10- to 50 keV, T_{eff} increases monotonically.

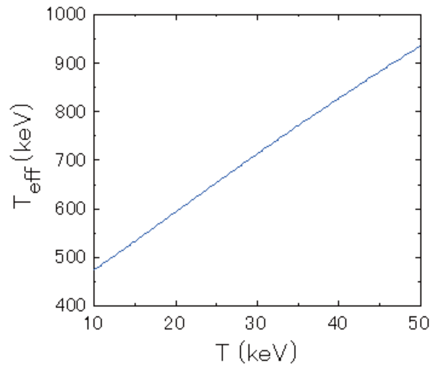

Fig. 4. Correlation between plasma temperature T and effective α knock-on triton temperature T_{eff}.

4. Gamma-Ray-Emission Rate and Energy Spectrum

The γ-ray yield $Y_{0.981}$ found for T = 10–50 keV and n_{Li}/n_T = 1 % are plotted in **Fig. 5**. We can see that the emission of 0.981-MeV γ-rays is dominated by the α knock-on tritons; the roles of other energetic or thermal tritons can be ignored. In other words, the 0.981-MeV γ-line clearly reflects the presence of the α knock-on tritons.

It is interesting to compare the γ-ray flux predicted here with that from other diagnostic processes. We choose the ^{9}Be$(\alpha,n_1)^{12}$C* reaction, which generates 4.44-MeV photons and has been vigorously used for energetic particle diagnostics in JET plasma experiments.[13–16] Under the plasma conditions considered here, n_{Be}/n_T = 1 % and T = 20 keV the ^{9}Be(α,n_1) reaction yield was estimated to be $Y_{4.44} \sim 4\times10^{10}$ $m^{-3}s^{-1}$. At the same time, Fig. 5 shows that the yield $Y_{0.981}$ is at the level of 7×10^{10} $m^{-3}s^{-1}$, proving to be twice higher. Thus, the 0.981-MeV γ-ray flux is not small, and the ^{6}Li(t,p_1) reaction may be considered for plasma diagnostics in machines of next generation. However, detection of the 0.981-MeV γ-signal would be more difficult than 4.44-MeV γ-rays because of unfavorable background condition in the range of low-energy photons.

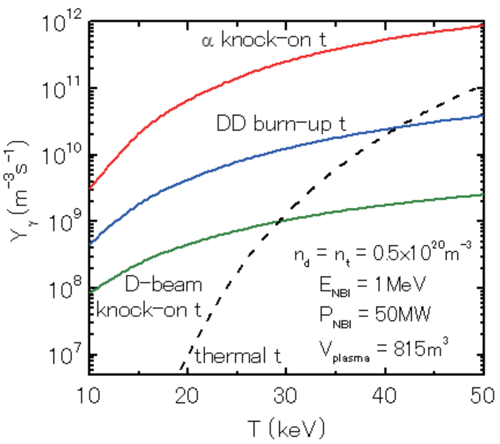

Fig. 5. 0.981-MeV γ-ray yields calculated for n_{Li}/n_T = 1 %.

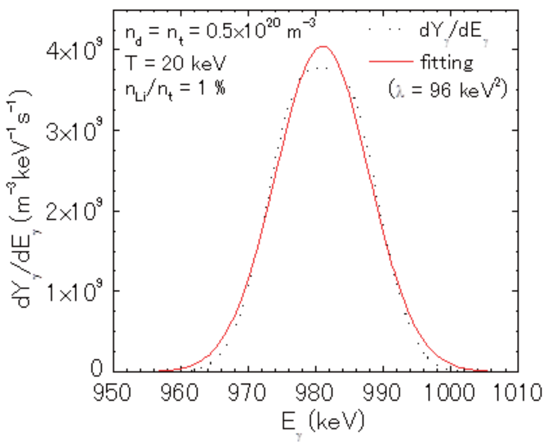

Fig. 6. Emission spectrum of the 0.981-MeV γ-rays in the case of T = 20 keV and $n_D = n_T = n_e/2 = 0.5\times10^{20}$ m^{-3} together with Gaussian function fitting.

The emission spectrum of the 0.981-MeV γ-rays, dY_γ/dE_γ, is determined by the spectrum of ^{8}Li* ions produced in the ^{6}Li$(t,p_1)^{8}$Li* reaction. The function dY_γ/dE_γ calculated for T = 20 keV and $n_d = n_t = n_e/2 = 0.5 \times 10^{20}$ m^{-3} is shown in **Fig. 6**. The full width of half-maximum of this spectrum is estimated to be 18 keV. This broadening reflects the ^{8}Li* spectrum which in turn is governed by the shape of the energy distribution of the α knock-on tritons.

5. Diagnostic Scenario

Using the approximated distribution, Eq. (1), the 0.981-MeV γ-ray yield can be represented as a function of effective temperature T_{eff} and concentration n_{eff} of α knock-on tritons:

$$\begin{aligned} Y_\gamma &\approx \sqrt{\frac{2}{m_t}}\frac{n_{Li}n_{eff}}{T_{eff}} \times \int_{E_C}^{\infty} \sqrt{E_t}\exp\left(-\frac{E_t - E_C}{T_{eff}}\right)\sigma(E)dE_t \\ &\equiv \sqrt{\frac{2}{m_t}} n_{Li} n_{eff} \frac{I(T_{eff})}{T_{eff}} \end{aligned} \quad (2)$$

The γ-ray emission spectrum can be well fitted to a Gaussian distribution:

$$\frac{dY_\gamma}{dE_\gamma} \propto \exp\left[-\frac{(E_\gamma - E_0)^2}{\lambda}\right] \quad (3)$$

Here E_0 = 0.981 MeV, and λ represents the broadening of the fitting curve and has dimension of square energy. The Gaussian distribution with λ = 96 keV^2 reproduces properly dY_γ/dE_γ in Fig. 6.

It was found that there is the pronounced correlation between λ and T_{eff} shown in **Fig. 7**. With increasing T_{eff}, the α knock-on tritons reach high energies, resulting in the γ-ray emission spectrum with the wider broadening.

Once the parameter λ is assessed from the experimental data on dY_γ/dE_γ, then T_{eff} could be determined by use of the prove curve in Fig. 7.

Equation (2) indicates that once T_{eff} is determined with a fine accuracy, then we can assess n_{eff} from the experimental γ-ray yield Y_γ.

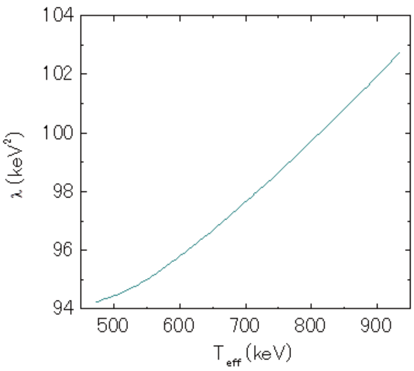

Fig. 7. Correlation between slope factor λ of the γ-ray emission spectrum and effective temperature T_{eff} of α knock-on tritons.

6. Confined α-particle diagnostics

One can also obtain information on the confinement property of fusion-born α-particles in burning DT plasmas. The theoretical curve in Fig. 4, T_{eff} and T derived experimentally should be used for this purpose. If the experimental plot of (T_{eff},T) is placed onto the theoretical curve in Fig. 4, then one can reasonably consider the confinement of the α-particles to be classical, i.e., the α-particles exhibit the classical slowing-down behavior described by the Fokker-Planck equation. If not, the α-particles anomalously escape from the plasma core and accordingly their confinement property is deteriorated. In the latter case, because of losses of the α-particles at energy below the average birth energy of E_0 = 3.52 MeV, the relative fraction of the α-particles with high energy around E_0 become larger, resulting in the effective temperature T_{eff} of the α knock-on tritons becoming higher. Accordingly, the experimental (T_{eff},T) plot would be placed above the theoretical curve.

7. Concluding Remarks

We showed that the 0.981-MeV γ-rays emitted in the ^{6}Li (t, p_1) ^{8}Li* reaction have an important application for diagnostics of the α knock-on tritons and α-particles in burning plasmas. If these γ-rays are detected, we can obtain information on key parameters of α knock-on triton population (T_{eff}, n_{eff})

and confinement properties of fusion-born α-particles by comparing experimental data on the 0.981-MeV γ-ray yield and emission spectrum with the theoretical calculations.

Here we must refer to some restrictions in applying the above diagnostics method. First, if it is impossible to measure the γ-ray emission spectrum with fine energy resolution, the broadening parameter λ cannot determined accurately. In this situation, neither n_{eff} nor the α-particle confinement property can be diagnosed because T_{eff} cannot be estimated from λ. Second, the proposed diagnostic scenario is useful only in the case that the behavior of energetic tritons is classical. If the energetic tritons escape from the plasma during slowing-down, approximation the slop distribution becomes unavailable, so the diagnostic scenario would fail.

Acknowledgments

This work was supported by Grant-in-Aid for Scientific Research of the Ministry of Education, Culture, Sports, Science and Technology of Japan under the Scientific Research of Priority Areas, “Advanced Diagnostics for Burning Plasmas”.

References

[1] V.G. Kiptily, *et al*., “Gamma-ray diagnostics of energetic ions in JET”, *Nucl. Fusion* **45** (2002) 999.
[2] V.G. Kiptily, *et al*., “First γ-ray measurements of fusion–particles in JET trace tritium experiments”, *Phys. Rev. Lett.* **93** (2004) 115001.
[3] V.G. Kiptily, *et al*., “Gamma- ray imaging of D and alpha ions accelerated by ion cyclotron heating in JET plasmas”, *Nucl. Fusion* **45** (2005) L21.
[4] M. Nakamura, Y. Nakao, V.T. Voronchev, H. Matsuura, O. Mitarai, “ Kinetic analysis of γ- ray-generating reactions for fuel ion and energetic particle diagnostics of DT fusion plasma”, *J. phys. Soc. J.* **75** (2006) 024801.
[5] M. Nakamura, Y. Nakao, V.T. Voronchev, “On the enhancement of nuclear reaction rates in high-temperature plasma”, *Phys. Lett. A* **359** (2006) 663.
[6] M. Nakamura, Y. Nakao, V.T. Voronchev, “Use of the $^6\mathrm{Li}+\mathrm{T}$ nuclear reaction for diagnostics of energetic particles in burning plasmas” *Nucl. Inst. Meth. Phys. Res. A* **580** (2007) 1052.
[7] Y. Nakao, M. Nakamura, V.T. Voronchev, “Use of the γ- rays from the $^6\mathrm{Li}\,(t,p_1)\,^8\mathrm{Li}^*$ reaction for studying knock-on tritons in the core of fusion plasmas”, *Fusion Sci. Technol*. **52** (2007) 1045.
[8] S.N. Aramovich, B.Ya. Gujovsky, V.N. Protopopov, *Izv. Akad. Nauk. Kaz. SSR, Ser. Fiz. Mat*. **4** (1984) 24.
[9] V.T. Voronchev, K.I. Kukulin, Y. Nakao, *Phys. Rev. E* **63** (2001) 026413.

16. Theoretical Studies on Reaction Mechanisms of Unstable Nuclei

K. Ogata[1], T. Matsumoto[2,3], S. Hashimoto[4], K. Minomo[1], Y. Iseri[5], M. Kohno[6], S. Chiba[4], T. Hamada[1], Y. R. Shimizu[1], T. Ye[7], Y. Watanabe[7], and M. Yahiro[1]

[1] *Department of Physics, Kyushu University, Fukuoka 812-8581, Japan*
[2] *RIKEN Nishina Center, Wako 351-0198, Japan*
[3] *Meme Media Laboratory, Hokkaido University, Sapporo 060-8628, Japan*
[4] *Advanced Science Research Center, Japan Atomic Energy Agency, Ibaraki 319-1195, Japan*
[5] *Department of Physics, Chiba-Keizai College, Chiba 263-0021, Japan*
[6] *Physics Division, Kyushu Dental College, Kitakyushu 803-8580, Japan*
[7] *Department of Advanced Energy Engineering Science, Kyushu University, Kasuga, Fukuoka 816-8580, Japan*

e-mail: ogata@phys.kyushu-u.ac.jp (K. Ogata)

Recent studies on reactions of unstable nuclei by means of the continuum-discretized coupled-channels method (CDCC) are briefly reviewed. The topics covered are: four-body breakup processes for ^{6}He induced reaction, microscopic description of projectile breakup processes, and new approach to inclusive breakup processes.

1 Introduction

Breakup reaction is an important tool to extract not only structural information on weakly-bound nuclei but also dynamical properties of reaction systems involving such fragile nuclei. The most successful theoretical model to describe breakup reactions of weakly-bound nuclei is the continuum-discretized coupled-channels method (CDCC) [1, 2], which was proposed and developed by Kyushu group about 25 years ago. Recently, some important developments on CDCC have been made. In this paper we review our recent studies with CDCC on some reaction systems. The following three topics are covered: i) four-body breakup processes for ^{6}He induced reaction, ii) microscopic description of projectile breakup processes, and iii) new approach to inclusive breakup processes.

In Sec. 2, a brief introduction to CDCC is described. The aforementioned topics are discussed in Sec. 3 and we give summary in Sec. 4.

2 The continuum-discretized coupled-channels method (CDCC)

In CDCC [1, 2], the total wave function of the reaction system is expanded in terms of a complete set of the internal states of the projectile (P):

$$\Psi = \phi_0\chi_0 + \int_0^\infty \phi_k\chi_k dk, \tag{1}$$

where ϕ_0 and ϕ_k are the wave functions of P in the ground and continuum states, respectively, and χ's denote the corresponding wave functions between P and the target nucleus (T). k is the momentum that specifies the energy of P; if P has a two-body structure, k is the relative momentum of the constituents of P. We assume in Eq. (1) that P has one bound state just for simplicity.

The most essential assumption of CDCC is the truncation of the continuum of P, with introducing a cutoff momentum $k_{\max}$. Then we discretize the continuum up to $k_{\max}$ into a finite number of states, i.e., discretized continuum states. There are several choices for the discretization method: the average method, the mid-point method and the pseudostate method. The first one that takes an average of the continuum states within a certain range of k has most widely been used. After the truncation and discretization, we have the CDCC wave function of the reaction system:

$$\Psi^{\mathrm{CDCC}} = \sum_{i=0}^{i_{\max}} \hat{\phi}_i \hat{\chi}_i, \tag{2}$$

where i is the index of the ground ($i = 0$) and the discretized continuum ($0 < i \leq i_{\max}$) channels; the symbol $\hat{}$ denotes a result of discretization.

In CDCC, we assume that the set of $\{\hat{\phi}_i\}$, which defines the modelspace of CDCC, forms a complete set in the space that is significant for a reaction process considered. In other words, the CDCC wave function is not exact in entire space but can be used as an exact solution in evaluation of physics observables; note that a transition matrix contains a residual interaction that has a finite range. Furthermore, the theoretical foundation of CDCC has been established in connection with the distorted-wave Faddeev equation in Ref. [3], and a solution of CDCC is shown to have a proper asymptotic form in Ref. [4].

3 Reaction studies with CDCC

In this section, we review our recent works very briefly. See the references cited in the following subsections for the details of the formalism, numerical calculation, other results, and further discussion.

3.1 Four-body breakup processes for ^{6}He induced reaction

To describe a breakup process of a three-body projectile like ^{6}He, we need discretized continuum states of the three-body system. It is very difficult to obtain them by directly solving a three-body scattering problem. However, if we diagonalize a Hamiltonian of ^{6}He, we automatically obtain the eigenstates both below and above the three-body threshold energy. The latter states (the pseudostates) can be assumed as discretized continuum states. Thus, we obtain the total wave function of the four-body system, i.e., the three-body projectile and the target nucleus, in terms of finite number of channels. This four-body CDCC was established in Ref. [5]; for the calculation of ^{6}He wave functions, the Gaussian expansion method [6] that has been highly successful in few-body physics is adopted. Four-body CDCC is applied to the ^{6}He elastic scattering by ^{209}Bi near the Coulomb barrier energy [7] and shown to reproduce experimental data very well. Another finding is that breakup effects of ^{6}He on the elastic cross section, i.e., virtual breakup processes, are very important.

Recently, Rodríguez-Gallardo and collaborators [8] developed an alternative four-body CDCC, with directly calculating a three-body scattering states of ^{6}He. The method also reproduces well the elastic cross section of ^{6}He on ^{208}Pb near the Coulomb barrier energy. As future work, systematic analysis of four-body breakup will be necessary. Another important subject is the extension of four-body CDCC to 5- and 6-body reaction systems; we are planning to achieve this by incorporating cluster-orbital shell-model (COSM) wave functions [9].

The description of breakup spectrum is a hot topic of four-body CDCC. Since CDCC uses discretized continuum states, the resulting breakup cross sections are discrete. In Fig. 1 we show

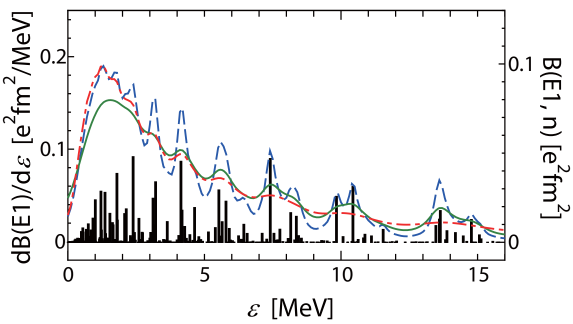

Figure 1: E1 strength distribution of ^{6}He as a function of ϵ. The bars show $B(\mathrm{E1};n)$ from the 0^+ ground state to the n th pseudostates of ^{6}He. The solid, dashed, and dash-dotted lines respectively show the smeared E1 strength distributions assuming the Lorentzian form with the width of 0.5, 0.2, and $0.1(\epsilon_n + 0.975)$ MeV; ϵ_n denotes the eigenenergy of the n th pseudostate.

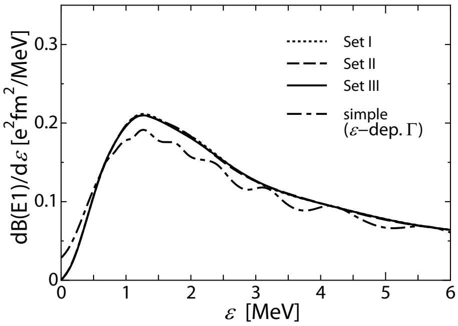

Figure 2: E1 strength distribution of ^{6}He as a function of ϵ obtained with the smoothing method in Ref. [10]. The dotted, dashed, and solid lines show the results with different modelspace of the ^{6}He wave function (see Ref. [10] for details). Also shown for comparison by the dot-dashed curve is the result of the simple smoothing method with a energy-dependent width, i.e., the dash-dotted line in Fig. 1.

by histogram a typical example of the discrete result of the energy distribution of the electric dipole (E1) strength $dB(\mathrm{E1})/d\epsilon$ for ^{6}He, with ϵ the breakup energy of ^{6}He measured from the three-body ($^4\mathrm{He}+n+n$) threshold. To compare the result of CDCC with experimental data, we must construct a smooth spectrum from the histogram. Note that a simple smearing procedure assuming a Lorentzian form, with any choice of parameters, does not work at all, as shown by the three lines in Fig. 1. Thus, we proposed a new smoothing method [10] with the use of the Lippmann-Schwinger equation , which was found to successfully reproduce a smooth $dB(\mathrm{E1})/d\epsilon$, if experimental resolution is taken into account; the result is shown in Fig. 2.

The alternative four-body CDCC [8] can construct a smooth spectrum of breakup observable much easier, in principle, than the original four-body CDCC, since in the former the three-body scattering states are directly calculated. At this stage, however, because of the limited modelspace, it seems difficult to compare the result shown in Ref. [8] with experimental data. Very recently, another smoothing procedure using the complex scaling method [11] has been proposed in Ref. [12] and shown to work very well to obtain smooth breakup cross sections.

3.2 Microscopic description of projectile breakup processes

An essential ingredient of CDCC for systematic analysis of breakup reactions is optical potentials between A and individual constituents of P, which are not always available phenomenologically. Thus, we need a microscopic framework to obtain optical potentials for various reaction system in a wide range of incident energies.

For nucleon-nucleus potential, the method proposed by Brieva and Rook [13] has widely been used to obtain a microscopic local potential. Recently, it has been shown in Ref. [14] that the Brieva-Rook (BR) localization is valid for wide range of incident energies, by directly comparing the result of BR calculation with the solution of the exact nonlocal Schrödinger equation. In Fig. 3 we show the elastic differential cross sections of the proton scattering on ^{90}Zr at (a) 65 MeV and (b) 800 MeV. The solid and dashed lines respectively show the results of the exact

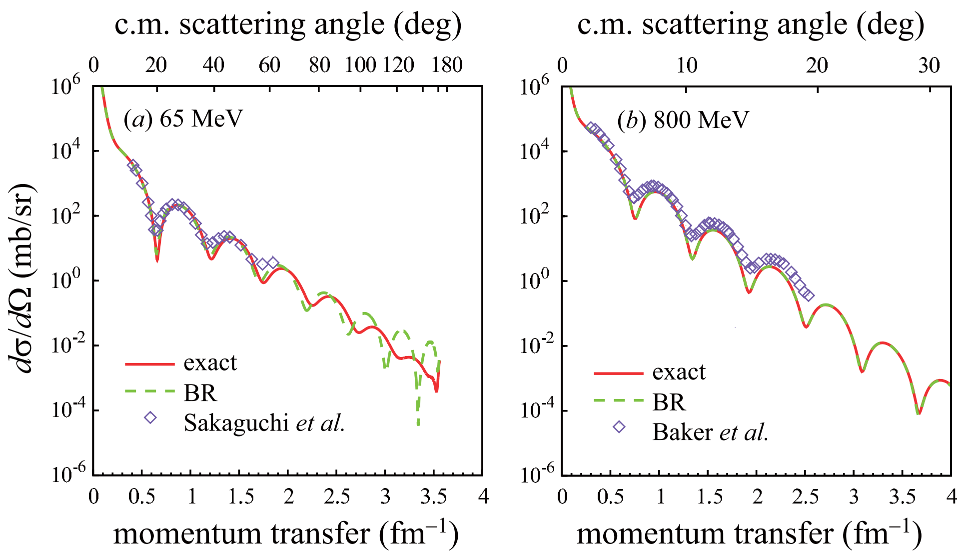

Figure 3: The elastic differential cross sections of the proton scattering on ^{90}Zr at (a) 65 MeV and (b) 800 MeV. The solid lines represent the results of the exact calculation, while the dashed lines show the results of the calculation with the BR localization. Experimental data are taken from Refs. [17, 18].

calculation and the BR localization.

For nucleus-nucleus potentials, Furumoto and collaborators [15] have done intensive study with proposing a new nucleon-nucleon g matrix [16] that contains three-body force effects phenomenologically.

Therefore, we are ready for systematic analysis of experimental data of breakup processes of unstable nuclei. We call CDCC with microscopic optical potentials *microscopic CDCC*.

3.3 New approach to inclusive breakup processes

Let us consider the ^{7}Li(d, nx) reaction. Here x means that the final state except for the neutron is not specified. This inclusive breakup process is called also a stripping or incomplete fusion process. In Ref. [19] we propose a new method to describe the inclusive breakup cross section with decomposing the total fusion cross section:

$$\sigma_{\rm TF} = \frac{2\mu}{\hbar^2 K} \left|\langle\Psi\,| -W_p - Wn |\,\Psi\rangle\right|. \tag{3}$$

In Eq. (3), Ψ is the total wave function of the $p+n+{}^7$Li three body system calculated with CDCC, μ and K are, respectively, the reduced mass and relative momentum between d and ^{7}Li, and W_p (W_n) is the imaginary part of the proton (neutron) optical potential for ^{7}Li. In Ref. [19], we divide the integration region into four:

$$\begin{aligned}\int d\mathbf{r}_p \int d\mathbf{r}_n \;=\; & \int_{r_p<r_p^{\rm ab}} d\mathbf{r}_p \int_{r_n<r_p^{\rm ab}} d\mathbf{r}_n + \int_{r_p<r_p^{\rm ab}} d\mathbf{r}_p \int_{r_n>r_p^{\rm ab}} d\mathbf{r}_n \\ & + \int_{r_p>r_p^{\rm ab}} d\mathbf{r}_p \int_{r_n<r_p^{\rm ab}} d\mathbf{r}_n + \int_{r_p>r_p^{\rm ab}} d\mathbf{r}_p \int_{r_n>r_p^{\rm ab}} d\mathbf{r}_n,\end{aligned} \tag{4}$$

with introducing absorbing radii for proton ($r_p^{\rm ab}$) and neutron ($r_n^{\rm ab}$). The first term on the right-hand-side (r.h.s.) of Eq. (4) corresponds to the process in which both proton and neutron are absorbed. The second (third) term on r.h.s. represents the process in which only proton (neutron) is absorbed. Note that the contribution of the fourth term is negligible. Thus, if we take just the second term, we can obtain the cross section of the inclusive (d, nx) process.

The point is how to determine the absorbing radii. In Ref. [19] we use the result of theoretical analysis of the ^{7}Li(d, nx) reaction at 40 MeV; we analyzed in Ref. [20] the double differential cross section data [21] by summing up the elastic breakup cross section calculated with CDCC and the stripping cross section calculated with the Glauber model. The data are reproduced very well with no free parameter, except for the contribution of the preequilibrium and evaporation processes that are negligible where the stripping process is important. Thus, we conclude that the integrated value of the stripping cross section calculated with the Glauber model can be regarded as an experimental value. The absorbing radii are fixed to reproduce this value at 40 MeV.

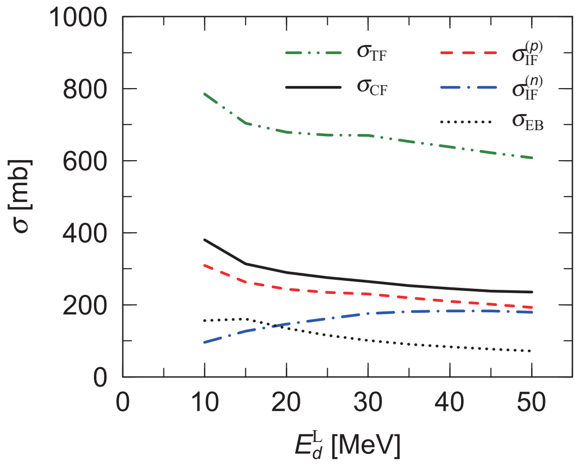

Figure 4: Results of the total fusion cross section $\sigma_{\rm TF}$ (dash-double-dotted line), complete fusion cross section $\sigma_{\rm CF}$ (solid line), proton-absorbed cross section $\sigma_{\rm IF}^{(p)}$ (dashed line) and neutron-absorbed cross section $\sigma_{\rm IF}^{(n)}$ (dash-dotted line) for the deuteron induced reaction on ^{7}Li as a function of the deuteron incident energy $E_d^{\rm L}$. The dotted line represents the elastic breakup cross sections calculated with CDCC.

We show in Fig. 4 the result of the inclusive breakup cross sections as a function of the deuteron incident energy. The dashed (dash-dotted) line shows the proton-absorbed (neutron-absorbed) cross section and the solid line is the complete fusion cross section. These three values are comparable above 30 MeV, and much larger than the elastic breakup cross section shown by the dotted line. Another finding is the energy dependence of the dashed and dash-dotted lines is very different at low energies. This difference comes from different energy dependence of the proton and neutron optical potentials [22, 23] adopted.

Description of the double-differential cross sections of inclusive processes with CDCC will be important future work. For this purpose, recently we have developed Eikonal Reaction Theory (ERT) [24]. Results of calculation with ERT will be soon reported.

4 Summary

In this paper, some recent studies on breakup reactions by means of the continuum-discretized coupled-channels method (CDCC) are briefly reviewed. Future plans described in the preceding subsections will be very important for further understanding of the reaction mechanisms of unstable nuclei.

References

[1] M. Kamimura, M. Yahiro, Y. Iseri, Y. Sakuragi, H. Kameyama, and M. Kawai, Prog. Theor. Phys. Suppl. **89**, 1 (1986).

[2] N. Austern, Y. Iseri, M. Kamimura, M. Kawai, G. Rawitscher, and M. Yahiro, Phys. Rep. **154**, 125 (1987)

[3] N. Austern, M. Yahiro, and M. Kawai, Phys. Rev. Lett. **63**, 2649 (1989); N. Austern, M. Kawai, and M. Yahiro, Phys. Rev. C **53**, 314 (1996).

[4] R. A. D. Piyadasa, M. Kawai, M. Kamimura, and M. Yahiro, Phys. Rev. C **60**, 044611 (1999).

[5] T. Matsumoto, E. Hiyama, K. Ogata, Y. Iseri, M. Kamimura, S. Chiba, and M. Yahiro, Phys. Rev. C **70**, 061601(R) (2004).

[6] E. Hiyama, Y. Kino, and M. Kamimura, Prog. Part. Nucl. Phys. **51**, 223 (2003).

[7] T. Matsumoto, T. Egami, K. Ogata, Y. Iseri, M. Kamimura, and M. Yahiro, Phys. Rev. C **73**, 051602(R) (2006).

[8] M. Rodríguez-Gallardo, J. M. Arias, J. Gómez-Camacho, A. M. Moro, I. J. Thompson, and J. A. Tostevin, Phys. Rev. C **80**, 051601(R) (2009).

[9] Y. Suzuki and K. Ikeda, Phys. Rev. C **37**, 410 (1988); A. Aoyama, T. Myo, K. Katō, and K. Ikeda, Prog. Theor. Phys. **116**, 1 (2006).

[10] T. Egami, T. Matsumoto, K. Ogata, and M. Yahiro, Prog. Theor. Phys. **121**, 789 (2009).

[11] J. Aguilar and J. M. Combes, Commun. Math. Phys. **22**, 269 (1971); E. Balslev and J. M. Combes, Commun. Math. Phys. **22**, 280 (1971).

[12] T. Matsumoto, K. Katō, and M. Yahiro, Phys. Rev. C **82**, 051602(R) (2010).

[13] F. A. Brieva and J. R. Rook, Nucl. Phys. A **291**, 299 (1977); ibid. **291**, 317 (1977); ibid. **297**, 206 (1978).

[14] K. Minomo, K. Ogata, M. Kohno, Y. R. Shimizu, and M. Yahiro, J. Phys. G **37**, 085011 (2010).

[15] T. Furumoto, Y. Sakuragi, and Y. Yamamoto, Phys. Rev. C **79**, 011601(R) (2009).

[16] T. Furumoto, Y. Sakuragi, and Y. Yamamoto, Phys. Rev. C **78**, 044610 (2008).

[17] H. Sakaguchi *et al.*, Phys. Rev. C **26**, 944 (1982).

[18] F. T. Baker *et al.*, Nucl. Phys. A **393**, 283 (1983).

[19] S. Hashimoto, K. Ogata, S. Chiba, and M. Yahiro, Prog. Theor. Phys. **122**, 1291 (2009).

[20] T. Ye, Y. Watanabe, and K. Ogata, Phys. Rev. C **80**, 014604 (2009).

[21] M. Hagiwara *et al.*, Fusion Sci. Technol. **48**, 1320 (2005).

[22] S. Chiba *et al.*, Phys. Rev. C **58**, 2205 (1998).

[23] T. Ye, Y. Watanabe, K. Ogata, and S. Chiba, Phys. Rev. C **78**, 024611 (2008).

[24] M. Yahiro, K. Ogata, and K. Minomo, in preparation.

17. Thermal / epi-thermal neutron spectrometer with a ^{3}He position sensitive proportional counter

Masao ITO*, Isao MURATA
Division of Electronic and Information Engineering, Osaka University
Yamada-oka 2-1, Suita, Osaka, 565-0871 Japan
*E-mail: ito@ef.eie.eng.osaka-u.ac.jp

At present, measurement of energy spectrum for thermal and epi-thermal neutrons becomes crucial to apply to the medical, as well as physical applications. In the present paper, we described the preliminary result of ongoing development of a new thermal and epi-thermal neutron spectrometer using the detection depth information measured by a ^{3}He position sensitive proportional counter.

1. Introduction

Spectrum measurement of thermal and epi-thermal neutrons is becoming crucial recently considering possible applications such as boron neutron capture therapy (BNCT). But there is no direct technique to measure the low-energy neutron spectrum. In the low-energy neutron measurement, there are some conventional ways. The most frequently used ways are a gas counter like BF_3, ^{3}He and fission chamber. However, they have too large Q-values compared with the incident neutron energy to detect the energy correctly. Next is the foil activation method, which uses several types of foils and unfolding code to estimate the neutron spectrum. This method is available only by off-line analysis and the unfolding process is regarded more-or-less as an underdetermined problem. If the neutron source is pulsed, the time-of-flight method can be used. It needs a complicated technique in processing detector signals with electronic modules. However, the resulting accuracy is known to be commonly high.

In BNCT facilities, the major problem in the neutron spectrum measurement is how precisely the energy could be determined. So in this study we have been developing a new spectrometer which aimed at realization of measurement of the low-energy neutrons from thermal to 10keV. We have developed a prototype detector of ^{3}He position sensitive proportional counter. The spectrometer acquires the information as to how deep an incident neutron has reached in the detector and where the nuclear reaction with the detection gas by the neutron has occurred. The multi-parameter MCA system was set-up for measuring signals from the detector in the two dimensional space. The response function of the detector, that is, the detection position distribution of each energetic neutron, is calculated from the neutron cross section data.

The neutron spectrum can be derived by unfolding the measured detection position (depth) distribution with the response function of the detector. This time, we measured thermal neutrons which are produced by moderating fast neutrons emitted from an AmBe source using a graphite column. The thermal column was designed by MCNP5[1] and constructed for the present test measurement with the prototype detector. In this paper, the details of the developed detector are presented and ongoing test measurement results are briefly summarized.

2. Measurements Technique and Equipments

2.1 Unfolding

There is no direct method to measure the low energy neutron spectrum as mentioned before. So this time we employed an unfolding process. It requires a certain difference of physical quantity to expand and view the energy difference in the low-energy region. The difference can make the neutron to be identified via one-to-one correspondence. Practically in the present method it is based on the fact that lower energy neutrons have a larger reaction cross section value and high energy neutrons have a smaller one. The reaction cross section changes are exhibited as the detection position (depth) changes. The response matrix **R(E,r)dr** can theoretically be deduced as $\sum(E)\exp(-\sum(E)\cdot r)\cdot dr$, where $\sum(E)$[1/cm] is the macroscopic cross section and **E** is the neutron energy. Measured detection depth distribution **y(r)** and neutron energy spectrum **x(E)** are related by the next equation, $y(r)= R(E,r)\cdot x(E)$. Thus, the measured reaction position distribution could be unfolded with an appropriate unfolding code in order to estimate the neutron energy spectrum. For the unfolding process, we adopted the Bayes theorem to derive neutron spectrum[2,3].

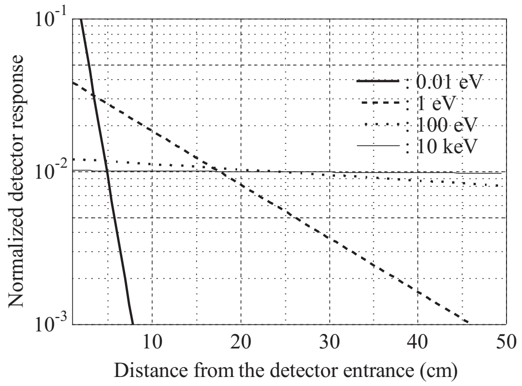

Fig.1 Response function of the detector.

2.2 Detector

In this study, we have to know the detection position (depth) distribution of an incident low-energy neutron. The position sensitive proportional counter can identify where the incident neutron reacts with the inner gaseous material. ^{3}He is selected as the detection gas, which has an extremely large reaction cross section in the low energy region. The gas pressure and detector length are deeply related to each other. To make the detector length short, the gas pressure must be increased so that the measurable energy range expands widely. This time we developed a new position sensitive proportional counter shown in Fig.2. The length of detector is 50cm, 2.53cm in diameter. A copper pipe is seen at the center for bottling ^{3}He into the counter. The ^{3}He gas pressure is 0.5Mpa.

In Fig.2, the block diagram of the measurement circuit is shown together with the photo. The induced charge in the counter is divided according to the ratio of distances from the side edges. Two signals from both ends of the detector are measured by two MCAs to obtain a two dimensional counter for one output and the sum of the two by the coincidence counting technique.

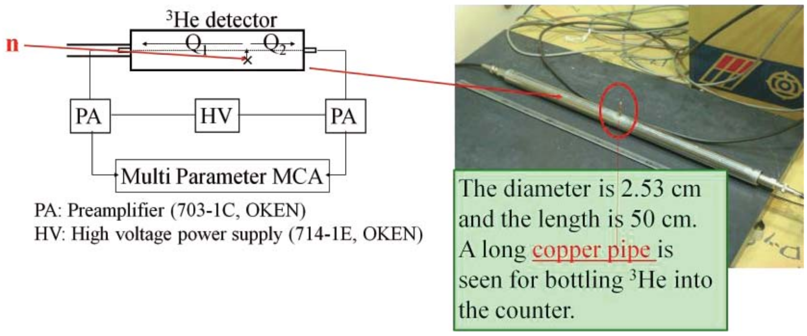

Fig.2 Schematic block diagram and ^{3}He detector.

2.3 Calculation and Setting

The experiment was carried out at OKTAVIAN facility of Osaka University, Japan. For measurement of thermal/epithermal neutrons, we designed a graphite thermal column with an AmBe source by MCNP5 calculations. The calculation model is shown in Fig.3. Using graphite as neutron moderator, a rectangular shape (100 x 100 x 100 cm^3) graphite thermal column was constructed. The AmBe neutron source was located at several distances, D [cm], from the thermal column surface. The neutron spectrum at the ^{3}He proportional counter positioned at 100cm from the thermal column was calculated and the most reasonable setting was examined from the calculation results. The key point is that the ^{3}He proportional counter was so set that the neutron beam direction became perpendicular to the axis of the detector in the measurement for an aim to ascertain the detection position of neutron in the detector. But in an real application, the incident particle direction must be parallel to the detector axis. We have calculated both of these situations.

Fig.4 shows the MCNP calculation results in some distances, D (20cm,40cm,60cm,80cm and 100cm). From the results, we set the moderator thickness D to 50cm. At 50cm, the ratio between Thermal/MeV is enough high and the neutron number density is not so low. The calculated spectrum will be used to verify the unfolding result obtained from a parallel incidence experiment.

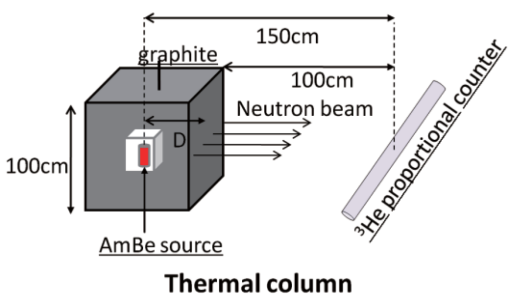

Fig.3 Calculation model.

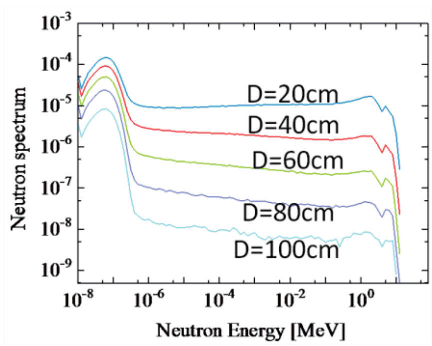

Fig.4 MCNP calculation results.

3. Results and discussion

3.1 Multi parameter MCA measurement

A two dimensional spectrum of signals measured by the ^{3}He position sensitive proportional counter is shown in Fig.5. In the figure, the horizontal axis shows the sum of the two signals and the vertical axis shows one of the two signals. It was confirmed that the detection position information could successfully be extracted. The vertical axis value means the detection depth position from the detector edge. There are no cadmium collimators in the measurement, meaning that neutrons are entering the detector from the side surface uniformly. Full energy peaks marked with a red circle show the detection position distribution, y(r), in the detector by projecting on the y-axis. But, y(r) is not a clear detection position distribution as shown in the figure. In Fig.5, there is a zigzag curve formed with the full energy peaks and thus y(r) seems to be not a uniform distribution. One of the reasons is existence of the copper pipe of the detector. So we must make the identification system connecting between the two-dimensional figure and the detection depth spectrum. It means that it is necessary to make one-to-one correspondence between the position of the full energy peak in the figure and the real detection position in the detector. And it is quite important to fix the detectable reaction depth to define the measurable neutron energy range. For these requirements, in the next step, we carried out measurements with a cadmium collimator put around the detector.

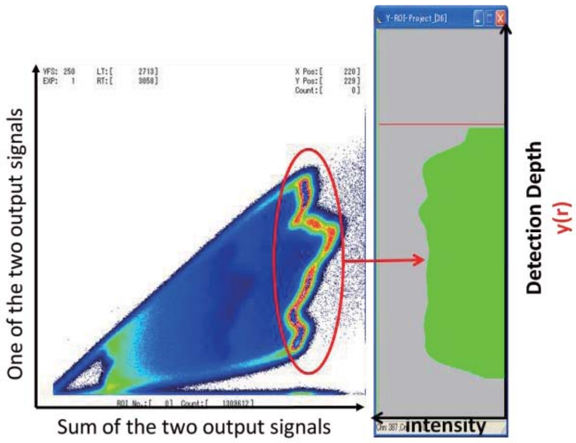

Fig.5 Two dimensional MCA result.

3.2 Detection position identification

For the collimator we used a cadmium cover, which has a large (n,γ) reaction cross section for thermal neutrons. Incident thermal neutrons are mostly blocked by the collimator and detected only from an open window of 1cm width. The schematic view for the test measurement is shown in the left figure in Fig.6. To establish the one-to-one correspondence, we have measured several tens times by moving the open window from one edge to another at every 1cm. Incident neutrons are perpendicular to the detector axis as shown in the figure.

In the right figure, several cadmium collimators were rolled around the detector to demonstrate the position sensitive detector performance. The center positions of 7 open windows were 4cm, 9cm, 16cm, 25cm, 32cm, 39cm and 49cm from one side edge, at which each of the full energy peaks was expected to be observed. There are several peaks in the spectrum. Each peak was assigned to each position carefully. The 9cm, 16cm, 25cm, 32cm, 39cm peaks were clearly identified. But no full energy peaks for the 4cm and 49cm signals were observed, and thus they could not be identified. From this result and other additional experiments it was found that we could obtain the detection position distribution at Z=6cm~44cm.

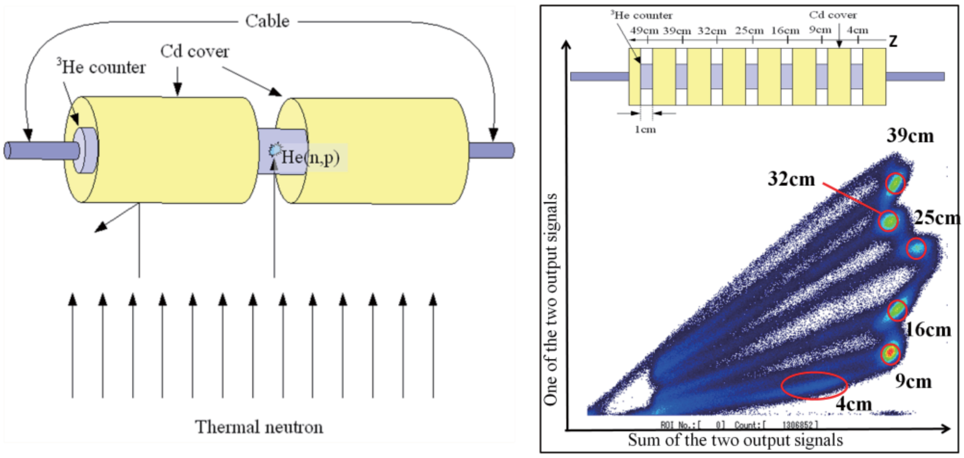

Fig.6 Position detection by the Cd collimator.

3.3 Measurable neutron energy range

Limit of measureable detection depth can affect the measurable neutron energy range. The measurable energy range was derived by the experimental results described in the previous section and the response matrix of the detector. At 6cm in depth, there exists an enough large value in the response matrix for neutrons of over 0.005eV. And over 1keV, the response difference was too small to discriminate energy. Consequently, this detector can be expected to measure neutrons of 0.005eV~1keV, which mostly cover the thermal/epithermal region. For the BNCT facilities these energy neutrons will be used and this spectrometer can obtain the crucial information of the neutrons.

4. Future works

We have been carrying out basic research & development for the thermal/epithermal neutron spectrometer. From this series researches, we made it appear that the detection position could be distinguished in the test measurement. In the next phase, the incident direction of neutrons is changed to be parallel to the detector axis, as shown in Fig.7, in order to check how well the neutron spectrum could be reproduced from the measured detection depth distribution. For this purpose, several neutron sources having different neutron spectra are to be utilized, i.e., mono-energetic thermal neutrons at JRR-3M, JAEA, thermal/epithermal neutrons at OKTAVIAN facility of Osaka University and 8 keV neutrons at FRS facility of JAEA. We will use them to check one-to-one correspondence between the direction depth distribution and the incident neutron energy through measuring the response function. Finally we will confirm whether the neutron energy spectrum will be reproduced by unfolding the detection depth distribution with the response matrix using the Bayes theorem.

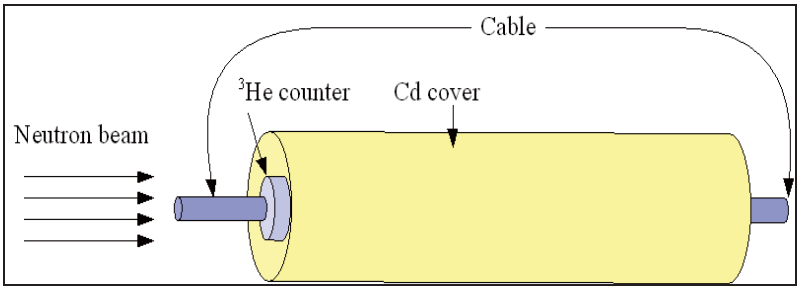

Fig.7 Schematic view of parallel incidence experiment.

5. Conclusion

We have been carrying out the series studies concerning the thermal/epithermal spectrum measurement especially for BNCT facilities. In the present study, we have developed a ^{3}He position sensitive proportional counter for the thermal/epithermal neutron spectrometry. The measurement system with a multi parameter MCA was designed and developed for the measurement.

A thermal neutron field was designed by MCNP5 calculation and constructed for the measurement of the detection position of the ^{3}He counter. From the measurement, the detection position distribution could be obtained as a two dimensional spectrum. But the detection depth distribution needed to have a strict one-to-one correspondence with the real detection position. So a cadmium collimator with an open window was put on and it was confirmed that the position information could correctly be obtained. From the measurement, the detector was confirmed to work appropriately in Z=6~44cm out of the detector depth signals. It means in other words that the measurable energy range was thus limited to 0.005eV~1keV.

In the next phase, we will carry out the real detection depth measurement with incident neutrons being parallel to the detector axis. For that purpose, several neutron sources are taken into consideration to be utilized for confirming one-to-one correspondence between the point of the direction depth distribution and the detection position in the detector, together with the response of the detector for the incident neutron energy.

References

[1] X-5 Monte Carlo Team: MCNP-A General Monte Carlo N-Particle Transport Code, 2003 X-5 Monte Carlo Team: MCNP—A general Monte Carlo N-particle transport code, version 5, Los Alamos National Laboratory, Los Alamos, New Mexico, USA, April 2003.

[2] I.Murata et al. "Low-energy neutron spectrometer using position sensitive proportional counter —Feasibility study based on numerical analysis" Nuclear Instruments and methods in Physics Research A 589 (2008) 445-454

[3] S.Iwasaki: "A new approach for unfolding PHA problems based only the Bayes' Theorem", Proc. 9th International Symposium on Rector Dosimetry, Prague, Chezk Republic, pp. 245-252 (1996).

18. Measurement of $^{151,153}Eu$ Neutron Capture Cross Sections using a pair of C_6D_6 Detectors

Jae Hong LEE*, Jun-ichi HORI, Ken NAKAJIMA
Research Reactor Institute, Kyoto University
Kumatori-cho, Sennan-gun, Osaka 590-0494, Japan
* E-mail: zelloseve@rri.kyoto-u.ac.jp

In the present study, we have measured the neutron capture cross sections of ^{151}Eu and ^{153}Eu by the time-of-flight (TOF) method in the range of 0.03 eV to keV region using a 46 MeV electron linear accelerator at the Research Reactor Institute, Kyoto University (KURRI). We employed a pair of C_6D_6 liquid scintillators for the capture γ-ray measurement. The energy dependent neutron flux was derived with the standard cross sections of the $^{10}B(n,\alpha\gamma)$ reaction. A pulse-height weighting technique was applied to observed γ-ray spectra to determine the capture yields of $^{151,153}Eu$. The weighting function was obtained using the response function of a pair of C_6D_6 liquid scintillators that were calculated with a Monte-Carlo simulation code EGS5 (Electron Gamma Shower Version 5). The present results were compared with the previous experimental data and the evaluated values of JENDL-4.0.

1. Introduction

Recently, a great interest has been taken in burn-up credit for criticality safety in the transportation, storage and treatment of spent nuclear fuel. Burn-up credit is a concept in criticality safety evaluation that takes into account for the reduction in reactivity of spent fuel due to the composition change during irradiation. Neutron capture cross section data of fission product (FP) play an important role in burn-up credit. According to the reference of [1], twelve FP isotopes (^{95}Mo, ^{99}Tc, ^{103}Rh, ^{133}Cs, $^{143,145}Nd$, $^{147,149,150,152}Sm$, ^{153}Eu, ^{155}Gd) are recommended to be considered in burn-up credit. The objective of this work is to measure neutron capture cross sections of ^{153}Eu and ^{151}Eu. ^{153}Eu is one of the most important FPs for burn-up credit application. ^{151}Eu has a large capture cross section and is contained in the sample of enriched ^{153}Eu that used in this work. Therefore, the experimental data of ^{151}Eu are also necessary to correct the ^{153}Eu capture yield including the effect of ^{151}Eu as an impurity in the sample.

2. Experiments

The capture cross section measurements were carried out by the TOF method using the linac at the KURRI. A photo-neutron target of Ta was adopted as a pulsed neutron source for the neutron TOF measurement. The experimental arrangement with a pair of C_6D_6 scintillators is shown in Fig. 1. The distance between the sample and the neutron source was 12.1±0.02 m. Output signals from the scintillators were summed up and stored with the Yokogawa's WE7562 multi channel analyzer as a two dimensional data of pulse height (PH) and TOF.

The accelerator was operated in two different modes as shown in Table 1: one was for the measurement below 1 eV with a repetition rate of 50 Hz and another was for the measurement above about 1 eV with a repetition rate of 200 Hz. In the latter case, a Cd sheet of 0.5 mm in thickness was inserted into the TOF beam line to suppress the overlap components of low energy neutrons from the previous pulsed due to the high frequency. Pulse width was 100 ns for each mode.

The characteristics of the samples are summarized in Table 2. The samples of ^{151}Eu and ^{153}Eu were packed in aluminum foils 20 mm in diameter and 0.08 mm in thickness. The enriched ^{10}B sample was used for the measurement of the incident neutron flux on the sample. The sample of ^{10}B was packed in an aluminum case (25 mm in diam., 0.4mm in thickness).

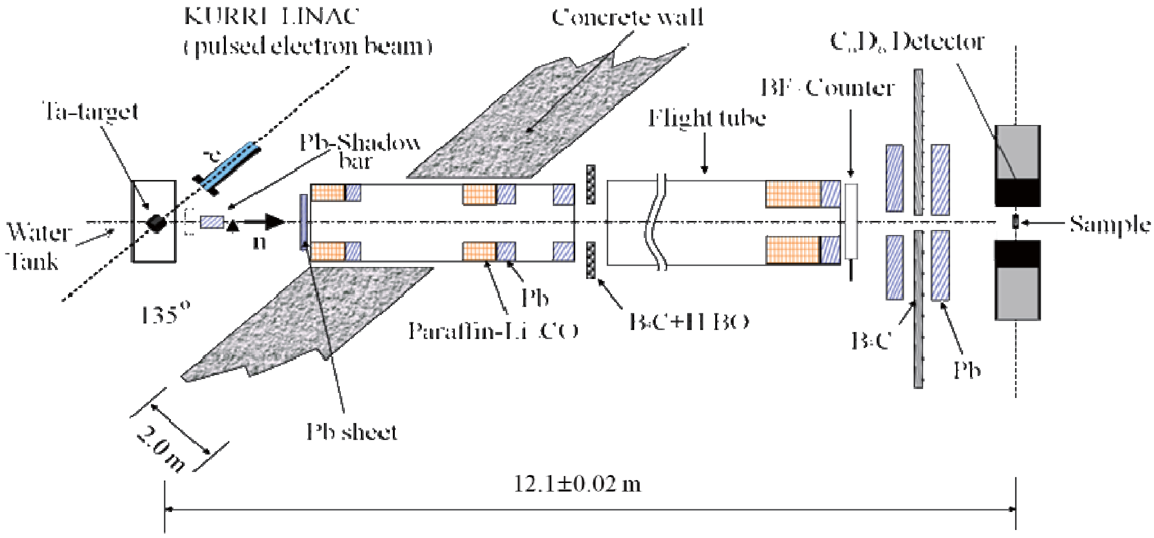

Fig.1. Experimental arrangement for the capture cross section measurement

Table 1. Details of the measurement conditions

		High Energy measurement	Low Energy measurement
LINAC Condition	Repetition rate	200 Hz	50 Hz
	Pulse width	100 nsec	100 nsec
	Average current	63.0 A	16.5 A
	Cd filter	On	off

Table 2. Physical parameters of the samples used in the experiment

Sample	^{151}Eu	^{153}Eu	^{10}B
Chemical Form	Oxide (Eu_2O_3)	Oxide (Eu_2O_3)	Metal powder
Isotope Composition	^{151}Eu : 97.60%	^{153}Eu : 99.71%	^{10}B: 96.98%
	^{153}Eu : 2.4%	^{151}Eu: 0.29%	^{11}B: 3.02%
Weight (g)	0.115	0.114	3.60
Thickness (g/cm^2)	0.0288	0.0285	0.947
Number of atoms	3.86×10^{20}	3.87×10^{20}	5.55×10^{22}
Size of sample	2.0×2.0 cm^2	2.0×2.0 cm^2	2.2 cm in diam.

3. Data Processing and Analysis

3.1 Neutron Capture Cross Section

The neutron capture cross sections for ^{151,153}Eu were obtained by the following relation:

$$\sigma_{cs}(E_n) = f_{cs}(E_n)\cdot\frac{Y_s(E_n)}{\phi_0(E_n)\cdot N_s x_s} \tag{1}$$

where the subscript "*S*" means an objective nuclide of ^{151}Eu or ^{153}Eu. N_s and x_s are the atomic density and sample thickness, $\sigma_{cs}(E_n)$ is the neutron capture cross section, $Y_s(E_n)$ is the energy dependent neutron capture yield, $\phi_0(E_n)$ is the incident neutron flux on the sample and $f_{cs}(E_n)$ is the correction function. The correction for the neutron self-shielding and multiple scattering in each sample was made by the MCNP-4C (Monte-Carlo Code for Neutron and Photon Transport, version 4C) [2] with the nuclear data taken from JENDL-4.0 [3]. As for ^{153}Eu, the correction for the capture yields due to the isotopic impurity in the sample was also done by using the present results of ^{151}Eu. The methods to derive the incident neutron flux and the neutron capture yield are briefly described in the following sections.

3.2 Incident Neutron Flux

A ^{10}B sample was used to determine the incident neutron flux on the sample. The $^{10}B(n,\alpha\gamma)^7Li$ reaction emits a single γ ray of 478 keV. It means that the detection efficiency for the reaction is independent of neutron energy. Then, the neutron flux $\phi_0(E_n)$ is given by the following relation:

$$\phi_0(E_n) = \frac{C_B(E_n)}{\varepsilon_B Y_B(E_n)} \tag{2}$$

where the subscript "*B*" means ^{10}B. $C_B(E_n)$ is the counting rate at energy E_n, $Y_B(E_n)$ is the energy dependent capture yield for the $^{10}B(n,\alpha\gamma)^7Li$ reaction, ε_B is the detection efficiency for the 478-keV γ ray which was calculated with the EGS5 [4]. The neutron capture yield $Y_B(E_n)$ was obtained by the Monte Carlo calculation with the MCNP-4C. The nuclear data used for the Monte-Carlo simulation were taken from JENDL-4.0.

3.3 Neutron Capture Yield

The γ-ray detection efficiency of the pair of C_6D_6 liquid scintillators is small enough not to count two or more γ rays per capture event. Therefore, the efficiency for detecting capture events depends on decay modes of compound nucleus. By applying a weighting function, *W(I)*, on the observed PH spectrum, the detector can be treated as a total energy detector having a γ-ray detection efficiency proportional to an incident γ-ray energy [5]. Since the sum of γ-ray energies emitted from a capture event is independent of decay modes, the efficiency for detecting capture events is also proportional to the excitation energy of capture state.

The weighting function, *W(I)*, was defined as follows:

$$\sum_I W(I)R(I,E_\gamma) = E_\gamma \tag{3}$$

where $R(I, E_\gamma)$ is the response function defined as the probability that a γ ray with an energy of E_γ emitted from the sample position into isotropic was detected in the *I*-th channel of the PH spectrum. The response functions for discrete γ-ray energies from 0.5 to 7.0 MeV were obtained by the calculation with the EGS5 and the experiments with standard γ-ray sources as shown in Fig. 2. The weighting function was determined by means of a least square fitting so as to minimize the following χ^2:

$$\chi^2 = \sum_i \left\{ \sum_I W(I)R(I,E_i) - E_i \right\}^2 \Big/ E_i^2 \tag{4}$$

The weighting function for the pair of C_6D_6 liquid scintillators is shown in Fig. 3.

The neutron capture yield was obtained as follows:

$$Y = \frac{\sum_I S(I)W(I)}{BE + E_n} \tag{5}$$

where *S(I)* is the capture γ-ray PH spectrum, *BE* is the neutron binding energy of target nucleus, E_n is the incident neutron energy. The capture γ-ray PH spectrum, *S(I)*, was obtained by subtracting the background(BG) from the foreground PH spectrum corresponding to each TOF region. The BG spectrum was estimated from the measurements with an empty case.

4. Results and Discussion

(1)^{151}Eu

The preliminary neutron capture cross sections of ^{151}Eu were obtained in the neutron energy region from 0.03 eV to 100 keV as shown in Fig. 4. A number of experiments were reported for ^{151}Eu and they are also shown in the figure for comparison. The present results give good agreement with those experimental data, and hence we can conclude that the validity of the weighting function derived in this work was confirmed.

(2)^{153}Eu

The preliminary neutron capture cross sections of ^{153}Eu were obtained in the neutron energy region from 0.03 eV to 4 keV as shown in Fig. 5. Widder measured the capture cross sections in the region from 0.01 to 10 eV, using a reactor with a fast chopper [6]. The results of Widder are larger than the present results by about 20 % in the thermal energy region. On the other hand, the evaluated values of JENDL-4.0 show good agreement with the present ones below 1 eV. In the energy range from 100 eV to 4 keV, the present data agree well with the experimental data by Konks *et al.*[7] and Moxon *et al.*[8], while the discrepancy between the evaluated values of JENDL-4.0 and the present results ranges from 5 to 40 %. An undesirable structure is clearly observed around 0.6 eV. There is a possibility that the correction for ^{151}Eu as an isotopic impurity was not completely made.

5. Conclusion

The preliminary neutron capture cross sections of ^{151}Eu and ^{153}Eu have been measured from 0.03 eV to the keV region with a pair of C_6D_6 detectors by the TOF method. As for ^{151}Eu, the present data agree well with the previous experimental data and the evaluated values of JENDL-4.0. Therefore, the validity of the weighting function derived in this work was confirmed. As for ^{153}Eu, the results of Widder are larger than the presents by about 20 % at the thermal energy. The evaluated values of JENDL-4.0 are in good agreement with the present ones except the energy region from 100 eV to 4 keV.

Acknowledgement

The authors would like to express their thanks to the linac staff of the KURRI for making it possible to operate the accelerator steadily. They would also like to express their thanks to Dr. Takumi Kubota for cooperation on calculation with the EGS5, and to Prof. Samyol Lee and Mr. Naoya Abe for their helpful discussions.

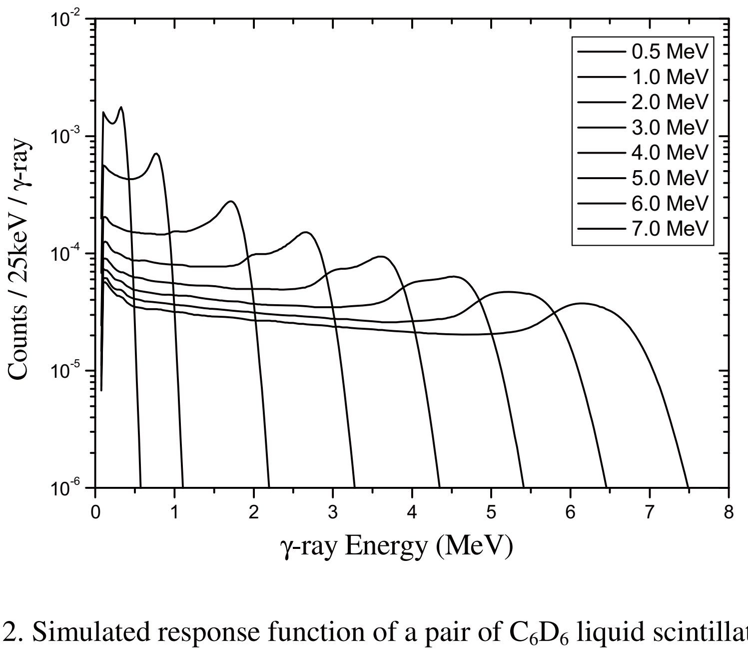

Fig. 2. Simulated response function of a pair of C_6D_6 liquid scintillators

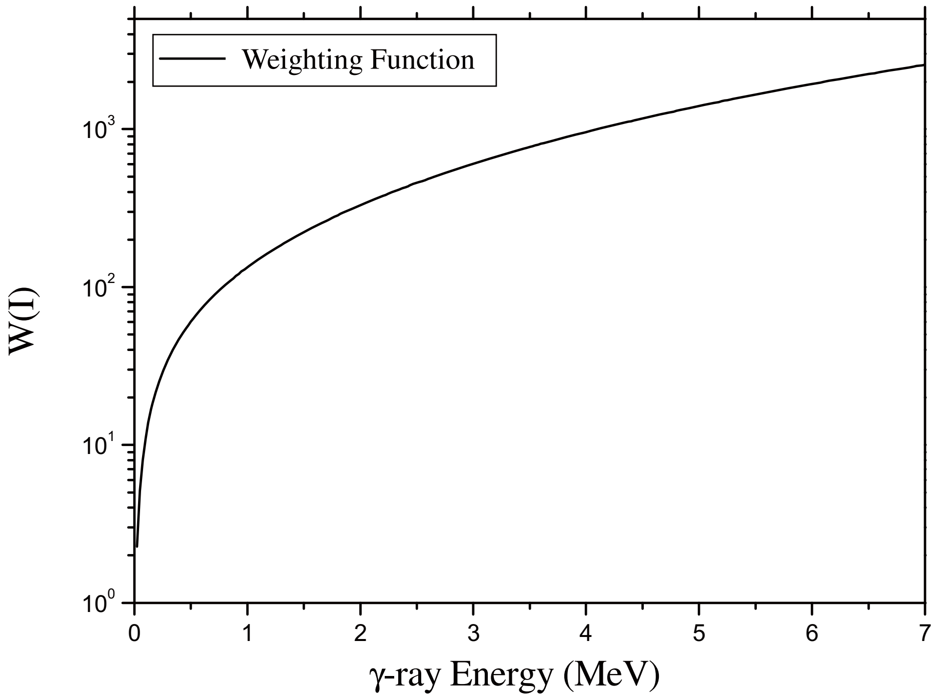

Fig. 3. Weighting function W(I) of a pair of C_6D_6 liquid scintillators

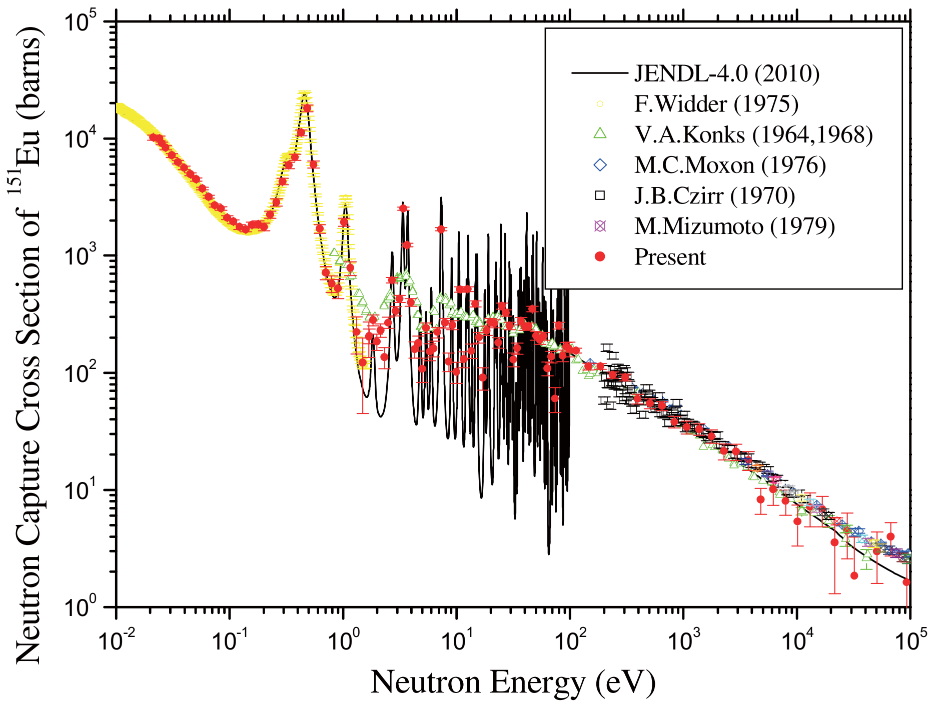

Fig. 4. Neutron capture cross sections of ^{151}Eu

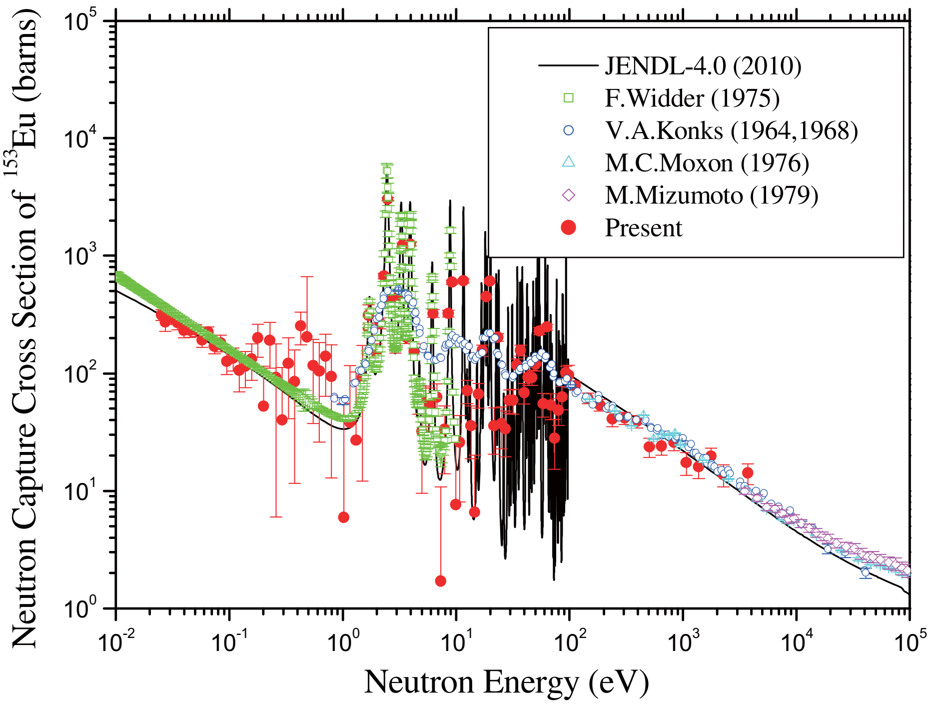

Fig. 5. Neutron capture cross sections of ^{153}Eu

References

[1] Nuclear Fuel Cycle Facility Safety Research Committee, "A Guide Introducing Burnup Credit, Preliminary Version", JAERI-Tech 2001-055, (2001) [in Japanese].

[2] J. F. Briesmeister, Ed. "MCNP-A general Monte Carlo N-Particle Transport code, version 4c," LA-13709-M (2000)

[3] K. Shibata, *et al.*, "JENDL-4.0: A New Library for Nuclear Science and Engineering," *J. Nucl. Sci. Technol.*, **48**, 1 (2011).

[4] H. Hirayama, *et al.*, The EGS5 Code System, Stanford Linear Accelerator Center Report SLAC-R-730 (2005).

[5] R. L. Macklin, J. H. Gibbons, "Neutron Capture Cross Sections of ^{151}Eu and ^{153}Eu from 3 to 2200 keV," *Phys. Rev.*, **159**, 1007 (1987).

[6] F. Widder, "Neutron Capture Cross Section Measurements in Theenergy Region from 0.01 to 10 Electron Volts," Proc. of Conf. on 2.Symp.on Neutr.Capt.Gamma Ray Spectrosc., Petten, 265, (1974).

[7] V.A.Konks, Y.P.Popov, Y.I.Fenin, "Radiative Capture of Neutrons by Nuclei with A = 140-200," *Soviet J. Nucl.Phys.*, **7**, 310(1968)

[8] M.C.Moxon, D.A.J.Endacott, J.E.Jolly, "The Neutron Capture Cross-Section of ^{151}Eu and ^{153}Eu in the Energy Range 0.1 to 100 keV," *Nucl. Energy*, **3**, 399 (1976)

19. Measurement of Resonance Parameters of ^{155,156,157,158,160}Gd by using pulsed neutrons with energy ranges from 10 eV to 1 keV

Yeong-Rok Kang*, Tae-Ik Ro
Department of Physics, Dong-A University, Busan 604-714, Korea
Email: tiro@donga.ac.kr

Guinyun Kim, Manwoo Lee
Department of Physics, Kyungpook National University, Daegu 702-701, Korea

Y. Danon, M.J Rapp, D. Williams
Department of Mechanical, Aerospace, and Nuclear Engineering, Rensselaer Polytechnic Institute
Troy, New York 12180-3590

G. Leinweber, D.P Barry, R.C. Block
Bechtel Marine Propulsion Corporation, Knolls Atomic Power Laboratory
P.O. Box 1072, Schenectady, New York 12301-1072

We explored neutron interactions with Gadolinium isotopes in the energy region from 10 eV to 1 keV at the electron linear accelerator facility at the Rensselaer Polytechnic Institute (RPI). The neutron capture measurements were made at a flight path of 25 m with a 16-segment sodium iodide multiplicity detector by using the time-of-flight technique. Five high-purity gadolinium isotopes (^{155}Gd, ^{156}Gd, ^{157}Gd, ^{158}Gd, and ^{160}Gd) and two natural gadolinium samples were used for the neutron capture measurement. Resonance parameters for ^{155,156,157,158,160}Gd were obtained by using the multilevel R-matrix Bayesian code SAMMY. The samples are placed in the center of a cylindrical 16-segment thallium activated sodium iodide NaI(Tl) detector. Each NaI(Tl) piece is pie shaped and optically separated from each other. All of the NaI(Tl) pieces are housed within an aluminum can with photomultipliers attached to each pie shaped segment. Many new resonances of the epithermal region are proposed, and other resonances previously identified in the literature have been revised. The poor match of the ENDF/B-VII.0 parameters to the current data is significant, and substantial improvement to the understanding of gadolinium cross sections is presented, particularly above 180.4 eV where the ENDF/B-VII.0 resolved region for ^{155}Gd ends. As a result, fitting data above 180.4 eV was performed without initial estimates for resonance locations and widths as a challenging task. Also new fitting result of ^{157}Gd above 306.4eV of the upper limit of ENDF/B-VII.0 was presented.

1. Introduction

The neutron capture cross-sections of gadolinium (Gd) isotopes are important in the design of reactors, as well as in nuclear-reaction and astrophysical studies. Since the major portion of the natural Gd capture cross-sections is due to ^{155}Gd and ^{157}Gd, an accurate knowledge of the cross-sections for those isotopes is also of importance to calculate the reactor characteristics when Gd is used as a burnable poison in light water reactors. The purpose of the present work was to measure the neutron capture cross-sections and to determine resonance parameters for Gd isotopes that are an improvement over the current gadolinium evaluations. In addition, the data are important for examining the availability of Gd as a control material for fast reactors.[1]

In the region from 1.0 to 300.0 eV, most of the resonances occur in ^{155}Gd and ^{157}Gd. In these two isotopes, ENDF resonance parameters are based on Mughabghab and Chrien[2], Simpson[3], and Fricke et al.[4] The other high-abundance isotopes, ^{158}Gd and ^{160}Gd, have few resonances, and their resonance parameters are based on Mughabghab and Chrien[2], and Rahn et al.[5] The minority isotopes are ^{152}Gd and ^{154}Gd. Its resonance parameters come from Anufriev et al.[6] and Macklin.[7] This is the first experiment to use high-purity Gd isotopes of ^{155}Gd, ^{156}Gd, ^{157}Gd, ^{158}Gd, ^{160}Gd. Table I lists the isotopic content of the gadolinium samples used in this experiment.

A more detailed description of the present measurement and analysis is given in Ref. 8.

TABLE I
General information about elemental Gadolinium

Properties/Sample	^{155}Gd	^{156}Gd	^{157}Gd	^{158}Gd	^{160}Gd
Isotopic Composition [%]					
^{152}Gd	0.04	<0.01	<0.02	<0.1	<0.01
^{154}Gd	0.64	0.11	0.16	<0.1	0.02
^{155}Gd	91.74	1.96	0.81	0.96	0.18
^{156}Gd	5.11	93.79	2.21	1.7	0.32
^{157}Gd	1.12	2.53	90.96	3.56	0.43
^{158}Gd	0.94	1.2	5.08	92	0.93
^{160}Gd	0.41	0.41	0.8	1.82	98.12
Sum of %	100.0	100.0	100.02	100.04	100.00
Atomic Wt.	155.04 ± 0.25	155.965±0.079	156.92 ±0.16	157.80 ± 0.22	159.871±0.099
Weight [mg]	203.3 ± 0.2	197.7 ± 0.2	357.5 ± 0.2	353.0 ± 0.2	193.5 ± 0.2
Thickness [mm]	0.109 ± 0.001	0.106 ± 0.001	0.205 ±0.003	0.209 ± 0.005	0.104 ± 0.002
Diameter [mm] or Size	18.06 ± 0.03	18.13 ± 0.05	15.22 ± 0.26	15.35 ± 0.30	18.14 ± 0.09
Area [mm^2]	256.15	258.03	235.70	232.48	258.46
Grams/cm^2	0.0793676	0.0766190	0.1516759	0.1518410	0.0748665
Atoms/b	0.0003083 ± 0.0000012	0.0002959 ± 0.0000016	0.000582 ± 0.000014	0.000580 ± 0.000016	0.0002820 ± 0.0000027

2. EXPERIMENTAL PROCEDURE

The electron linear accelerator (linac) facility at the Rensselaer Polytechnic Institute (RPI) was used to explore neutron interactions with Gd isotopes in the energy region from 10 eV to 1 keV. The electron beam impinges on a water-cooled tantalum target where electrons interact and produce bremsstrahlung, which generates photoneutrons. The resulting neutrons are moderated and collimated as they travel through a long evacuated flight tube to the sample and detector. Table II gives some details of the experimental conditions including neutron targets, overlap filters, pulse repetition rate, flight path length, and channel widths. The neutron energy for a detected event is determined using the time-of-flight (TOF) technique. The RPI LINAC is an L-band traveling wave electron accelerator that is capable of producing electrons up to 60 MeV. Figure I is a layout of the RPI LINAC facility.

The RPI capture detector[9] is a 30.5-cm-diamx30.5-cm-high hollow cylinder that contains 16 sections of thallium activated sodium iodide NaI(Tl) scintillator crystals. The cylinder is split perpendicular to its axis into two rings, and each ring contains eight equally sized pie-shaped NaI(Tl) segments. Each NaI(Tl) segment is optically isolated and hermetically sealed within an aluminum can and mounted on an RCA 8575 photomultiplier. The samples are placed by a computer-controlled sample changer into the center of the capture detector. The sample changer is capable of holding up to eight samples. The boron carbide liner (enriched in ^{10}B) around the sample reduces the scattering background by absorbing the neutrons that are scattered from the sample and preventing the scattered neutrons from being detected in the NaI(Tl) crystal. The detector system discriminates against the 478-keV gamma-ray from ^{10}B (n;α,γ) reactions. The efficiency of the capture detector is ~75 % for a single 2 MeV gamma-ray. The efficiency of a detecting a capture event in gadolinium is close to 100 % and varies slightly by isotope and sample thickness. Reference 10 contains a description of the detector and its signal-processing electronics. Neutron capture data-taking and data-reduction techniques at the RPI are described in Refs. 11 and 12.

The large amount of data collected in each capture measurement was subject to statistical integrity checks to verify the stability of the linac, the capture detector, and associated beam monitors. Any data that failed the integrity test were eliminated. Next, the data were dead-time corrected, normalized to beam monitors, and summed. The background was determined using normalized data measured with an empty aluminum can mounted on the sample changer. This background was subtracted from the normalized and summed capture spectra. The 16 individual capture spectrums were then summed into a single total spectrum.

When an incident neutron is captured in the sample, a compound nucleus in an excited state is formed. The compound nucleus then de-excites to the ground state with the subsequent emission of gamma rays. The detection of these gamma rays allows one to measure the fraction of neutrons of a given energy that are captured if the incident neutron flux is known. This fraction of captures is known as the capture yield. Thus, for a uniform thickness sample and a parallel neutron beam incident perpendicularly to this sample, the capture yield is defined as the number of detected capture gamma rays divided by the product of the detector efficiency times the number of incident neutrons. Mathematically speaking, the capture yield is defined as the number of captures per incident neutron. In time of flight measurements the capture yield, Y_i in TOF channel i was calculated by

$$Y_i = \frac{C_i - B_i}{K\phi_{smi}}, \tag{1}$$

where

C_i= dead-time-corrected and monitor-normalized count rate of the sample measurement

B_i= dead-time-corrected and monitor-normalized background counting rate

K= detector efficiency and flux normalization factor

Φ_{smi}= smoothed, background-subtracted, and monitor-normalized neutron flux shape.

The incident neutron flux shape was determined with the use of a thick $^{10}B_4C$ sample that is mounted on the sample changer. The measured flux shape is usually normalized directly to a saturated capture resonance. This capture yield and its associated statistical uncertainty provided input to the SAMMY data analysis code[13] that extracted the neutron resonance parameters.

TABLE II
Gadolinium Experimental Details

Experiment	Overlap Filter	Neutron-Producing Target	Average Beam Current (μA)	Beam Energy (MeV)	Pulse Width (ns)	Channel Width (ns)	Pulse Repetition Rate (pulse/s)	Flight Path Length (m)
Epithermal Capture	Boron cabide	Bare Bounce	17.28	57	18	12.8	225	25

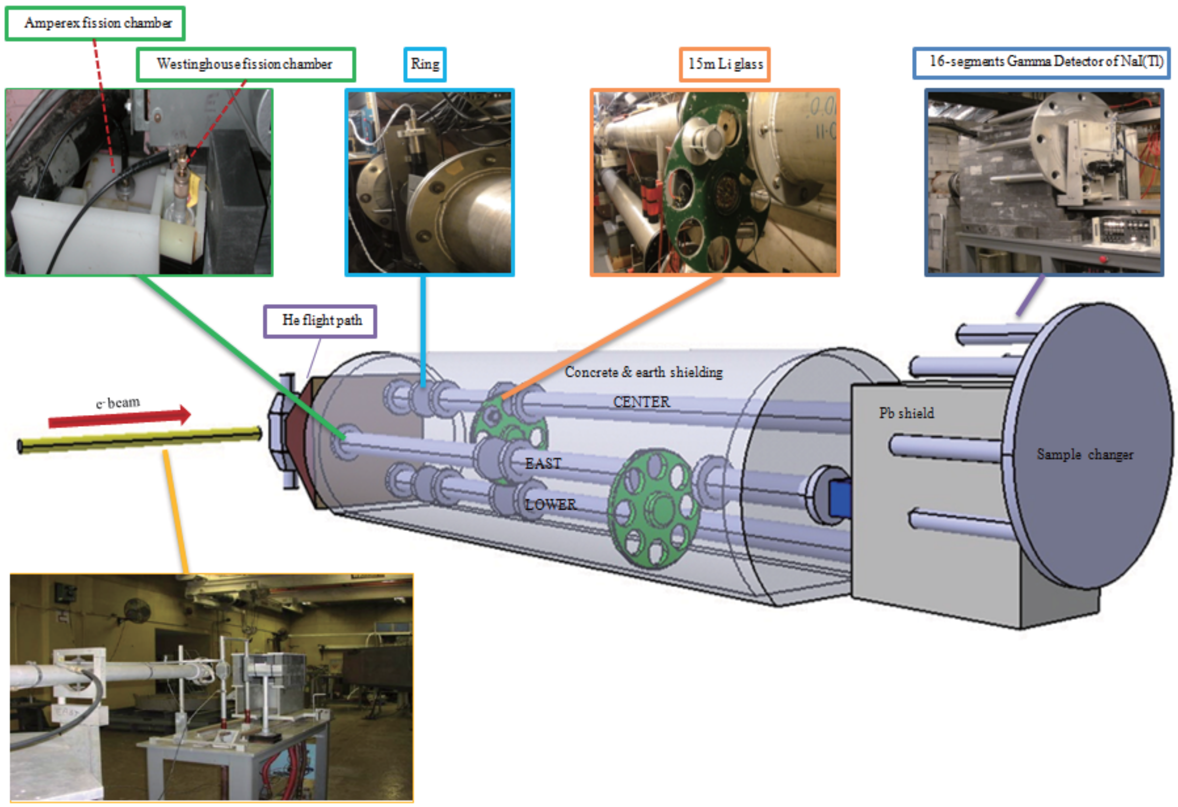

Fig. 1. Layout of the RPI LINAC facility.

3. RESULTS AND CONCLUSIONS

Data were dead time corrected, run-summed, beam-monitor-normalized, and background-corrected. Final processed data were reduced to capture yield. The Resonance parameters, neutron width Γn, radiation width Γγ, and resonance energy E_0, were extracted from the capture using the SAMMY version 8 multilevel R-matrix Bayesian code.[7] The resolved resonance energy region for ^{155}Gd and ^{157}Gd in the ENDF/B-VII.0 evaluation ends at 180.4 eV and 306.4 eV. As a result, fitting data above 180.4 eV and 306.4 eV were performed with initial estimates for resonance locations width-a challenging task. ^{155}Gd and ^{157}Gd were observed new resonance as shown in Figure 2. The details of resonance parameters for Gd isotopes are obtained and will be reported in the separated paper.

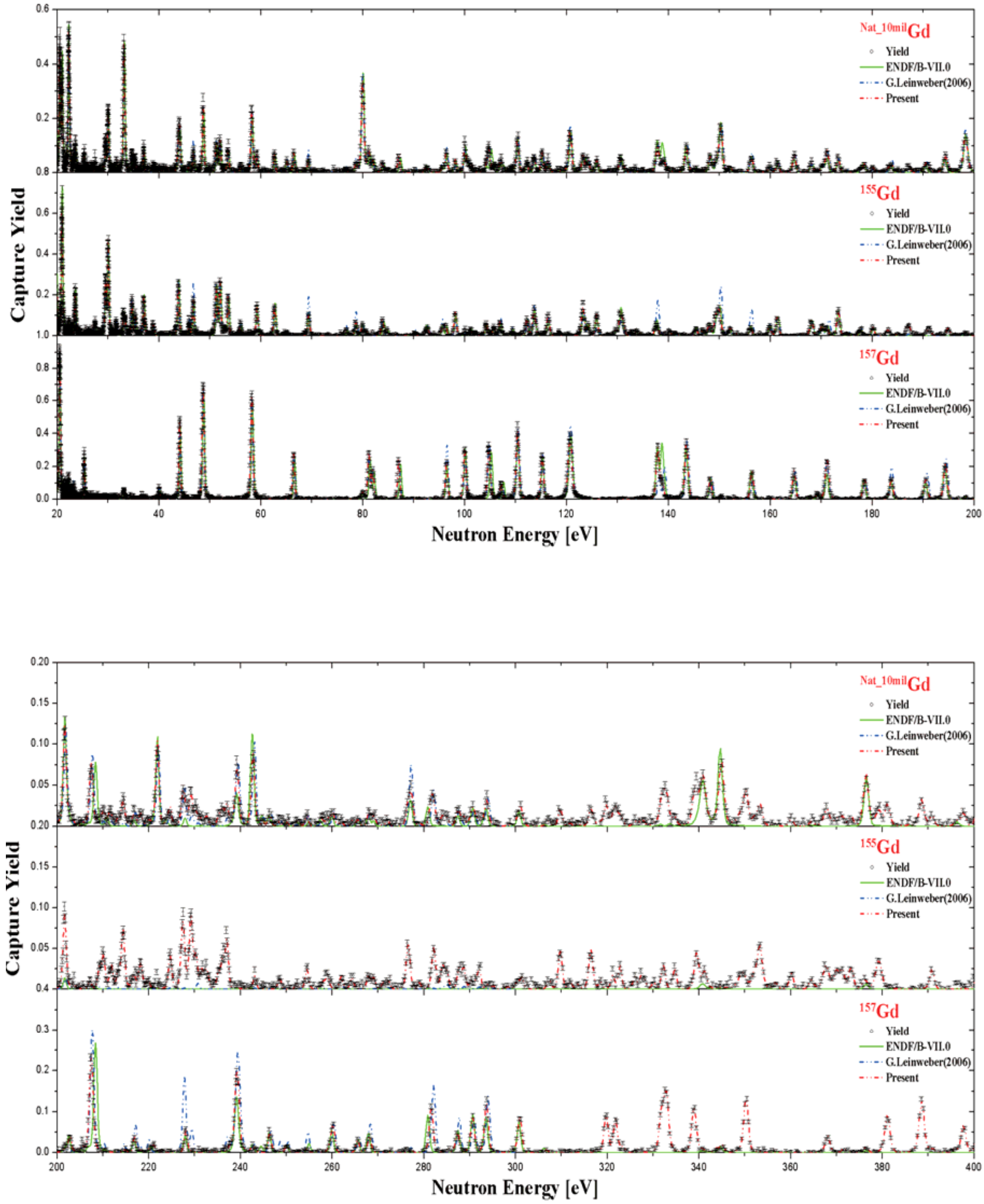

Fig. 2. An overview of the data and SAMMY fits in ^{155}Gd and ^{157}Gd.

REFERENCES

[1] W.C. Chung, T.I. Ro, G.N. Kim, M. Igashira, T. Ohsaki, "Measurement of Neutron Capture Cross-Section for ^{155}Gd and ^{157}Gd Isotopes in the Neutron Energy Range from 10 to 90 keV," J. Korean Phys. Soc. **48**, 4 (2006).

[2] S. F. MUGHABGHAB and R. E. CHRIEN, "S-Wave Neutron Strength Functions of the Gd Isotopes," Phys. Rev., **180**, 1131 (1969).

[3] F. B. SIMPSON, "Neutron Resonance Parameters for ^{147}Sm, ^{149}Sm, ^{155}Gd, and ^{157}Gd," Bull. Am. Phys. Soc., **2**, 42 (NA7) (1957).

[4] M. P. FRICKE, W. M. LOPEZ, S. J. FRIESENHAHN, A. D. CARLSON, and D. COSTELLO, "Neutron Resonance Parameters and Radiative Capture Cross Section of Gd from 3 eV to 750 keV," Nucl. Phys. A, 146, 337 (1970).

[5] F. RAHN, H. S. CAMARDA, G. HACKEN, W. W. HAVENS, Jr., H. I. LIOU, and J. RAINWATER, "Neutron Resonance Spectroscopy: ^{154,158,160}Gd," *Phys. Rev. C (Nucl. Phys.)*, **10**, 1904 (1974).

[6] V. A. ANUFRIEV, S. I. BABICH, and S. M. MASYONOV, EXFOR/CINDA Database, www.nndc.bnl.gov, NNDC/CINDA　EXFOR Accession #40984 (1987).

[7] R. L. MACKLIN, "Neutron Capture Resonances of ^{152}Gd and ^{154}Gd," *Nucl. Sci. Eng.*, **95**, 304 (1987).

[8] G. LEINWEBER, D. P. Barry, M . J. Trbovich, J. A. Burke, N. J. Drindak, H. D. Knox, and R. V. Ballad, R.C. Block, Y. Danon, L. I. Severnyak, "Neutron Capture and Total Cross-Section Measurements and Resonance Parameters of Gadolinium" *Nucl. Sci. Eng.*, **154**, 261-279 (2006).

[9] Drindak, N.J., "A Multiplicity Detector for Neutron Capture Measurements", M.S. Thesis, Rensselaer Polytechnic Institute (1987).

[10] R. E. SLOVACEK, R. C. BLOCK, Y. DANON, C. WERNER, G.-U. YOUK, J. A. BURKE, N. J. DRINDAK, F.FEINER, J. A. HELM, and K.W. SEEMANN, "Neutron Cross-Section Measurements at the Rensselaer LINAC," Proc. Topl. Mtg. Advances in Reactor Physics, Knoxville, Tennessee, April 11–15, 1994, American Nuclear Society (1994).

[11] G. LEINWEBER, J. A. BURKE, H. D. KNOX, N. J. DRINDAK, D. W. MESH, W. T. HAINES, R. V. BALLAD, R. C. BLOCK, R. E. SLOVACEK, C. J. WERNER, M. J. TRBOVICH, D. P. BARRY, and T. SATO, "Neutron Capture and Transmission Measurements and Resonance Parameter Analysis of Samarium," *Nucl. Sci. Eng.*, **142**, 1 (2002).

[12] G. LEINWEBER, J. BURKE, C. R. LUBITZ, H. D. KNOX, N. J. DRINDAK, R. C. BLOCK, R. E. SLOVACEK, C. J. WERNER, N. C. FRANCIS, Y. DANON, and B. E. MORETTI, "Neutron Capture and Total Cross-Section Measurements and Resonance Parameter Analysis of Zirconium up to 2.5 keV," *Nucl. Sci. Eng.*, **134**, 50 (2000).

[13] N. M. LARSON, "Updated Users' Guide for SAMMY: Multilevel R-Matrix Fits to Neutron Data Using Bayes' Equations," ORNL/TM-9179/R8, ENDF-364/R2 Oak Ridge National Laboratory (2008).

20. Measurement of Deuteron Induced Thick Target Neutron Yields at 5 MeV and 9 MeV

Keiichi HIRABAYASHI[1], Tomoya NISHIZAWA[1], Haruhiko UEHARA[1], Hidetaka HIRANO[1], Daisuke MORIGUHCI[1], Tsuyoshi KAJIMOTO[1], Nobuhiro SHIGYO[1], Kosuke HIDAKA[1], Yuki OSHIMA[1], Makoto MAEDA[1], Takashi YASUMUNE[1], Keisuke MAEHATA[1], Yuta TAJIRI[2], Hiroshi UMISHIO[2], Shusuke HIRAYAMA[2], Shinichirou ABE[2], Yukinobu WATANABE[2] Kenshi SAGARA[3], Sunao MAEBARA[4], Hiroki TAKAHASHI[4], Hironao SAKAKI[4]

[1] Department of Applied Quantum Physics and Nuclear Engineering, Kyushu University, Motooka, Fukuoka, 819-0395, Japan
[2] Department of Advanced Energy Engineering Science, Kyushu University, Kasuga, Fukuoka, 816-8580, Japan
[3] Department of Physics, Kyushu University, Hakozaki, Fukuoka, 812-8581, Japan
[4] Japan Atomic Energy Agency, Tokai-mura, Naka-gun, Ibaraki, 319-1195, Japan
Corresponding author.E-mail：keiichi@kune2a.nucl.kyusyu-u.ac.jp

The double differential thick target neutron yields from 5MeV and 9 MeV deuteron incidence were measured at the Kyushu University Tandem Accelerator Laboratory. A copper, a titanium and a niobium foils which are thick enough for a deuteron to stop in the foils were placed at the center of a vacuum chamber. An NE213 liquid organic scintillator was employed to detect neutrons emitted from targets and placed at 9 directions from 0° to 140° . To consider the contribution of scattered neutrons from the floor, we also measured neutron yields with an iron shadow bar located in front of the scintillator. Because incident deuteron beam was not pulsed and the Time-of-Flight method was not applied, the energy spectrum was derived from unfolding the light output spectrum using the FORIST code. The detection efficiency was calculated with the SCINFUL-QMD code. The experimental results were compared with the calculation data of the TALYS and PHITS2 codes and moving source model calculation, and it turned out that the calculation data does not reproduce the experimental ones satisfactorily.

1. INTRODUCTION

In the IFMIF-EVEDA (International Fusion Material Irradiation Facility-Engineering Validation and Engineering Design Activity)[1] activities in the framework of EU-Japan Bilateral Agreement for the Broader Approach for Fusion, an accelerator has been developed for demonstration of 9 MeV - 125 mA deuteron beam[2]. Most of secondary neutrons and γ rays are estimated to be produced at the beam dump and the matching section between an RFQ and a drift tube linac. A copper or a titanium is a possible material as the beam dump. Reliable evaluation of radiation dose by the deuteron incident nuclear reactions and analysis of shielding data by deuteron beam is essential for safety license to the accelerator facility. Information of the double differential neutron thick target yields for deuteron incidence as the neutron source term is important for the accurate radiation dose estimation. However, experimental data of deuteron induced neutron yields are scarce below 10 MeV.

The purpose of this study is experimentally to obtain the double differential neutron thick target yields for 9 MeV and 5 MeV deuteron induced to copper and titanium targets. The experimental results are compared with the calculation data of the TALYS[3],PHITS2[4] code and MS(moving source)[5] calculation.

2. EXPERIMENT

2.1 Experimental Setup

The experiment was performed at the 1st target room in the Kyushu University Tandem Accelerator Laboratory. The experimental setup is illustrated in Fig. 1.

The deuteron beam from the tandem accelerator was delivered to a compact vacuum target chamber in the target room. The chamber was electrically insulated from other experimental apparatus and the ground of the experimental room in order to acquire the deuteron beam current.

The target chamber 260 mm in diameter equipped a target frame which enabled to mount up to 4 target foils at the center of the chamber. A 2 cm high aperture was set at the beam line height of the chamber in order to reduce neutron scattering at the stainless wall of the chamber. The aperture was covered with a 125 μm thick Mylar film to keep a vacuum inside the chamber.

A 0.2 mm thick copper, a 0.3 mm thick titanium and 0.2 mm thick niobium foils were chosen as targets and set at the target frame of the vacuum chamber. These target thicknesses were calculated enough to completely stop the incident deuteron by the SRIM code[6].

NE213 liquid organic scintillators 50.4 mm thick and 50.4 mm in diameter optically coupled with a Hamamatsu H1942 and an H6410 photomultiplier were adopted as neutron detectors. The electronic pulse signal as the light output of the scintillator was carried to the electronics and recorded as integrated charge information into 2 ADCs with different length of gates to separate neutron and γ ray events.

The measurement directions were 0°, 15°, 30°, 45°, 60°, 75°, 90°, 120° and 140°. The distances from the target to the neutron detector were varied from 1.6 to 2.4 m.

In order to obtain contribution of neutrons from floor and wall in the experimental room, the measurement which an iron shadow bar 150 mm × 150 mm × and 300 mm thick was set between the target and the neutron detector for each direction as background measurement.

Examples of charge spectra for foreground and shadow bar (background) measurements normalized by the number of incident deuteron for a copper target are indicated in Fig. 2.

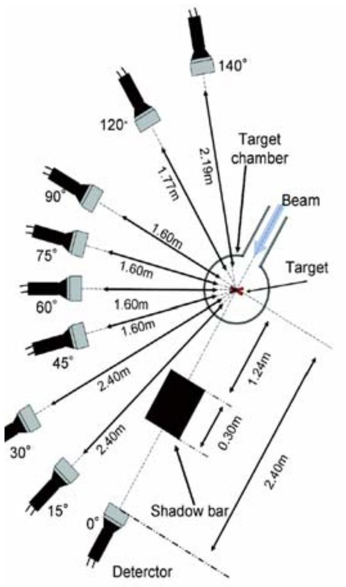

Fig. 1: Experimental setup for the deuteron incident measurement at the Kyushu University Tandem Accelerator Laboratory.

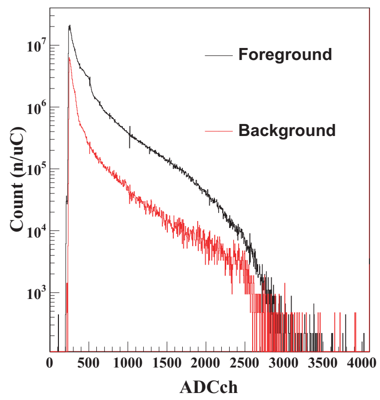

Fig. 2: Examples of raw ADC ch spectra normalized by the number of incident deuteron for a copper target. Upper and lower lines stand for foreground and background measurements,respectively.

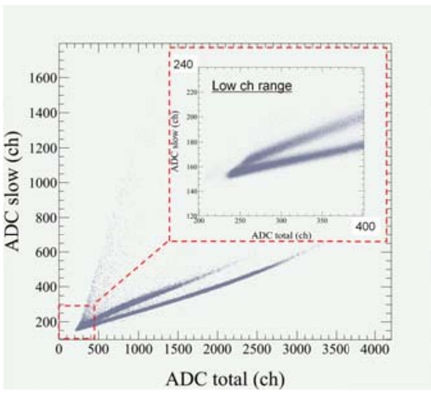

Fig. 3: The two dimensional plot of neutron and γ ray discrimination using the two gate integration method.

2.2 Data Analysis

First, γ ray events were separated from the charge spectra using the two gate integration method because the NE213 scintillator is sensitive to γ rays in addition to neutrons. Figure. 3 shows the two dimensional plot of events were separated from γ ray ones in low light output region in the figure.

Second, the charge spectra of neutron events were converted to the amount in the unit of electron equivalent using γ rays from ^{133}Ba (Eγ = 0.36 MeV), ^{137}Cs (Eγ = 0.66 MeV),^{60}Co (Eγ = 1.17 and 1.33 MeV) and Am-Be (Eγ = 4.44 MeV) standard γ ray sources. The calibration curve was given by fitting the Compton edge of these γ rays. The relationship between the charge recorded into an ADC and the light output is shown in Fig. 4.

The time-of-flight method was not applied because the deuteron beam was delivered to the target vacuum chamber continuously and it was difficult to produce pulse beam at the accelerator facility. The neutron energy spectra were derived from unfolding the integrated charge spectra as the scintillation light output ones using the response functions of the NE213 scintillator. The response functions were calculated by the SCINFUL-QMD code[7]. Figure 5 indicates the calculated response functions.

The unfolding of the light output spectra were processed by the FORIST code[8].

3. RESULTS AND DISCUSSION

For validation of the unfolding method, the measurement of neutrons from an Am-Be and a ^{252}Cf as well known neutron energy spectra. The results of measurement is shown in Figs. 6 and 7. This result reproduce overall shape of neutron energy spectra by Marsh et al.[9]. However, the experimental data does not reproduce the structure in the region between 7 and 10 MeV. This is because the neutron energy Neutron Thick Target Yield [n/MeV/sr/μC] and the light output bins were roughly divided in the data

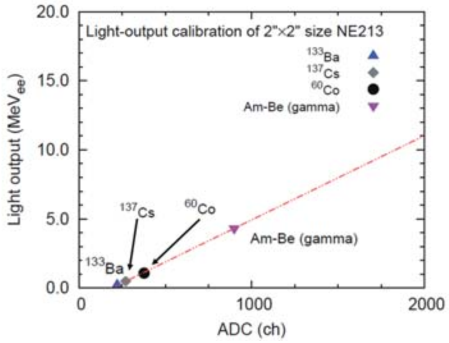

Fig. 4: The relationship between charge recorded into an ADC ch and electron equivalent light output.

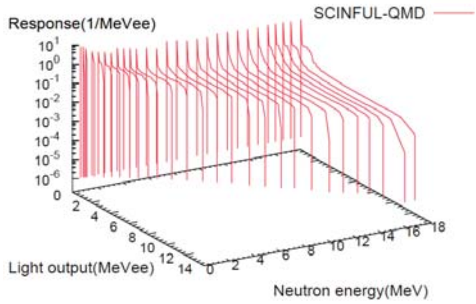

Fig. 5: Detector response functions of the NE213 scintillator calculated with the SCINFUL-QMD code.

analysis. The minimum neutron energy determined by the measurement was about 1-2 MeV.

The experimental results of the double differential neutron thick target yields for deuteron induced on a copper and a titanium targets are indicated in Figs. 7 and 8, respectively. Both neutron energy spectra for a copper, a titanium and a niobium targets show similar tendencies. The titanium total neutron yield is higher than that of other targets,and the that of niobium target is the least one. By comparison of incident deuteron energy, neutron thick target yields for 9MeV deuteron induced is much higher than 5 MeV deuteron induced one.

The experimental results were compared with the calculation data of the TALYS and PHITS2 codes and MS. The calculation values are also shown in Figs. 8 and 9. In TALS calculation, The An-Cai potential[10] for deuteron incidence was applied. The energy loss of deuteron in the thick target was considered in the calculation. For PHITS2 calculation, QMD+GEM was adopted. The PHITS2 calculation geometry is simplified one shown in Fig. 10. For MS calculation, we assumed the single component Maxwellian distribution.

Fig. 11 shows the comparison of energy integrated differential neutron yield for each target and incident deuteron energy. It is turned out that lighter nucleus target has a greater tendency to emit neutrons than heavy nucleus. The direction dependency of 9 MeV deuteron incident neutron yields are larger than 5 MeV deuteron incidence ones

TALYS code generally reproduces neutron energy spectra for copper and titanium target, but for niobium target,TALYS code reproduces experimental data insufficiently. And TALYS code underestimate neutron thick target yields for the titanium target above several MeV.

On the other hand, PHITS2 code overestimates neutron thick target yields for the titanium target above several MeV. However, below several MeV region, PHITS2 and TALYS shows similar tendency.

The MS calculation generally reproduces neutron energy spectra for each target and incident deuteron energy except for high energy region.

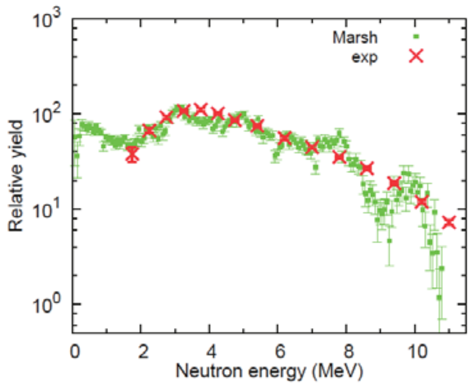

Fig. 6: The results of measured neutron energy spectra of Am-Be compared with data acquired by Marsh et al.[9].

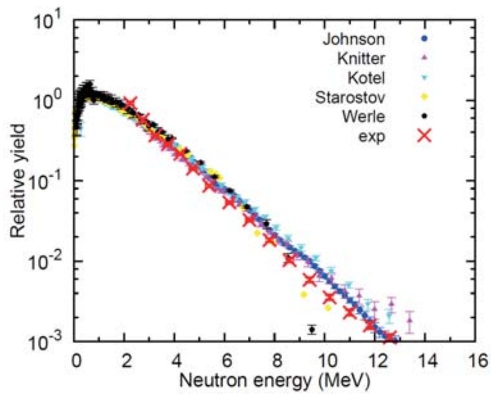

Fig. 7: The results of measured neutron energy spectra of ^{252}Cf

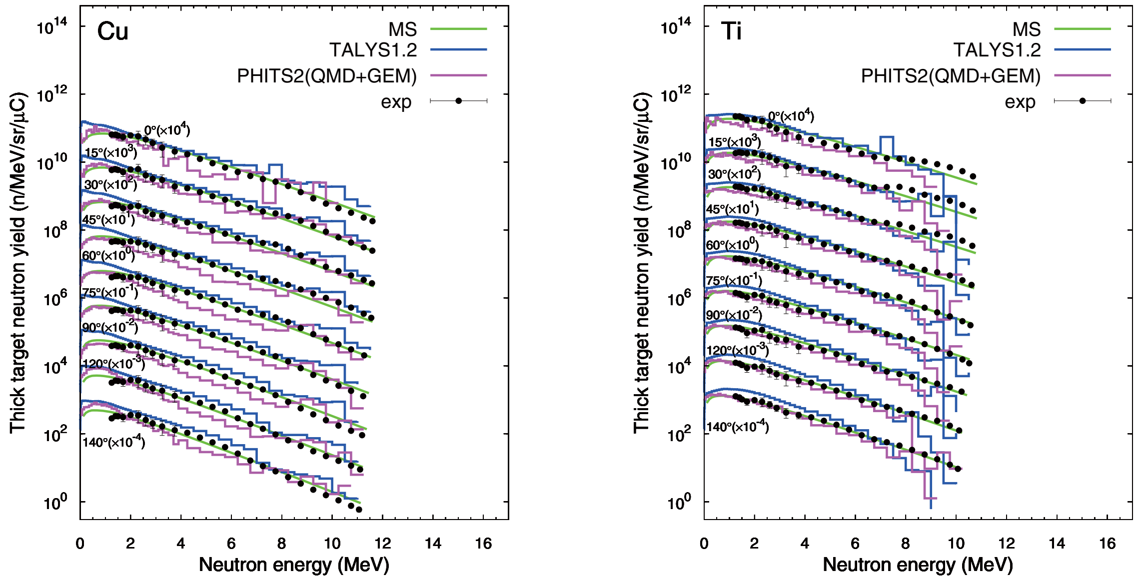

Fig. 8: The double differential neutron thick target yield for 5 MeV deuteron induced to a copper and titanium target. Marks, solid lines stand for experimental data and calculation values by version 1.2 of the TALYS and PHITS2 codes and MS calculation, respectively.

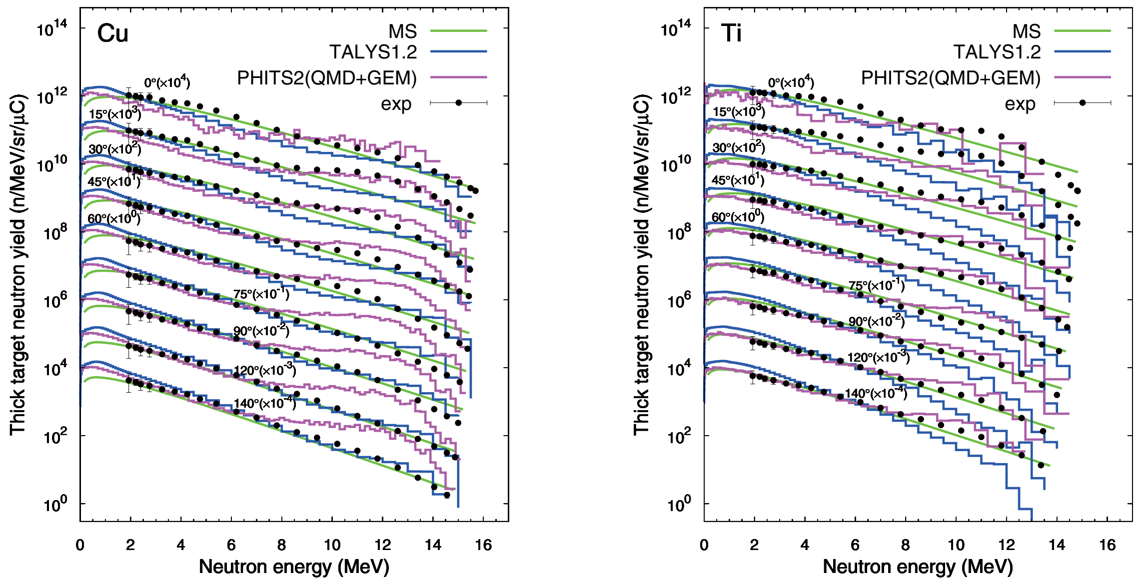

Fig. 9: The double differential neutron thick target yield for 9 MeV deuteron induced to a copper, titanium and niobium target. Marks, solid lines stand for experimental data and calculation values by version 1.2 of the TALYS and PHITS2 codes and MS calculation, respectively.

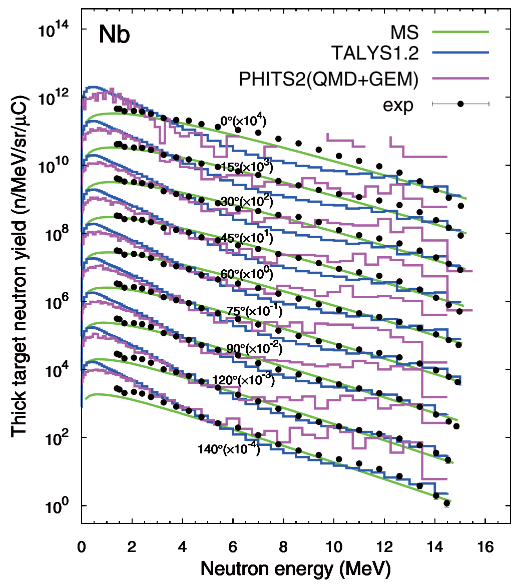

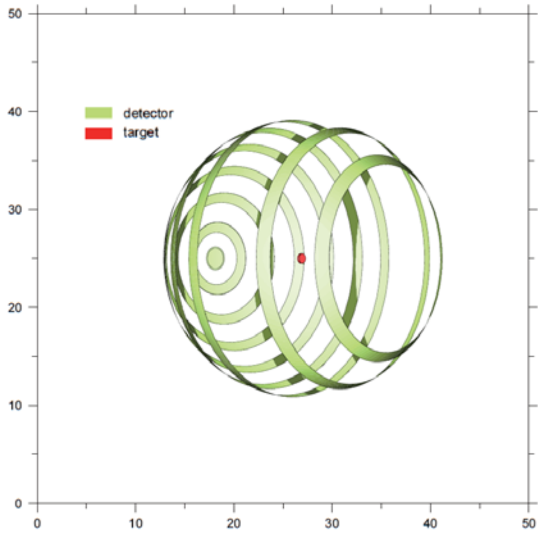

Fig. 10: The PHITS2 calculation geometry.

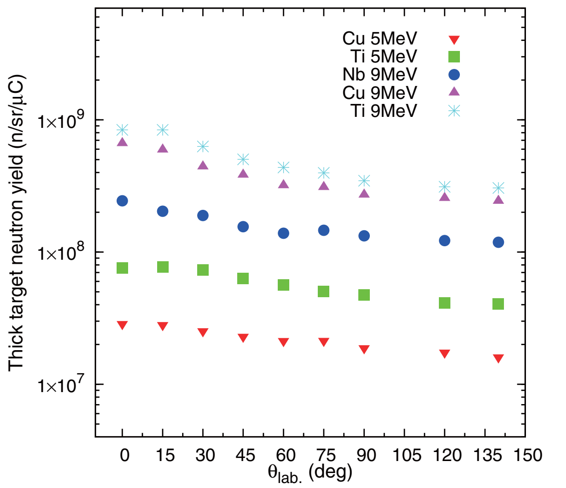

Fig. 11: Comparison of differential neutron yield.

4. FUTURE WORKS

The proton acceleration experiment will be arranged before deuteron acceleration in the IFMIF-EVEDA. It is helpful to see the differences of TTNY between deuteron and proton incidence. We estimated proton induced TTNY using the PHITS2 code with JENDL-HE nuclear data library, and compared them with measurement data of deuteron induced TTNY.

Figure 12 shows the differential neutron thick target yield of 30° for 9 MeV deuteron induced to a copper, titanium and niobium target and that of 9 MeV proton induced to the each targets. The 9 MeV proton induced TTNY is much smaller than experimental data of the 9 MeV deuteron incident one.

Figure 13 illustrates the total neutron yield for 9 MeV deuteron incident to the copper and that of proton incidence ones. The total neutron yield is derived by energy and solid-angle integration of double differential neutron yield. Due to lack of experimental data below 2 MeV, experimental data was extrapolated by TALYS calculation data normalized with experimental data at 2 MeV. For copper target, proton induced total neutron yield is 24 times smaller than deuteron induced one.

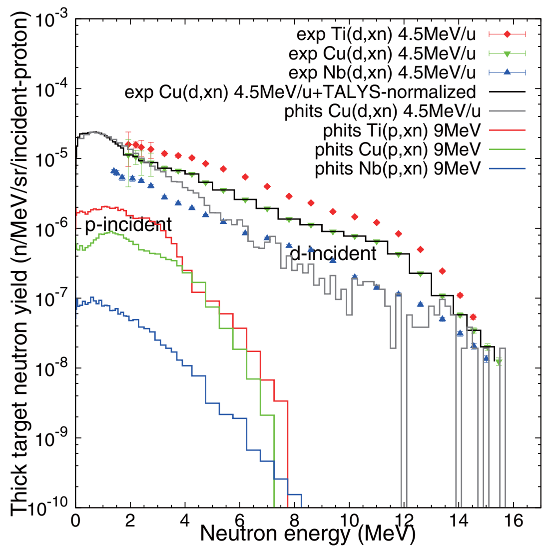

Fig. 12: The comparison of double differential neutron thick target yield of 30° (p,xn) and (d,xn).

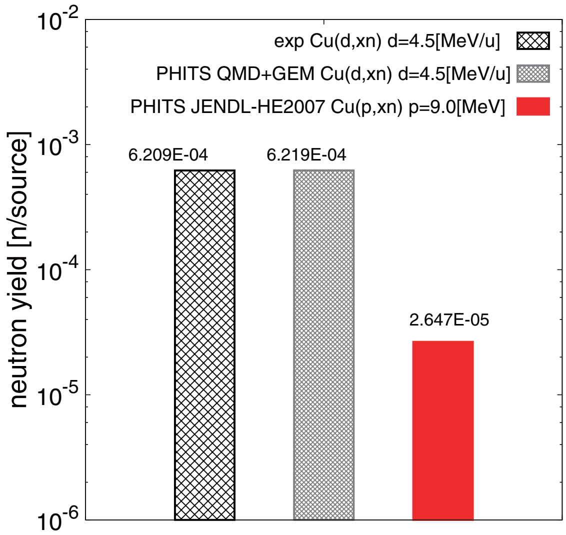

Fig. 13: The comparison of total neutron yield for 9 MeV deuteron incident to the copper and that of proton incidence total neutron yield.

5. SUMMARY

The double differential neutron yields from 5 MeV and 9 MeV deuteron incident on a copper, a titanium and a niobium thick targets were measured for reliable radiation dose evaluation at the high power deuteron accelerator facility. The light output spectra were unfolded by the FORIST code in order to derive the neutron energy spectra because it was unable to generate pulsed deuteron beam. The TALYS and PHTS2 codes and MS calculation data do not reproduce the experimental ones acceptably, especially in higher neutron energy region.

The 9 MeV proton induced thick target neutron yield is also estimated using PHITS2 code with JENDL-HE nuclear data library. The 9 MeV proton induced thick target neutron yield is much smaller than experimental data of the 9 MeV deuteron incident one.

ACKNOWLEDGMENTS

This study was carried out under the joint research between JAEA and Kyushu University for the IFMIF-EVEDA Project.

REFERENCES

[1] P. Garin, M. Sugimoto and on behalf of the Project Team and all associated Institutes, "Main baseline of IFMIF/EVEDA project," Fusion Eng. Des., 84, 259(2009).

[2] A. Mosnier, A. Ibarra and A. Facco, "THE IFMIF-EVEDA ACCELERATOR ACTIVITIES," Proceedings of EPAC08, Genoa, Italy, June 23-27, 2008, THPP077.

[3] A.J. Koning, S. Hilaire and M. Duijvestijn, "TALYS-1.2 User Manual," 70(2009).

[4] H. Iwase, et al., J. Nucl. Sci. and Teshnol. Vol.39, No.11, 1142 (2002).

[5] Bogatskaya, I. G., et al. : Phys. Rev., C22, 209 (1980).

[6] J.F. Ziegler, J.P. Biersack and U. Littmark, "The Stopping and Range of Ions in Solids," Pergamon Press, New York,2009.

[7] D. Satoh, T. Sato, N. Shigyo and K. Ishibashi, "SCINFUL-QMD: Monte Carlo Based Computer Code to Calculate Response Function and Detection Efficiency of a Liquid Organic Scintillator for Neutron Energies up to 3 GeV," JAEA-Data/Code 2006-023 2006.

[8] R.H. Johnson, D.T. Ingersoll, B.W. Wehring and J.J Dorning, "NE-213 Neutron Spectrometry System for Measurements from 1.0 to 20 MeV," Nucl. Instrum. Meth.,145, 337(1977).

[9] J.W. Marsh, D.J. Thomas and M. Burke, "High resolution measurements of neutron energy spectra from Am-Be and Am-B neutron sources," Nucl. Instrum. Meth., A366,

[10] D.G. Madland, "Proceedings of a Specialists Meeting on preequilibrium nuclear reactions, Semmering,Austria, February 10-12," 103(1988).

21. Systematic Measurement of Neutron and Gamma-ray Yields on Thick Targets Bombarded with 18 MeV Protons

Masayuki HAGIWARA [1)], Toshiya SANAMI [1)], Yosuke IWAMOTO [2)], Norihiro MATSUDA [2)], Yukio SAKAMOTO [2)], Yoshihiro NAKANE [2)], Hiroshi NAKASHIMA [2)], Kazuyoshi MASUMOTO [1)], Yoshitomo UWAMINO [3)]

[1)] High Energy Accelerator Research Organization, KEK, Oho 1-1, Tsukuba-shi, Ibaraki-ken 305-0801
[2)] Japan Atomic Energy Agency, Shirakata-shirane 2-4, Tokai-mura, Naka-gun, Ibaraki-ken 319-1184
[3)] RIKEN, Hirosawa 2-1, Wako-shi, Saitama-ken 351-0198
e-mail: hagi@post.kek.jp

Differential thick target yields (TTYs) of neutrons and γ-rays induced by 18 MeV protons have been measured at nine laboratory angles between 0- and 150-degrees using various targets (^{9}Be, ^{nat}C, ^{27}Al, ^{nat}Cu, ^{181}Ta and $^{18}H_2O$), in order to assess the nuclear data libraries and calculation codes for the proton-induced reaction at low energies. 5.08 cm diameter × 5.08 cm long NE213 scintillators were employed with pulse-shape-discrimination technique for separation of neutron and γ-ray events. The neutron and γ-ray events were analyzed by a time-of-flight (TOF) technique and an unfolding technique, respectively. The measured TTYs were compared with calculation results on the basis of the several nuclear data libraries and physical models.

1. Introduction

Nuclear data on proton-induced neutron and γ-ray production in the energy range from 10 to 20 MeV is important to execute the shielding design and to estimate activation of low-energy accelerator facilities such as medical-purpose accelerators for production of radiopharmaceuticals in positron emission tomography (PET) and a neutron source of boron neutron capture therapy (BNCT). The energy and angular distribution of neutrons produced though interactions between incident protons and accelerator components should be estimated for radiation safety as well as clearance of the facility. However, the experimental data on the energy and angular distribution for production of neutrons as well as γ-rays are very scarce especially for proton energies from 10 to 20 MeV[1)]. So far, estimation of shielding and activation of such facilities was performed using nuclear data libraries and calculation codes such as PHITS[2)], LA150 and MCNPX[3)]. The accuracy of the codes and nuclear data library for such a low energy region should be checked by experimental data, because most of physical models for proton-induced reactions implemented in the codes were developed to describe reactions of high-energy particles. In this paper, we describe the systematic measurements of neutron and γ-ray energy spectra from various targets (^{9}Be, ^{nat}C, ^{27}Al, ^{nat}Cu, ^{181}Ta and $^{18}H_2O$) induced by 18 MeV protons, and comparisons between the experimental data and calculation results.

2. Experiment

The experiment were carried out using the AVF cyclotron (K=110) at the Takasaki Ion Accelerators for Advanced Radiation Application (TIARA) facility of Japan Atomic Energy Agency (JAEA). A schematic view of the experimental apparatus is illustrated in Fig.1. A proton beam accelerated by the cyclotron was transported to HB-1 beam line, which is equipped with a 60-cm diameter vacuum chamber. Neutron detectors were set at nine laboratory angles (0, 15, 30, 45, 60, 75, 90, 120, and 150°) with distances of 2.0 – 4.0 m from the target. The beam transported to the target was thinned to lower the beam frequency with a beam chopper in order to obtain TOF spectra down to a lower energy region by avoiding frame-overlap in the time-of-flight spectrum. In the present experiment, the beam chopper was operated at 1/7 and the beam frequency was 20.1 MHz. A detailed description of the target room is given in ref. 4.

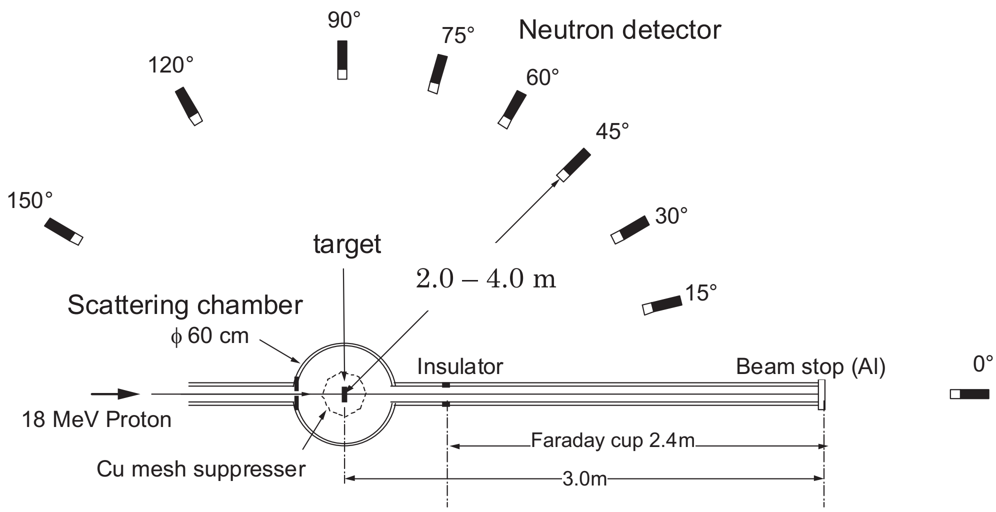

Fig. 1. Illustration of experimental setup at the HB-1 course in TIARA (horizontal view)

The thicknesses of targets (2.8 mm, 2.8 mm, 3.0 mm, 2.8 mm and 6 mm for ^{9}Be, ^{nat}C, ^{27}Al, ^{nat}Cu, ^{181}Ta and $^{18}H_2O$, respectively) were determined to be thicker than the full-stop thickness for 18 MeV proton incidence using the SRIM code[5]. The targets were set on a remote-controlled target holder together with a beam viewer and a blank target in the vacuum chamber. The target holder was insulated from the ground and served as a Faraday cup to read the beam current. The beam spot and current was also checked with the beam viewer and blank target, which protons passed through, by reading the beam current at a beam stop.

Neutrons and γ-rays emitted from the target were detected with organic liquid scintillators (5.08-cm-diameter × 5.08-cm-thick NE213) equipped with an electric circuit for pulse-shape discriminations (PSD) and time-of-flight (TOF) measurements[4)]. The beam current was measured using a current integrator connected to the target. These digital data were collected with the CAMAC system event by event using the Kakuken on-line data acquisition system (KODAQ) for off-line analysis[6)].

3. Data analysis

Neutron TOF spectra were obtained by gating the events with the two light output data (total component and slow component) on the two-dimensional graphical plots after removing random background events. The pulse height distribution of the light output was calibrated with γ-rays from a ^{241}Am-Be, ^{60}Co, and ^{137}Cs source with energies of 4.43 MeV, 1.173 and 1.333 MeV, and 0.662 MeV, respectively. The detector bias was set at 1.3 MeV for neutrons. The TOF spectra were converted into neutron energy spectra, according to the Lorentz conversion[5)]. The energy spectrum data were normalized by dividing with the detector solid angle, an integrated charge of the incident beam. The detection efficiency was calculated using the Monte Carlo code SCINFUL-R[7)].

Experimental uncertainties were estimated on the basis of systematic error propagation. Statistical uncertainties were generally below 10% but increased to above 10% at the highest energy. The uncertainty of detector efficiency with the SCINFUL-R code was estimated to be 5%[8)]. The uncertainties of beam current measurements were estimated to be 5%.

The energy spectrum of prompt γ-rays was measured with the same NE213 scintillator of 5.08 cm thickness and diameter. After discriminating the γ-ray events from those of neutrons by the PSD method, the energy spectrum of γ-rays emitted within 50 ns around the prompt γ-ray peak was obtained with the unfolding technique using the FERDOU code[8)]. The response functions of γ-rays for the incident energies up to 20 MeV were calculated by applying the EGS4 code[9)].

3. Results

The TTYs of neutrons obtained from various targets for each emission angle are shown in Figs.2, 3, 4, 5, 6, and 7 with the corresponding calculation results obtained with MCNPX ver. 2.5. The energy spectra covered from 1.5 MeV up to 16 MeV. The highest energy was consistent with each reaction Q-value, e.g. (-2.44 MeV) of the ^{18}O(p,n)^{18}F reaction. The

MCNPX calculation was performed based on the nuclear data libraries of LA150, TENDLE-2009[10], and the implemental models, an intranuclear cascade model (Bertini[11]) and an evaporation model (Dresner[12]). The calculation results generally reproduce the measured energy spectra, considering that these models are initially intended for use in the high-energy nuclear reaction with energies above 100 MeV.

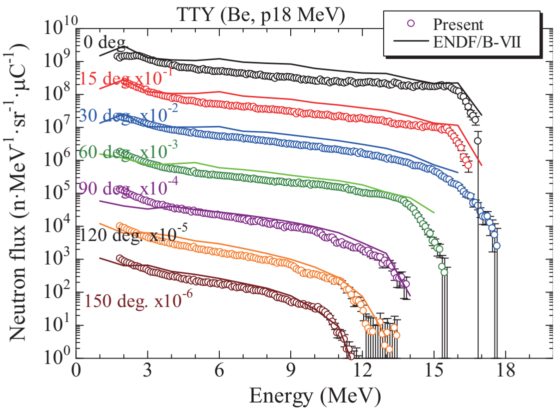

Fig.2 TTY of neutrons from p-Be reaction

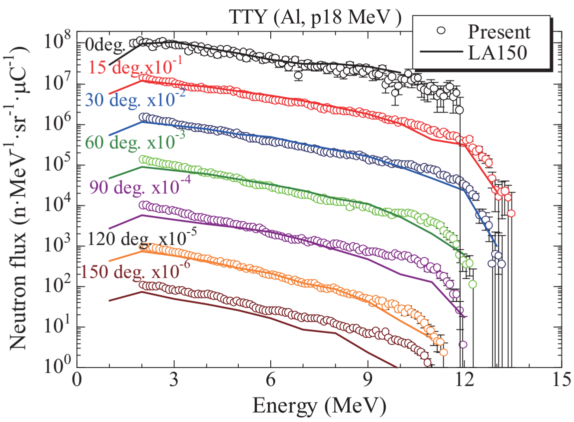

Fig.3 TTY of neutrons from p-Al reaction

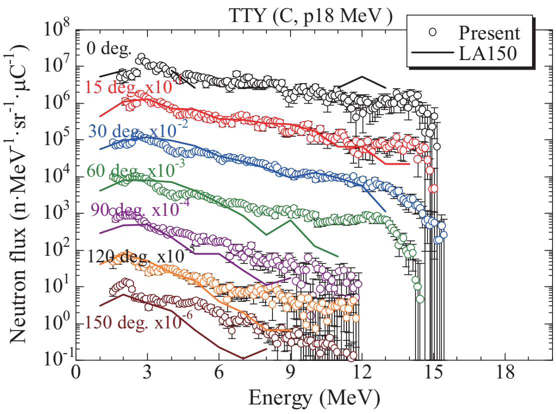

Fig.4 TTY of neutrons from p-C reaction

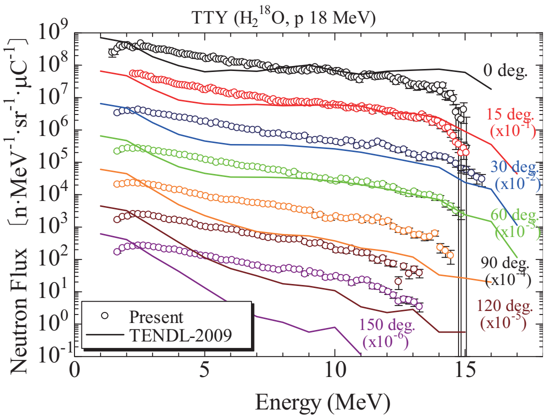

Fig.5 TTY of neutrons from p-$H_2{}^{18}O$ reaction

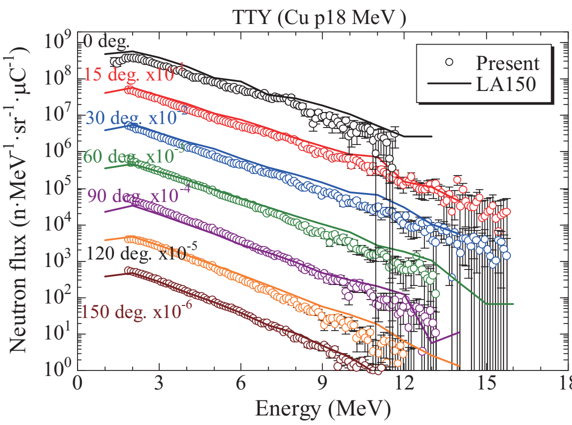

Fig.6 TTY of neutrons from p-Cu reaction

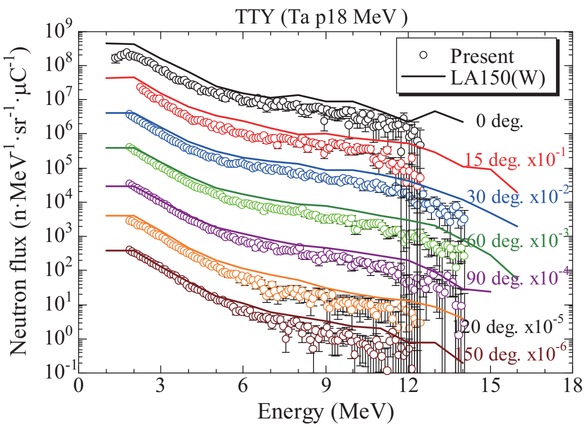

Fig.7 TTY of neutrons from p-Ta reaction

Figures 8, 9, 10, 11, 12 and 13 provide a comparison of the γ-ray spectrum at 15 degree for the various targets bombarded by 18 MeV protons with calculated results by MCNPX. The calculation result generally well reproduces the measured energy spectra except for the some peaks shown in the measured results.

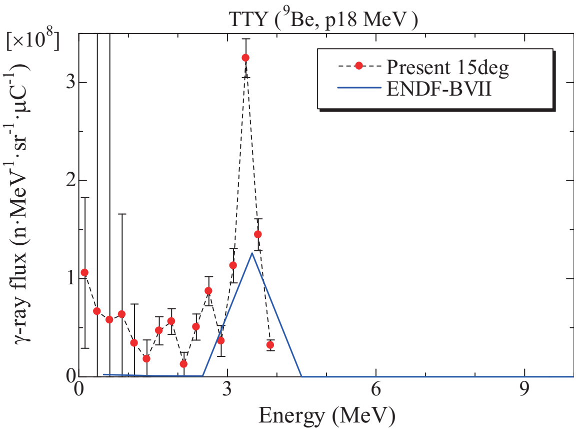

Fig.8 TTY of γ-rays from p-Be reaction

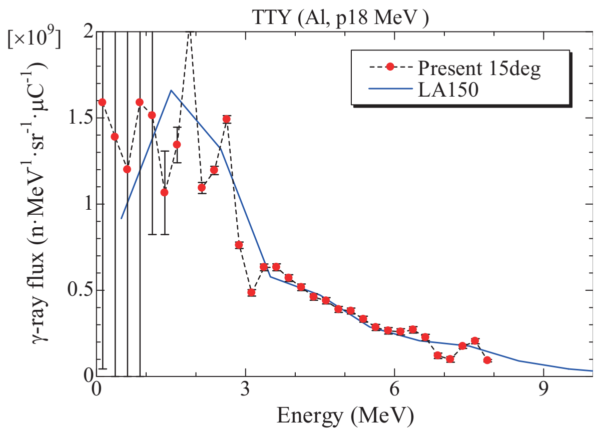

Fig.9 TTY of γ-rays from p-Al reaction

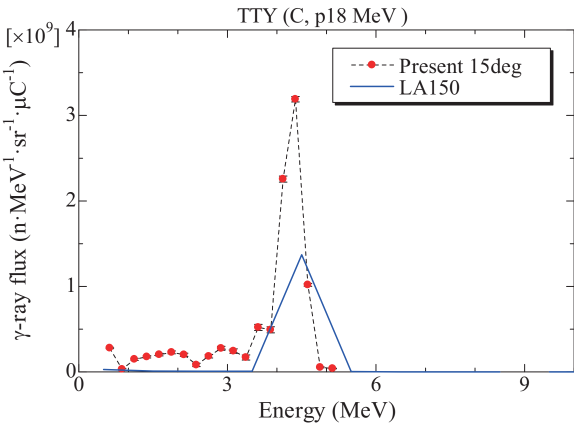

Fig.10 TTY of γ-rays from p-C reaction

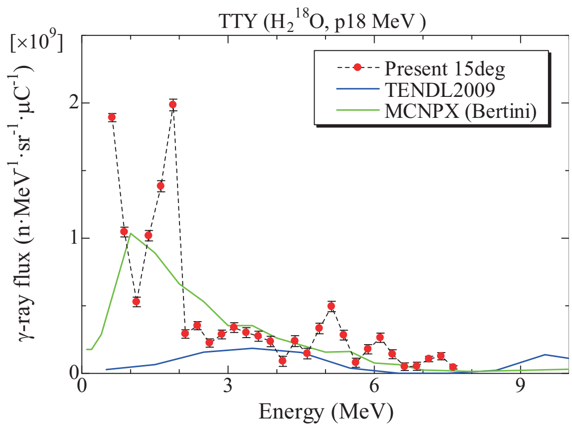

Fig.11 TTY of γ-rays from p-$H_2{}^{18}O$ reaction

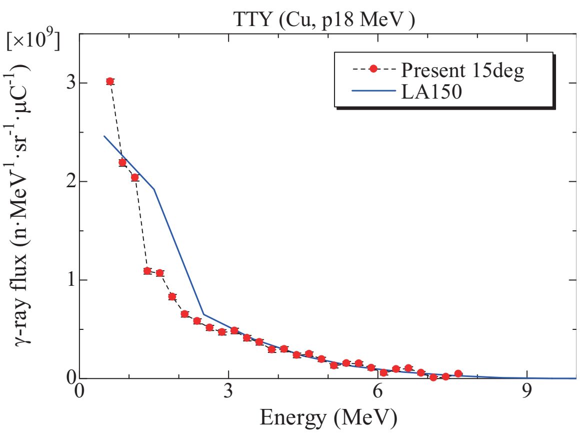

Fig.12 TTY of γ-rays from p-Cu reaction

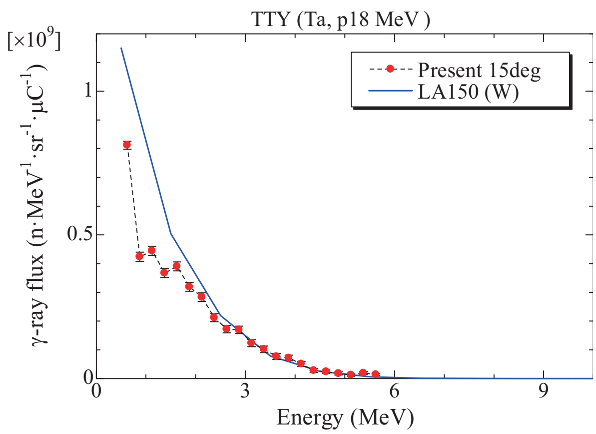

Fig.13 TTY of γ-rays from p-Ta reaction

4. Summary

We measured double-differential TTYs of neutrons and γ-rays from various thick targets at nine laboratory angles (0, 15, 30, 45, 60, 75, 90, 120, and 150°). The incident beam was 18 MeV protons and fully stopped in the target. The experimental TTY data were obtained at energies above 1.5 MeV for neutrons and 0.6 MeV for γ-rays. The TTY spectra have high-energy neutrons up to 16 MeV. The measured energy and angular distributions were compared with calculations by the MCNPX based on the LA150, TENDL-2009, and Bertini + Dressner model. For the neutron energy distributions, the calculated results agreed fairly well with the experimental data, except some spectra at backward directions. The MCNPX calculation of γ-ray spectrum result generally well reproduces the measured energy spectra except for the some peaks shown in the measured results.

REFERENCES

[1] R. Méndez, M. P. Iñiguez, J. M. Martí-Climent, I. Peñuelas, H. R. Vega-Carrillo and R. Barquero, *Phys. Med. Biol.*, **50**, 5141-5152 (2005).

[2] K. Niita, N. Matsuda, Y. Iwamoto, H. Iwase, T. Sato, H. Nakashima, Y. Sakamoto and L. Sihver, JAEA-Data/Code 2010-022 (2010).

[3] M. B. Chadwick, P. G. Young, S. Chiba, S. C. Frankle, G. M. Hale, H. G. Hughes, A. J. Koning, R. C. Little, R. E. MacFarlane, R. E. Prael, and L. S. Waters, *Nucl. Sci. Eng.*, **131**, 293 (1999).

[4] Y. Iwamoto, Y. Sakamoto, N. Matsuda, Y. Nakane, K. Ochiai, H. Kaneko, K. Niita, T. Shibata and H. Nakashima, *Nucl. Instr. and Meth. A*, **598**, 687-695 (2009).

[5] J. F. Ziegler, J. P, Biersack, U. Littmark, *The Stopping and Range of Ions in Solids* Pergamon Press, New York (1984).

[6] K.Omata and Y.Hujita, INS-Rep-884, Institute for Nuclear Study, University of Tokyo, 1991.

[7] S. Meigo, *Nucl. Instrum. Methods in Physics Research* **A 401** 365 (1997)

[8] K. Shin, Y. Uwamino and T. Hyodo, *Nucl. Technol.*, **53** (1981) 78.

[9] W.Nelson, H.Hirayama, D.W.O.Rogers, "The EGS4 Code System" SLAC-265, Stanford University, Stanford (1985).

[10] A.J. Koning, D. Rochman, TENDL-2009: consistent TALYS-based Evaluated Nuclear Data Library including covariance data, OECD/NEA JEF/DOC-1310, November 2009, http://www.talys.eu/tendl-2009.

[11] H. W. Bertini, *Phys. Rev.*, **188**, 1711 (1969)

[12] L. Dresner, ORNL-TM-196, Oak Ridge National Laboratory (1962).

22. Production of light charged particles from silicon bombarded by 175 MeV quasi mono-energetic neutrons

Shusuke HIRAYAMA[1], Yukinobu WATANABE[1], Yuuki NAITOU[1], Pernilla ANDERSSON[2], Riccardo BEVILACQUA[2], Cecilia GUSTAVSSON[2], Anders HJALMARSSON[3], Michael ÖSTERLUND[2], Stephan POMP[2], Alexander PROKOFIEV[3], Vasily SIMUTKIN[2], Henrik SJÖSTRAND[2], Milan TESINSKY[4], Udomrat TIPPAWAN[5] and Satoshi KUNIEDA[6]

[1]*Department of Advanced Energy Engineering Science, Kyushu University, Kasuga, Fukuoka 816-8580, Japan*
[2]*Department of Physics and Astronomy, Uppsala University, Box 516, SE-751 20 Uppsala, Sweden*
[3]*The Svedberg Laboratory, Uppsala University, Box 533, SE-751 21 Uppsala, Sweden*
[4]*Department of Nuclear and Reactor Physics, Royal Institute of Technology, 106 91 Stockholm, Sweden*
[5]*Plasma and Beam Physics Research Facility, P.O.Box 217, 50200, Thailand*
[6]*Nuclear Data Center, Japan Atomic Energy Agency, Tokai, Ibaraki 319-1195, Japan*
Email: hirayama@aees.kyushu-u.ac.jp

We have measured double differential cross sections of protons and alphas produced from silicon induced by 175 MeV quasi mono-energetic neutrons using the Medley setup at the TSL neutron beam facility in Uppsala University. The measured data are analyzed using the exciton model incorporating the Iwamoto-Harada-Sato (IHS) coalescence model, with particular attention to the energy dependence of the pick-up radius parameter ΔR in the IHS model.

1. Introduction

Recently, single event effects (SEEs) caused by cosmic-ray neutrons in logic and memory circuits have been recognized as a key reliability concern for modern microelectronic devices. When electronic memory circuits are exposed to neutron radiation, secondary ions are produced by nuclear interaction with atomic nuclei in materials. The released charge can cause a flip of the memory information in a bit, which is called a single-event upset (SEU). Recent work has elucidated that the contribution from secondary light ions (i.e., p, d, t, ^{3}He and α) to SEU becomes increasingly important as the size of microelectronic devices becomes smaller and smaller [1,2]. Therefore, reliable nuclear data for neutron-induced light ion production over a wide incident energy range are strongly required to simulate accurately the SEEs including SEU. However, there is no measurement for silicon target in the energy range of more than 100 MeV.

In the present work, we have measured double-differential production cross section of p, d, t, ^{3}He, and α from silicon bombarded by 175 MeV quasi mono-energetic neutrons. The experimental data are compared with the exciton model calculations in which we use the surface coalescence model proposed by Iwamoto, Harada, and Sato [3]. The results of proton and alpha production are reported in this paper.

2. Experimental method

Details of the experimental set up have been reported in Refs.[4,5]. A thin silicon target placed in the Medley chamber was irradiated by quasi mono-energetic neutrons generated by the ^{7}Li(p,n)^{7}Be reaction. The target consisted of double silicon wafer discs and its size was 0.96mm thick and 25 mm in diameter. Energy and angular distributions of light-ions produced from the silicon target were measured with the Medley setup. The Medley setup was composed of eight telescopes placed at angles from 20° to 160° in steps of 20°. Each telescope consisted of two silicon surface barrier detectors (50~60 μm and 1000 μm) as the ΔE detector and a CsI(Tl) detector as the E detector. Moreover, the incident neutron spectrum was measured using the same setup with both 5mm-thick polyethylene (CH_2) target 25mm in diameter and

1mm-thick carbon target 22mm in diameter by means of a conventional proton recoil method. The $^{7}Li(p,n)^{7}Be$ reaction produced peak neutrons and low-energy tail neutrons. Time-of-flight (TOF) measurements were used in the off-line analysis in order to reduce the contribution of low-energy tail neutron in the accepted incident neutron spectrum.

3. Data analysis

Data analysis procedure based on ΔE-E particle identification technique is basically the same as in the previous measurements at 96 MeV[6-8]. Energy calibration of all detectors was made using the relation between measured pulse height and calculated energy deposition in each detector as follows. Events in the ΔE-E bands were fitted with respect to the energy deposition in the ΔE detectors, which was determined from the thickness and the energy loss calculated SRIM code[9]. A linear response is expected for silicon detectors in the measured range of energy. ΔE detectors were calibrated using the point where each charged particle starts to punch through the detectors. For the energy calibration of the E detectors, the following approximate expression was applied to protons and alpha particles, which reflects a non-linear relationship between the light output and the energy deposition in the CsI(Tl) scintillator[10]:

$$E = a + bL + c(bL)^2 \qquad \text{for hydrogen isotopes,} \qquad (1)$$

$$E = a + bL + c\ln(1 + dL) \qquad \text{for helium isotopes,} \qquad (2)$$

where L is the light output, and a, b and c are the fitting parameters. The parameter c depends on the kind of charged particles. The efficiency correction due to the reaction losses in the CsI(Tl) scintillator was implemented using the same method as reported in Ref.[11].

The incident neutron spectrum accepted by the TOF gate was obtained from the net recoil proton spectrum from np scattering in the measurement of polyethylene target. Details of deriving neutron spectrum have been reported in Ref.[8]. The obtained neutron spectrum is shown in Fig.1. After the TOF gate cut, about half of the accepted neutrons are included in the peak component around 175 MeV and the rest is composed of the low energy tail. The tail component below 70 MeV is negligibly small as shown in Fig.1.

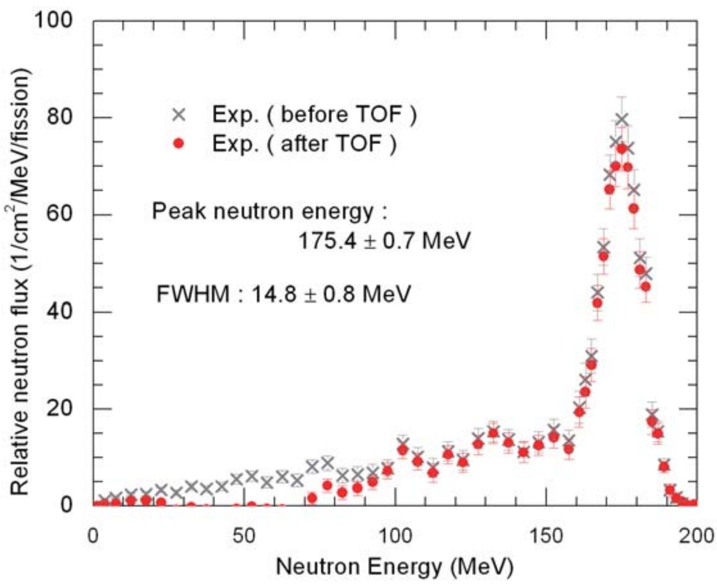

Fig.1 Accepted quasi mono-energetic neutron spectrum. Cross and solid circle are measured data, respectively before and after the TOF gate cut.

The measured double-differential cross sections for light-ion production in silicon were determined using the following expression:

$$\frac{d^2\sigma(\theta,E)}{dEd\Omega}=\frac{Y_{\mathrm{Si}}(\theta,E)}{Y_{\mathrm{H}}}\frac{N_{\mathrm{H}}}{N_{\mathrm{Si}}}\frac{\Phi_{\mathrm{CH_2}}}{\Phi_{\mathrm{Si}}}\frac{\Omega_{\mathrm{CH_2}}}{\Omega_{\mathrm{Si}}}\frac{d\sigma_{\mathrm{H}}}{d\Omega}\frac{f_{\mathrm{CH_2}}(E)}{f_{\mathrm{Si}}(E)}\frac{1}{\Delta E}, \tag{3}$$

where $Y_{\mathrm{Si}}(E,\theta)$ is the net counts in a certain energy bin ΔE at laboratory scattering angle θ for each particle, Y_{H} is the net counts in the recoil proton peak. The number of the net counts due to np scattering is obtained using measurement at 20° for both polyethylene and carbon targets. The np scattering spectrum is deduced by subtracting the contribution of C(n,xp) reaction from polyethylene measurement. The effective efficiency which includes the energy loss effect in the CsI(Tl) scintillator is $f(E)$, Φ is the relative neutron flux and N is the number of the target nuclei. The differential np scattering cross section ($d\sigma_H/d\Omega$) is taken from NN-online[12]. In Eq. (3), the solid angle $\Delta\Omega$ was given under an assumption that the target is treated as a point source. It was confirmed that this assumption is valid by a comparison of the PHITS simulation between a point source and a plane source, in which the difference is only 1%.

Thickness of the reaction target causes non-negligible effects on both energy-loss and particle-loss of generated light ions. As a consequence, the measured spectrum is distorted in the low-energy region. To correct these effects, we used the TCORR code [13] developed previously in the data analysis of light-ion production measurements with the Medley setup.

4. Theoretical analysis with the preequilibrium exciton model

The measured double-differential cross sections are analyzed using the exciton models with focus on pre-equilibrium particle emission. As mentioned in the preceding section, the experimental data contains the events from tail-neutron down to 70 MeV. Therefore, the measured spectra should be compared with the following folding spectrum:

$$\sigma^{fold}(E_n,E_i,\theta_i)=\int_{E_{lower}}^{E_{upper}}\sigma^{cal}(E_n,E_i,\theta_i)W(E_n)dE_n\ , \tag{4}$$

where E_{i} and θ_{i} are the emission energy and angle for charged particle i, $W(E_{\mathrm{n}})$ is the ratio of the number of neutrons around E_{n} to the number of peak neutrons, E_{lower} (=70MeV) is lower limits of the neutron energy selected by TOF cut, E_{upper} (=175 MeV) is the peak neutron energy, and $\sigma^{\mathrm{cal}}(E_{\mathrm{n}}, E_{\mathrm{i}}, \theta_{\mathrm{i}})$ is the calculated double-differential cross section.

The GNASH code is designed to calculate particle production cross sections from the statistical decay and pre-equilibrium processes. To take account of pick-up contributions from pre-equilibrium light-ion production, the Iwamoto-Harada-Sato (IHS) coalescence model [3] has recently been incorporated into the GNASH code [15]. The GNASH code outputs the angle-integrated emission spectra in the center of mass (c.m.) system. After that, double-differential cross sections were obtained using the Kalbach systematics [16] in order to compare them with the present measurements. The c.m.-to-lab transformation was made using the kinematics of one-particle emission.

Both transmission coefficients and inverse reaction cross sections needed for GNASH with the IHS model were calculated using optical potential parameters (OMPs). The OMPs were chosen on condition that OMPs are available up to the maximum energy of emitted particles. As a result, we used Koning and Delaroche [17] for protons and neutrons, An and Cai [18] for deuterons, Pang et al. [19] for tritons and ^{3}He particles, and Avrigeanu, Hodgson and Avrigeanu [20] for alpha particles. In the GNASH calculation, the Kalbach normalization factor was 120 MeV^3 which was determined by analysis of (n,xp) spectra for incident energies up to 96 MeV. The single-particle state density g= A/13 was used, where A is the mass number.

Some adjustable parameters are included in the IHS coalescence model. In the present analysis, we have investigated intensively the energy dependence of the ΔR parameter (i.e., the pick-up radius of surface region), which was chosen to be 1.0 fm from the analyses of (p,xα) data for energies below 70 MeV in the original paper [3]. It is also known that the Fermi energy is somewhat sensitive to the slope of pre-equilibrium energy spectrum. It was chosen to be 40 MeV from our preliminary analysis.

5. Results and discussion

Figure 2 shows experimental and calculated double-differential (n,xp) cross sections from 20° to 140° in steps of 40°. The experimental data are plotted by closed circles, showing a strong angular dependence at high emission energies above 20 MeV. The solid curves present the GNASH calculations with the IHS model. The calculations reproduce generally well the measured spectra except for 20°. The calculations underestimate the experimental data from 110 MeV to high-energy end at 20°.

In Fig.3, experimental and calculated double-differential (n,xα) cross sections are shown at 20°, 60°, 80° and 120°. The experimental data are plotted by closed circle. The dashed curves denote the calculations of the GNASH code with the IHS model with ΔR =1.0 fm. These calculations underestimate the measured spectra above 30MeV at all angles, especially at 20°.

We have paid attention to the ΔR parameter used in the IHS model to improve this underestimation. According to the recent IHS model analysis [15], ΔR was found to have the energy dependence. Therefore, the energy-dependence was investigated on the basis of the analyses of Al(p,xα) data over the wide energy range up to 200 MeV [21-24], because Al is an adjacent nucleus to Si. We have determined an optimum ΔR value for each experimental data under the condition that ΔR is less than 1.6 fm corresponding to alpha-particle's radius. As shown in Fig.4, the deduced ΔR values are nearly 1.1 fm in the incident energy range below 70 MeV [23,24] close to the original values, 1.0 fm, whereas they are more than 1.4 fm in the incident energy range above 120 MeV [21,22]. Finally the energy-dependence of the ΔR parameter was obtained by fitting each ΔR value with the Woods-Saxon function as shown by the solid curve in Fig.4. The energy-dependent ΔR starts to increase gradually from nearly 70 MeV and approaches to 1.6 fm in the energy range of more than 160 MeV. The calculations with the energy–dependent ΔR parameter are shown by the solid curves in Fig.3, reproducing the measured data better than the original calculations with ΔR=1.0 fm. This suggests that the use of the energy-dependent ΔR parameter is necessary in the IHS model calculations for incident energies above 70 MeV.

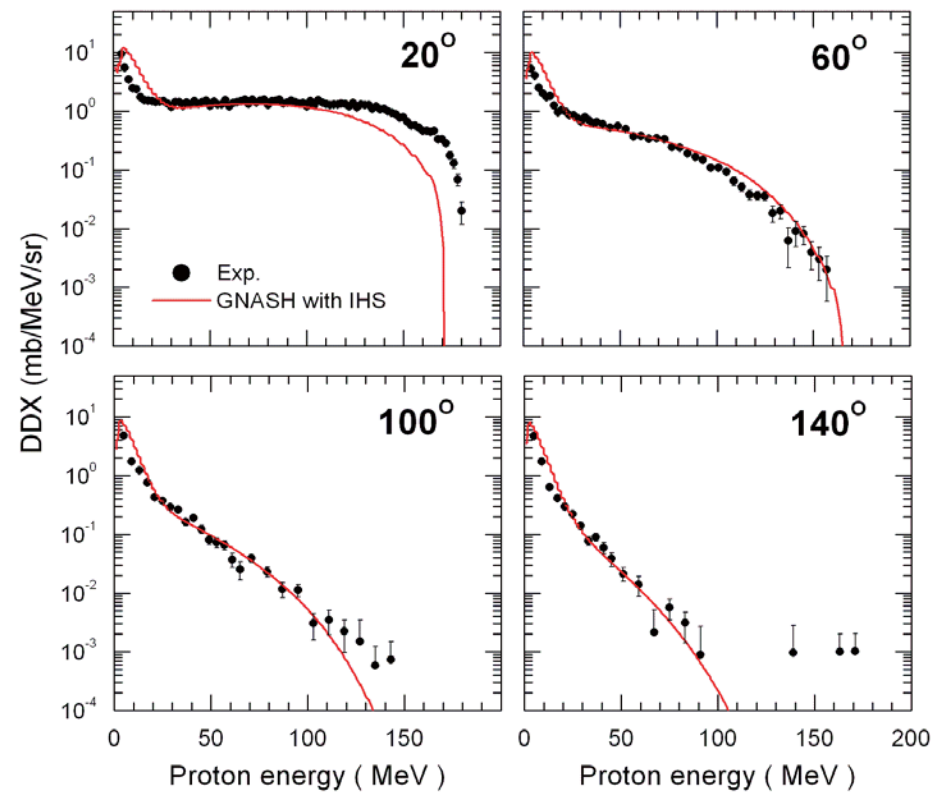

Fig. 2 Comparison between measured (n,xp) spectra from 20° to 140° in steps of 40° and calculation results of GNASH code with IHS model.

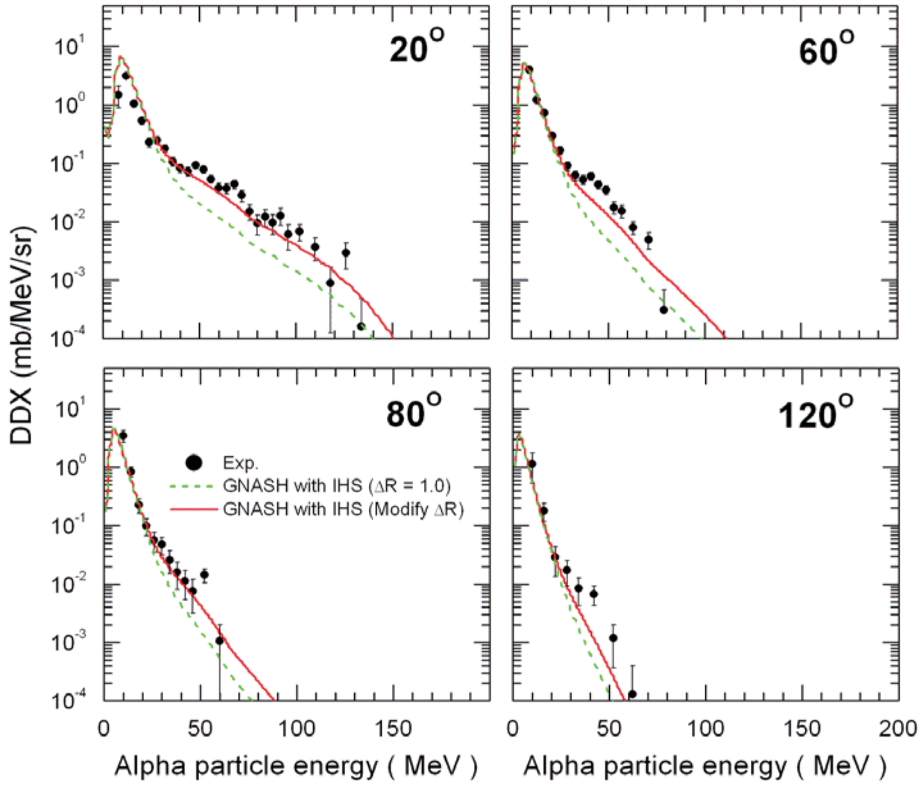

Fig. 3 Comparison between measured (n,xα) spectra at 20°, 60°, 80° and 120° and calculation results of GNASH code with IHS model. The dashed curves denote the calculation results with ΔR=1.0 fm. The solid curves present the calculation result using the energy-dependent ΔR parameter given in Fig.4.

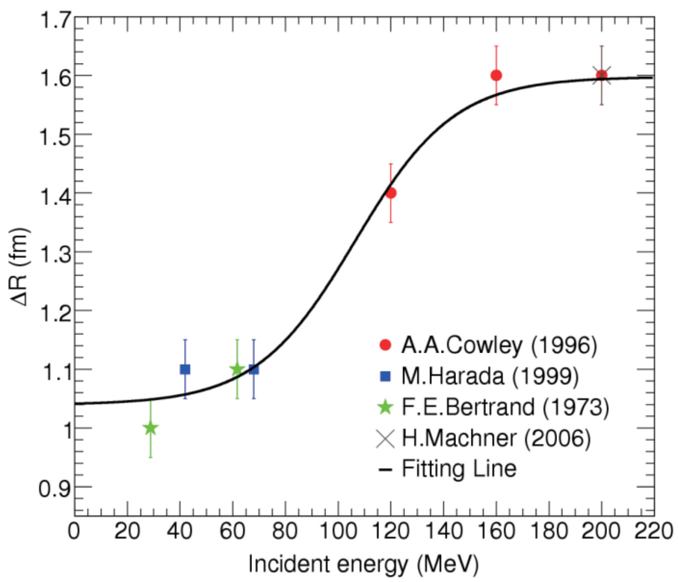

Fig. 4 Energy-dependence of ΔR parameter. Each symbol shows optimum ΔR parameter determined for each experimental data. The solid curve denotes the result of fitting with the Woods-Saxon function.

6. Summary and conclusions

The double-differential (n,xp) and (n,xα) cross sections for silicon were measured with 175 MeV quasi mono-energetic neutrons at the The Svedberg Laboratory (TSL) using the time-of-flight method. The measured cross sections were compared with the GNASH calculations to benchmark the exciton model incorporating the Iwamoto-Harada-Sato (IHS) model. For proton production, the GNASH calculation is in generally good agreement with the measurement over a wide angular range except at 20º. From our analysis of preequilibrium alpha emission over a wide incident energy range, we have found clearly the energy dependence of ΔR parameter used in the IHS model to reproduce the measured (n,xα) data.

In the future, we plan to make similar data analyses for production cross section of deuteron, triton and ^{3}He measured in the present experiment.

Acknowledgements

We would like to thank the staff of the The Svedberg Laboratory for their assistance during the experiments. U. T. expresses his gratitude to the Thailand Research Fund (TRF) for financial support under Project No.MGR5280165. This work was supported in part by the Semiconductor Technology Academic Research Center (STARC) joint research program.

References

[1] S. Abe, S. Hirayama, Y. Watanabe *et al.*, *Proc. Int. Conf. on Nuclear Data for Science and Technology*, Jeju Island, Korea, April 26-30, 2010, in press.
[2] H. Kobayashi, N. Kawamoto, J. Kase *et al.*, *Proc. the 47th IEEE Int. Reliability Physics Symposium (IRPS)*, 206-211, Montreal, Quebec, Canada, April 26-30, 2009.
[3] A. Iwamoto and K. Harada, *Phys. Rev.* **C26**, 1821 (1982).
[4] S. Pomp, A. Prokofiev, J. Blomgren *et al.*, *Proc. Int. Conf. on Nuclear Data for Science and Technology*, Santa Fe, USA, Sept. 26-Oct. 1 AIP Conf. Proc. **769**, 780-783 (2005).
[5] M. Hayashi, Y. Watanabe, R. Bebilacqua et al., *Proc. Int. Conf. on Nuclear Data for Science and Technology*, April 22-27, 2007, Nice, France, EDP Sciences, pp. 1091-1094 (2008).
[6] U. Tippawan, S. Pomp, A. Atac *et al.*, *Phys. Rev.* **C69**, 064609 (2004).
[7] R. Bevilacqua, S. Pomp, V. Simutkin et al., *Radiation Measurement* **45**, 1145-1150 (2010).
[8] S. Hirayama, Y. Watanabe, Y. Naitou et al., *Proc. Int. Conf. on Nuclear Data for Science and Technology*, Jeju Island, Korea, April 26-30, 2010, in press.
[9] SRIM-2008 , URL : http://www.srim.org/.
[10] S. Dangtip, A. Atac, B. Bergenwall *et al.*, *Nucl. Instr. Meth.* **A452**, 484-504 (2000).
[11] S. Hirayama, Y. Watanabe, Y. Naitou et al., *Proc. of the Fifth Int. Symp. on Radiation Safety and Detection Technology ISORD-5,* July 15-17, 2009, Kitakyushu, Japan, in press
[12] SAID Nucleon Nucleon scattering database. URL: http://gwdac.phys.gwu.edu.
[13] S. Pomp and U. Tippawan, *Nucl. Instrum. Methods Phys. Res.* **A572**, 893 (2007).
[14] P. G. Young, E. D. Arthur, M. B. Chadwick, Los Alamos National Laboratory Report No LA-12343-MS (1992)
[15] S. Kunieda, S.Hirayama, T.Fukahori et al., *Proc. Int. Conf. on Nuclear Data for Science and Technology*, Jeju Island, Korea, April 26-30, 2010, in press.
[16] C. Kalbach, *Phys. Rev.* **C37**, 2350 (1988).
[17] A. J. Koning and J. P. Delaroche, *Nucl. Phys.* **A713**, 231 (2003).
[18] H. An and C. Cai, *Phys. Rev.* **C73**, 054605 (2006).
[19] D. Y. Pang, P. Roussel-Chomaz, H. Savajols et al., *Phys. Rev..* **C79**, 024615 (2009).
[20] V.Avrigeanu, P. E. Hodgson and M. Avrigeanu, *Phys.Rev.* **C49**, 2136 (1996).
[21] H. Machner, D. G. Aschman, K. Baruth-Ram et al., *Phys. Rev.* **C73**, 044606 (2006).
[22] A. A. Cowley, G. J. Arendse, J. W. Koen, *Phys. Rev.* **C54**, 778-783 (1996).
[23] M. Harada, Y. Watanabe, A. Yamamoto et al., *J. Nucl. Sci. and Technol. Suppl*. **1**, 687-691 (2000).
[24] F. E. Bertrand and R. W. Peelle, ORNL report ORNL-4799, (1973); *Phys. Rev.* **C8**, 1045 (1973).

23. Measurement of deuteron-production double differential cross sections by 290 MeV/u oxygen beams on C, Al and Cu targets at forward angles

Kazuya TAHARA, Yohei FUKUDA, Shiro NINO, Yuki YANAGITA,
Genichiro WAKABAYASHI, Yusuke UOZUMI
Department of Applied Quantum Physics and Nuclear Engineering, Faculty of Engineering, Kyushu University
744 Motooka, Nishi-ku, Fukuoka 819-0395
e-mail: tahara-k@nucl.kyushu-u.ac.jp
Yusuke KOBA, Naruhiro MATSUFUJI
National Institute of Radiological Sciences, 4-9-1 Anagawa, Inage-ku, Chiba 263-8555

We measured deuteron-production double differential cross sections (DDXs) by 290 MeV/u oxygen beams on carbon, aluminium and copper targets at forward angles. The deuteron energies were measured with the spectrometer which consisted of GSO(Ce) crystals and plastic scintillators. The measured DDXs were compared with the calculated ones with PHITS code. The simulation results generally agreed with the measured ones. The measured results will be useful as the benchmark of existing simulation codes and for the future improvements.

1. Introduction

Recently, heavy ion induced reactions are of great interest in the field of medicine and engineering. Light fragments such as hydrogen and helium produced from the reactions are especially important in the treatment planning of cancer therapy, the design calculation of heavy ion accelerator facilities and the dose estimation for manned space flights due to their long ranges in human bodies or constructional materials. Therefore the nuclear data on light fragments are eagerly needed.

In addition, it has been known that there are differences between measured results and simulated ones with existing calculation codes such as PHITS code [1]. For this reason, the experimentally measured nuclear data will be useful as the benchmark of existing simulation codes and for the future improvements.

In the present study, the double differential cross sections (DDXs) on deuteron production reactions are investigated for oxygen incidence upon carbon, aluminium and copper targets at forward angles. The measured DDXs were compared with the calculated ones by PHITS code.

2. Experimental set up

The experiments were carried out at the heavy ion accelerator facility HIMAC (Heavy Ion Medical Accelerator in Chiba) of the National Institute of Radiological Sciences in Japan. Fig. 1 shows the experimental setup. Oxygen beams were accelerated by a ring synchrotron up to 290 MeV/u and bombarded the targets. The thicknesses of carbon, aluminium and copper targets were 4 mm. A thin plastic scintillator (beam monitor) was placed upstream of the target in order to measure the number of incident oxygen ions. The size of the plastic scintillator was 1 mm thick and 150 mm × 150 mm square. The active collimator is a plastic scintillator of 10 mm thick and 40 mm × 40 mm square with a circular aperture of 15 mm in diameter at the centre. The diameter of the aperture defined the solid angle of the measurement.

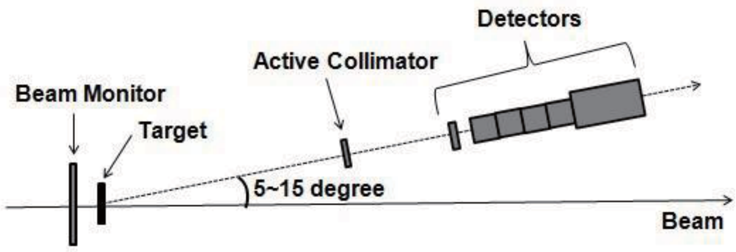

Fig.1. Schematic experimental arrangement

The deuterons emitted from the nuclear reactions in the targets were detected by stacked scintillator spectrometer placed at 5, 10 and 15 degrees relative to the beam line. The flight path between the target and detectors was 600 mm at 5 degrees, and it was 325 mm at 10 and 15 degrees.

Fig. 2 shows the configuration of the spectrometer. The spectrometer were in principle a ΔE-E counter telescope consisting of a plastic scintillator, four cubic GSO(Ce) crystals and a cylindrical GSO(Ce) crystal. The plastic scintillator was 10 mm thick and served as ΔE detector. The cubic crystals had 43 mm edge length. The cylindrical crystal was 60 mm in diameter and 120 mm in length. Photomultiplier tubes (PMTs) viewed one faces of the plastic scintillator and GSO(Ce) crystals.

Fig.2. Schematic drawing of the stacked scintillator spectrometer used in our measurements

Signals were processed in a standard electronic setup of NIM modules, such as discriminators and coincidence circuitry. The output charges from PMTs were digitized with CAMAC ADC and the digital data were recorded event-by-event on the hard disk of a PC for subsequent off-line analyses.

We also measured background events using an empty target frame for the following two reasons. One reason is due to beam halo which could distort energy distributions, the other is to eliminate the events caused by nuclear reactions in the beam monitor.

3. Off-line analysis

Double differential cross sections were determined through off-line analysis. The recorded pulse heights of signals were converted into particle energy using the Bethe-Bloch equation [2] and Birks equation [3] taking into account the nonlinearity between light output and energy deposition. Particle identification was carried out by using PI technique [4]. The particle identification quantity, PI, is given by,

$$PI = E_{total}^{b} - \left(E_{total} - \Delta E\right)^{b} \qquad (1)$$

where E_{total} is the total energy deposited in the spectrometer, the ΔE is the amount of energy deposited in the transmission detector and b is the parameter whose value was employed to be 1.73 to obtain best separation. Fig. 3 shows the example of a two-dimensional plot of PI versus particle energy for the oxygen induced reactions on the carbon target at 5 degrees. The thick belt lying at around PI = 200 corresponds to proton good events, which stopped in the crystal through the electronic interaction. On the other hand, the belt lying at around PI = 300 corresponds to deuteron events.

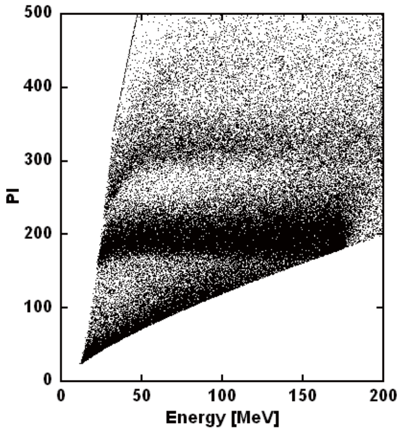

Fig.3. Two-dimensional plot of PI versus particle energy for the oxygen induced reactions on the carbon target at 5 degrees.

In the present work, DDXs were obtained by the following equation,

$$DDX = \frac{Y}{N_b \times N_t \times E_d \times \Omega \times \varepsilon_p \times \varepsilon_D} \qquad (2)$$

where Y is the number of deuterons per energy bin, N_b is the number of incident particles on a target, N_t is the number of atomic nuclei in the target, E_d is the width of an energy bin, Ω is a solid angle, ε_p is the peak efficiency, and ε_D is the efficiency of data acquisition system. The value of Y was obtained by the following way. First, PI projection spectrum was generated for each energy bin of 20 MeV width from the two-dimensional plot of PI versus energy. Fig. 4 shows the example of PI projection spectrum in the energy bin of 70-90 MeV for the oxygen induced reactions on the carbon target at 5 degrees. As is shown in Fig. 3, the peak around PI = 300 corresponds to deuteron events. The deuteron yield Y was obtained by fitting the histogram of deuteron events with a Gaussian function.

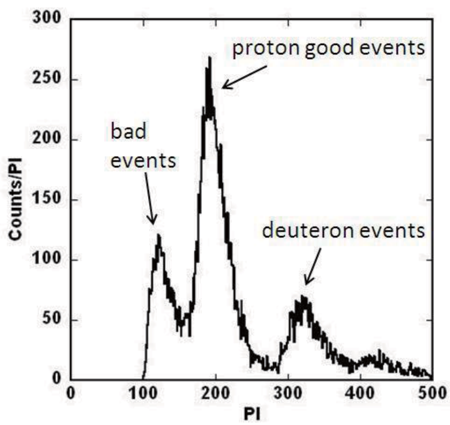

Fig.4. PI projection spectrum in the energy bin of 70-90 MeV for the oxygen induced reactions on the carbon target at 5 degrees.

4. Results and discussion

The double differential cross sections obtained in our study are shown in Figs. 5, 6 and 7 for carbon, aluminium and copper targets, respectively. The error bars in the figures only show statistical uncertainties. In each figure, the measured DDXs are shown together with calculated ones by PHITS code.

In Fig. 5, the simulated results on carbon target generally agreed with the measured ones at 10 and 15 degrees. The overestimations by PHITS code calculation were observed in the energy region over 400 MeV at 5 degrees.

As is shown in Fig. 6 and Fig. 7, the result on aluminium and copper targets are similar to the result on carbon target. The overestimation by PHITS code calculation was observed in the energy region over 400 MeV at 5 degrees.

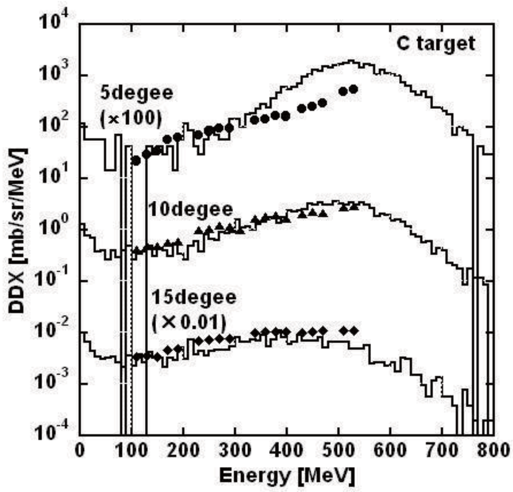

Fig. 5. Deuteron production DDXs for 290 MeV/u oxygen incidence on carbon target, together with the PHITS code calculations (solid lines).

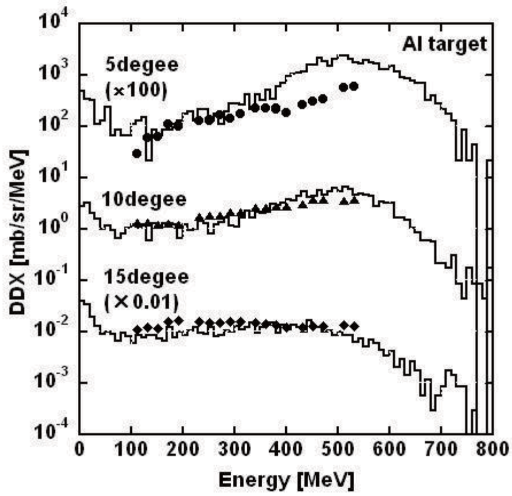

Fig. 6. Deuteron production DDXs for 290 MeV/u oxygen incidence on aluminium target, together with the PHITS code calculations (solid lines).

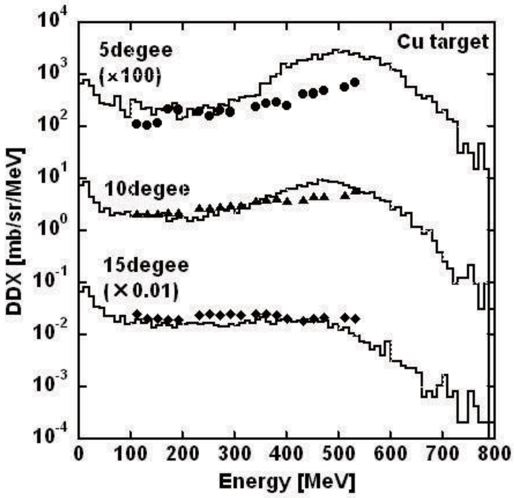

Fig. 7. Deuteron production DDXs for 290 MeV/u oxygen incidence on copper target, together with the PHITS code calculations (solid lines).

5. Conclusion

In this study, the DDXs on deuteron production reactions are investigated for oxygen incidence upon carbon, aluminium and copper targets using the GSO(Ce) scintilator spectrometer. As results, the DDXs were obtained in energy region from 100 MeV to 540 MeV at forward angles of 5, 10 and 15 degrees. The measured DDXs were compared with the calculated ones by PHITS code. The simulated results generally agreed with the measured ones but discrepancies were observed in the energy region over 400 MeV at 5 degree. The experimental data will be useful as the benchmark of existing simulation codes and for the future improvements of simulation codes.

Acknowledgements

The experiment was carried out under the Research Project with Heavy Ions at NIRS-HIMAC. This work was partially supported by the Ministry of Education, Science, Sports and Culture, Grant-in-Aid for Young Scientists.

References

[1] K. Niita, et al., Phys. Rev., C52, 2620 (1995)
[2] F.L.R. Vinagre, C.A.N. Conde, Nucl. Instrum. Meth, A450, 365 (2000)
[3] Birks J.B, " The Theory and Practice of Scintillation Counting" , Pergamon Press 456 (1964)
[4] M. Makino, R. Eisberg, D. Ingham, and C. Waddell, Nucl. Instrum. Meth. 81, 125 (1970)

24. Study of the BGO detector for the measurement of the double differential cross sections of cluster production reactions

Aleksandre MZHAVIA*, Yuki YANAGITA*, Masahiko UEYAMA*, Naoto Nakamura*, Yusuke UOZUMI*, Genichiro WAKABAYASHI*, Yusuke KOBA** and Masashi TAKADA**

* Department of Applied Quantum Physics and Nuclear Engineering

Kyushu University, 744, Motooka, Nishi-ku, Fukuoka 819-0395, Japan

e-mail: mzhavia@nucl.kyushu-u.ac.jp

** National Institute of Radiological Sciences

The accelerator driven system (ADS) has been recognized as one of most attractive options for the nuclear transmutation of the high level nuclear waste. We may expect ADS to dramatically reduce the hazard level of the nuclear waste and to operate as the energy generator. To realize ADS, it is necessary to conduct a number of fundamental researches and technical developments in the various areas. Double differential cross section (DDX) data of nucleon-actinide reactions is of the high importance for the nuclear waste transmutation facilitated by the ADS.

1. Introduction

In order to obtain high-quality nuclear data of DDX (Double Differential Cross Sections), it is necessary to use a detector that offers the moderate energy resolution of a few percent and a wide energy acceptance covering from almost zero up to the maximum emission energy. Moreover, detection efficiency should be high enough for the usage of a thin target. A crystal array detector is the most suitable one under these conditions and the only solution above 100 MeV.

A new crystal array detector has been proposed for conducting the charged particle cross section measurements with the actinide targets for a study of accelerator transmutation of nuclear waste. The detector enables both the Time-of-Flight and the Pulse-Height measurements in an energy range from 10 MeV to 600 MeV. Since the detector is planned to cover secondary particles from protons to ^{4}He, in the present research we investigated characteristics of BGO crystals in terms of the light output and the peak efficiency for charged particle bombardments.

2. Crystal array detector, light output experiments

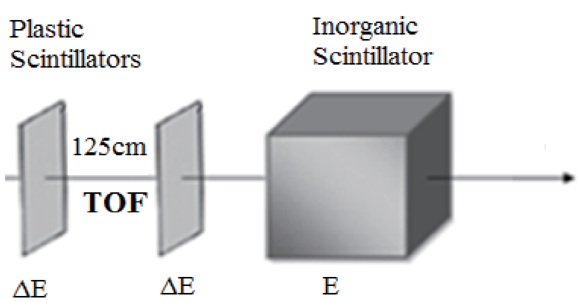

Fig.1. The detector concept schematic.

The new detector system enables nuclear data measurement in a 600-MeV range. It utilizes both the Pulse Height and TOF in proton measurements. The detector concept is illustrated briefly in the Fig.1, it consists from two sections; one is a crystal detector based on the ordinal ΔE-E method, and the other the TOF section following the crystal. The detector proposed presently is expected to offer the best characteristics in fulfilling the required specifications, such as energy resolution and the energy acceptance.

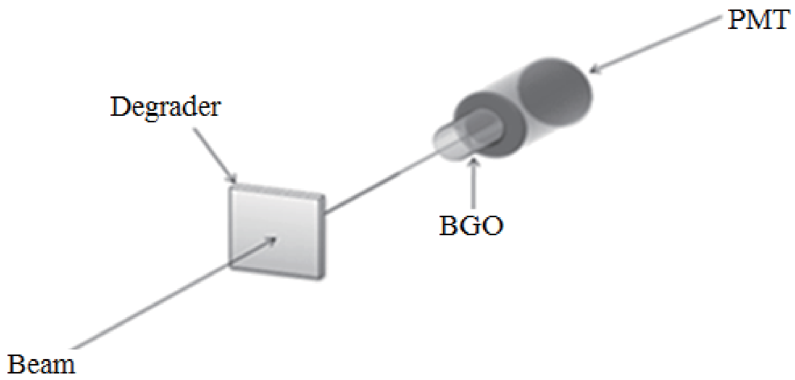

Fig.2. Our experimental setup.

We used the setup [Fig.2.] for the BGO light output measurement for Proton and Alpha particles. In this case the beam energy is changed using a degrader. The light output response of a BGO crystal was measured using Proton and ^{4}He ions of energy ranges from 25 MeV up to 100 MeV. Experiments were made at the cyclotron facility National Institute of Radiological Sciences (NIRS), Japan. The energy dependence is found to be interpreted well by the Birks equation [1], consistent with the presented data from Ref. [2].

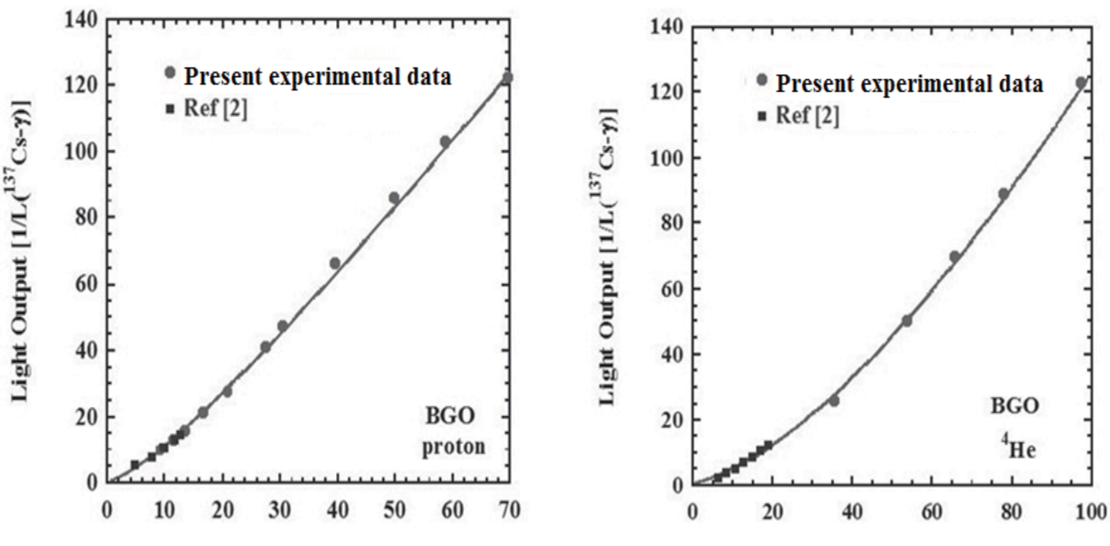

Fig.3. Light output response of BGO to proton (left) and ^{4}He (right).

3. Peak efficiency calculation

The peak efficiency of the BGO detector, which is required for the accurate determination of the DDX (Double Differential Cross Sections), was also investigated in terms of nuclear reactions and multiple Coulomb scattering.

Since the yield obtained from the experiments is less than the incident on the detector, the Peak efficiency needs to be corrected; the yield obtained from the experiments is divided on true (total) yield:

$$\frac{N_{Peak}}{N_{Total}} = P, \qquad (1)$$

Were N_{Peak} is the Yield obtained from the experiments and the N_{Total} is the true yield.

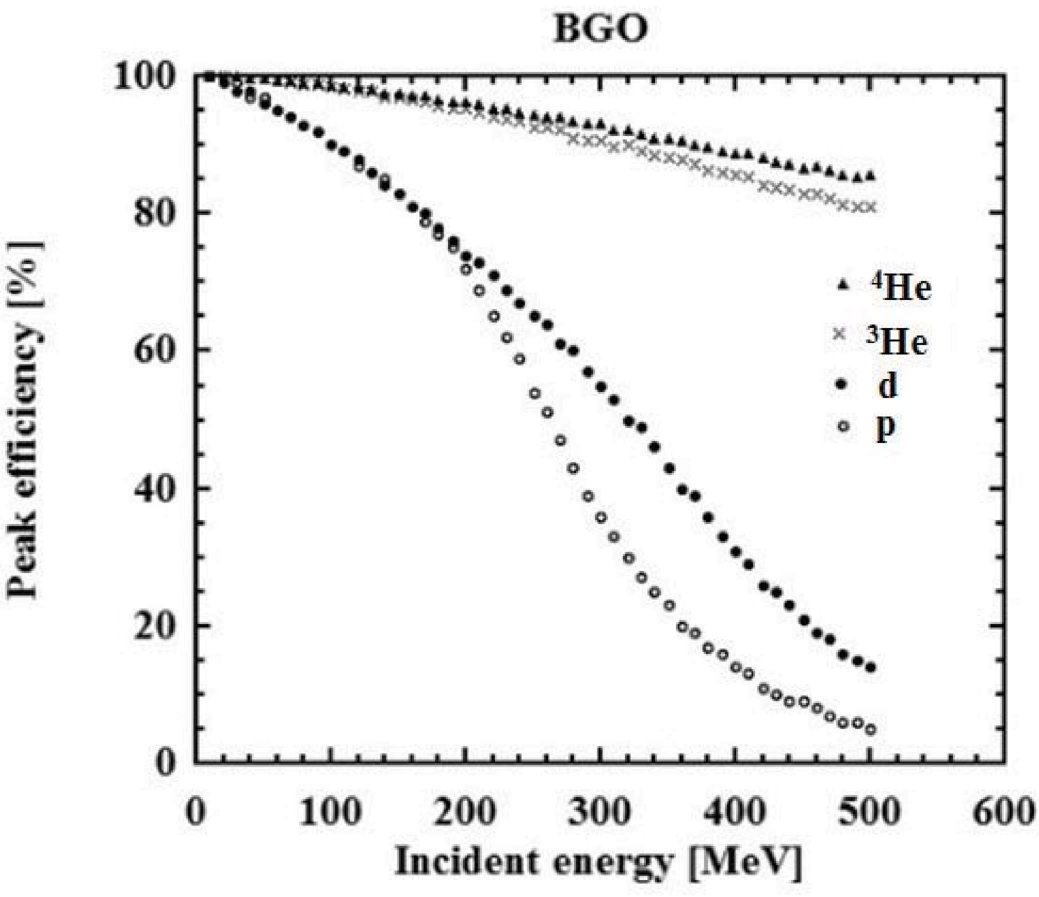

Fig. 4. Peak efficiency of the BGO detector.

In Fig. 4 are shown the peak efficiency curves of a BGO crystal to charged particles as the function of particle energy. They were calculated by a Monte Carlo procedure, which takes multiple coulomb scattering and nuclear reactions into consideration.

4. Off line data analysis

Double differential cross sections were determined through off-line analysis. The recorded pulse heights of signals were converted into particle energy using the Bethe-Bloch equation [4] and the Birks equation [1] taking into account the nonlinearity between light output and energy deposition. Particle identification was carried out by using PI technique [5]. The particle identification quantity, PI, is given by,

$$PI = E_{total}^{b} - (E_{total} - \Delta E)^{b} \ , \qquad (2)$$

Where E_{total} is the total energy deposited in the spectrometer, the ΔE is the amount of energy deposited in the transmission detector and b is the parameter whose value was employed to be 1.73 to obtain best separation.

5. Conclusion

In order to develop a new detector system, we have investigated the light output response and peak efficiencies of BGO crystals with respect to Proton and Alpha particles. The BGO crystal has good properties for the needs of our measurements. The experimental results showed a good agreement with the calculated curves by Birks equation.

References:

[1] J.B. Birks. "The Theory and Practice of Scintillation Counting" (Macmillan, New York) 1994.

[2] EA Bakkum, Van Engelen, R.Kamermans et al., Nucl. Instr. & Meth. 225, 46 (1984). (330-334)

[3] T. Kin et al., Physical Revew C, Vol.72, 014606 1-9 (2005).

[4] N.Tsoulfanidis, Measurement and Detection of Radiation, Second Edition, Taylor & Francis, p. 124, 1995.

[5] Makino, M., Eisburg, R., Inghum, D. and Waddell, C.: "A Method for Reducing the Effect of Nuclear Reaction in Stopping Detectors", Nuclear Instruments and Methods, Vol. 81, pp. 125-131, 1970.

25. Measurement of Neutron-Production Double-Differential Cross Sections for 290 MeV/u Oxygen Ion Incidence

*Daisuke MORIGUCHI[a], Haruhiko UEHARA[a], Tsuyoshi KAJIMOTO[a]
Keiichi HIRABAYASHI[a], Hidetaka HIRANO[a], Tomoya NISHIZAWA[a]
Nobuhiro SHIGYO[a], Yusuke UOZUMI[a], Daiki SATOH[b], Toshiya SANAMI[c]
Yusuke KOBA[d], Masashi TAKADA[d], Naruhiro MATSUFUJI[d]

[a] *Department of Applied Quantum Physics and Nuclear Engineering Kyushu University*
744 Motooka, Nishi-ku, Fukuoka 819-0395, Japan
[b] *Japan Atomic Energy Agency*
2-4 Shirakatashirane, Tokai, Naka-gun, Ibaraki 319-1184, Japan
[c] *High Energy Accelerator Research Organization*
1-1 O-ho, Tsukuba, Ibaraki 305-0801, Japan
[d] *National Institute of Radiological Sciences*
4-9-1 Anagawa, Inage-ku, Chiba 263-8555, Japan

email : moriguchi@kune2a.nucl.kyushu-u.ac.jp

Neutron-production double-differential cross sections for 290 MeV/u oxygen ion incidence on carbon target were measured with NE213 liquid organic scintillators by time-of-flight technique. NE213 liquid organic scintillators 12.7 cm in diameter and 12.7 cm thick were placed in the directions of 15°, 30°, 45°, 60°, 75° and 90°. The typical flight path length was 4.0 m. In order to reduce neutrons from the beam dump, an iron and a concrete shield was placed between the detectors and the beam dump. For measurement of background, a shadow bar was set between the target and each detector. Neutron detection efficiencies were obtained by calculations with a Monte Carlo simulation code SCINFUL-QMD. The cross sections were obtained for neutron energy above 3.6 MeV. The experimental results were compared with the calculation data of the PHITS2 code.

1. Intorduction

As increasing the number of patients enrolled in carbon-ion cancer therapy, the potential risk of radiation-induced second cancers has become a serious issue, especially for young patients [1, 2]. It is thus important to investigate the risk, including the contribution of secondary particles that are inevitably produced within the patient and beam line devices due to the potency of their biological effect. In particular, it is important to know contribution of secondary neutrons because the secondary neutron has a strong penetrability and gives undesired dose to normal tissues in a wide area [3]. Recently, a plan to investigate contribution of secondary neutron using simulation codes is furthered. However, the reliability of calculation codes has been evaluated limitedly, because the reports of data of carbon-ion incident neutron-production double-differential cross sections (DDX) on biological elements are very few [4, 5]. The experimental cross sections of neutron-production are required to be simulated with high accuracy. Especially, the accurate data around neutron energy of several MeV is required because such an energy neutron has a large relative biological effectiveness (RBE). Therfore, we measured the neutron-production double-differential cross sections for 290 MeV/u oxygen ions incidence on a carbon target of natural isotopic composition. Because of diffculty in preparation of a oxygen target, we performed the ^{nat}C(^{16}O, xn) DDX measurement to conduct inverse reaction analysis. The experimental data are compared with calculated results by the PHITS2 code [6].

2. Experimental procedure

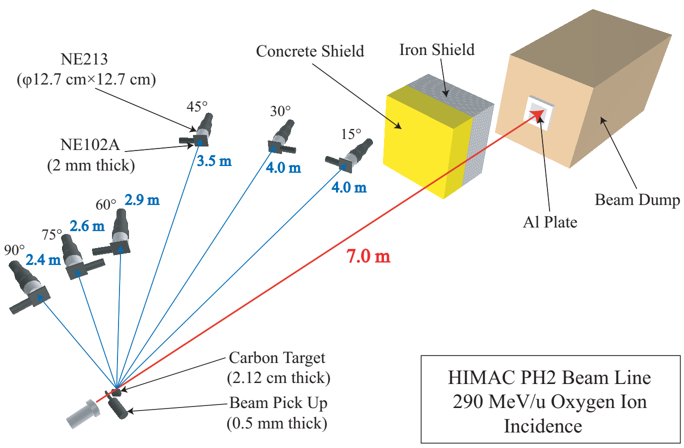

Fig. 1: Illustration of experimental setup

The experiment was carried out at the PH2 beam line at the heavy ion accelerator facility HIMAC of the National Institute of Radiological Sciences, Chiba, Japan. A schematic view of the experimental arrangement is illustrated in Fig. 1. The 290 MeV/u oxygen ions were employed as incident particles and a carbon plate of natural isotopic composition was chosen as an irradiation target. The beam emerged from a vacuum duct through a 100 μm thick aluminum window. Before impinging on the target, the beam traversed a beam pick up detector, which was an NE102A plastic scintillator in front of the target. The beam pick up detector provided the signal for the time-of-flight (TOF) measurement and the number of incident particles. The detector was 3 cm in diameter and was 0.5 mm thick so as to reduce the energy loss of incident beam inside it. The beam irradiated the carbon target, having the dimension of $5 \times 5 \times 1.5\,\mathrm{cm}^3$. A carbon plate was placed at an angle of 45° to the beam line as a target. The beam traveled in the air and stopped at a beam dump placed 7 m downstream from the target.

Emitted neutrons were detected with NE213 liquid organic scintillators, which dimension was 12.7 cm in diameter and 12.7 cm thick. The NE213 detectors were placed to measure angular distributions at 15°, 30°, 45°, 60°, 75° and 90°. Scintillation lights from the NE213 liquid organic scintillators are originated from as well as γ-rays and charged particles. Since the synchrotron was operated in a pulse mode (0.3 Hz repetition cycle) and incident oxygen beam intensity was very weak in level of $10^4 \sim 10^5$ particles/3.3 s, the number of incident oxygens can be individually counted. A veto detector, $150 \times 150 \times 2\,\mathrm{mm}^3$, made of NE102A plastic scintillator, was set in front of each NE213 scintillator to eliminate charged particle events.

In order to reduce neutrons from the beam dump, a couple of an iron of 63 cm thick and a concrete of 50 cm thick shields was placed between the detectors and beam dump. For measurement of background neutrons, the measurement with an iron shadow bar of 110 cm thick set between a target and detector were carried out.

3. Data analysis

In this measurement, the beam pick up detecter detects not only the single incident oxygen events but also the plural incident oxygen events. As clearly shown in Fig. 2, when two or three projectiles pass through the beam pick up detecter coincidentally, the pulse heights appear twice or three times higher than that of single projectile. The ratio of events obtained by single projectile to the all events was employed to correct the number of projectiles.

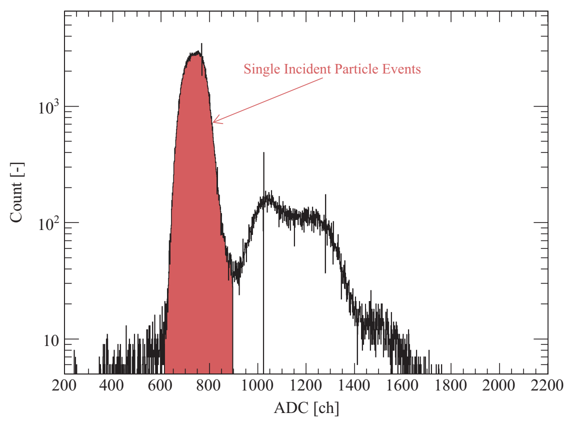

Fig. 2: spectrum of the beam pick up detector

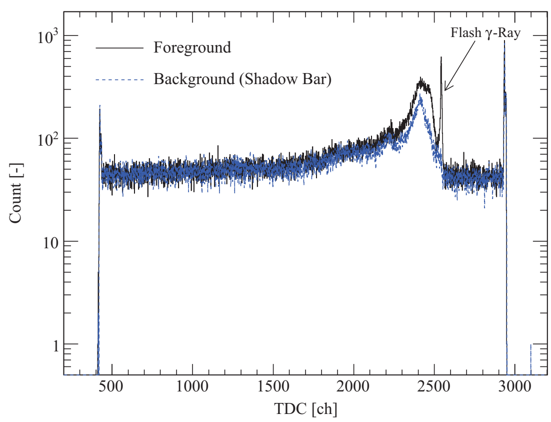

Fig. 3: An example of TOF spectra

Typical measured TOF spectra are shown in Fig. 3. Both foreground and background spectra contain neutron and γ-ray events. The flash γ-rays were generated from the target

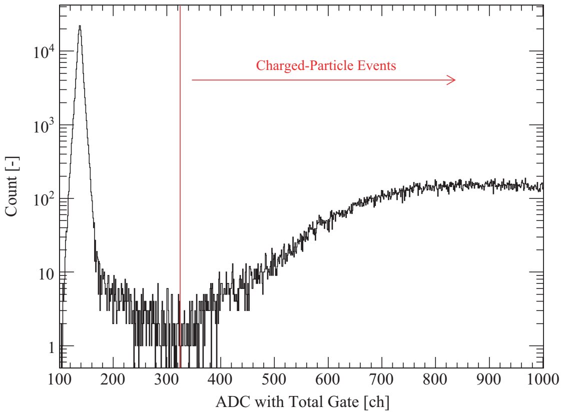

Fig. 4: spectrum of the veto detector

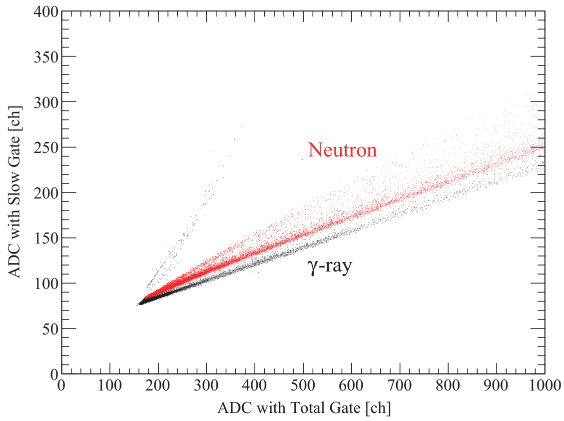

Fig. 5: Two dimensional plots of two ADC outputs, total and slow, for neutron-γ-ray discriminaton

nuclei excited by incident oxygens and shown as a sharp peak in this figure. This peak was utilized as the base time for the neutron TOF.

The charged particle events were excluded using the data from the veto detectors as shown in Fig. 4. To discriminate neutron and γ-ray events, the two-gates charge integration method was adopted. Figure 5 presents an example of two-dimensional scatter plot for total- and slow-gated electric charges of NE213 signals. The total gate width was 300 ns and that of the slow gate was 250 ns after delay of 50 ns from the start point of the total gate. One can see neutron and γ-ray events were separated well. The flash γ-ray events were not included in this figure because they were already excluded by the TOF.

Neutron spectra were obtained by subtracting the results of the background measurement from those of the foreground, after normalization with the number of incident oxygens.

The number of neutron-detection events were converted into the double-differential cross sections using neutron detection efficiencies. The efficiencies were obtained by calculations with a Monte Carlo simulation code SCINFUL-QMD [7]. This code is capable of calculating the detection efficiency for various sizes of organic scintillators for incident neutron energies up to 3 GeV. The neutron detection efficeincies were calculated with ^{60}Co bias.

4. Results and discussion

The neutron-production double-differential cross sections are indicated in Fig. 6 for incident oxygen energies of 290 MeV/u on C. The vertical error bars consist of statistical errors and the horizontal ones are composed of FWHM of flash γ-ray peak. The experi-

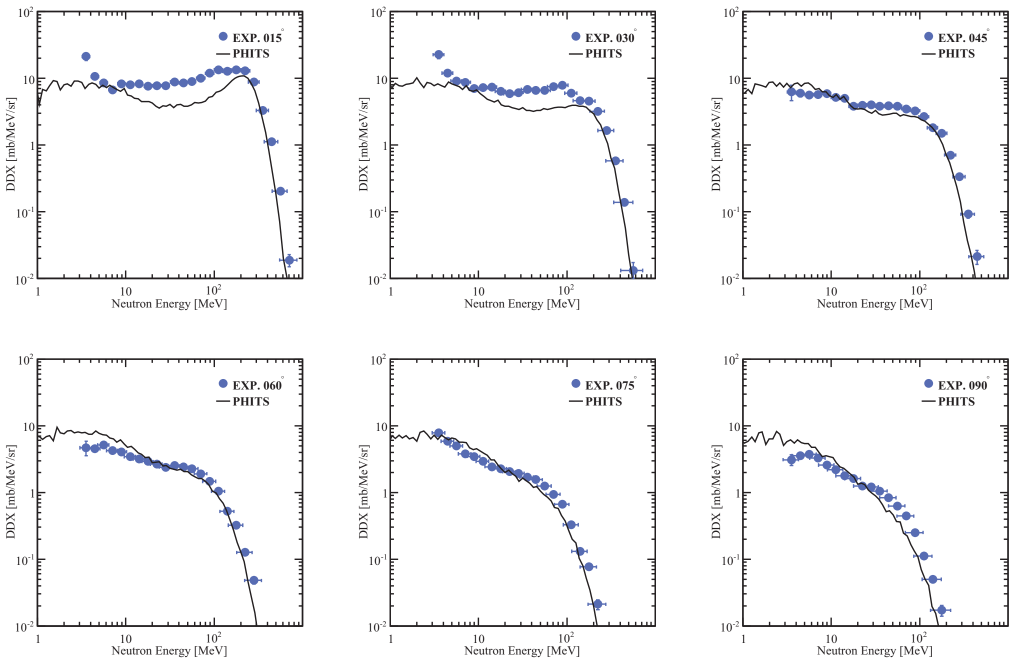

Fig. 6: Measured double-differential cross sections at incident oxygen energies of 290 MeV/u on C. They are compared with the PHITS2 calculations.

mental data are compared with PHITS2 calculations. The calculation values reproduces our experimental results of 45°, 60°, 75° and 90° reasonably well. However, the calculated values tend to underestimate the cross sections at 15° and 30°.

5. Summary

We measured the double-differential cross sections for $(\mathrm{O}, x\mathrm{n})$ reaction. The 290 MeV/u oxygen ions were used as incident particles. An NE102A plastic scintillator and NE213 liquid organic scintillator were employed to monitor the number of incident oxygen particles and to detect emitted neutrons, respectively. The neutron detection efficiencies were obtained by calculations with a Monte Carlo simulation code SCINFUL-QMD. The results were obtained with the TOF technique. The cross sections were obtained for neutron energy above 3.6 MeV. At overall range of energies, reasonable agreements were obtained between the experimental data and the PHITS2 calculations at 45°, 60°, 75° and 90°, while the calculated values tend to underestimate the cross sections at 15° and 30° in the 10∼200 MeV region.

Acknowledgement

We are grateful to Dr. T. Murakami and staffs of the HIMAC for their generous support of our experiments. This work was supported by Grant-in-Aid for Scientific Reserch (B) 22360406.

References

[1] C. Z. Jarlskog, and H. Paganetti, "Risk Developing Second Cancer from Neutron Dose in Proton Therapy as Function of Field Characteristics, Organ, and Patient Age," *Int. J. Radiation Oncology Biol. Phys.*, **72**, 228(2008).

[2] E. J.Hall, "Intensity-Modulated Radiation Therapy, Protons,and Risk of Second Cancers," *Int. J. Radiation Oncology Biol. Phys.*, **65**, 1(2006).

[3] B. Clasie, A. Wroe, H. Kooy, N. Depauw, J. Flanz, H. Paganetti, and A. Rosenfeld,, "Assessment of out-of-field absorbed dose and equivalent dose in proton fields," *Med. Phys.*, **37**, 311(2010).

[4] Y. Iwata, T. Murakami, H. Sato, H. Iwase, T. Nakamura, T. Kurosawa, L. Heilbronn, R. M. Ronningen, K. Ieki, Y. Tozawa, and K. Niita, "Double-differential cross sections for the neutron production from heavy-ion reactions at energies E/A=290–600 MeV," *Phys. Rev.*, **C64**, 054609(2001).

[5] D. Moriguchi, Y. Nakamura, T. Kajimoto, Y. Koba, M. Ueyama, M. Yoshioka, N. Shigyo, Y. Uozumi, D. Satoh, T. Sanami, M. Takada, and N. Matsufuji, "Measurement of Neutron-Production Cross Sections for 290 MeV/u Carbon Ion Incidence," Proc. Int. Conf. on Nuclear Data for Science and Technology, Jeju Island, Korea, April 26-30, 2010, in press.

[6] K. Niita, N. Matsuda, Y. Iwamoto, H. Iwase, T. Sato, H. Nakashima, Y. Sakamoto, and L. Sihver, "PHITS: Particle and Heavy Ion Transport code System, Version 2.23," JAEA-Data/Code 2010-022, Japan Atomic Energy Agency, (2010).

[7] D. Satoh, T. Satoh, N. Shigyo and K. Ishibashi, "SCINFUL-QMD: Monte Carlo Based Computer Code to Calculate Response Function and Detection Efficiency of a Liquid Organic Scintillator for Neutron Energies up to 3 GeV," JAEA-Data/Code 2006-023, Japan Atomic Energy Agency, (2006).

26. Neutron yields for reaction induced by 120 GeV proton on thick copper target

Tsuyoshi KAJIMOTO[1], Toshiya SANAMI[2], Yosuke IWAMOTO[3], Nobuhiro SHIGYO[1], Masayuki HAGIWARA[2], Kiwamu SAITOH[2], Hiroshi NAKASHIMA[3], Kenji ISHIBASHI[1], Hee-Seock LEE[4], Eric RAMBERG[5], Richard COLEMAN[5], Doug JENSEN[5], Aria SOFA[5], Nikolai V. MOKHOV[5], Anthony F. LEVELING[5], David J. BOEHNLEIN[5], Kamran VAZIRI[5]

[1] *Kyushu University, 744 Motooka, Fukuoka 819-0395 Japan*
[2] *High Energy Accelerator Research Organization, 1-1 Oho, Tsukuba 305-0801 Japan*
[3] *Japan Atomic Energy Agency, 2-4 Shirakata Shirane, Tokai-mura, Ibaraki 319-1195 Japan*
[4] *Pohang Accelerator Laboratory, Pohang, Kyungbuk 790-784 Korea*
[5] *Fermi National Accelerator Laboratory, Batavia, IL 60510-5011 USA*

e-mail : kajimoto@kune2a.nucl.kyushu-u.ac.jp

We developed an experimental method to measure neutron energy spectrum for 120 GeV proton on a thick copper target at Fermilab Test Beam Facility (FTBF). The spectrum in the energy range from 16 to 1600 MeV was obtained for 60 cm long copper target by time-of-flight technique with an NE213 scintillator and 5.5 m flight path.

1 Introduction

Energy spectra of neutrons generated from an interaction with beam and materials are important to design shielding structure of high energy accelerators. Until now, the energy spectra for the incident energy up to 3 GeV have been measured by several groups, Ishibashi et al. [1], Amian et al. [2], and Leray et al. [3]. In the energy region above 3 GeV, few experimental data are available because of small number of facilities for neutron experiment. On the other hand, concerning simulation codes, theoretical models for particle generation and transportation are switched from intermediate to high energy one around this energy. The spectra calculated by the codes have not been examined using experimental data.

In shielding experiments using 120 GeV hadron beam, experimental data shows systematic differences from calculations [4]. Hagiwara et al. have measured leakage neutron spectra behind iron and concrete shield from 120 GeV proton on target at anti-proton target station in Fermilab by using Bonner Spheres with unfolding technique [5]. In CERN, Nakao et al reported experimental results of neutron spectra behind iron and concrete wall from 120 GeV/c proton and pion mixed beam on copper by using NE213 liquid scintillators with unfolding technique [6]. Both of the results reported systematic discrepancies between experimental and calculation results. Therefore, experimental data are highly required to verify neutron production part of calculations.

In this study, we developed an experimental method to measure neutron energy spectrum for 120 GeV proton on target. The neutron energy was determined using time-of-flight technique. We used the Fermilab Test Beam Facility (FTBF) [7] in Fermilab that provided 120 GeV proton beam with intensity of 2×10^5/4 sec in every minute. The point of this study was determination of experimental configuration to satisfy enough statistic and energy resolution of neutrons.

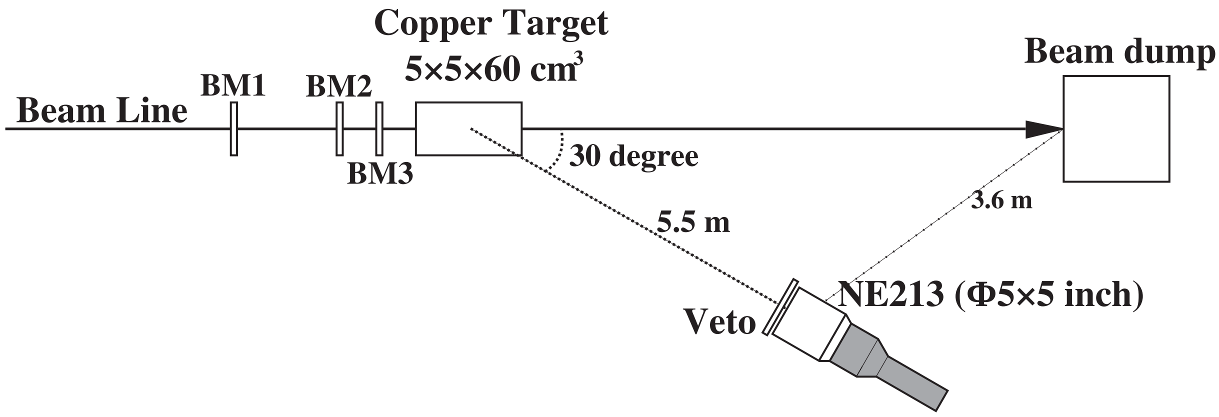

Fig. 1 Schematic view of experimental setup. 120 GeV proton beam comes from left side. Number of protons were counted by three plastic scintillator (BM1,2,3). Copper target, the dimension of which is 5 x 5 x 60 cm, was placed on the beam path. NE213 scintillator with Veto plastic scintillator was placed at 5.5 m from the target, 30° with respect to beam axis.

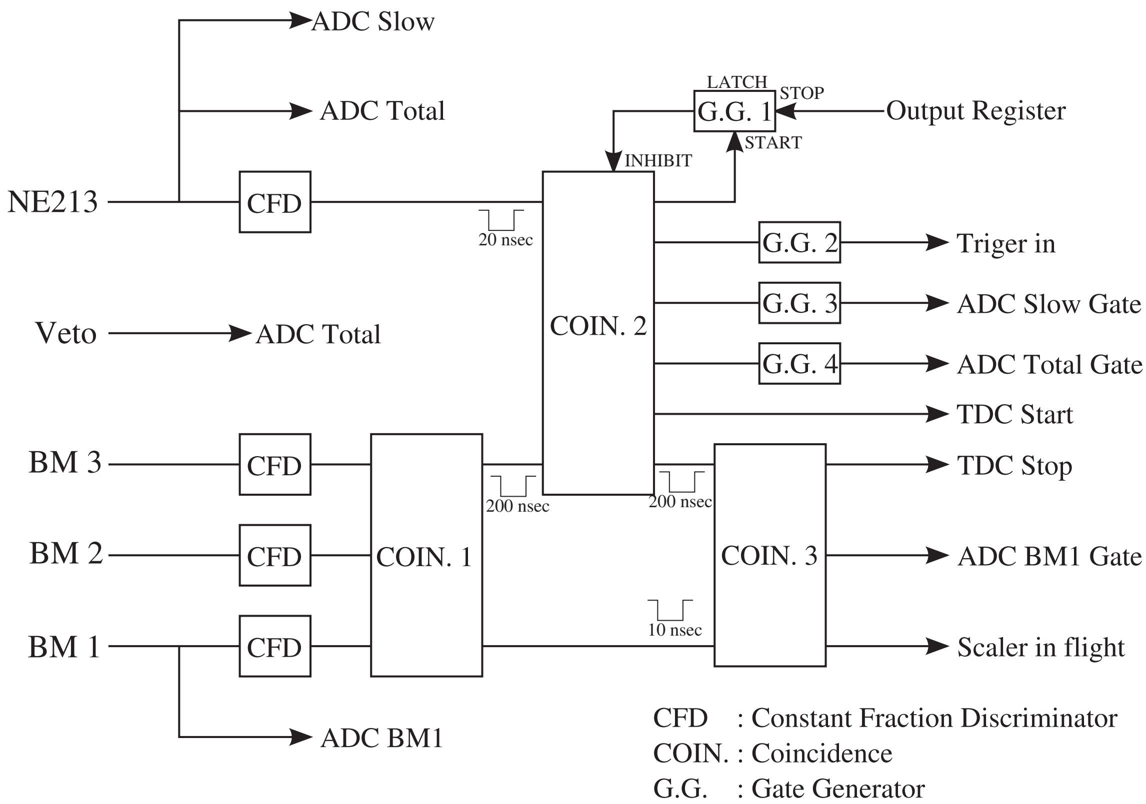

Fig. 2 Block diagram of data acquisition electronics. The electronics consisted of standard NIM and CAMAC modules. Trigger signal for data accumulation was generated from coincidence of the NE213 scintillator and the BMs. the time difference between coincidence of the BMs and the NE213 scintillator were stored as neutron flight time. Integrals of signals from the NE213 scintillator, the BM1, and veto detector were digitized using ADCs. Counts of the *scaler in flight* were recorded for correction of multi proton event during neutron time-of-flight.

2 Experiment

Figure 1 shows schematic view of experimental arrangement. The 120 GeV proton from the main injector are delivered to an area of 8×20 m^2. The number of incident protons were counted by three thin NE102A plastic scintillators (Beam monitors - BM 1, 2 and 3) which were located at upstream the target. The beam profile and position were monitored by a multi-wire proportional chamber. The sigma of beam radius was about ϕ 5 mm at the target position. The copper block, the dimension of which was 60 cm long and 5×5 cm^2 cross section, was employed as the neutron production target. The neutron detector was located at 5.5 m from the target and 30° with respect to the beam axis.

An NE213 liquid scintillator with 12.7 cm diameter, 12.7 cm long was employed as the neutron detector. The scintillator is suitable for neutron time-of-flight measurement due to pulse shape discrimination capability and fast decay time of its scintillation. To eliminate charged particles, a 2 mm thick NE102A plastic scintillator as the veto detector was placed in front of the NE213 scintillator.

Figure 2 shows a block diagram of data acquisition electronics. The electronics consisted of standard NIM and CAMAC modules. Trigger signal for data accumulation was generated from coincidence among the NE213 scintillator and the BMs. The data were recorded event by event. The time difference between the BMs and the NE213 scintillator was recorded with a TDC for determination of neutron time-of-flight. Charge-sensitive ADCs were employed in order to record total component charge of pulses from the NE213 scintillator, the BM1, and the veto detector. Slow component charge of pulse from the NE213 scintillator was also recorded for pulse shape discrimination. In addition, the number of protons during 200 ns before neutron signal was recorded (*scaler in flight* in Fig. 2) to ensure that time-of-flight was determined properly, as described in the next section.

Target-in measurement was carried out with beam intensity of 2×10^5 protons /min, during 3.5 hours. The counts of the BMs and the NE213 scintillator were 5×10^7 and 8×10^6, respectively. The dead time of data acquisition was about 62 %. Target-out measurement was also performed to check contribution of background neutron from the dump since the dump was closer than one from the target, as shown in Fig. 1.

3 Analysis

The energy spectra of neutrons, i.e. double differential thick target neutron yield (TTNY), $d^2Y(E)/dEd\Omega$, was deduced by the following equation,

$$\frac{d^2Y(E)}{dEd\Omega} = \frac{C(E)}{\phi\cdot\varepsilon(E)\cdot\Omega\cdot\Delta E} \tag{1}$$

where E is the neutron energy, $C(E)$ the neutron counts in an energy bin, ϕ the number of protons, $\varepsilon(E)$ the neutron detection efficiency, Ω the solid angle subtended by neutron detector, and ΔE the width of energy bin. Neutron events were identified by charged particle discrimination based on the veto detector signal, and gamma-ray discrimination based on the pulse shape of the NE213 scintillator. Neutron energy was determined by time-of-flight technique. We eliminated neutron event which could not uniquely determine its time-of-flight since two or more protons were counted by BM1 during neutron flight. The elimination was performed using data of "scalar in flight" and ADC BM1 shown in Fig.2. The "scalar in flight" was effective when the counts belong in different beam bunch. The ADC BM1 was effective when the counts belong in a same bunch. The count loss from the eliminations was corrected through the correction factor for the number of protons, as described in the next paragraph.

The number of protons was determined using the following equation,

$$\phi = \phi_{bm} \cdot \rho_{tof} \cdot \rho_{multi} \tag{2}$$

where ϕ_{bm} is the count of coincidence among the BMs, ρ_{tof} is the ratio of events that consist of single proton count during neutron flight to all events, and ρ_{multi} is the ratio of events that consist of single proton in a beam bunch to events of single proton count during neutron flight. The former and later could be determined using data of "scalar in flight" and ADC BM1 shown in Fig.2. The numerical values of ρ_{tof} and ρ_{multi} were 0.82 and 0.46, respectively.

The neutron detection efficiency, $\varepsilon(E)$, was determined experimentally based on the ^{238}U(n, f) cross sections [8] at Los Alamos Neutron Science Center (LANSCE). The detail of the experiment will be discussed in elsewhere. **Figure 3** shows the detection efficiency determined from the experiment as well as calculations by SCINFUL-QMD code [9]. The difference between experimental and calculation data was less than 15 % except for energy region from 80 to 150 MeV. Therefore, the uncertainty of the detection efficiency was determined as 10 %.

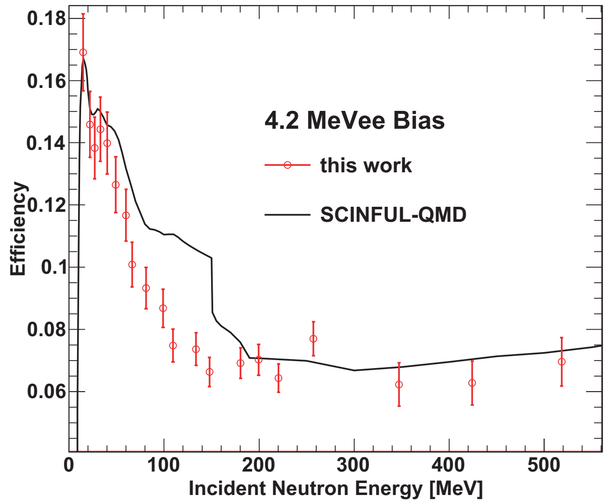

Fig. 3 Experimental and calculated neutron detection efficiencies of the NE213 scintillator at 4.2 MeVee bias.

4 Results and discussions

Figure 4 shows TTNY as well as one for target-out measurement. The experimental data cover the energy region between 16 and 1600 MeV. The threshold energy was attributed to the lower limit of detection efficiency. The upper energy was determined with considering the energy resolution for time-of-flight. Enough statistics were obtained since the uncertainty from statistics was 3 % for 1600 MeV at maximum. The uncertainty of experimental results was dominated by that of the detection efficiencies. Therefore, the detection efficiency of NE213 scintillator should be studied further for high energy neutrons to improve accuracy of TTNY.

As shown in Fig. 4, the target-out result shows markedly increase at 80 MeV. The fact indicates the target-in result includes contribution of background neutron from the beam dump. As well as the dump, certain amount of

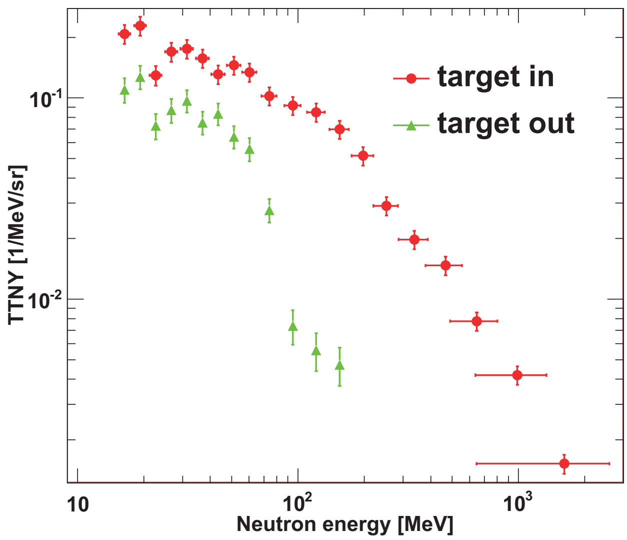

Fig. 4 Double differential neutron yield for 120 GeV proton incidence on 60 cm copper target. The results are compared with results of target out measurement, and include neutrons from floor and dump below 200 MeV.

background neutrons is expected from the floor scattering. These background neutrons have less impact in the energy region above 200 MeV because events from the dump and the floor have longer flight time than that from target. The background can be reduced by relocation of the dump.

The energy resolution of the TTNY was determined from the following equation

$$\frac{\sigma}{E} = \gamma(\gamma+1)\sqrt{\left(\frac{\sigma_L}{L}\right)^2 + \left(\frac{\sigma_t}{t}\right)^2} \qquad (3)$$

where E is neutron energy, γ is the Lorentz factor, L is the flight length, σ_L is the uncertainty of flight path, t is the flight time, and σ_t is the uncertainty of flight time. The geometrical component, σ_t , was derived from the thickness of the target (0.6 m) and the detector(0.13 m). The time component, σ_t, was estimated by the full width at half maximum (FWHM) of the prompt gamma peak on the time-of-flight spectra. The σ_t was determined to be 0.68 ns under the present condition. **Figure 5** shows the energy resolution. The total neutron energy resolution was better than 28 % below 1 GeV. The energy resolution can be improved by using thinner target since statistics were enough under the present experimental condition.

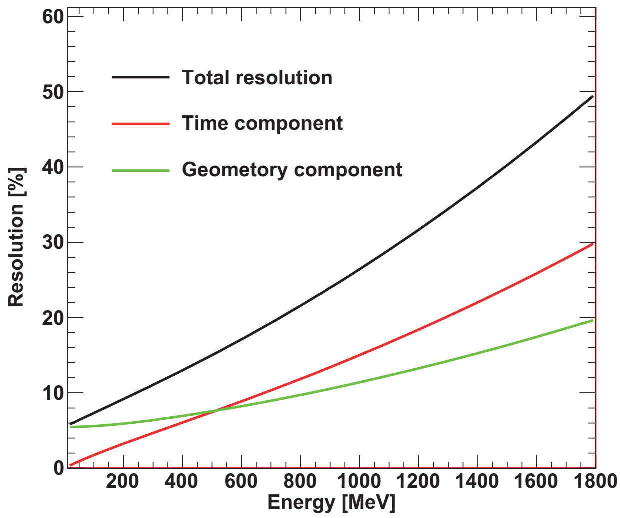

Fig. 5 Energy resolution for TOF measurement. The geometry component depends on thickness of the target and the NE213 scintillator. The time component is derived by full width at half maximum of flash gamma peak.

5 Summary

We developed the experimental method of TTNY measurement from 120 GeV proton on copper. The TTNY covers the energy range from 16 to 1600 MeV. The effects from multiple protons in a single neutron events could be eliminated successfully using the electronics circuit. It is important to reduce error of the neutron detection efficiency in high energy region for accurate TTNY. It should be noted that the present results provides prospect of a thin target experiment with improved energy resolution.

The measurement with a thin target can be anticipated to obtain systematic data taking for target mass and angle. For the measurement, contribution of background from the dump and the floor can be removed by the measurement with shadow bar. The data would be standard as the bench mark data of neutron production spectrum by high energy proton. It must contribute to the improvement and development of neutron production models in simulation code.

Acknowledgement

This work is supported by grant-aid of ministry of education (KAKENHI 21360473) in Japan. Fermilab is a U.S. Department of Energy Laboratory operated under Contract DE-AC02-07CH11359 by the Fermi Research Alliance, LLC.

References

[1] K. Ishibashi, H. Takada, T. Nakamoto, *et al.*, *"Measurement of Neutron-Production Double-Differential Cross Sections for Nuclear Spallation Reaction Induced by 0.8, 1.5 and 3.0 GeV Protons"*, J. Nucl. Sci. Technol., **34**, 529-537 (1997).

[2] W. B. Amian, R. C. Byrd, C. A. Goulding, *et al.*, *"Differential neutron production cross sections for 800-MeV protons"*, Nucl. Sci. Eng., **112**, 78 (1992).

[3] S.Leray, F.Borne, S.Crespin, *et al.*, *"Spallation neutron production by 0.8, 1.2, and 1.6 GeV protons on various targets"*, Phys. Rev., **C65**, 044621 (2002).

[4] H, Nakashima, N. V. Mokhov, Y. Kasugai, *et al.*, *"JASMIN: Japanese-American Study of Muon Interactions and Neutron detection"*, Proc. SATIF-10, Geneva, Switzerland, June 2-4, 2010, to be published.

[5] M. Hagiwara, T. Sanami, Y. Iwamoto, *et al.*, *"Shielding experiments at high energy accelerators of Fermilab (III): neutron spectrum measurements in intense pulsed neutron fields of the 120-GeV proton facility using a current bonner sphere technique"*, Proc. ISORD-5, Kitakyushu, Japan, July 15-17, 2009, to be published.

[6] N. Nakaoa, S. Taniguchi, S. H. Rokui, *et al.*, *"Measurement of neutron energy spectra behind shielding of a 120 GeV/c hadron beam facility"* Nucl. Instr. and Meth. **A562**, 950 (2006).

[7] http://www-ppd.fnal.gov/MTBF-w/

[8] P. W. Lisowski, A. Gavron, W. E. Parker, *et al.*, *"Fission cross sections in the intermediate energy region,"* Proc. Specialists' Meeting on Neutron Cross Section Standards for the Energy Region above 20 MeV, Uppsala, Sweden May 21–23, 177 (1991).

[9] D. Satoh, T. Sato, N. Shigyo, *et al.*, *"SCINFUL-QMD: Monte Carlo based computer code to calculate response function and detection efficiency of a liquid organic scintillator for neutron energies up to 3 GeV"*, JAEA-Data/Code, 2006-023(2006).

27. Comparison of Neutron Production from Heavy-ion Reaction using PHITS and FLUKA

Cheol Woo LEE, Young-Ouk LEE

Korea Atomic Energy Research Institute, 1045 Daeduck-daero, Yuseong-gu, Daejeon, Korea

e-mail: cwll@kaeri.re.kr

In this study, heavy ion transport codes, PHITS and FLUKA were compared in the view of the radiation shielding. The neutron production rates were calculated using these two codes and the results were compared with the measurement. C-12 ion beam with the energy of 400 MeV/n and graphite target was used in the calculation of the neutron production. The angular distributions of the secondary neutrons from the thick target were compared and applied in the shielding calculations. By using these neutron source terms, the differences of the dose rate behind of the shield materials, concrete, due to the neutron spectrum was evaluated. The shielding design margin for the n-TOF experimental room using heavy ion beam in the accelerator facility in Korea was evaluated.

I. Introduction

With increasing multi-purpose use of high energy heavy ion accelerators, secondary particle production and transport by high-energy heavy ions are an important issue in the design of the heavy ion accelerator rooms and facility. At present, the development of a heavy ions accelerator with the acceleration energy of 400 MeV/n is under consideration in Korea. And we have a plan to build a n_TOF measurements room in the heavy ion accelerator facility. But there have been no experience to construct a heavy ion accelerator of the high energy above 100 MeV/n and perform the radiation shielding design in Korea.

This study is a preliminary analysis of the simulation codes for the heavy ion transport through the benchmark calculations for the evaluation of the secondary radiation source terms and the difference of the calculation for the shielding design.

II. Calculations and Results

Heavy-ion transport codes containing an event generator and physics models to simulate the heavy-ion transport and nuclear-nuclear reactions requires following some features.

- *reliable description of cross-sections and particle yields from a fraction of eV to TeV for heavy-ion projectiles*
- *leading particles (elastic, diffractive and inelastic)*
- *evaluate nuclide inventory or residuals*
- *simulate electromagnetic process and describe the magnetic field for charged particles*

There are many Monte Carlo codes satisfying these requirements like as FLUKA, PHITS, GEANT4, MARS15, MCNPX and SHIELD. Of these, FLUKA and PHITS were selected in this study considering benchmarking conditions, geometrical model, kinds of heavy ions, measurements for benchmarking, energy of particles, etc.

The inelastic interaction of the incoming projectiles and the target nuclei interact leads to the production of secondary particles via different processes, such as fragmentation, fusion, Fermi break-up, and de-excitation. The produced particles are mostly protons, neutrons and light fragments. The secondary neutrons are more important in the view of the prompt radiation shielding.

The production yields of the secondary neutrons, mostly differential in both, energy and angle are compared by using the three codes. These simulations can also be divided in two categories.

The first one is a thin target which thickness is in the order of one interactions length. The comparisons of the results from thin target are very valuable assessing the quality of the models of a Monte Carlo particle code and hint at the origin of possible flaws as they try to isolate different physics processes.

The second, thick target is more meaningful as they allow for a comparison of the degree of agreement of double-differential production yields at a different target depth. These data provide an integral check of accumulated effects, including scattering, and absorption of the particles traversing the target material. In the following only thick target simulations for secondary neutron production are considered.

1. Description of the Codes

(1) PHITS

PHITS is the multi-purpose 3-D Monte Carlo transport code system for all particles and heavy ions with all energies up to 200 GeV.[1] Below 10 MeV/nucleon, only the ionization process for the nucleus transport is taken into account, but above 10 MeV/nucleon the nucleus−nucleus collisions up to 100 GeV/nucleon is described by the simulation model JQMD (JAERI Quantum Molecular Dynamics).

For the ionization process of the charged particles and nuclei, the SPAR code is used for the average stopping power, the first order of Moliere model for the angle straggling, and the Gaussian, Landau, and Vavilov theories for the energy straggling around the average energy loss according to the charge density and velocity. In addition to the SPAR code, the ATIMA package, developed at GSI, has been implemented as an alternative code for the ionization process. The total nucleus−nucleus reaction cross-section, as an alternative to the Shen formula, NASA systematics developed by Tripathi was also adopted.[2] In this study, the PHITS code of version 215 was used.

(2) FLUKA

FLUKA is a general purpose tool for calculations of particle transport and interactions with matter, covering an extended range of applications spanning from proton and electron accelerator shielding to target design, calorimetry, activation, dosimetry, detector design, Accelerator Driven Systems, cosmic rays, neutrino physics, radiotherapy etc.[3] FLUKA implements both DPMJET and RQMD as event generators to simulate nucleus-nucleus interactions.

De-excitation and evaporation of the excited residual nuclei is performed by calling the FLUKA evaporation module. At medium/high energy (above a few GeV/n) the DPMJET model is used. DPMJET is a Monte Carlo model for sampling hadron-hadron, hadron-nucleus and nucleus-nucleus collisions at accelerator and cosmic ray energies (Elab from 5-10 GeV/n up to 1011 GeV/n) based on the two components Dual Parton Model in connection with the Glauber formalism. The DPMJET model is not valid for energies below a few GeV/nucleon.

For this reason, RQMD model is used to enable FLUKA to treat ion interactions from ≈100 MeV/n up to 5 GeV/n. The RQMD is a relativistic model based on "Quantum Molecular Dynamics" (QMD). This is an approach where individual nucleons evolve according to an effective Hamiltonian, involving two– and three–body interaction terms.[4] In this study, the FLUKA code of version 2006 was used.

2. Calculations

In this study, the reactions of carbon ion beam with 400 MeV/n on graphite target was considered. Therefore, two kinds of calculations, FLUKA using RQMD model and PHITS using JQMD, were performed to compare with the measurement. The secondary neutron fluxes were calculated at the angles of 0^0, 30^0, 60^0 and 90^0. The measurement data from experiments in HIMAC facility in Japan were used in benchmarking.[5] The calculation model was constructed considering the experiment condition in HIMAC.

3. Neutron Production

Double differential neutron yield in the angular range of 0^0-90^0 with respect to the carbon ion beam was calculated using PHITS and FLUKA codes. The results of benchmark calculations were presented in the **Figure 1 to Figure 4** compared with the experiments.

In the forward direction, in the angle of 0^0, the PHITS and FLUKA had been in a good agreement with experiments in the energy range under 100 MeV and over 300 MeV. PHITS had underestimated about 40 % of maximum near the neutron energy of 200 ~ 300 MeV. The FLUKA code has overestimated about 20 % of maximum at the same region. In the angle of 30^0 and 60^0, PHITS showed the underestimations in the whole energy range. FLUKA showed the underestimations in the high energy region and over estimations in the low energy region. But the both of two codes shows differences under the 20 % maximum for a few energy bins. At the angle of 90^0, both of the two codes were in good agreement with the measurements

The main difference between two codes was the shape of the neutron spectra in the angle of 30^0 and 60^0. In the lateral shielding design, this difference affects the dose rate for the very thick shield material. The ratio of the high energy neutrons to the low energy neutrons affects the reduction rate of the dose rate after passing the thick shield.

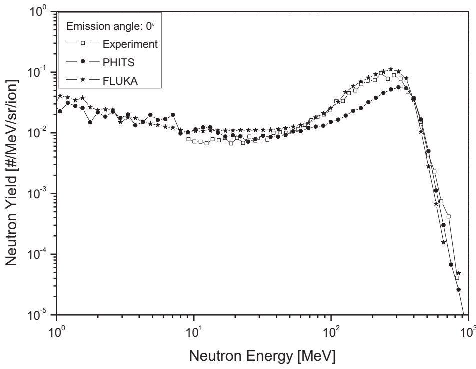

Fig 1. Thick-target neutron yields at the emission angle of 0^0

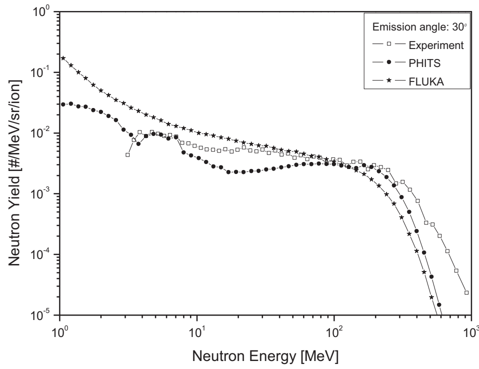

Fig 2. Thick-target neutron yields at the emission angle of 30^0

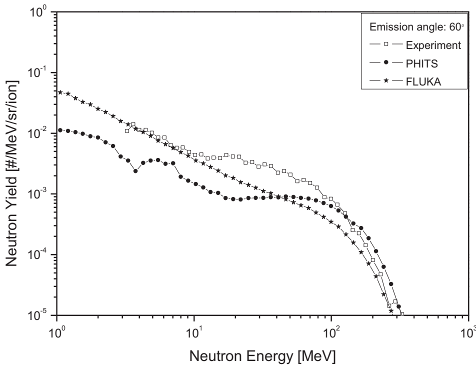

Fig 3. Thick-target neutron yields at the emission angle of 60^0

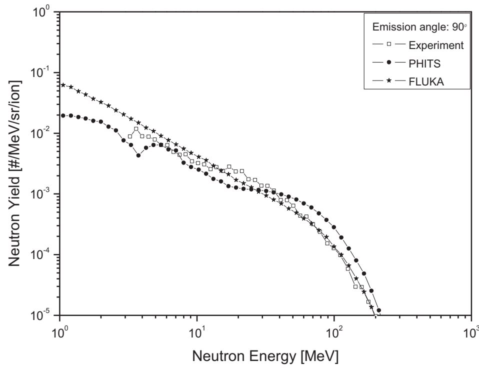

Fig 4. Thick-target neutron yields at the emission angle of 90^0

4. Evaluation of the Differences in Shielding Calculation

The neutron dose rates behind the concrete shield were calculated using the neutron spectra calculated with PHITS and FLUKA codes. The evaluated Neutron Dose distributions behind of the concrete shield were shown in the **Figure 5 to Figure 8.**

For the neutron source at the angle of 0^0 and 90^0, the dose rates were under a factor of 1.2 and showed a same trend. For the neutron source at the angle of 30^0 and 60^0, the dose rates were under a factor of 1.4 but the dose rate calculated from PHITS was higher than those from FLUKA after passing the concrete shield of 10 0 ~ 150 cm thick . This is due to the differences of the production of the high energy neutrons. The shape of the neutron spectrum calculated by PHITS changed more hardly than those by FLUKA.

III. Conclusion

The simulations for C-12 ion beam with the energy of 400 MeV/n impinging on the target were performed by using PHITS and FLUKA codes. The angular distributions of the secondary neutrons from the thick target were compared with the measurement and the differences of the dose rate behind of the shield materials, concrete, due to the neutron spectrum was evaluated. The thick target yield from this study were evaluated in the differences under 40 % compared with measurement and the dose rates behind of the concrete shield were under a factor of 1.4. It will be expected that the use of the PHITS and FLUKA codes is reasonable for the heavy ion reactions and shielding calculations consider a margin with a factor of 1.4 for the radiation shielding design, for the n-TOF experimental room using heavy ion beam in the accelerator facility in Korea.

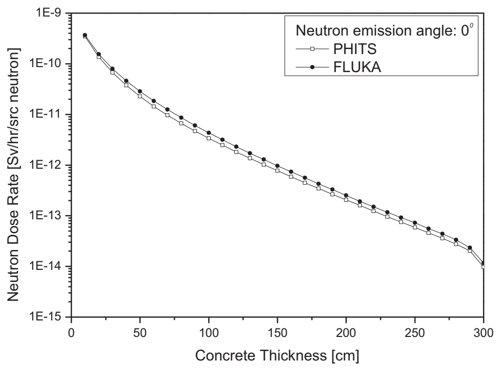

Fig 5. Neutron dose rate at the emission angle of 0^0

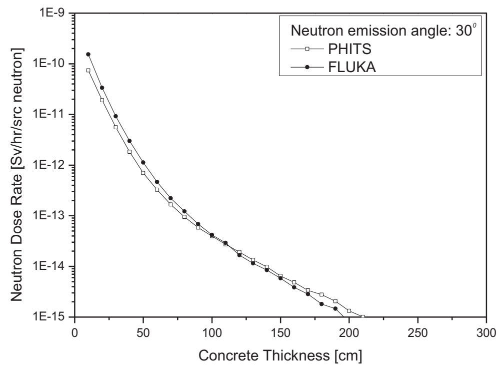

Fig 6. Neutron dose rate at the emission angle of 30^0

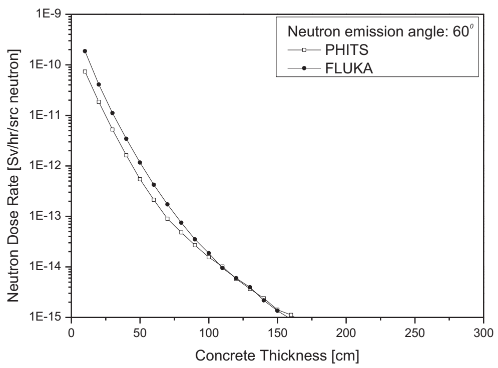

Fig 7. Neutron dose rate at the emission angle of 60^0

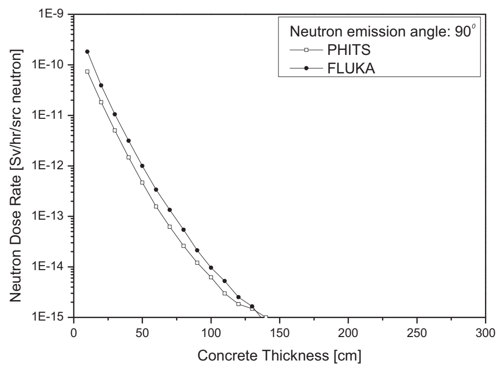

Fig 8. Neutron dose rate at the emission angle of 90^0

References

[1] Koji Niita, Tatsuhiko Sato, Hiroshi Iwase, Hiroyuki Nose, Hiroshi Nakashima, and Lembit Sihver, "PHITS – a particle and heavy ion transport code system," *Radiation Measurements* 41, 1080-1090 (2006).

[2] Koji Niita, et. Al., "Nuclear Reaction Models in Particle and Heavy ion Transport code System, PHITS," *Proc. First International Workshop on Accelerator Radiation Induced Activation*, Oct. 13-17, 2008, PSI, Switzerland (2008)

[3] Alfredo Ferrari, Paola R. Sala, Alberto Fass`o and Johannes Ranft, "FLIKA: a muliti-particle transport code," CERN-2005-010, CERN (2005)

[4] F. Ballarini, et. Al., "The FLUKA code: an overview," *Journal of Physics*, Conference Series 41, 151-160 (2006)

[5] Takasi Nakamura and Lawrence Heilbronn, *Handbook on Secondary Particle Production and Transport by High-energy Heavy Ions*, World Scientific, 13-16 (2006).

28. DPA Calculations for Heavy-ion and Proton Incident Reactions in High-energy Region Using the PHITS Code

Yosuke IWAMOTO[1], Koji NIITA[2], Tomotsugu SAWAI[1],
R.M. RONNINGEN[3], Thomas BAUMANN[3]
[1]Japan Atomic Energy Agency, Tokai-mura, Naka-gun, Ibaraki-ken 319-1195 Japan
[2]Research Organization for Information Science and Technology, Tokai-mura, Naka-gun, Ibaraki-ken 319-1195 Japan
[3]National Superconducting Cyclotron Laboratory, Michigan State University, East Lansing, MI 48824 U.S.A.
e-mail: iwamoto.yosuke@jaea.go.jp

Radiation damage in solids caused by various particles in wide range of energy is measured in a common unit, DPA (Displacement per Atom). The DPA model in the Particle and Heavy Ion Transport code System (PHITS) has recently been developed using Coulomb scattering to evaluate the energy of target PKA's created by the projectile and the secondary from nuclear reactions. For the Coulomb scattering, a universal one-parameter differential scattering cross section equation introduced by J. Lindhard et. al. is employed. The number of displacements in a cascade damage caused by a PKA was evaluated by the NRT model. We compared PHITS results for the 130 MeV/u ^{76}Ge and proton into W reactions with calculated results of TRIM, which is widely used and cannot treat nuclear reactions. PHITS gives good agreements with TRIM results for DPA values by PKA's directly created by the projectile such as ^{76}Ge and proton. On the other hands, for the proton incident reaction, PKA's created by the secondary particles is more dominant than PKA's by the projectile in DPA calculations. Therefore, TRIM leads to sever underestimation where projectile energy is high enough to create nuclear reactions. PHITS is more reliable code than TRIM for DPA calculations, especially in the high-energy region and proton incidence.

1. Introduction

As the power of proton and heavy-ion accelerators is increasing, the prediction of the structural damage to materials under irradiation is essential. The average number of displaced atoms per atom of a material DPA serves as its quantitative measure: DPA=$\phi t \sigma$ where σ is the radiation damage cross section; and ϕt is the irradiation fluence, i.e., the product of the ion beam density and the bombardment time. The level of the radiation damage in DPA units is used, for example, to estimate radiation damage of the target and magnet material for heavy-ion and proton incident reactions in Rare Isotope Beam Facility (FRIB) [1] and J-PARC facility [2]. Since Particle and Heavy Ion Transport code System (PHITS) [3] was used for the radiation protection study of the conception design of FRIB and J-PARC, it was recently enhanced with the capability of making realistic prediction of radiation induced damage to materials. In this paper, we describe the new model of DPA calculations in PHITS and compare with the prediction of TRIM code [4], which is widely used for the damage calculations. Calculations and comparison will be reported for 130-MeV/u ^{48}Ca and 130MeV proton into W target.

2. DPA calculations in PHITS

2.1 Overview of DPA calculation in PHITS

High energy ions traveling a target lose their energy in three ways; nuclear reaction, electron excitations and Coulomb scatterings. The lower the projectile energy is, the higher the energy transfer to the target atom via Coulomb scattering is. The target atom directly hit by the projectile has usually much lower energy than the projectile itself and, therefore, has a larger cross-section for Coulomb scattering with other target atoms. Thus the primary knock-on atom (PKA) creates localized cascade damage where many target atoms are displaced from their original lattice site leaving same number of interstitials and vacancies. These point defects and their clusters affect the macroscopic properties, such as hardness.

The conditions of various irradiations will be described by using the damage energy to characterize the displacement cascade. This is defined as the initial energy of target PKA, corrected for the energy lost to electronic excitations by all of the particles composing the cascade. There are mainly two processes to produce the target PKA for heavy-ions and proton incident reactions as shown in **Fig. 1**. One is the Coulomb scattering due to PKA's directly created by the projectile, and the other is that due to PKA's created by the secondary particles. The energy of the secondary charged particles is obtained by PHITS calculations using the nuclear reaction model of JQMD [5] and Bertini [6] for heavy-ion and proton, respectively.

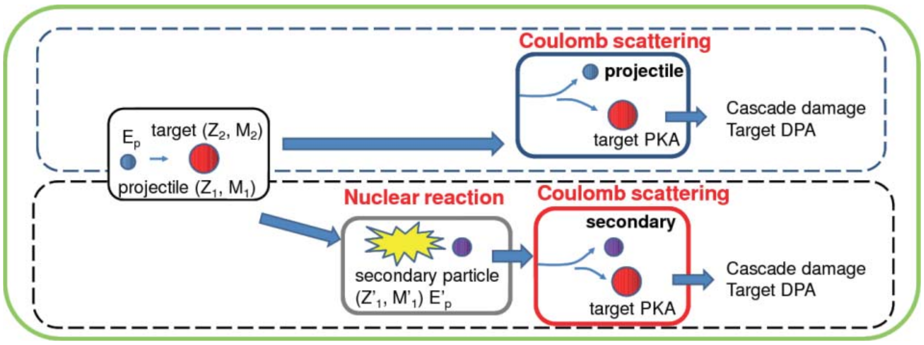

Figure 1 Overview of DPA calculations in PHITS.

2.2 Coulomb scattering with target atom

Scattering cross section obtained using the Rutherford cross-section is a function of six major parameters: $d\sigma = f(Z_1, Z_2, E, \theta_c, M_1, M_2)$. To simplify differential cross-section calculations even further, J. Lindhard, V. Nielsen, and M. Scharff [7] introduced a universal one-parameter differential scattering cross section equation in reduced notation:

$$d\sigma_{\mathrm{sc}} = \frac{\pi a_{TF}^2}{2}\frac{f(t^{\frac{1}{2}})}{t^{3/2}}\,dt \qquad (1)$$

where t is a dimensionless collision parameter defined by

$$t \equiv \varepsilon^2 \frac{T}{T_{max}} = \varepsilon^2 sin^2\left(\frac{\theta_c}{2}\right) \qquad (2)$$

where T is the transferred energy to the target and T_{max} is the maximum transferred energy as

$$T_{max} = \frac{4M_1M_2}{(M_1+M_2)^2}E_p \qquad (3)$$

Where E_p is the projectile energy. ε is the dimensionless energy as

$$\varepsilon \equiv \frac{a_{TF}}{d_c} = \frac{a_{TF}E}{Z_1Z_2e^2} \qquad (4)$$

In the above expression, d_c is the unscreened (i.e., Coulomb) collision diameter or distance of closest approach for a head-on collision (i.e., b=0), and a_{TF} is the screening distance.

Lindhard et al. considered $f(t^{1/2})$ to be a simple scaling function and the variable t to be a measure of the depth of penetration into the atom during a collision, with large values of t representing small distances of approach. $f(t^{1/2})$ can be generalized to provide a one parameter universal differential scattering cross section equation for interatomic potential such as screened and unscreened Coulomb potentials. The general form is

$$f\left(t^{\frac{1}{2}}\right) = \lambda t^{\frac{1}{2}-m}[1+(2\lambda t^{1-m})^q]^{-1/q} \quad (5)$$

where λ, m, and q are fitting variables, with λ=1.309, m=1/3 and q=2/3 for the Thomas-Fermi version [8] of $f(t^{1/2})$. The value of $t^{1/2}$ increases with an increase in a dimensionless energy ε, scattering angle in the CM system, and impact parameter. The Coulomb scattering cross section in the energy region above the displacement threshold energy can be calculated from the following expression:

$$\sigma_{sc} = \int_{t_d}^{t_{max}} d\sigma_{\mathrm{sc}}/dt\,dt \qquad (6)$$

where t_{max} in dimensionless is equal to ε^2 from equation (2) when θ=π. t_d is the displacement threshold energy in dimensionless given by equation (4). Displacement threshold energy E_d is typically in the range between 20 and 90 eV for most metals.

2.3 Damage cross sections

To estimate the damage cross sections the NRT formalism of Norgett, Robinson, and Torrens and Robinson [9] is employed as a standard to determine that fraction of the energy of the PKA of the target which will produce damage, e.g., further nuclear displacements. The displacement cross sections can be evaluated from the following expression:

$$\sigma_{damage} = \int_{t_d}^{t_{max}} d\sigma/dt \times \nu(Z_{target}, A_{target}, T_{target})dt \qquad (7)$$

Z_{target}, A_{target} are the numbers for the recoil target atom and T_{target} is the PKA energy of target. Equation (7) indicates the scattering cross section multiplied by the number of defects.

Based on the Kinchin and Pease formula [10] modified by Norgett et al. and using the Lindhard slowing-down theory, the number of defects produced in irradiated material is calculated

$$\nu\left(\mathrm{Z_{target}}, \mathrm{A_{target}}, \mathrm{T_{target}}\right) = \mathrm{N_{NRT}} \qquad (8)$$

Where N_{NRT} is the number of defects calculated by

$$N_{NRT} = \frac{0.8 \cdot T_{damage}}{2 \cdot T_{threshold}} \quad (9)$$

The constant 0.8 in the formula is the displacement efficiency given independent of the PKA energy, the target material, or its temperature. The value is intended to compensate for forward scattering in the displacement cascade of the atoms of the lattice. T_{damage} is the "damage energy" transferred to the lattice atoms reduced by the losses for electronic stopping in the atom displacement cascade and is given by Norgett, Robinson, and Torrens.

$$T_{damage} = \frac{T}{1 + k_{cascade} \cdot g(\varepsilon)} \qquad (10)$$

Where T is the transferred energy to target atom given by equation (2) as

$$T = T_{max} \times \frac{t}{\varepsilon_p^2} \qquad (11)$$

where ε_p is the dimensionless projectile energy given by equation (4) and the projectile energy E_p. The parameters $k_{cascade}$, and $g(\varepsilon)$ are as follows:

$$k_{cascade} = 0.1337 Z_{target}^{\frac{1}{6}} \left(Z_{target}/A_{target}\right)^{1/2} \quad (12)$$

$$g(\varepsilon) = \varepsilon + 0.40244 \cdot \varepsilon^{3/4} + 3.4008 \cdot \varepsilon^{1/6} \qquad (13)$$

ε is the dimensionless transferred energy given by equations (4) and (11). The following equation shows the summary from equations (7), (9), and (10).

$$\sigma_{damage} = \int_{t_d}^{t_{max}} d\sigma_{\mathrm{scat.}}/dt \; \frac{0.8}{2 \cdot T_d} \frac{T}{1 + k_{cascade} \cdot g(\varepsilon)} dt \qquad (14)$$

Figure 2 shows a damage cross sections (eq. 14) and Coulomb scattering cross sections ($T > E_d$) (eq. 6) with threshold energy of 25 eV for the Ge + W scattering. As the cross section for Coulomb scattering ($T > E_d$) is much larger (~10^7 – 10^9 b) than the nuclear reaction cross section (~mb order) which are treated in PHITS, it is difficult to calculate the DPA using full Monte Carlo calculation with Coulomb scattering in PHITS because of spending much time for calculations. Therefore, only a part of the transferred energy to the target T is calculated by PHITS, and damage cross sections is estimated with Eq. (14). Note that this calculation does not include the self-healing of lattice defects.

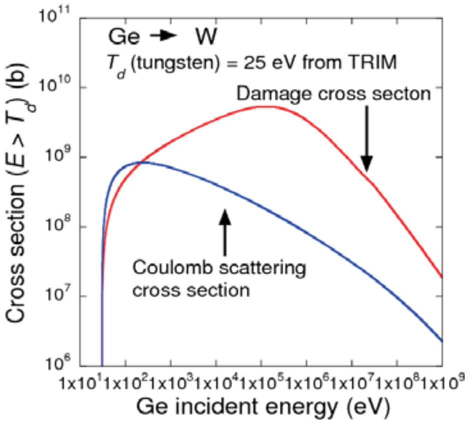

Figure 2 Damage and Coulomb cross sections for the Ge -> W scattering.

3. DPA calculation example

Based on the above formalisms, we calculated DPA distributions in W target for 130 MeV/u ^{76}Ge and proton irradiations. The number of ions is 9.45×10^{16}. Calculated results were compared with those of TRIM as shown in **Figure 3**. We selected "Quick Calculation of Damage" for TRIM option for DPA calculation. The damage calculated with this option is the quick statistical estimates based on the Kinchin-Pease formalism. TRIM treats just Coulomb scattering for the projectile and cannot produce secondary particles from nuclear reactions. PHITS gives good agreements with TRIM results for DPA values by PKA's directly created by the projectile such as ^{76}Ge and proton. On the other hands, for the proton incident reaction, PKA's created by the secondary particles is more dominant than PKA's by the projectile in DPA calculations. Damage calculation only by PKA's directly created by the projectile, such as TRIM, may lead to sever underestimation where projectile energy is high enough to create nuclear reactions. We conclude that PHITS is more reliable code than TRIM for DPA calculations, especially in the high-energy region and proton incidence.

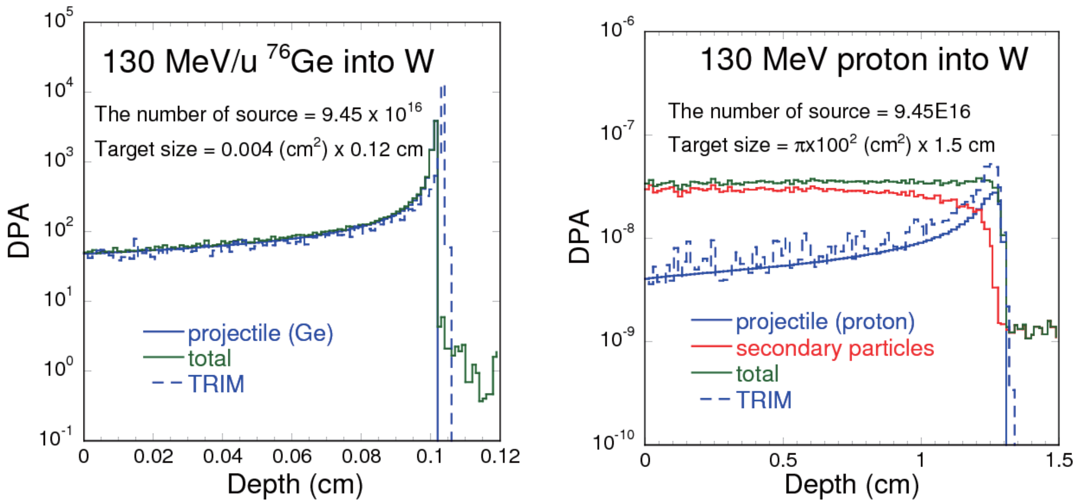

Figure 3 DPA calculation using PHITS and TRIM for the 130 MeV/u ^{76}Ge into W (left) and proton into W (right).

4. Summary

We described our formalism for calculating damage to materials and implementation into PHITS of the DPA evaluation. DPAs are calculated using Coulomb scattering by the target PKA's created by the projectile and the secondary from nuclear reactions. We compared PHITS results for the 130 MeV/u ^{76}Ge and proton into W reactions with calculated results of TRIM, which is widely used and cannot treat nuclear reactions. PHITS gives good agreements with TRIM results for DPA values by PKA's directly created by the projectile such as ^{76}Ge and proton. For the proton incident reaction, PKA's created by the secondary particles is more dominant than PKA's by the projectile in DPA calculations. TRIM may lead to sever underestimation where projectile energy is high enough to create nuclear reactions. Therefore, PHITS is more powerful code than TRIM for the damage calculations especially in the high-energy accelerator facilities.

References

[1] Facility for Rare Isotope Beams websites, Available at: http://www.frib.msu.edu/.

[2] J-PARC websites. Available at: http://j-parc.jp/index-e.html.

[3] K. Niita, N. Matsuda, Y. Iwamoto, H. Iwase, T. Sato, H. Nakashima, Y. Sakamoto and L. Sihver: JAEA-Data/Code 2010-022 (2010).

[4] J. F. Ziegler, "The Stopping and Range of Ions in Solids", by J. F. Ziegler, J. P. Biersack and U. Littmark, Pergamon Press, New York, 1985, http://www.srim.org/

[5] K. Niita, et al.: Phy. Rev. C, 52, 2620 (1995).

[6] H. W. Bertini: Phys. Rev. 188, 1711 (1969).

[7] J. Lindhard, V. Nielsen, M. Scharff and P.V. Thomsen: Mat. Fys. Medd. Dan. Vid. Selsk., Vol. 138, No. A1815 (1965).

[8] K.B. Winterbon, P. Sigmund and J.B. Sanders: Mat. Fys. Medd. Dan. Vid. Selsk. 37, 14 (1970).

[9] M.J. Norgett, M.T. Robinson and I.M. Torrens: Nucl. Engineering and Design, 33, 50 (1975).

[10] G.H. Kinchin and R.S. Pease, Rep. Progr. Phys., 18, 1 (1955).

29. Developments in INC model for extension for low energy region and cluster-induced reactions

Masakatsu YOSHIOKA, Yusuke SAWADA, Sho NOGAMINE and Yusuke UOZUMI
Department of Applied Quantum Physics and Nuclear Engineering
Kyushu University, 744, Motooka, Nishi-ku, Fukuoka 819-0395, Japan
e-mail: yoshioka-m@nucl.kyushu-u.ac.jp

There is an increasing demand to make INC applicable at low incident proton (or neutron) energies from 200 MeV down to 20 MeV. Another request for INC is the extension to light-cluster induced nuclear reactions. We modified the INC model to include refraction and nucleon correlation. The new model indicated reasonable agreements with the experimental data of (p, p'x) at bombarding energies 20 – 100 MeV, (d, d'x), and (α, p) reactions.

1. Introduction

The particle transport code PHITS [1] uses the intranuclear cascade (INC) model as the nuclear reaction model. To realize the event generator model in the incident energy range above 20 MeV, INC must be modified to obtain good predictive power in this low energy domain. The feature of INC should be the hard NN collision and the straight trajectory of nucleons inside nucleus. Due to the hard NN collision, the direct reactions are not reproduced. Although a great portion of outgoing particle spectra are contributed by the direct reaction component, there are still wide continua at beam energies around 20 MeV. Here, we restrict ourselves to improve the trajectory. We investigate influence of diffraction to (p,p'x) reactions.

The other question of PHITS may be light-cluster induced nuclear reactions. Nucleus-nucleus reactions are treated by the quantum molecular dynamics (QMD) model in PHITS. It gives good accounts of outgoing nucleon spectra from $^{12}C+^{12}C$ reactions at 200-400 MeV/u. However, large discrepancies are shown in light-cluster induced reactions such as (d,d'x) reactions and (α, px) reactions. Although INC does not consider clusters, we succeeded in cluster emission from proton-nucleus reaction. We apply the same prescription in describing the incident cluster to extend INC to cluster induced reactions.

In the present work, we first investigate improvement of the INC applicability in low energy range. Secondly, we extend the INC model to light cluster induced reactions. Physics idea is explained briefly, and then the proposed model is validated via comparison with experimental data.

2. Model

2.1 Outline of intranuclear cascade model

The prescription of the present INC model calculation is detailed in Ref. [2]; here we describe sole the essential points. Initially, the nucleus is considered to be sphere containing consistent nucleons with complete isospin degeneracy. Each nucleon has position and momentum and travels inside the nucleus freely. The time evolution of each nucleon is given by

$$d\vec{r}(t) = \frac{\vec{P}}{m}\Delta t.$$

When two nucleons approach within a distance equivalent to the nucleon-nucleon cross section, they undergo a collision. Pauli blocking, this is essential in fermionic interaction process, is introduced phenomenologically. The scattering angle is determined randomly to reproduce experimental angular distributions in a way that covers energy and momentum.

2.2 Diffraction for low-energy reactions

In bombarding energy range below 100 MeV, nuclear diffraction plays a significant role in large angle scattering. The quantum feature of nucleon-nucleus interactions is described by the stochastic scattering prescription [3], which is used to reproduce NN scattering in many nuclear reaction models such as INC and QMD. We display in fig. 1 the conceptual diagram about refraction effect. The gross tendency of elastic scattering angular distributions was parameterized to introduce nucleon diffraction phenomenon. The influence was treated in the final state interaction. Presently, kinetics due to diffraction is considered.

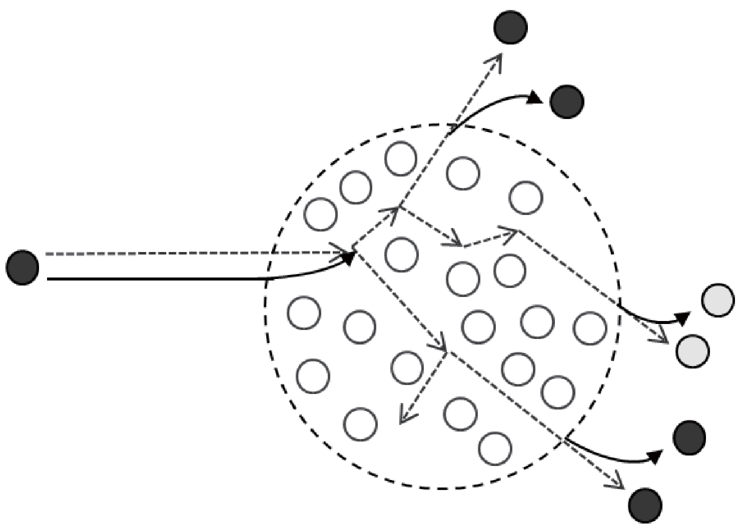

Fig. 1 Conceptual diagram about refraction effect. Black lines are refraction effect. Dashed lines are previous model.

2.3 Cluster-induced reactions

We have introduced nucleon correlations into the initial and the final state interaction [4] to explain cluster productions from proton-nucleus reactions. The initial state interaction generates cluster state as a higher order component of ground state wave function of target nucleus. We use the same fashion to describe the ground state of incident cluster, deuteron and α particle.

3. Comparison with experimental data

In order to investigate the predictive power of the proposed our INC model, we carried out calculations double differential cross-sections and compared with experimental data.

3.1 Low-energy (p,p’x) reactions

We display in fig. 2 the typical results of our calculation of the low-energy reactions. The solid lines are the present results, dashed lines are the previous ones and Dots are experimental data. We can see the backward angles energy spectrums are improved, with the exception of direct process.

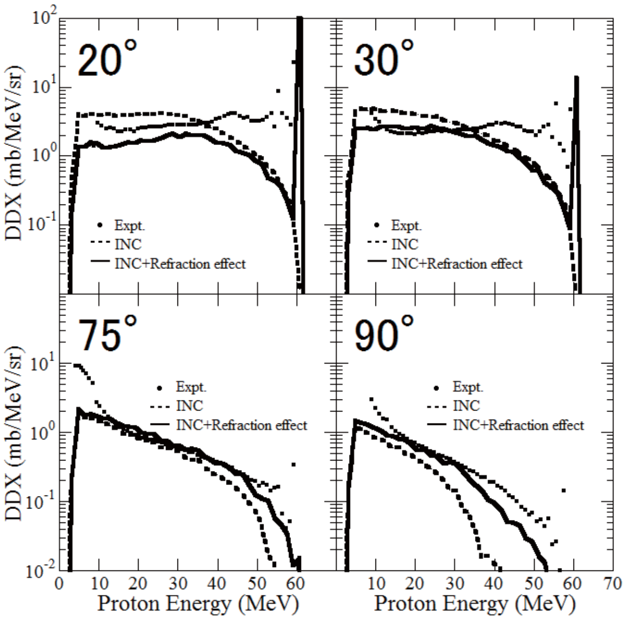

Fig. 2 Comparison between calculated and experimental data of ^{56}Fe(p,p’x) at 61.5 MeV.

3.2 Cluster-induced reactions

We display in figs. 3 - 6 the results of our calculation of the ^{12}C(α,p’x) at 400 MeV, ^{28}Si(α,p’x) at 400 MeV, ^{27}Al(α,p’x) at 720 MeV and ^{181}Ta(α,p’x) at 720 MeV. We display in fig. 7 and fig. 8 the results of our calculation of the ^{27}Al(d,d’x) at 100 MeV and ^{58}Ni(d,d’x) at 100 MeV. We display in fig. 9 and fig. 10 the results of our INC model and QMD model in PHITS of the deuteron spectrum for the cluster generation reactions.

We can see the calculated nucleon generation spectrums are overestimated at forward angle. By contrast, calculated spectrums have a good agreement with experimental data at the backward angles. We can see the calculated cluster generation results are not very good at the backward angles. Fig. 9 shows that INC model and QMD model have a good agreement with experimental data, but fig. 10 shows QMD model does not have a good agreement with experimental data.

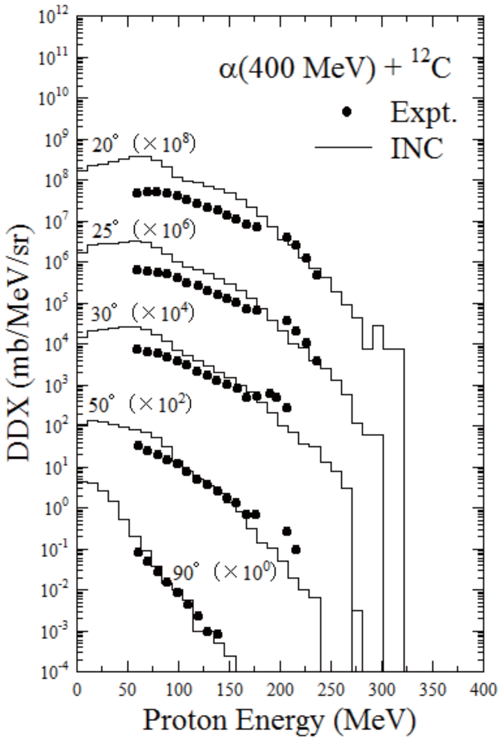

Fig. 3 Comparison between calculated and experimental data [5] of ^{12}C(α,p'x) at 400 MeV.

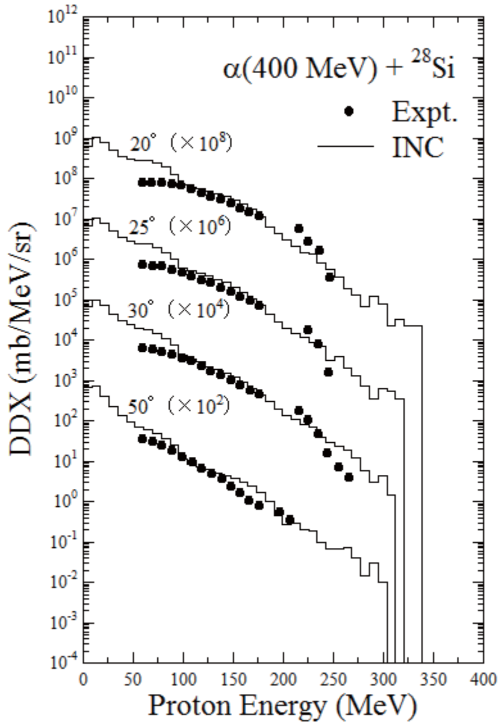

Fig. 4 Comparison between calculated and experimental data [5] of ^{28}Si(α,p'x) at 400 MeV.

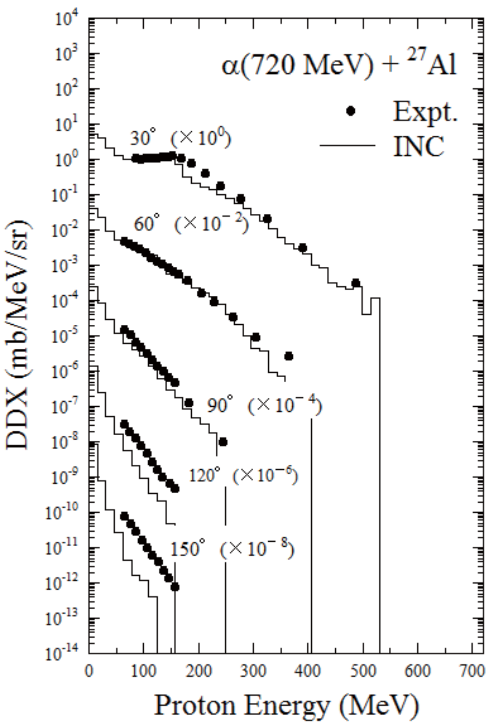

Fig. 5 Comparison between calculated and experimental data [6] of ^{27}Al(α,p'x) at 720 MeV.

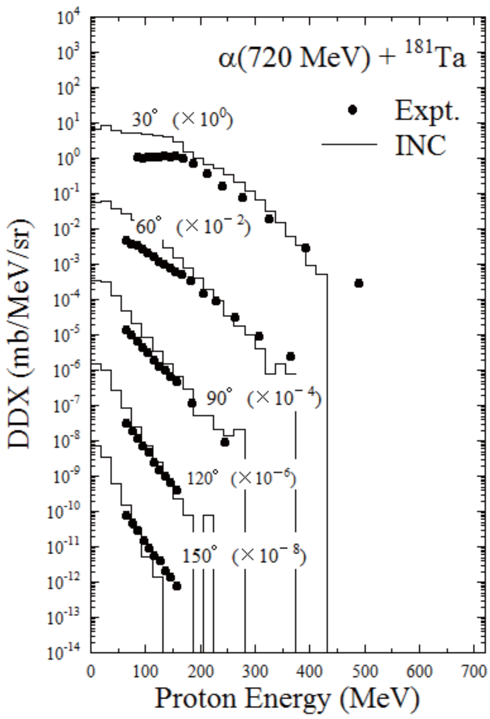

Fig. 6 Comparison between calculated and experimental data [6] of ^{181}Ta(α,p'x) at 720 MeV.

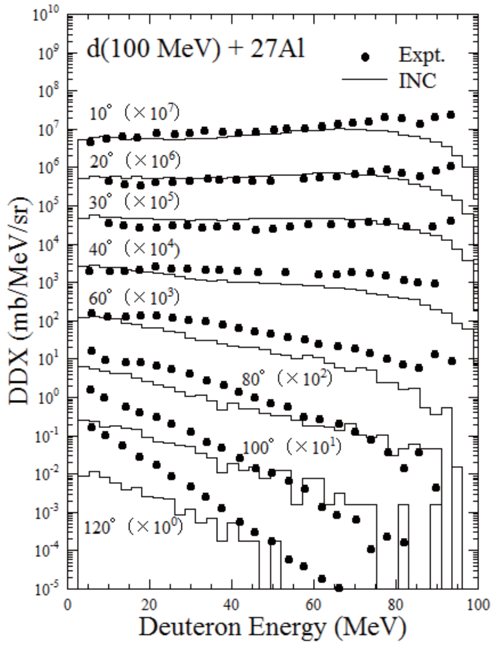

Fig. 7 Comparison between calculated and experimental data [7] of ^{27}Al(d,d'x) at 100 MeV.

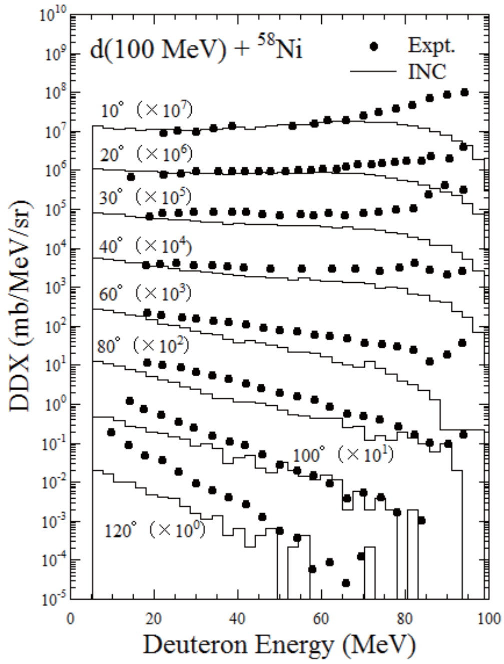

Fig. 8 Comparison between calculated and experimental data [7] of ^{27}Al(d,d'x) at 100 MeV.

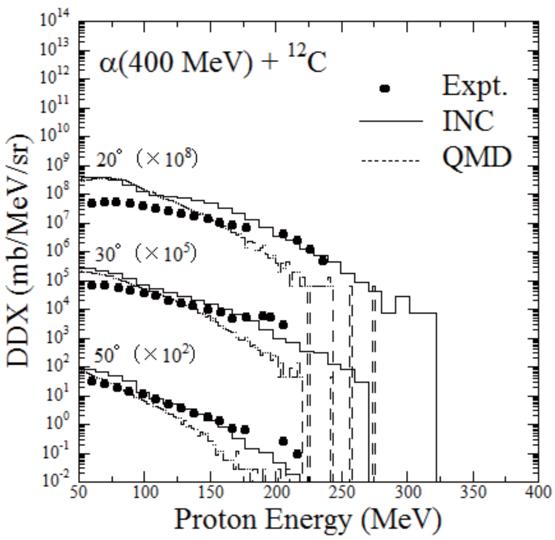

Fig. 9 Comparison among INC model, QMD model and experimental data of ^{12}C(α,p'x) at 400 MeV.

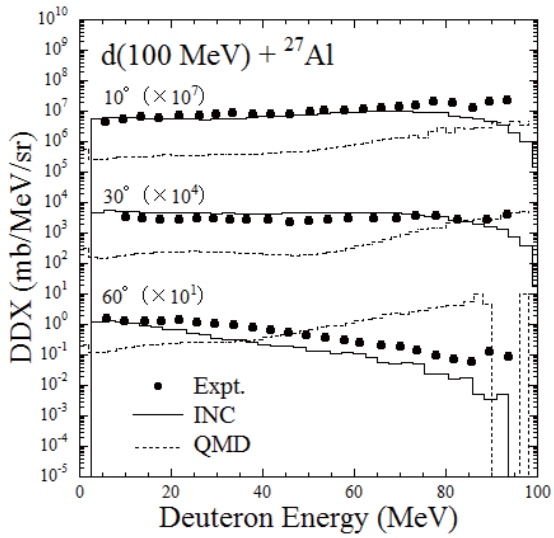

Fig. 10 Comparison among INC model, QMD model and experimental data of ^{27}Al(d,d'x) at 100 MeV.

4. Conclusion

We have investigated the low-energy reactions and cluster induced reactions of the INC model by comparing with the experimental data. We take nucleon correlation into incident-nucleon and emitted particle in our INC model to improve low-energy reactions. And we take extension to light-cluster induced reactions in our INC model, and we investigate a cluster-induced nucleon and cluster generation reactions.

Predictions our INC model is reasonably good.

References

[1] K. Niita, T. Sato, H. Iwase, H. Nose, H. Nakashima, L. Sihver: "PHITS-a particle and heavy ion transport code system", Radiation Measurement, **41**, Nos, 7-8, 1080-1090 (2006)

[2] H. Iwamoto: "New INC modek including nuclear correlation" in Japanese, Doctoral thesis, Kyushu-Univ. (2010)

[3] J. Cugnon, D. D' Hote and J. Vandermeulen: "Simple parameterization of cross-section for nuclear transport studies up to GeV range", Nucl. Instr. Meth. B **111**, 215 (1996)

[4] Y. Uozumi and H. Iwamoto: "New inranuclear cascade model including nucleon correlations and wave motion", *To be submitted to Proc. Int. Conf. Nuclear Data for Science and Technology (ND2010)*, Jeju Island, Korea, Apr. 26-30, 2010.

[5] F. Kondo: " Study of nuclear reactions induced by 400 MeV alpha" in Japanese, Master thesis, Kyushu-Univ. (2003)

[6] K. R. Cordell, S. T. Thornton, L. C. Dennis, R.R. Doering, R. L. Parks and T. C. Schweizer: "Proton inclusive cross sections from 720 MeV α-nucleus reactions", Nucl. Phys. **A 362**, 431-444 (1981)

[7] D. Ridikas, W. Mitting, H. Savajols and P. Roussel-Chomaz: "Inclusive proton production cross sections in (d,xp) reactions induced by 100 MeV deutrons", Phys. Rev. C. **63**, 14610 (2000)

30. A Study of Pre-equilibrium Reaction Induced by Neutron for Nickel

Myeonghwan Mun*, Young-Ouk Lee , Hyeong Il Kim
Korea Atomic Energy Research Institute,
Daeduk-daero 1045, Dukjin-dong, Yuseong-gu, Daejeon, Korea
e-mail: mhmoon@kaeri.re.kr

Nuclear reaction models play an important role in producing the reasonable nuclear data which is needed not only for fundamental research in nuclear physics but also practical applications in the field such as nuclear technology, medicine and industry. The reaction models can be divided into three parts, direct, pre-equilibrium and compound reaction in terms of time scales. The direct and compound models have been developed well so as to reproduce experimental data, but the pre-equilibrium model is sometimes in discrepancies with the measurements available. With a focus on improvement of pre-equilibrium models, we have performed nuclear reaction calculations for natural nickel induced by neutron in the incident energy up to 20 MeV using the TALYS code and compared with the available experimental data.

1. Introduction

The nuclear cross sections are essential for the simulation of nuclear related applications such as the reactor core simulation, radiation shielding calculation in the accelerator, the spacecrafts and other nuclear facilities, and radioisotope production for medical and industrial applications. Because nickel is the important structural material almost omnipresent in any nuclear power reactor with iron, nuclear reaction data with high accuracy on nickel are of considerable importance for testing nuclear reaction models and for studying radiation damage.

Nuclear cross section data needed for those nuclear applications can be produced by fitting the measured data or by nuclear model calculations. However, it is almost impossible to obtain the measurements in a full energy region and for all physical quantities possible. The nuclear model calculations can cover the shortcomings of the experiments and help for one to comprehend the nuclear reaction mechanism. In these days, nuclear reaction codes employing the up-to-date nuclear theory can describe the detail nuclear reaction mechanism through the rapid developments of modern computing system.

This work aims at understanding a comprehensive nuclear reaction mechanism and producing the more accurate nuclear data for nickel required at nuclear related fields. Especially this work focuses on the pre-equilibrium reaction which shows some discrepancies with the measured data unlike direct and compound ones. The employed nuclear reaction code is Talys [1] which provides a complete and accurate simulation of nuclear reactions in the 1keV-200 MeV energy range.

2. Nuclear reaction models

Nuclear reactions are described by several models which are linked together to calculate nuclear cross sections. An outline of the general theory and modeling of nuclear reactions can be given in many ways. These can be distinguished as three main types of reaction mechanisms according to their reaction times. A direct reaction happens after one or two collisions inside the target nucleus on a short time scale (typically $\sim 10^{-22}$ s). On the other hand, the compound reaction that proceeds via the formation of the compound nucleus occurs in the relatively long time ($10^{-16} \sim 10^{-18}$ s). The pre-equilibrium reaction takes place at intermediate time ($10^{-20} \sim 10^{-22}$ s) between direct and compound reactions. Figure 1 shows the cross sections as a function of outgoing neutron energy and the contribution of each reaction mechanism.

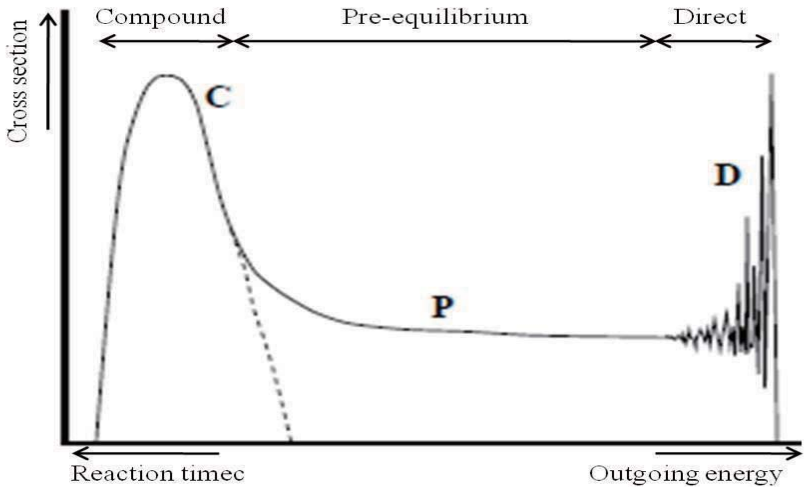

Fig. 1. Scheme of the outgoing particle spectrum.

2-1. Nuclear reaction models in TALYS code

TALYS is a comprehensive computer code system for the analysis and prediction of nuclear reactions like EMPIE code [2]. This code has been used for the complete and accurate analysis of basic experimental or to evaluate nuclear data for applications. It provides a simulation of nuclear reactions which involve neutrons, protons, deuterons, tritons, gamma-rays, ^{3}He- and alpha-particles as projectiles and ejectiles, in the incident energy range from 1 keV to 200 MeV and for target nuclides of mass between 12 and 239. It involves various nuclear models such as level density, the optical model, compound reactions by Hauser-Feshbach statistical model theory, pre-equilibrium processes by two-component exciton model theory and fission. It calculates total and partial cross sections, energy spectrum angular distributions, double-differential spectra, residual production cross sections and recoils. In addition, all the calculated data can be stored in files separately. An overview of the nuclear models that are implemented in TALYS is shown Figure 2.

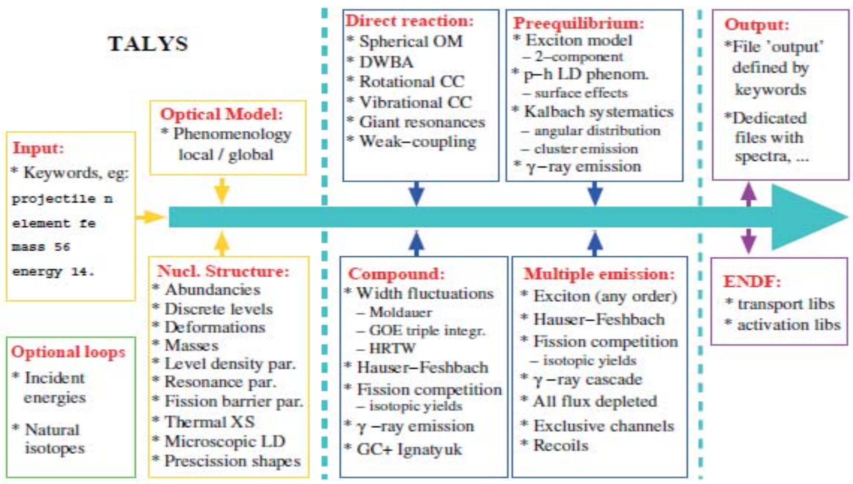

Fig. 2. Nuclear models in TALYS.

2-2. Pre-equilibrium reaction model

Pre-equilibrium emission plays an ever more important role in nucleon-induced reactions as the incident energy increases above 10 MeV. Several theoretical models, semi-classical or quantum mechanical, have been developed to account for emission of pre-equilibrium reactions over the last many years. Among these, the semi-classical exciton model [3] proposed by J.J. Griffin in 1966 is widely used in practical applications because of the reason that it is easy to carry out computationally.

In the exciton model, the nuclear state is characterized, at any moment during the reaction, by the total energy E^{out} and the total number of particles p above and holes h below the Fermi energy. The feature of the exciton model is a time-dependent master equation which describes the probability of transition to more or less complex particle-hose state so-called exciton states as well as transitions to the particle emission. In the exciton model, the basic formula of differential cross section for the emission of particle k with energy E_k can be expressed as

$$\frac{d\sigma_k^{PE}}{dE_k} = \sigma^{CF} \sum_{p_\pi = p_\pi^0}^{p_\pi^{max}} \sum_{p_\nu = p_\nu^0}^{p_\nu^{max}} W_k(p_\pi, h_\pi, p_\nu, h_\nu)\tau(p_\pi, h_\pi, p_\nu, h_\nu) \times P(p_\pi, h_\pi, p_\nu, h_\nu)$$

The expression for $P(p_\pi, h_\pi, p_\nu, h_\nu)$ contains the adjustable transition matrix element M^2 for each possible transition between neutron-proton exciton configurations. The matrix element is given by

$$M^2 = \frac{C_1 A_p}{A^3}\left[7.48C_2 + \frac{4.62\times10^5}{\left(\frac{E^{tot}}{n.A_p} + 10.7C_3\right)^3}\right]$$

where C_1, C_2 and C_3 are adjustable constants, which enable a fit to angle-integrated outgoing neutron and proton spectra.

Semi-classical models, such as the exciton model, have some problems to express angular distributions. Therefore the double-differential cross sections are obtained from the calculated energy spectra using the kalbach systematic [4].

3. Results

The energy and energy-angle spectra of secondary particles are essential. We compare the calculations of the nuclear reaction code TALYS with the existing experimental data of S. Matsuyama et al. [5], A. Takahashi et al. [6] and N. Yabuta et al. [7]. The neutron spectra and angular distributions calculated by TALYS code are illustrated in figure 3~6. Our calculations are obtained through adjusting the transition rates with the energy-dependent matrix elements.

As shown in Figures 3 and 4, the angular distributions for outgoing neutrons spectra are in rather good agreements with experimental data of N. Yabuta et al. at 14 and 18 MeV. In addition, the results have similar experimental data at low angle than large angle. Figures 5 and 6 describe the angle-integrated emission spectra for (n, xn) reactions at 14 and 18 MeV. These results agree well with the experimental data at 14 MeV but show some discrepancies at 18 MeV.

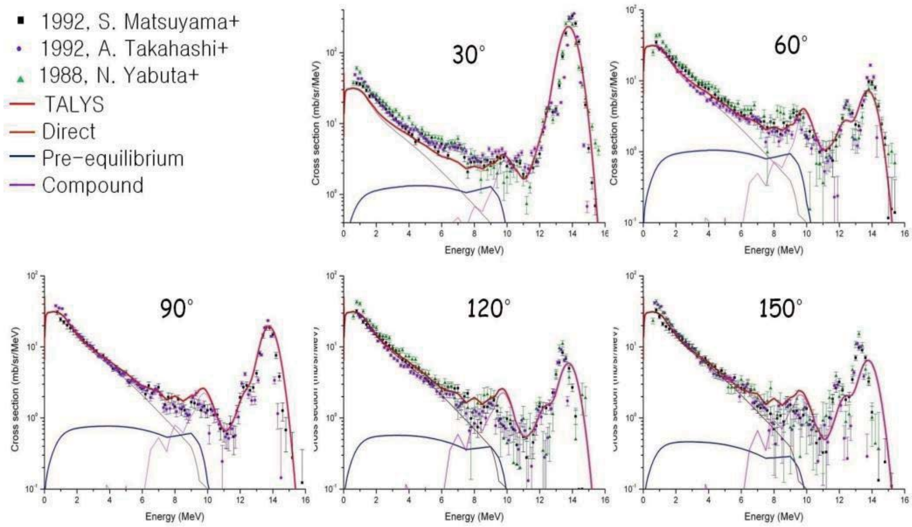

Fig. 3. The angular distributions for ^{nat}Ni neutron spectra at 14 MeV

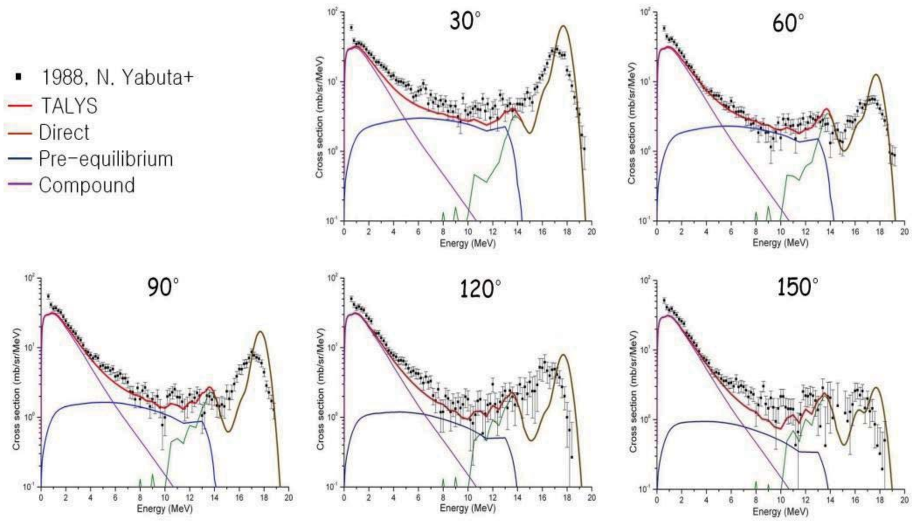

Fig. 4. The angular distributions for ^{nat}Ni neutron spectra at 18 MeV

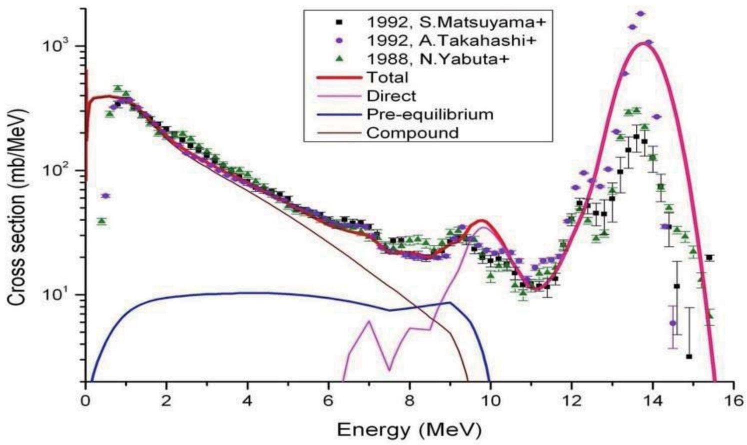

Fig. 5. The angle for ^{nat}Ni neutron spectra at 18 MeV

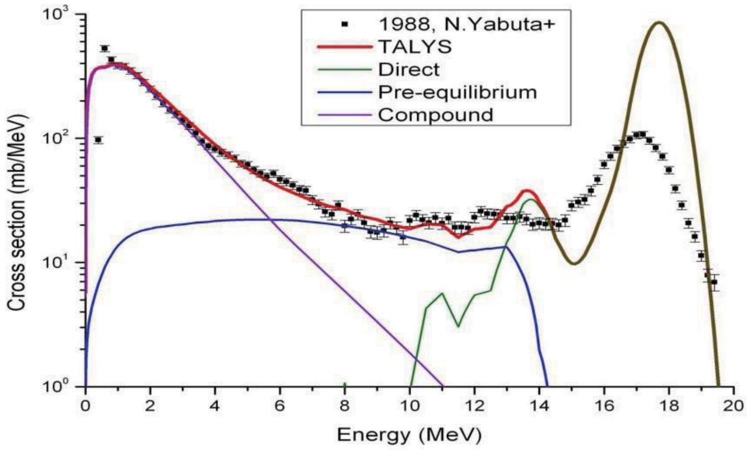

Fig. 6. The angular distributions for ^{nat}Ni neutron spectra at 18 MeV

4. Conclusion

Neutron-induced reactions on natural nickel have been studied using TALYS at the incident energy 14 MeV and 18 MeV. The neutron-induced differential cross sections have been compared with the available experimental data. Our calculations are in reasonable agreements with the measured data through adjusting the transition rates with the energy-dependent matrix elements at 14 MeV but show some discrepancies at 18 MeV. The Multistep direct/compound model showed similar under estimations for the emitted angle-dependent neutron spectra and larger discrepancies as incident neutron energies increase.

References

[1] A. Koning, S. Hilaire and M. Duijvestijn, TALYS-0.64 A nuclear reaction program, Report 21297/04.62741/P FAI/AK/AK, NRG Petten, 2004.
[2] M. Herman et al., Nucl. Data Sheets, 108 (2007) 2655.
[3] J. J. Griffin, Phys. Rev. Lett. 17 (1966) 478.
[4] Kalbach, C., Phys. Rev. C 37 (1988) 2350.
[5] MATSUYAMA S., OKUBO T., and BABA M. et al., Measurement of double differential neutron emission cross sections of Mo, Ta and W, JAERI-M-93-046［R］. Tokyo: JAERI, 1992.
[6] Takahashi A., Gotoh M., Sasaki Y., Sugimoto H., Double and Single Differential Neutron Emission and Integral Cross Sections at 14.1 MeV for Iron, Nickel and Oxygen. Tech. Rep. No. OKTAV-A-92-01, OKTAVIAN Reports of Original Papers and Data Tables, Japan, 1992.
[7] N. Yabuta and M. Baba et al., Double-differential neutron emission cross sections of Cr, Fe, Ni and Al, Conference on Nuclear Data For Science and Technology, Mito (1988), p. 291.

31. Preliminary evaluations and covariances of neutron-induced reactions for ^{237}Np and ^{240}Pu above resonance region

Hyeong Il Kim, Myeonghwan Mun, Do Heon Kim, Choop-Sup Gil, and Young-Ouk Lee
Korea Atomic Energy Research Institute
e-mail: hikim@kaeri.re.kr

Preliminary evaluations of neutron-induced cross section data including covariance matrices for ^{237}Np and ^{240}Pu above resonance region have been performed according to the needs of evaluation data with high accuracy for minor actinides, which are increasing for Advanced Fuel Cycle (AFC) design and nuclear safeguards applications. This work aims at providing the reliable evaluation data and their covariances above resonance region rather than a full energy range from 10^{-5} eV to 20 MeV. The nuclear reaction model calculations above resonance region have been performed with the EMPIRE code system that has been used to provide a number of consistent and complete evaluations. Covariance data have been generated by the KALMAN code implemented in the EMPIRE system (EMPIRE-KALMAN).

1. Introduction

Neutron-induced cross sections with covariances for Minor Actinides (MA) play a great role for an AFC design and safeguard applications as well as the design of new generation of nuclear reactors (GEN-IV), while the evaluations of the existing libraries, such as ENDF/B-VII.0 [1], JENDL-3.3 [2], and JEFF-3.1 [3] were performed about 20 ~ 30 years ago and then partially modified when new measured data had been reported. The neutron-induced evaluation for ^{237}Np of ENDF/B-VII.0, for instance, was released in 2006, but it was partially modified for fission and elastic cross sections, and average number of delayed neutrons from ENDF/B-VI in 1990 which had been propagated from previous version ENDF/B-V. The neutron cross section evaluations in those existing libraries were mainly performed by empirical fitting to the available measurements rather than model calculations with consistency. These kinds of evaluations can reproduce well the reactions of which the appropriate experimental data are available, while they could predict wrong cross sections for reactions if no or inappropriate experimental data are available.

In response to this situation, a KAERI-ORNL collaborative project was launched and charged with the neutron induced evaluations with covariances in the neutron-incident energy range up to 20 MeV for ^{237}Np and ^{240}Pu. KAERI is in charge of the nuclear data evaluations of fast neutron region including covariances, the merging them with resonance and its covariance data generated by ORNL, the checking the merged files as a s et of the CSEWG checking codes and the performing the benchmark test. This evaluation above resonance region is completely new for all physical quantities possible with the exception of average number of prompt (ν_p) and delayed (ν_d) neutrons released per fission event and fission spectra taken from JENDL-4.0 [4] which was released in May 2010.

We produced the preliminary neutron-induced evaluation files including covariance data for ^{237}Np and ^{240}Pu above resonance and compared them with the available experimental data and the existing libraries such as ENDF/B-VII.0, JEFF-3.1 and JENDL-4.0.

2. Neutron-induced evaluations

Nuclear data evaluation above resonance region has been performed with the EMPIRE [5] code system that has been used to provide a number of consistent, complete evaluations. The EMPIRE code calculates cross sections for all relevant reaction channels, angular distributions, exclusive and inclusive particle- and γ-spectra, double-differential cross sections, and spectra of recoils. Above resonance region, a number of nuclear reaction models have been developed to reproduce the measured data. Nuclear reactions models in the Empire code can be classified into three major classes: (i) optical model and direct reactions (Coupled-channels (CC) and Distorted-wave Born approximation (DWBA), (ii) preequilibrium emission, and (iii) Hauser-Feshbach statistical decay [6].

Parameterization of the optical model potential (OMP) is one of the most important tasks in the evaluation above resonance region. The good OMP guarantees reproductions of experimental data and, more importantly, a reliable prediction of unmeasured physical observables. We employed an isospin-dependent coupled-channels optical model potential containing a dispersive term for neutrons (Category number is 2408) from Reference Input Parameter Library (RIPL-II) [7]. The OMP parameters are recognized as reasonable ones if nuclear reaction calculations employing them reproduce the available experimental data such as total and elastic cross sections, and angular distributions of elastic scattering. However, ^{237}Np and ^{240}Pu considered in this work have insufficient experimental data except for those of total cross sections. Figure 1 shows the total and elastic cross sections compared to the measurements and to the ENDF/B-VII.0, JENDL-4.0 and JEFF-3.1 evaluations. Our results are in good agreement with the measured data of total cross sections for ^{237}Np and ^{240}Pu to the exclusion of the data measured low obviously. On producing elastic cross sections, we excluded the measured data of ^{237}Np with too big systematic/statistical error and those of ^{240}Pu no error.

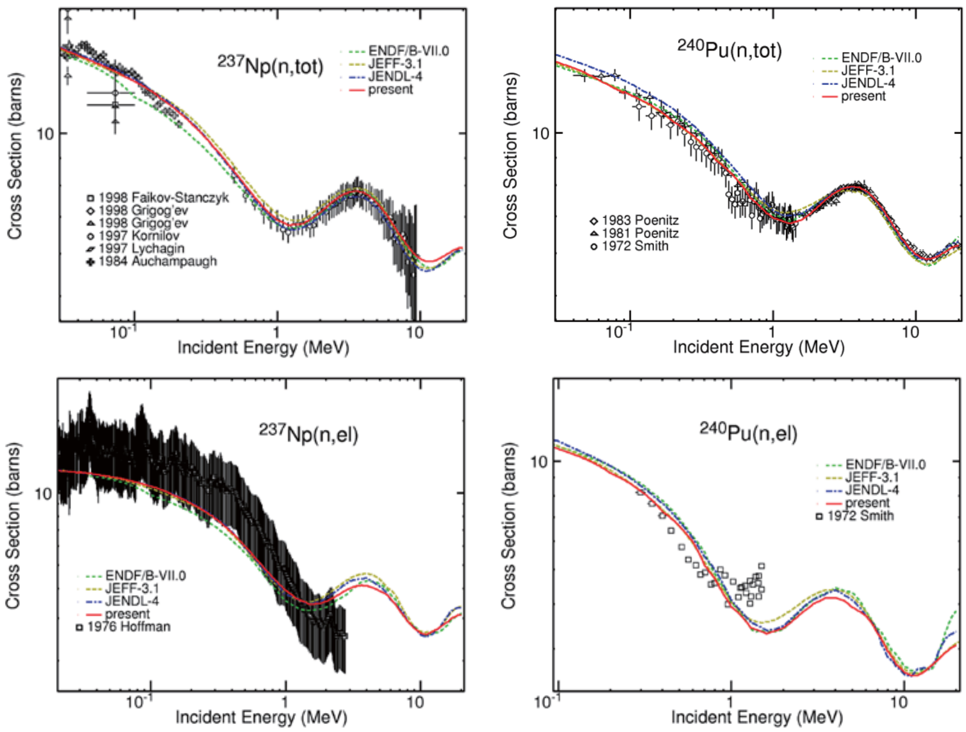

Fig. 1. Total and elastic cross sections for ^{237}Np and ^{240}Pu compared to the measurements and the ENDF/B-VII.0, JENDL-4.0 and JEFF-3.1 evaluations.

Because the minor actinides are usually considered as the deformed nuclides, the coupled channel calculations are recommended to good effect. In coupled-channel (CC) calculation, proper coupling provides cross sections for inelastic scattering to collective levels and related angular distributions of scattered neutrons. The DWBA calculations on several discrete levels were added so as to reproduce the measured data of the inelastic scattering cross sections on discrete levels. The CC and DWBA calculations can be ensured from double differential cross section or emitted neutron spectra. Double differential cross sections (DDX) of emitted neutrons are shown in Figure 2 at the neutron incident energies 1.46 MeV, 1.77 MeV and 2.47 MeV for ^{237}Np. As shown in Figure, the spectral energy region just below the elastic peak shows the effect of direct processes employing the CC+DWBA calculation. The straight line above the elastic peak is due to neutrons emitted from fission. The calculated cross sections are in good agreements with the measured data [8]. The angle integrated spectra of emitted neutron by incident neutron energy 14 MeV are shown in left plot of Figure 2. The emitted neutron spectra have similar shape for ^{237}Np and ^{240}Pu because the emitted neutron from fission reaction gives a dominant effect in spectra induced by neutron for actinides. Nevertheless, as shown in Figure, the shapes of nuclides just below the elastic peak are somewhat different due to the effects of CC and DWBA calculations.

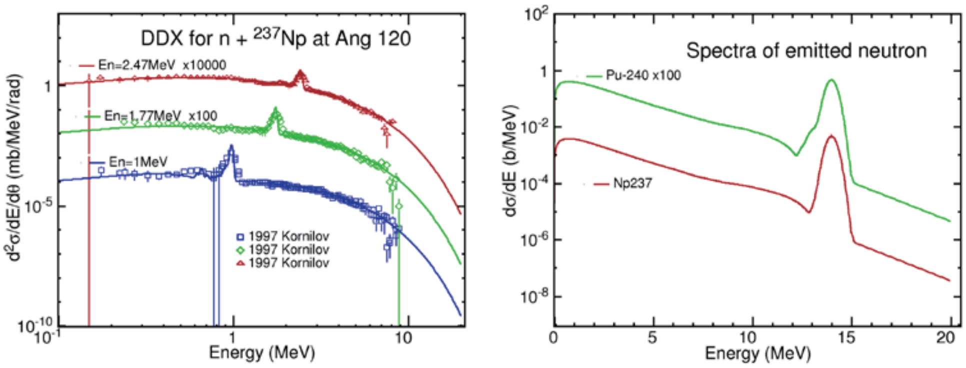

Fig. 2. Double differential cross section(DDX) compared with the measured data for ^{237}Np at neutron incident energies 1, 1.77 and 2.47 MeV. The left plot shows neutron spectra for ^{237}Np and ^{240}Pu at neutron incident energies 14 MeV.

The CC and DWBA calculations give big effects on direct reactions, and the transmission coefficients generated from them play a core role in other reaction channels, such as inelastic, capture, (n,2n) and (n,f). These reaction channels are calculated the Hauser-Feshbach statistical model which needs nuclear properties such as discrete levels, level densities and gamma strength function as well as the transmission coefficients. We employed the Empire-specific level densities and their parameters were adjusted by the cumulative fitting to known nuclear discrete levels taken from ENSDF and available experimental data. The gamma strength function developed by Plujko was employed. The Capture and (n,2n) cross sections of of ^{237}Np and ^{240}Pu are shown in Figure 3. When the experimental data are available, our results are in good agreement with them and appear similar trends with the ENDF/B-VII.0, JENDL-4.0 and JEFF-3.1 evaluations. However, each library brings out a different result for reaction, if no measurement is available. For instance, (n,2n) cross section of ENDF/B-VII.0 shows strange results just above threshold energy and is lower than those of other libraries up to 15 MeV. (n,2n) cross sections for ^{240}Pu of JENDL-4.0 is higher than those of other libraries. Because no measurements are available, it is difficult to determine which one is better, while we know that the increasing of (n,2n) cross sections in these region should brings down fission cross section which is more competitive reaction.

The fission probability has been incorporated into the Hauser-Feshbach statistical model which describes particle emissions. Of several fission models available in this code, we took into account the transmission coefficients derived in the WKB approximation within an optical model through a double humped fission barrier. Figure 4 shows fission cross sections of ^{237}Np and ^{240}Pu compared to the measurements and the ENDF/B-VII.0, JENDL-4.0 and JEFF-3.1 evaluations. Our results reproduce the up-to-date measurements by Basunia for ^{237}Np, and Tovesson [9] and Laptev [10] for ^{240}Pu, while ENDF/B-VII.0, JENDL-4.0 and JEFF-3.1 are close to the data by Lisowski which are measured in 1988. As mentioned above, the low fission cross sections of JENDL-4.0 give rise to the increase of (n,2n) cross sections.

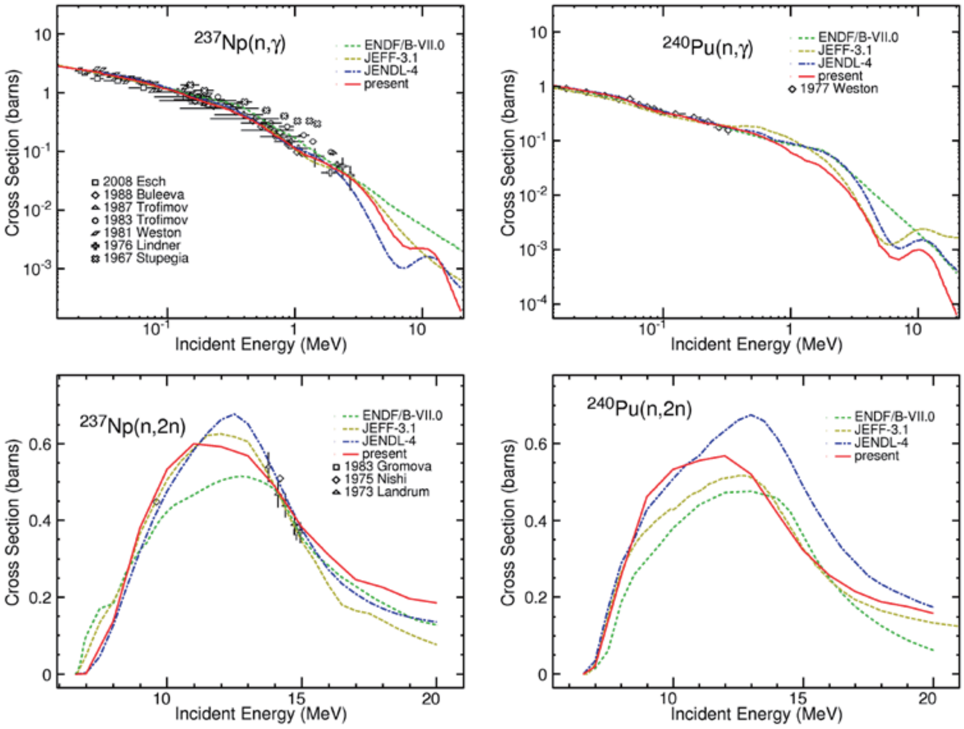

Fig. 3. Capture and (n,2n) cross sections of ^{237}Np and ^{240}Pu compared with the ENDF/B-VII, JENDL-4.0 and JEFF-3.1 evaluations.

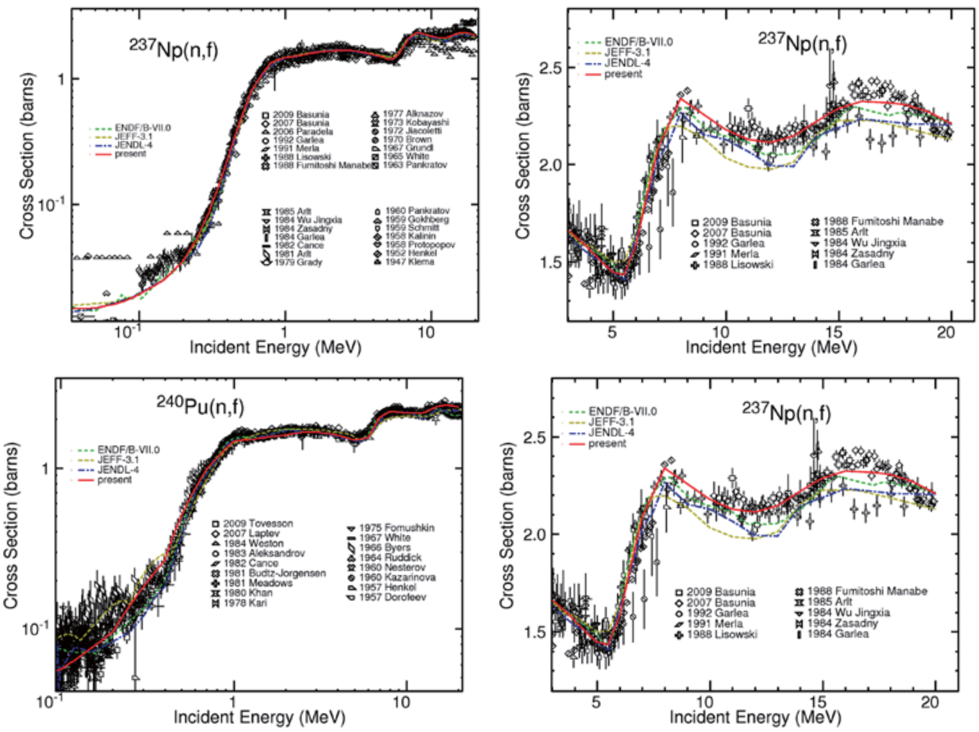

Fig. 4. Fission cross sections of of ^{237}Np and ^{240}Pu compared to the measurements and the ENDF/B-VII, JENDL-4.0 and JEFF-3.1 evaluations.

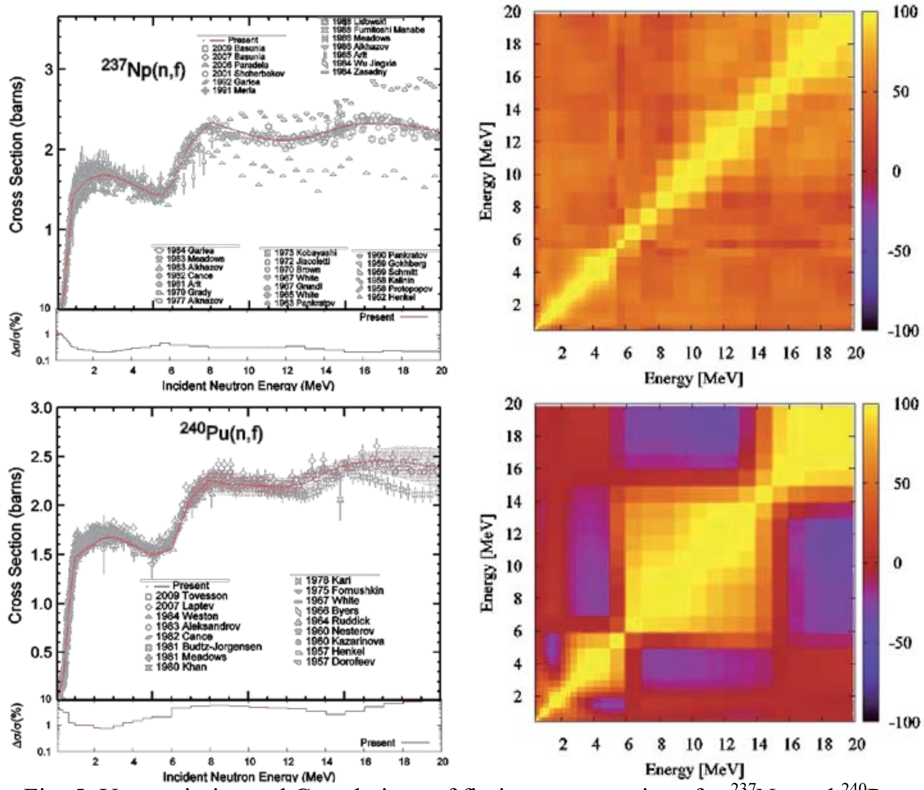

Fig. 5. Uncertainties and Correlations of fission cross sections for ^{237}Np and ^{240}Pu.

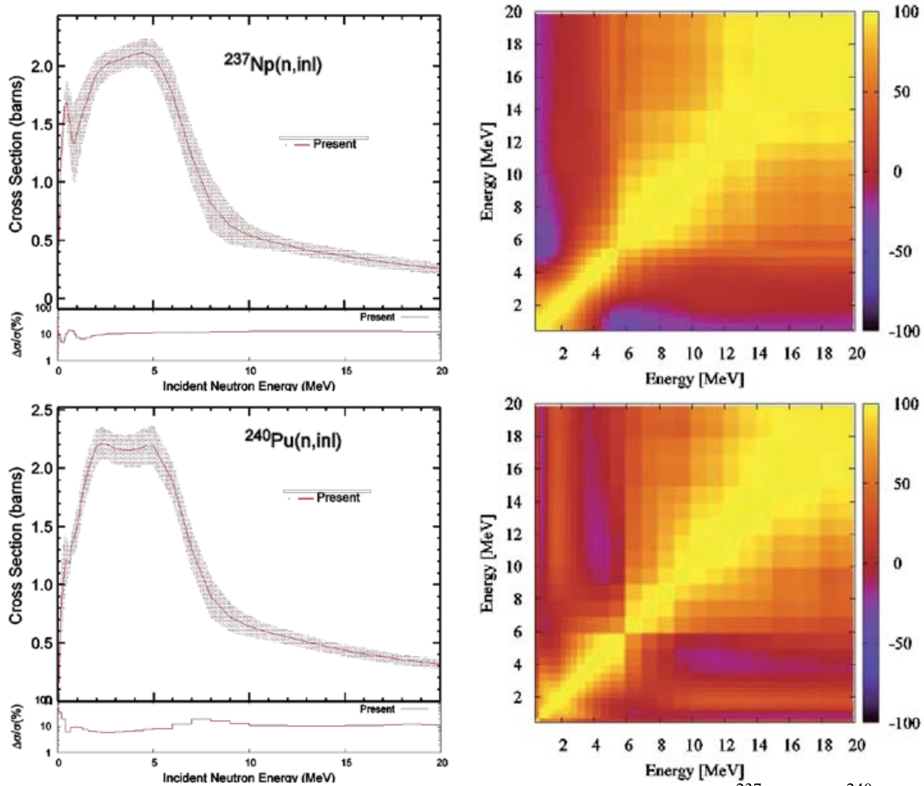

Fig.6. Uncertainties and Correlations of inelastic cross sections for ^{237}Np and ^{240}Pu.

3. Covariance data

Covariance data have been generated by the Kalman code implemented in the EMPIRE system

(EMPIRE-KALMAN). To generate covariance data, the Kalman code employs a sensitivity matrix calculated by the Empire code and measurements with uncertainties. The sensitivity matrix elements were calculated as a change of a given reaction cross section in response to the change of the particular model parameter. The measurements uncertainties are used to constrain variances of the models parameters. Thus the covariance data by this code accounts for the uncertainties of measurements and the model parameters ensuring that the final cross section uncertainties are at least as good as the smaller of two ones. However, if no experimental data are available, we need pseudo data which can constrain the uncertainties of model calculations. The sensitivity matrices in this work were obtained by variations of most relevant model parameters such as optical model, level densities, and the strengths of fission barriers. As preliminary results, about 10 % variations of model parameters around the optimal value were applied to determine their effects on total, elastic, inelastic, capture, fission, (n,2n) cross sections.

Figure 5 shows the uncertainties and correlations of fission cross sections of ^{237}Np and ^{240}Pu with available measurements. This appears the property of the Kalman filter which is at least as good as the smaller of both uncertainties of measurements and those of model calculations. Although it is somewhat doubtful that the total cross section uncertainties are 1 % or less, we will keep them at the moment. The reason showing different correlations between fission cross sections of ^{237}Np and ^{240}Pu is due to the measurements employed when the Kalman code worked. Figure 6 shows the uncertainties and correlations of inelastic cross sections for ^{237}Np and ^{240}Pu with no meausrements. In order to avoid too big uncertainties which could be generated by model calculation, we used pseudo cross section which can constrain the final cross section uncertainties to be 10% or less.

4. Conclusions

We produced the preliminary neutron-induced nuclear data including covariances for ^{237}Np and ^{240}Pu above resonance region. The neutron cross section data using the EMPIRE code system reproduce the measurements well, if available. Our cross section data based on the up-to-date nuclear physics theory can be reliable even if no measurement is available, because their competitive reactions reproduce measurements well. The covariance data were generated by the EMPIRE-KALMAN code which considers the sensitivity matrices calculated by EMPIRE and the measurements, if available. In case of no available measurements, we employed pseudo cross sections. However, too small uncertainties should be increased to a reasonable degree.

References

[1] M.B. Chadwick, "ENDF/B-VII.0: Next Generation Evaluated Nuclear Data Library for Nuclear Science and Technology," *Ncul. Data Sheets*, 107, 2931,(2006)

[2] K. Shibata, et al., "Japanese Evaluated Nuclear Data Library Version 3: JENDL-3.3," *J. Nucl. Sci. Technol.* 39, 1125 (2002)

[3] A. Koning, et al., "The JEFF-3.1 Nuclear Data Library", JEFF report21, ISBN 92-64-02314-3, 2006

[4] K. Shibata, et al., "JENDL-4.0: A New Library for Nuclear Science and Engineering," *J. Nucl. Sci. Technol.*, 48(1), 1-30 (2011)

[5] M. Herman, et al., "EMPIRE: Nuclear Reaction Model Code System for Data Evaluation", *Nucl. Data Sheets*, 108, 2655 (2007)

[6] W. Hauser, et al., "The inelastic scattering of neutrons", Phys. Rev., 87, 366 (1952)

[7] P. Young, et al., "Handbook for Calculations of Nuclear Reaction Data, RIPL-2", IAEA Tech. Rep. 1506, (2006), www-nds,iaea.org/RIPL-2/

[8] N. Kornilov, et al., "Inelastic Neutron Scattering and Fission Neutron Spectra for ^{237}Np", Proc. Intern. on Nuclear Data for Science and Technology, (1997)

[9] F. Tovesson, et al., "Neutron induced fission cross section of 237Np from 100 keV to 200 MeV", *Phys. Rev. C* 75, 034610 (2007)

[10] A.B. Laptev, et al., "Neutron Induced Fission Cross-Sections of 240Pu and 243Am in the Energy Range 1 – 200 MeV", *Nucl. Phys. A* 734, E45 (2004)

32. Effect of Newly-Measured Cross Sections of ^{157}Gd on Burnup Characteristics of High Burnup BWR UO_2 and MOX Assemblies

Yoshihira ANDO[1,*], Toru YAMAMOTO[1] and Peng Hong LIEM[2]

[1] Reactor Core and Fuel Reliability Group, Safety Standard Division
Japan Nuclear Energy Safety Organization (JNES)
TOKYU REIT Toranomon Bldg. 7F, 3-17-1, Toranomon,
Minato-ku, Tokyo 105-0001, Japan
[2] Nippon Advanced Information Service Corporation
Muramatsu 416, Tokai-mura Naga-gun Ibaraki-ken-1112, Japan
* E-Mail:ando-yoshihira@jnes.go.jp

Effect of newly-measured cross sections of ^{157}Gd by Leinweber et al. (2006) on burnup characteristics of high burnup BWR UO_2 and MOX assemblies was investigated by coupling burnup calculation using SRAC code with a modified JENDL-3.3 nuclear data library reflecting the above newly measured data. It was confirmed that meaningful differences on multiplication factors and fission distributions in the assemblies were observed mainly below 15GWd/t.

1 Introduction

Leinweber *et al.*[1] have reported new measurement data on neutron capture, total cross sections and resonance parameters of Gd isotopes. One of the prominent results was that the thermal (2200m/s) capture cross section of ^{157}Gd was 11% smaller compared with that in ENDF/B-VI.8[2]. Jatuffa *et al.*[3] have tested the newly-measured Gd isotope cross sections in the analysis of measured fission reaction rates of Gd_2O_3-UO_2 rods (Gd rods) in tested BWR UO_2 fuel assemblies in core physics experiments and reported that the new cross sections improved the discrepancy of the theoretically analyzed results from the measurements.

During the evaluation study of JENDL-4 [4], the adoption of the new measurement data was assessed. For this purpose a preliminary cross section library for a continuous energy Monte Carlo calculation code MVP[5] was prepared to test the new data of ^{157}Gd in the analysis of integral experiments [6]. Under this background, the present study was performed to evaluate the effect of the new data of ^{157}Gd on burnup characteristics of high burnup BWR UO_2 and MOX assemblies.

2 Comparison of Capture Cross Section of ^{157}Gd

Thermal capture cross sections of ^{157}Gd measured in experiments and adopted in recent nuclear data libraries are shown in Table 1, which were provided by K.Shibata[7] and the cross section adopted in nuclear data libraries were evaluated at 300K. In the evaluation of cross sections of JENDL-4.0, the data of Leinweber et al. were used. However, the background cross sections of ^{157}Gd below 0.1eV were determined through the sensitivity study using ICSBEP critical benchmark data [8].

Table 1 Comparison of thermal capture cross section of ^{157}Gd

<table>
<tr><th>Author</th><th>Energy (eV) ***</th><th>Capture Cross Section (barns)</th></tr>
<tr><td>Pattenden '58</td><td>0.0253</td><td>264000±4500</td></tr>
<tr><td>Tattersall '60</td><td rowspan="2">Maxwell</td><td>213000±2000</td></tr>
<tr><td>Groshev '62</td><td>240000±12000</td></tr>
<tr><td>Leinweber '06*</td><td rowspan="9">0.0253</td><td>226000</td></tr>
<tr><td></td><td></td></tr>
<tr><td>Mughabghab '06**</td><td>254000±815</td></tr>
<tr><td>JENDL-3.3</td><td>253681</td></tr>
<tr><td>JENDL-4.0</td><td>253251</td></tr>
<tr><td>ENDF/B-6.8</td><td>253747</td></tr>
<tr><td>ENDF/B-7.0</td><td>253747</td></tr>
<tr><td>JEF-2.2</td><td>253272</td></tr>
<tr><td>JEFF-3.1.1</td><td>253272</td></tr>
</table>

* : Calculated value based Leinweber et al. [1]

** : Evaluation

*** : Energy installed in EXFOR

3 Preparation of modified ^{157}Gd cross section

New point-wise cross sections of ^{157}Gd corresponding to the measurement of Leinweber et.al,.were prepared for a MVP library [6]. Comparisons of the new and old cross sections of ^{157}Gd were performed using MVP for a Gd_2O_3−UO_2 cell in high burnup BWR UO_2 and MOX assemblies shown in Figure 1. A new SRAC cross section library was prepared based on the above comparative results.

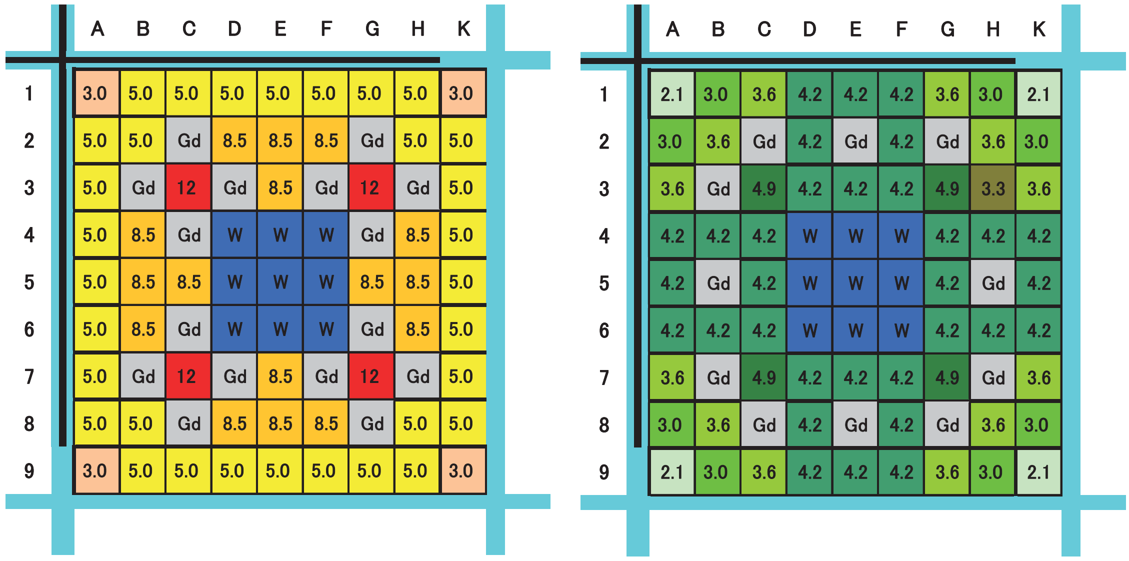

Average Total-Pu=4.9wt%、U-235 in MOX = 0.2wt%
Gd_2O_3 fuel : 2%wt-Gd and 4.9wt%-U235

Average U-235 =3.8wt%
Gd_2O_3 fuel : 5%wt-Gd and 3.6wt%-U235

Figure 1 High Burnup BWR Fuel Assembly

Burnup calculations in an assembly-geometrical-model were performed by SRAC code[9] with the 107 neutron energy group cross section library prepared from JENDL-3.3 as the base cases. The ratio of ^{157}Gd capture cross section between the modified and the original JENDL-3.3 libraries calculated by MVP is shown in Figure 2.

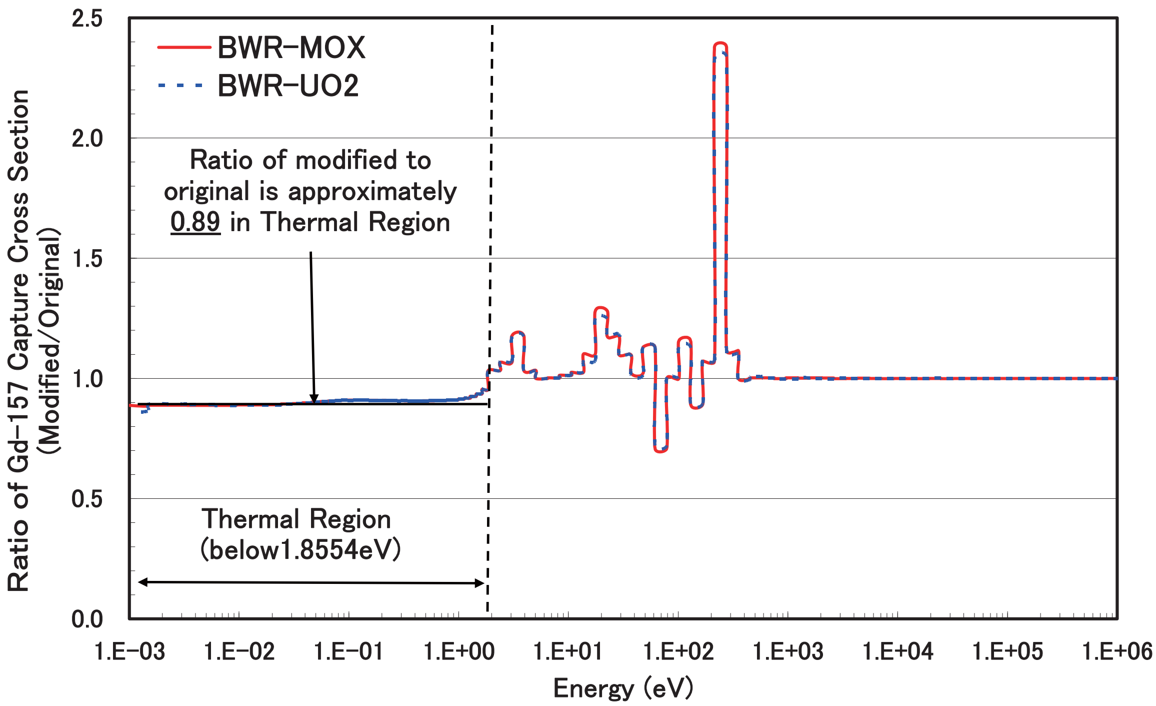

Figure 2 Ratio of ^{157}Gd capture cross section between modified and original libraries

A modified SRAC library was prepared where a correction factor 0.89 was applied to infinite dilution capture cross of ^{157}Gd in SRAC public thermal library prepared for the energy range below 1.8554eV. In the preparation of the modified cross section library, total cross sections were also adjusted corresponding to the correction of the capture cross sections, however, the shielding factors of capture cross sections of ^{157}Gd were not changed.

4 SRAC Burnup Calculation

Burnup calculations were performed with SRAC-Pij module using both the original and the modified JENDL-3.3 libraries. A 2D-infinite assembly model was applied as the burnup calculation model. Rated power histories of BWR fuel assembly were used, whose power density, pellet/moderator temperatures and in-channel void fraction were 50.4 kW/ l , 520℃/286℃ and 40%, respectively. Control blade was withdrawn in all the irradiation period and cooling period was not set up. The comparisons of neutron multiplication factors and fission rate distributions between the burnup calculations using the modified and the original libraries were performed and showed in Figs. 3 and 4, respectively.

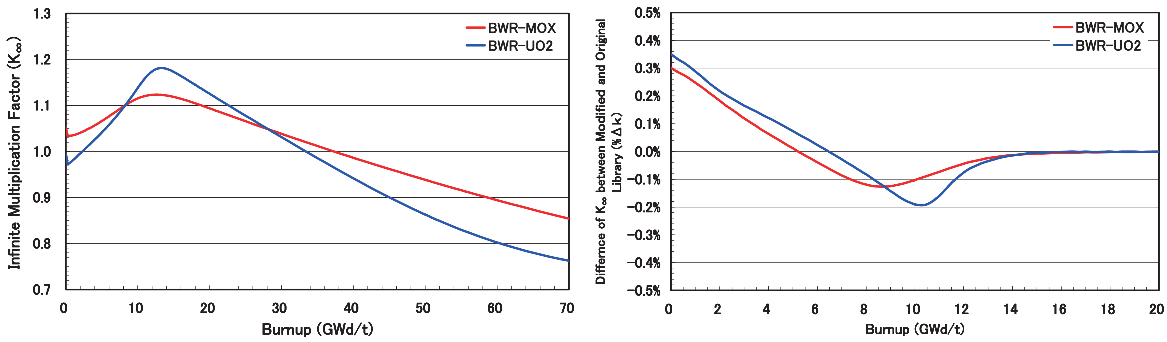

Figure 3 Comparison of Infinite Multiplication Factors

The differences in the infinite multiplication factors of the fuel assemblies between modified and original cross section library are 0.35%Δk in the UO_2 fuel assembly and 0.30%Δk in the MOX fuel assembly at the beginning of life (BOL), and they decrease with burnup and finally extinguish at 15GWd/t.

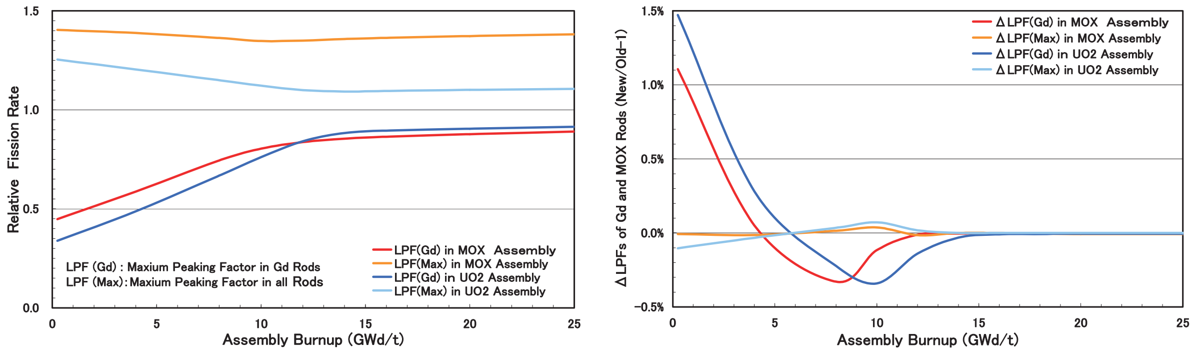

Figure 4　Comparison of Fission Rate Distribution

Peaking factors in Gd rods reach equilibrium state at 12GWd/t. Effect on fission rate distribution reveals mainly at the BOL and extinguishes at 15GWd/t. The comparison of fission rate distributions at the BOL is shown in Figure 5.

MOX

1.253	1.340	1.166	1.099	1.081	1.099	1.166	1.340	1.253
1.340	0.932	0.412	1.045	1.068	1.045	0.412	0.932	1.340
1.166	0.412	1.246	0.448	1.404	0.448	1.246	0.412	1.166
1.099	1.045	0.448				0.448	1.045	1.099
1.081	1.068	1.404				1.404	1.068	1.081
1.099	1.045	0.448				0.448	1.045	1.099
1.166	0.412	1.246	0.448	1.404	0.448	1.246	0.412	1.166
1.340	0.932	0.412	1.045	1.068	1.045	0.412	0.932	1.340
1.253	1.340	1.166	1.099	1.081	1.099	1.166	1.340	1.253

Max = 1.404、Min = 0.412

-0.24%	-0.21%	-0.16%	-0.19%	-0.20%	-0.19%	-0.16%	-0.21%	-0.24%
-0.21%	-0.08%	0.92%	0.05%	-0.08%	0.05%	0.92%	-0.08%	-0.21%
-0.16%	0.92%	0.17%	1.11%	-0.01%	1.11%	0.17%	0.92%	-0.16%
-0.19%	0.05%	1.11%				1.11%	0.05%	-0.19%
-0.20%	-0.08%	-0.01%				-0.01%	-0.08%	-0.20%
-0.19%	0.05%	1.11%				1.11%	0.05%	-0.19%
-0.16%	0.92%	0.17%	1.11%	-0.01%	1.11%	0.17%	0.92%	-0.16%
-0.21%	-0.08%	0.92%	0.05%	-0.08%	0.05%	0.92%	-0.08%	-0.21%
-0.24%	-0.21%	-0.16%	-0.19%	-0.20%	-0.19%	-0.16%	-0.21%	-0.24%

%-RMS＝1.02/ 0.50 for Gd/Average Rod

UO_2

1.045	1.165	1.172	1.254	1.209	1.254	1.172	1.165	1.045
1.165	1.021	0.338	0.980	0.339	0.980	0.338	1.021	1.165
1.172	0.338	1.077	1.144	1.201	1.144	1.077	0.338	1.172
1.254	0.980	1.144				1.144	0.980	1.254
1.209	0.339	1.201				1.201	0.339	1.209
1.254	0.980	1.144				1.144	0.980	1.254
1.172	0.338	1.077	1.144	1.201	1.144	1.077	0.338	1.172
1.165	1.021	0.338	0.980	0.339	0.980	0.338	1.021	1.165
1.045	1.165	1.172	1.254	1.209	1.254	1.172	1.165	1.045

Max = 1.254、Min = 0.338

-0.19%	-0.16%	-0.12%	-0.10%	-0.08%	-0.10%	-0.12%	-0.16%	-0.19%
-0.16%	-0.07%	1.51%	-0.01%	1.47%	-0.01%	1.51%	-0.07%	-0.16%
-0.12%	1.51%	0.02%	-0.05%	-0.06%	-0.05%	0.02%	1.51%	-0.12%
-0.10%	-0.01%	-0.05%				-0.05%	-0.01%	-0.10%
-0.08%	1.47%	-0.06%				-0.06%	1.47%	-0.08%
-0.10%	-0.01%	-0.05%				-0.05%	-0.01%	-0.10%
-0.12%	1.51%	0.02%	-0.05%	-0.06%	-0.05%	0.02%	1.51%	-0.12%
-0.16%	-0.07%	1.51%	-0.01%	1.47%	-0.01%	1.51%	-0.07%	-0.16%
-0.19%	-0.16%	-0.12%	-0.10%	-0.08%	-0.10%	-0.12%	-0.16%	-0.19%

%-RMS=1.49/0.62 for Gd/Average Rod

: Gd rod, : Max rod

Relative Fission Distribution at BOL (Original Library)

Relative Difference at BOL (Modified/Original-1)

Figure 5　Comparison of Fission Rate Distributions at BOL

The fission rates of Gd rods at the BOL increase by 1.1% and 1.5% in MOX and UO_2 fuel assemblies, respectively.

5　Conclusion

Following conclusions were obtained through the SRAC burnup calculation using the JENDL-3.3 original and modified library corresponding to the new measurement of ^{157}Gd by Leinweber et al.

・The correction factors for ^{157}Gd capture cross sections for SRAC calculations are approximately 0.89 in thermal region below 1.8554eV.

・The effects on the infinite multiplication factors of fuel assemblies are 0.35%Δk and 0.30%Δk respectively in the UO_2 and MOX fuel assembly at the beginning of burnup, decrease with burnup and extinguish at 15GWd/t.

・ Effects on fission rate distributions due to the change of ^{157}Gd cross sections reveals mainly at the beginning of life. The maximum effects on fission rates in Gd rods are 1.1% and 1.5% in MOX and UO_2 fuel assembly, respectively. The effects extinguish at 15GWd/t.

Accurate cross section evaluation of Gd isotopes, especially ^{157}Gd and ^{155}Gd (although not discussed in this paper) are very important in BWR nuclear fuel assembly design. More improvement needs to be done in the future study.

References

[1] G. Leinweber, D. O. Barry, M. J. Trbovich *et al.*,"Neutron Capture and Total Cross-Section Measurements and Resonance Parameters of Gadolinium," *Nucl. Sci. Eng.*, **154**, 261 (2006).

[2] P. F. Rose and C. L. Dunford, *ENDF-102 Date Formats and Procedures of the Evaluated Nuclear Data File ENDF-6*, BNL-NCS-44945, Rev.2, BNL (1997).

[3] F. Jatuffa *et al.*, "Impact of newly-measured gadolinium cross sections on BWR fuel rod reaction rate distributions, *Proc. Int. Conf. PHYSOR2008*, Interlaken, Switzerland, September 14-19, 2008, No. 219 (2008).

[4] K. Shibata, O. Iwamoto, T. Nakagawa *et al.*, "JENDL-4.0: A New Library for Nuclear Science and Engineering," (to be published to J. Nucl. Sci. Technol.).

[5] Y. Nagaya, K. Okumura, T. Mori *et al.*, *MVP/GMVP II: General Purpose Monte Carlo Codes for Neutron and Photon Transport Calculations Based on Continuous Energy and Multigroup Methods*, JAERI-1348 (2005).

[6] K. Okumura, private communication (2009)

[7] K. Shibata, private communication (2009)

[8] G. Chiba, K. Okumura, K. Sugino, et al. "JENDL-4.0 Benchmarking for Fission Reactor Applications,",J.Nucl. Sci. Technol. Vol. 48, No. 2, p. 1-16 (2011) (To be published)

[9] K. Okumura, T. Kugo, K. Kaneko *et al.*, *SRAC2006: A Comprehensive Neutronic Calculation Code system*, JAERI-Data/Code 2007-004 (JAERI), (2007).

33. Improvement of FP Decay Heat Calculation by Introducing TAGS Data
I . Gamma-Ray Energy Spectra.

Hideo TAJIMA , Tadashi YOSHIDA
Tokyo City University
Tamazutumi 1-28-1, Setagaya-ku, Tokyo 158-8557, Japan
e-mail: g1081008@tcu.ac.jp

Sample-irradiation measurements and summation calculations of FP decay-heat still disagree each other without a theoretical correction which was introduced in the JNDC FP Decay Data Library long before. This disagreement is caused by the pandemonium problem in the FP decay-data, on which the calculations are based. The pandemonium problem comes from the limitation of the current method of constructing the decay schemes of short-lived nuclides. Recently a series of new TAGS measurements was initiated by a European group. In the mean time, we plan to include these new TAGS data into JENDL to exclude the pandemonium problem without the theoretical correction. This procedure needs not only the average energies but also the energy spectra of the γ-rays and the β-particles. The TAGS data, however, provides us only with the β-feedings into energy-bins. So we have to estimate the energy spectra with the aid of theoretical consideration along with the TAGS results. For this purpose, we calculate the energy spectrum of the γ-ray on the basis of the β-feedings obtained by TAGS.

1. Introduction

Currently summation calculations are used widely for predicting the fission product (FP) decay heat from a reactor core or a spent fuel. This method is based on summing up all the recoverable energy contributions from all the individual FPs undergoing β-decay and the subsequent γ-transitions. This method, then, requires the average β-ray and the γ-ray energies (E_β and E_γ) per β-decay. Neutrino plays no role in this context because of its absolute insensibility to the surrounding materials. The total absorption gamma-ray spectrometer (TAGS) method is one of the best ways to know these average energies. This method enables us to obtain the average energies of the γ-ray and the β-particles per decay without any bias and to solve the *pandemonium problem*. The pandemonium problem is essentially the absence of our knowledge about the β-feedings to the highly excited states of the daughter nuclides. This problem is caused by the limitation of the current method for constructing the decay schemes[1][2] of short-lived nuclides on the basis of the high-resolution γ-ray measurements. When the β-feeding to the highly excited states are overlooked, the E_γ value is underestimated and the E_β value becomes too large. Recently, TAGS was successfully applied to measure some of the most important FP nuclides in the decay-heat calculation for Pu-239. This series of the new TAGS measurement was initiated by a European group, and a part of their novel result was published very recently [3]. We plan to include these new TAGS data eventually into JENDL (Japanese Evaluated Nuclear Data Library). This procedure needs not only the average energies but also the energy spectra of the γ-rays and the β-particles. But the TAGS data consist only of the β-feeding rates into energy-bins of the excited stats of the daughter with finite width. So we have to estimate the energy spectra with the aid of theoretical consideration along with the TAGS results. On this context, the present study aimes at establishing a way to estimate the energy spectra with combined knowledge of the TAGS β-feedings and the β-decay and the γ-decay theories.

2 . Comparison of European TAGS and Current Data

On the long-range point of view over decades of years, introducing the Gross theory into the FP decay heat calculations[4] was thought to be a provisional treatment. It was expected that the theoretical values of E_β and E_γ for important FPs would gradually be replaced by the data firmly based on some certain and reliable measurements which would be free from the pandemonium problem. Having this long-standing anticipation as a background, they stated the TAGS measurement led by a group of Valencia[5]. This measurement is able to detect all the β-feedings into the whole range of daughter's excitation energy up to the Q_β -value itself. Their results are shown in Figs. 1 ~ 7 along with the current data.

The β-feeding from Tc-104 to Ru-104 are compared between the TAGS and Table of Isotopes[1] in Fig. 3 among others. The TAGS data provide us only with the β-feedings into energy-bins representing the excitation energies of the daughter, or Ru-104. In this case, the TAGS supports the presence of the structures in the β-feedings, which the current data vaguely indicates. Further, the TAGS data provide us with the feedings up to much higher in the exciting energy, where the current decay scheme gives us no information. So, we adopt the data as it is in the energy range where the current level schemes say nothing.

3. Gamma energy spectrum calculation

When we introduce the decay data into the JENDL decay data file, we need not only the average energies of the γ-rays and the β-particles but also the β-feeding rate and the energy spectra of the radiations. Figure 8 shows the calculated γ-ray spectra starting from the TAGS β-feeding to the whole energy range from 0 (ground sate) to Q_β (the highest possible energy). On the other hand, Fig.9 shows the calculated spectra originating from the TAGS β-feeding to the high-energy part where no current decay schemes give us any information, in other words, only the latest TAGS measurement provides us with the β-feedings. Figure 10～14 show the γ-ray energy spectra calculated in the same way as in Fig.9. In these calculations, we used a computer code to calculate the γ-ray energy spectrum from a set of β-feedings, which was modeled and coded by Yoshida and Katakura [6]. This model is based on a simple γ-cascade with the Gilbert-Cameron level-density formula and the Brink-Axel giant dipole resonance.

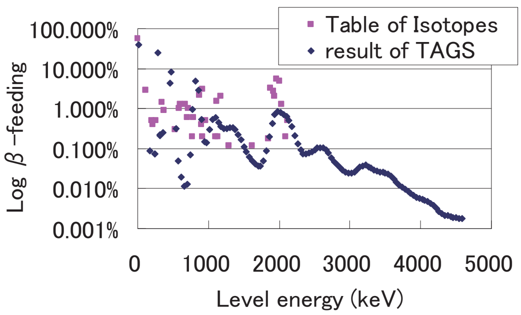

Fig.1 Beta-feeding from decay of Nb-101

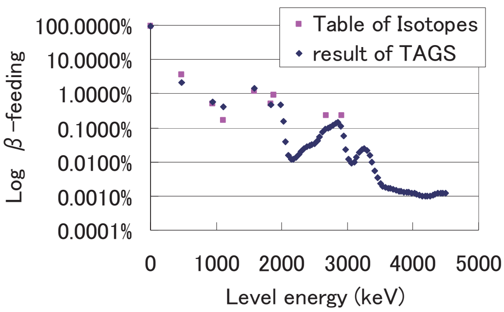

Fig.2 Beta-feeding from decay of Tc-102

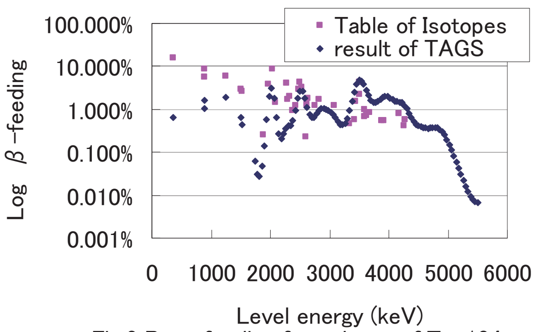

Fig.3 Beta-feeding from decay of Tc-104

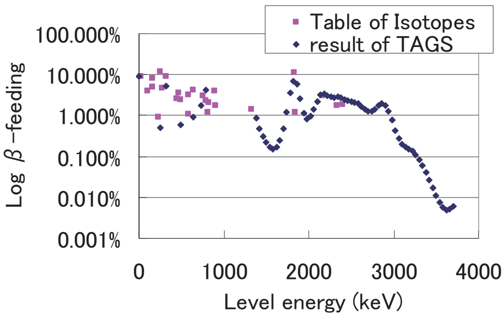

Fig.4 Beta-feeding from decay of Tc-105

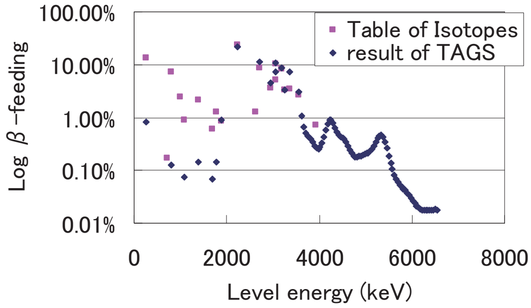

Fig.5 Beta-feeding from decay of Tc-106

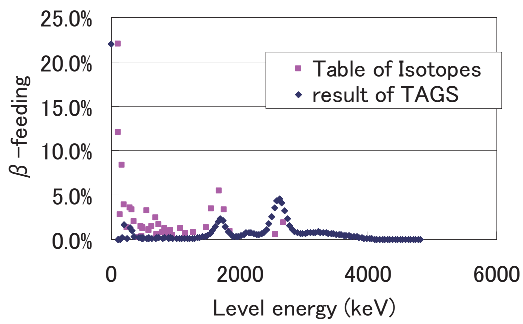

Fig.6 Beta-feeding from decay of Tc-107

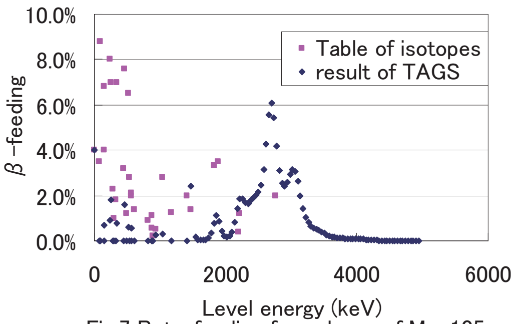

Fig.7 Beta−feeding from decay of Mo−105

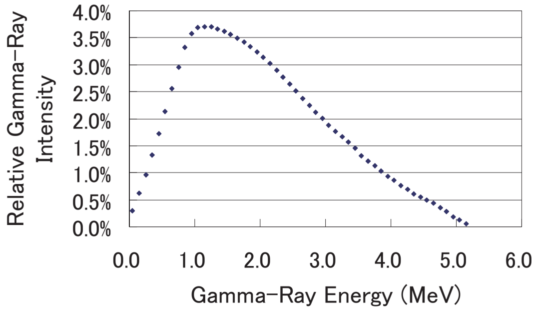

Fig.8 Spectrum of gamma-ray following Tc-104 decay

Starting from feeding to the whole energy range

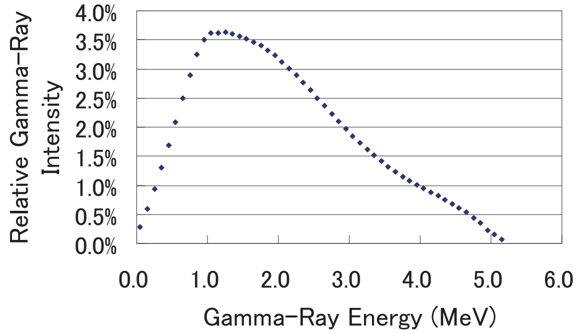

Fig.9 Spectrum of gamma-ray following Tc-104 decay

Starting from feeding to the high-energy range

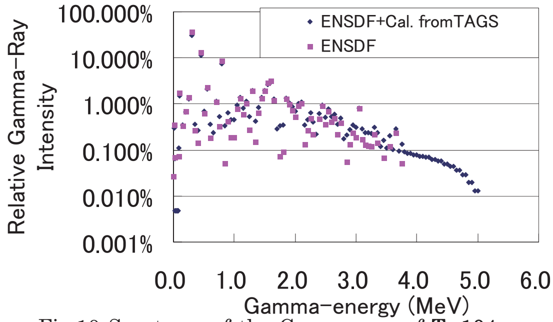

Fig.10 Spectrum of the Gamma-ray of **Tc-104** composed of the present calculation and high-resolution data

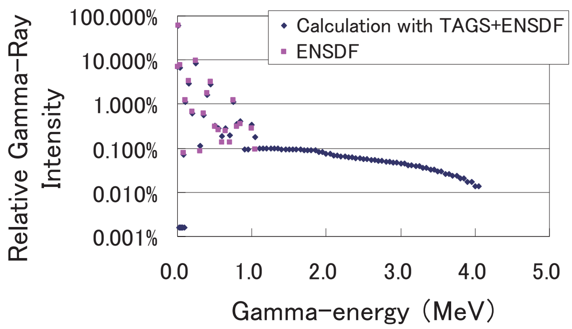

Fig.11 Spectrum of the Gamma-ray of **Nb-101**composed of the present calculation and high-resolution data

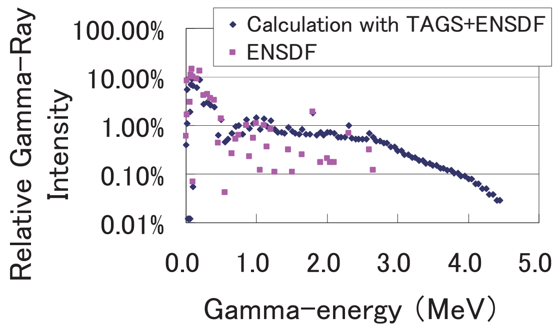

Fig.12 Spectrum of the Gamma-ray of **Mo-105** composed of the present calculation and high-resolution data

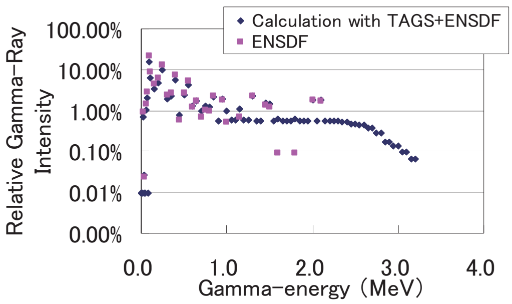

Fig.13 Spectrum of the Gamma-ray of **Tc-105** composed of the present calculation and high-resolution data

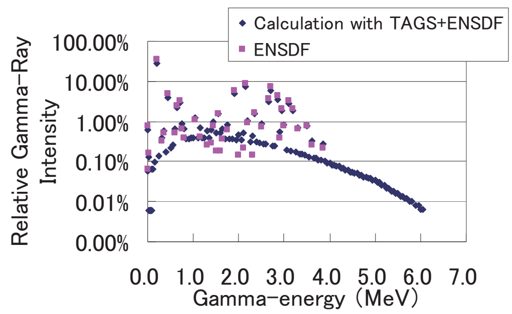

Fig.14 Spectrum of the Gamma-ray of **Tc-106** composed of the present calculation and high-resolution data

4. Discussion

Figure 8 shows the γ-ray spectrum calculated from the β-feedings obtained by the TAGS measurement and a continuous γ-ray cascade model mentioned in the preceeding chapter. The β-feedings go into the energy bins with fixed-width and, then, the γ-ray spectrum based on the TAGS results do not show any suructure and the resultant γ-ray spectrum becomes a single peaked broad distribution as seen here.

Figure 9 shows the calculated γ-ray spectrum originating from the β-feeding to the highest energy region where no measurement except for the TAGS gives the feeding, namely, above 4300keV (see Fig3). This calculation is not enough to make a complete γ-ray energy spectra to be included in JENDL. So existing discrete-line data from ENSDF are also taken into account for the γ-rays originated from the levels below 4300keV. In this sense we combined existing data and the latest TAGS data to obtain a complete γ-ray spectrum.

Figure 10～14 shows the γ-ray spectrum constructed by combining of the current high resolution data and the TAGS-based calculation as was described above. These results clearly shows us that the part of the spectrum calculated theoretically with the β-feedings obtained by TAGS measurement are not discrete. On the other hand, the part of the spectra taken from the current decay schemes has discrete structure. In order to take the balance of both components above into consideration, we need renormalization. This was done in a way to reserve both the E_β and the E_γ values determined by the TAGS measurement.

5. Conclusions

The present work is to introduce TAGS data into JENDL. For this purpose, we have to convert the β-feedings obtained by TAGS into the energy spectrum of both the β-particles and γ-rays in the ENDF/B format. Only the γ-ray spectrum is dealt with here for Nb-101, Tc-104,105,106 and Mo-105. The calculation of γ-ray spectra for Tc-102 and -107 is now underway. Furthermore, the calculation of β-ray spectra from the TAGS β-feeding is to be carried out. We tried to combine the current high resolution data with the latest TAGS data as far as the γ-ray spectrum is concerned. By doing this, we aim at advancement in performance of the summation calculation of decay heat by the JENDL decay data file.

References

[1] R. B. Firestone, V. S. Shirley (Eds.), Table of Isotopes, John Wiley & Sons, New York (1996).
[2] ENSDF, http://www.nndc.bnl.gov/ensdf
[3] A. Algora et al. Phys Rev. Lett. **105**, 202501 (2010) – published Nobenber 08 2010.
[4] T. Yoshida, R. Nakashima, J. Nucl. Sc;. Technol., **18**[6], 393-407 (1981).
[5] A. Algora et al., Int Conf. on Nuclear Data for Sci. Technol., Jeju, Korea (2010).
[6] T. Yoshida, J. Katakura, Nucl. Sci. Eng., **93,** 193-203 (1986).

34. Improvements of FP Decay Heat Summation Calculations by Introducing TAGS Data II. Priority Proposal for Future Measurements

Takayuki ARAI and Tadashi YOSHIDA
Tokyo City University, Tamazutsumi 1-28-1, Setagaya-ku, 158-8557 Tokyo, Japan
E-mail: g1181002@tcu.ac.jp

Summation calculations of fission-product (FP) decay heat for U-235, which do not agree well with sample-irradiation measurements, suffer from the pandemonium-problem. Decay data taken by a total absorption gamma-ray spectrometer (TAGS) is expected to be free from this problem. Therefore TAGS is, at least at present, an ideal source of the FP decay data to be used for calculating the mean β-ray and γ-ray energies of individual FP nuclides, and it can solve the discrepancy between calculations and measurements in the FP decay heat calculations. Here we propose a list of nuclides to be measured in the future TAGS program focusing our attention on the improvement of the decay heat summation calculation for U-235.

1. Introduction

The FP decay-heat summation calculations without any theoretical correction do not reproduce well the sample-irradiation measurements for U-235 [1]. This is because the decay-data of the individual FP nuclides contributing much to the U-235 decay-heat suffer from the *pandemonium-problem*. The pandemonium-problem is caused by missing β-feedings to the high energy regions of the daughter nuclides in the current decay schemes. As a result, the mean β-ray energy per decay (E_β) is overvalued and the mean γ-ray energy (E_γ) is undervalued. This leads to the failure of the summation calculations [2]. In the case of JENDL of Japan and ENDF/B-VI of America, the gross theory of beta decay was introduced for supplementing the calculation of E_β and E_γ in order to cope with the pandemonium-problem and, then, they lead to a good agreement between the calculations and the measurements. On the other hand, JEFF of Europe dose not introduce any theoretical correction for the decay data for the summation calculations. Therefore, the overvaluation of E_β and the undervaluation of E_γ are clearly identified in JEFF, which explicitly demonstrate the presence of the pandemonium-problem as a result. The latest calculation based on ENDF/B-VII does not agree with the sample-irradiation measurements in the same way as JEFF. This is because the authors of ENDF/B-VII do not introduce any theoretical correction to their library. They have changed their attitude against the pandemonium-problem at the time when they moved from ENDF/B-VI to ENDF/B-VII.

Here we propose a list of nuclides to be measured in the future TAGS program focusing our attention on the U-235 decay heat. It is necessary to revalue the mean β- and the γ-ray energies against the influence of pandemonium-problem for the better agreement between the summation calculations and the sample-irradiation measurements without introducing the theoretical correction.

2. TAGS Activities

The total absorption gamma-ray spectrometer (TAGS) consists of an isotope separator, a tape transport system, and a large NaI(Tl) scintillation detector. The TAGS system is expected to be free from the pandemonium-problem. Therefore, TAGS enable us to obtain the correct mean β- and γ-ray energies (E_β, E_γ) for the important individual FP nuclides.

In the early 1990's, R. C. Greenwood *et al* of Idaho Nuclear Laboratory (INL) started a series of TAGS measurements and, later, their results were published for 48 FP nuclides (INL/TAGS) [3]. These data, however, had not been introduced into the decay heat summation calculations for many years. Anyway, the relation between the failure of the summation-calculation and the pandemonium-problem were not known. Yoshida *et al.* suggested the relation between them [2] and Hagura *et al.* tried to introduce the INL/TAGS data into the summation calculations [4]. These studies showed that decay-heat summation calculations will agree well with the sample-irradiation measurement by introducing TAGS data appropriately.

In the late 1990's, INL had completed their TAGS activity. A new series of the TAGS measurements, however, is now going on by A. Algora *et al* (Universitat De Valencia of Spain) at an ion-source of University of Jyväskylä of Finland (UDV/TAGS) [5]. Table.1 shows a comparison of the UDV/TAGS and ENDF/B-VII where no theoretical correction is applied, and shows that these nuclides largely suffer from the pandemonium-problem. These nuclides were selected in order to improve the decay-heat calculation especially for Pu-239 by Subgroup 25 of WPEC [6]. Fig.1 shows the comparison of decay-heat summation calculation of Pu-239 before and after introducing the UDV/TAGS. This study shows clearly that TAGS measurements enable us to solve the pandemonium-problem [1].

Table 1 Comparison between ENDF/B-VII and UDV/TAGS [5] of mean β- and γ-ray energies

Nuclide	$T_{1/2}$ [s]	E_b [keV]		E_g [keV]	
		ENDF/B-VII	TAGS	ENDF/B-VII	TAGS
41-Nb-101	7.1	1966	1797	270	445
42-Mo-105	35.6	1922	1049	552	2407
43-Tc-102	5.28	1945	1935	81	106
43-Tc-104	1098	1595	931	1890	3229
43-Tc-105	456	1310	764	668	1825
43-Tc-106	35.6	1906	1457	2191	3132
43-Tc-107	21.2	2054	1263	515	1822

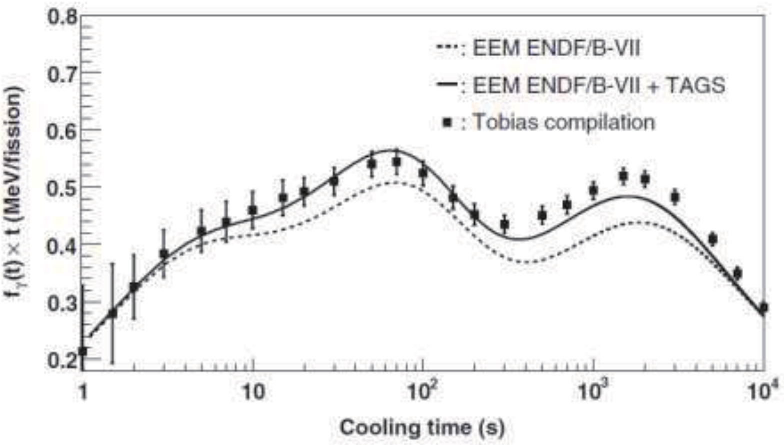

Figure 1　Comparison of the FP decay-heat calculations of the γ-ray component of Pu-239 before and after the introducing UDV/TAGS data (taken from A.Algora *et al.*[1])

3. Evaluation

3.1 Pandemonium Problem Revisited

The cause of the pandemonium-problem lies in the difficulty in detecting all of the large number of γ-rays emitted following a β-decay, and a lot of γ-rays, even though they were detected, cannot find their correct positions in the complex decay scheme.　They are called the *unplaced gammas*.　Therefore, nuclides having a lot of unplaced gammas are surely influenced by the pandemonium-problem.　In the case of short-lived nuclides, the highest known levels of their daughter nuclides tend to be much lower than their Q_β-values in the decay schemes now available, which are constructed on the basis of the current high-resolution γ-ray data.　In the case of JENDL, for most of the short-lived FP nuclides where the highest known levels in their daughter nuclides is much lower than $0.7 \times Q_\beta$, the gross theory of beta decay was introduced and this treatment lead to a good agreement between the calculations and the measurements [2].　When the β-feeding to a single particular level is very large, these nuclides tend to be free from the pandemonium-problem

[7]. For example, Table1 shows that Tc-102, whose β-feeding to the ground state is very large, proved to be free from the pandemonium problem, in other words, the current high-resolution data (ENDF/B-VII) and the UDV/TAGS give almost the same values for E_β and E_γ..

3.2. Important Nuclides for U-235 Decay Heat

Here we propose a list of nuclides to be measured in the future TAGS program focusing our attention on the improvement of decay heat summation calculation for U-235.

This study uses JENDL/FPD-2000 and the Evaluated Nuclear Structure Data File [8] (ENSDF). The library JENDL/FPD-2000 covers information on the decay data of 1229 fission products. This is used to search for the nuclides that contribute much to the decay heat of U-235. Detailed data of the searched nuclides (half-life, Q_β-value, and released energies *etc.*) are obtained from ENSDF. We examine whether the *pandemonium-problem* influences the selected nuclides from these data library, and evaluating the priority of the future TAGS measurements.

The points for selecting nuclides and deciding the priority are as follows.

i) The difference between the highest known level and Q_β-value.

When the difference is large, the nuclide has a large possibility of missing of the β-feeding to the high energy regions of the daughter nuclide in the current decay schemes by influence of the pandemonium-problem.

ii) The unplaced gammas.

The primary cause of *pandemonium-problem* is that a lot of γ–rays, though detected, failed to find their correct places in the complex decay scheme (unplaced gamma). The unplaced gammas can be confirmed by ENSDF. For example, Xe-141 has extremely many and high energy unplaced gammas. There are as many as 185 unplaced γ-rays besides 96 γ-rays which are correctly positioned in the complex decay scheme of Cs-141, its daughter nuclide.

iii) Contribution to the Pu-239 decay heat.

Calculation of the decay heat for Pu-239 is in a good agreement with the sample-irradiation measurements for the sake of the recent TAGS activity [5]. Therefore, when a nuclide's contribution to the decay heat of Pu-239 is large, it is reliable and not selected for the future TAGS measurements. However, this principle is not applied for the nuclides whose contribution to the decay heat for Pu-239 in the cooling-time range 200 – 10,000s is large. In this cooling-time range the disagreement still remains between the calculation and the measurements.

Table.2 lists the highest priority nuclides that are selected here. These nuclides are important in order to improve the disagreement between the summation calculation and the sample-irradiation measurement in U-235 decay heat.

Table 2 High priority list of the future TAGS measurements for U-235 Decay Heat

Nuclides	$T_{1/2}$	Q_β-value (A) [keV]	Highest level (B) [keV]	(B) / (A)*1	Cooling time*2 [s]	U-235*3 (C) [%]	Pu-239*4 (D) [%]	(C) / (D)
35-Br-89	4.40s	8155	4707	0.58	5.0E+00	2.34%	0.84%	2.78
35-Br-90	1.92s	10350	5730	0.55	1.5E+00	1.62%	0.78%	2.08
37-Rb-94	2.702s	10287	6064	0.59	3.0E+00	4.66%	2.88%	1.62
41-Nb-99m	2.6m	4004	2944	0.74	3.0E+02	2.45%	2.84%	0.86
43-Tc-103	54.2s	2662	1066	0.40	2.0E+02	1.52%	5.23%	0.36
51-Sb-133	2.5m	4003	2756	0.69	3.0E+02	4.28%	2.65%	1.61
53-I-139	2.280s	6806	1684	0.25	2.0E+00	0.98%	0.43%	2.26
54-Xe-140	13.60s	4060	2324	0.57	2.0E+01	3.20%	1.67%	1.92
54-Xe-141	1.73s	6150	1557	0.25	1.5E+00	1.13%	0.57%	1.99

*1 (B) / (A): ratio of the energy of the highest known level to the Q_β-value

*2 Cooling time: cooling time when the nuclide gives the maximum contribution

*3 U-235: The nuclide's contribution to the total decay heat of U-235

*4 Pu-239: The nuclide's contribution to the total decay heat of Pu-239

4. Conclusion

Here we propose a list of nuclides to be measured in the future TAGS program focusing our attention on the U-235 decay heat. It is necessary to revalue the mean β- and γ-ray energies of these nuclides for the better agreement between the summation calculations and the sample-irradiation measurements without introducing theoretical calculations. European group is trying to be still active after finishing TAGS measurements for Pu-239. We expect they could measure the nuclides listed here for U-235 in the near future.

Reference

[1] A. Algora *et al.,* Int. Comf. Nucl. Data to Sci. and Technol., Jeju, Korea (2010)

[2] T. Yoshida, R. Nakashima, J. Nucl. Sc;. Technol., **18**[6] (1981) 393-407

[3] R.C. Greenwood *et al.*, Nucl. Instrum. Methods, **A314** (1992) 514-540

[4] N. Hagura *et al.,* J. Nucl. Sci. Technol., **43**[5] (2006) 497-504

[5] A. Algora *et al.*, Phys. Rev. Lett., **105** (Nov., 2010) 202501

[6] http://www.oecd-nea.org/science/wpec/index.html

[7] N.Hagura *et al.*, J. Nucl. Sci. Technol., **47**[5] (2010) 492-500

[8] http://www.nndc.bnl.gov/ensdf/

35. Activation analyses by the beam losses in the IFMIF/EVEDA accelerator

Sunao MAEBARA[a], Hiroki TAKAHASHI[a], Hironao SAKAKI[b], Keiichi HIRABAYASHI[c], Kosuke HIDAKA[c], Nobuhiro SHIGYO [c], Yukinobu WATANABE[d] and Kenshi SAGARA[e]

[a] *IFMIF Development Group, Directorates of Fusion Energy Research, JAEA*

[b] *Photo Medical Research Center, JAEA*

[c] *Department of Applied Quantum Physics and Nuclear Engineering, Kyushu University*

[d] *Department of Advanced Energy Engineering Science, Kyushu University*

[e] *Department of Physics, Kyushu University*

e-mail:maebara.sunao@jaea.go.jp

In the IFMIF/EVEDA project, the engineering validation through Accelerator Prototype for deuteron CW beam acceleration up to 9MeV with output current of 125mA is planning at the BA site in Rokkasho, Aomori, Japan. The activation due to beam loss or stopping of deuterons is critical to achieve successful beam operation, analyses of source terms of radiation and activities in the accelerator structural materials, Cu, SUS316, Fe, etc., are indispensable for safety assessment to obtain permission of operation. Since there was no experimental data for Cu(d,nx) reaction in the range of 5-9MeV, deuteron induced thick target neutron yield at 5MeV and 9MeV were measured in collaboration with Kyushu University.

In this article, the experimental data at 9MeV is used as a source term in neutron transportation, and isotope productions in the materials; Copper, Iron and Stainless Steel, are evaluated by PHITS code.

1. Introduction

The International Fusion Materials Irradiation Facility (IFMIF) [1-3] has been conceived as an intense 14MeV neutron-source for a demonstration fusion reactor materials development next to the International Thermonuclear Experimental Reactor (ITER). The IFMIF provides an irradiation volume of 0.5 liter with a neutron flux of 10^{18} n/m^2/s or more using the neutron-generating D-Li stripping reaction. The required damage production rates for iron base specimens are 50dpa/y in an irradiation volume of 0.1 liter and 20 dpa/y in volume of 0.5 liter. In the top-level requirements of IFMIF accelerator system, a 40MeV deuteron beam with a current of 250mA has to be injected into liquid lithium flow, being realized by two independent beam lines of 125mA each. Furthermore, accelerator system availability of 88% or more with CW operation mode is required.

For providing materials to make a decision of IFMIF construction, Engineering Validation and Engineering Design Activities (EVEDA) under the Broader Approach (BA) agreement have been started in June 2007. In order to validate the most critical part of such an accelerator system development, the acceleration tests up to 9MeV by employing the deuteron beam of 125 mA, are planned at the BA site in Rokkasho, Aomori, Japan [4]. For domestic safety review, activation analysis and shielding analysis including sky shine are indispensable for the accelerator prototype. The activation is caused by beam loss in beam line, and neutrons generated and transported from the 9MeV-125mA beam dump. This article presents isotope productions by the beam loss of 9MeV-1μA for typical structural materials of Copper, Iron and Stainless Steel in the first step.

2. Analysis model

Since there is no experimental data of Cu(d,nx) reaction in the range of 5-9 MeV as shown in Fig.1(a), deuteron induced thick target neutron yield at 5 and 9MeV were measured in collaboration with Kyushu University using Tandem accelerator in 2009-2010.

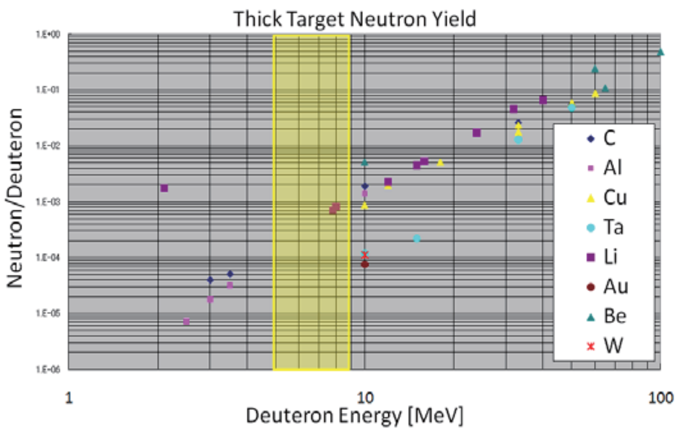

Fig. 1(a) Existing data of thick target neutron yield vs. deuteron energy, (b) Kyushu University Tandem accelerator

Samples of the neutron angular distributions in the angular of 0°, 60° and 90° at a 9 MeV-1μA deuteron beam and the neutron distribution in all direction are shown in Fig.2 The measured maximum energy of 15.2 MeV is consistent with Q-value of Cu65(d,n)Cu66 stripping reaction. For the neutron distribution in all direction, the measured energy spectra at angles, 0°, 15°, 30°, 45°, 60°, 75°, 90°, 120° and 140°, are used for a source term, and this source term is set for a point source in activation analysis . A spherical shape using the diameter of 50mm and the thickness of 5mm is selected for a simple structural model. In the center, this source is set. The material components of copper, iron and stainless steel are indicated in Table 1. As for nuclear reaction with each material component, the JENDL 4.0 is used for nuclear cross-section library. Isotopic productions in copper, iron and stainless steel are evaluated by PHITS code.

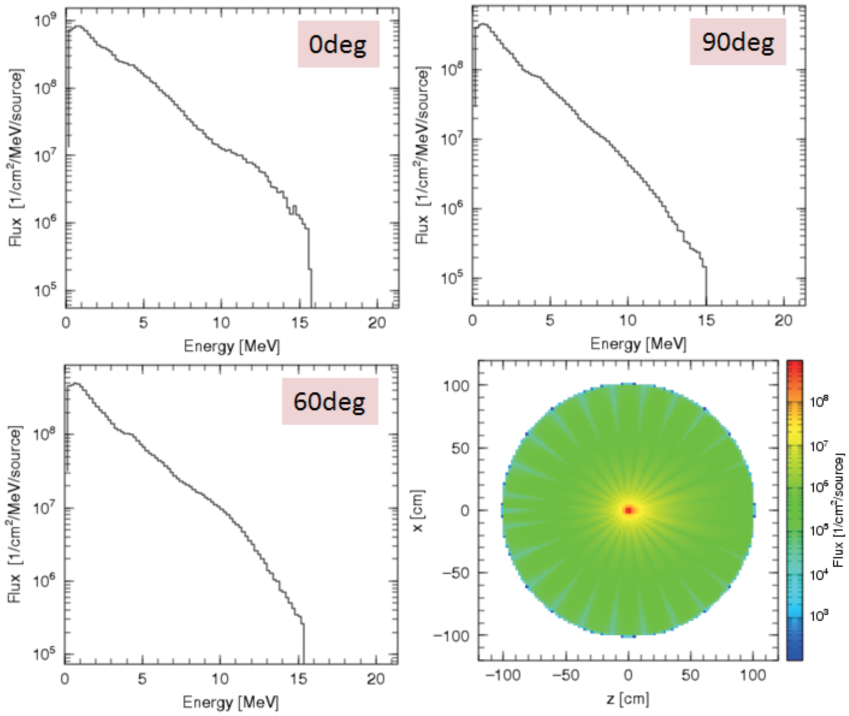

Fig.2 Samples of the neutron angular distributions in the angular of 0°, 60° and 90° at a 9MeV-1μA deuteron beam and the neutron distribution in all direction

Table 1 Material component of copper, iron and stainless steel

Copper	Iron	Stainless steel
63Cu: 69.1%	54Fe:5.8%	56Fe:5.06e-2*
65Cu:30.9%	56Fe:91.7%	52Cr:1.35e-2*
	57Fe:2.2%	58Ni:6.83e-3*
	58Fe:0.3%	62Ni:3.45e-3*
		54Fe:3.34e-3*
		60Ni:2.55e-3*
		Mo(nat):1.24e-3* etc.,

*Unit [10^{24} atoms/cm^3]

3. Analysis results

Analysis result of isotope productions in copper, iron and stainless steel material shows in Figs. 3, 4, and 5, respectively. In the Accelerator Prototype, commissioning tests for several years is planned, and the net accelerator tests with a 9MeV-125mA CW operation are going to be within a few months. Therefore, isotope productions having half-life shorter than 30 da ys, is dominant for the maintenance works and the decommissioning.

In this analysis results, it is found that the isotope productions of Ni65, Cu62, Cu64 and Cu66 in copper materials, the Cr51, Zn56, Zr57 in iron, and the Si31, Cr51, Cr55, Mn56, Mn57, Ni57, Ni65, Co61, Cu64, Cu66, Mo99 and Mo104 in stainless steel are important. Especially, Cu66 has half-life of 5.12 minutes, and the decay rate reaches a few 10 MBq level for half hour operation. The Cu66 decays by β-ray(2.64MeV) and γ-ray(0.833, 1.039MeV). For the productions in stainless steel, it is clearly confirmed that the use as accelerator structural materials has to be avoided as much as possible even if it for the Accelerator Prototype.

For the half time of longer than 30 days, it is found that isotope productions of Co60, Ni63 and Zn65 in copper and the productions of Mn54, Fe55, Fe59 and Co57 in iron are key isotopes for the IFMIF accelerator (life time of 20-30years) in future. Periodic exchanges for copper and iron are indispensable. For stainless steel material, isotopes of Mn53, Mn54, Fe55, Fe59, Co57, Co58, Co60, are keys. The use of aluminum material has to be aggressively considered instead of stainless steel material for the IFMIF accelerator in future. For each material of copper, iron and stainless steel, it is also revealed that deuteron (H2) of 10^3 [n/sec] is produced, and the reaction between deuteron beam and produced H2, furthermore, has to be evaluated.

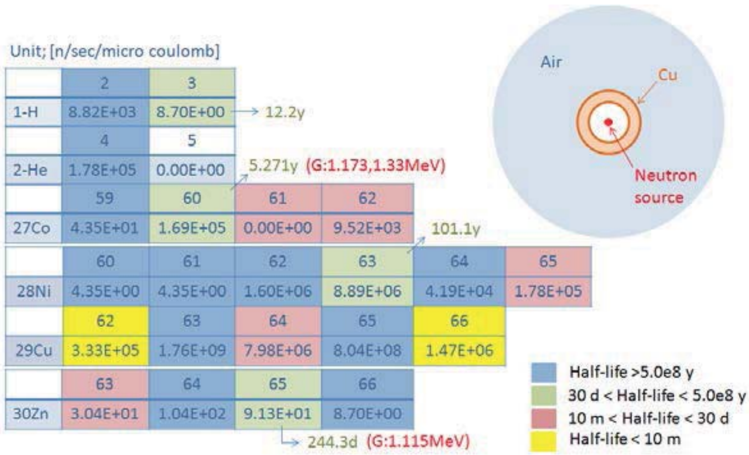

Fig. 3 Results of activities produced in copper and its geometry of transport calculation.

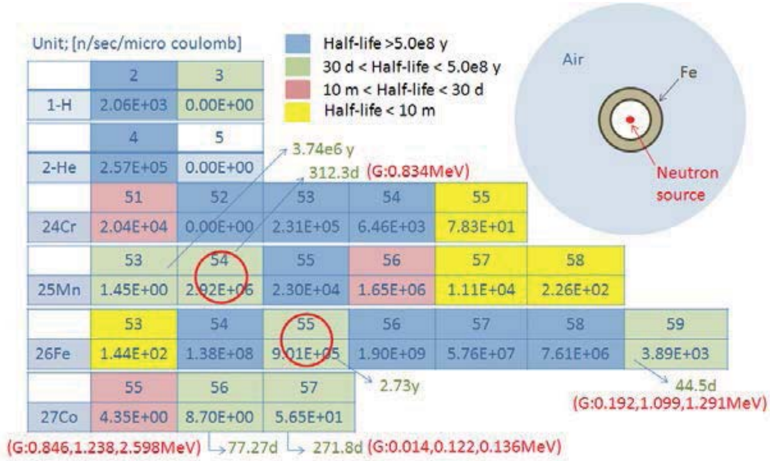

Fig. 4 R esults of activities produced in iron and its geometry of transport calculation.

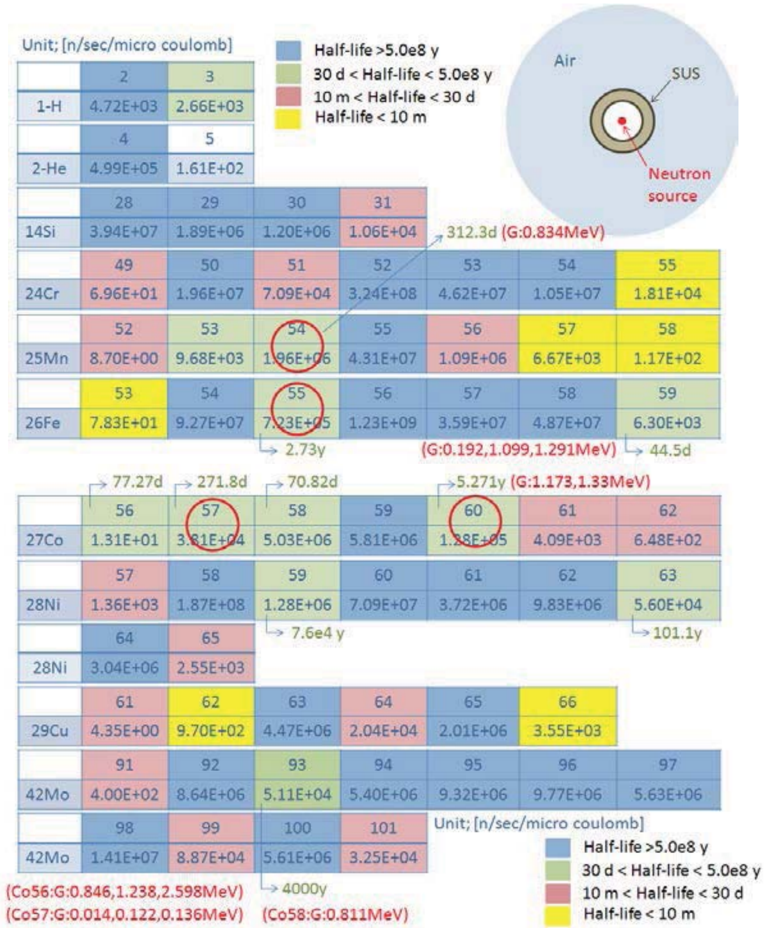

Fig. 5 Results of activities produced in stainless steel and its geometry of transport calculation.

4. Summary

For Cu(d, nx) reaction, deuteron induced thick target neutron yield at 9MeV was measured in collaboration with Kyusyu University. Using this experimental data as a source term, isotopic productions in copper, iron and stainless steel were calculated by PHITS code. In the preliminary results, the important isotopes produced in copper, iron and stainless steel by a 9 MeV-1μA beam loss are identified. In the Accelerator Prototype operation, it is found that the Cu66 reaches to a few 10 MBq level after half hour CW operation. For each material in copper, iron and stainless steel, evaluation of the reaction between deuteron beam and H2 produced in materials is indispensable in the next step, since the H2 production level will be 10^3 [n/sec]. The isotope production in stainless steel is so high that its use as accelerator structural materials has to be avoided in the Accelerator Prototype.

For the IFMIF accelerator (the life time of 20-30 years) in future, it is suggested that periodical exchange of copper and iron material is necessary, and the use of aluminum material has to be aggressively considered instead of stainless steel material.

In the next step, isotope productions including (d,d) reaction and the activation analysis by neutron scattering from the 9MeV-125mA beam dump are in progress.

References

[1]IFMIF-CDA Team (Ed.) M. Martone,ENEA Frascati Report, RT/ERG/FUS/96/17 (1996).

[2] T. KONDO, J. of Nucl. Mater. 258-263,47-55(1998)

[3] T. F. Shannon , J.of Nucl. Mater. 258-263,106-112(1998)

[4] MOSNIER, A., et al., Proc. 1st Int. Particle Accelerator Conf., Kyoto, Japan, 588-590(2010)

[5] N. Shigyo et.al., Proc. Int. Conf. of Nuclear Data for Science and Technology 2010 will be published.

36. Evaluation of gamma-ray and neutron energy in the IFMIF/EVEDA accelerator building

Hiroki TAKAHASHI[1*], Sunao MAEBARA[2], Hironao SAKAKI[3], Keiichi HIRABAYASHI[4], Kosuke HIDAKA[4], Nobuhiro SHIGYO[4], Yukinobu WATANABE[5], Kenshi SAGARA[6]

1. Directorates of Fusion Energy Research, Japan Atomic Energy Agency (JAEA), Rokkasho-mura, Aomori 039-3212, Japan

2. Directorates of Fusion Energy Research, JAEA, Tokai-mura, Naka-gun, Ibaraki 319-1195, Japan

3. Photo Medical Research Center, JAEA, Kizugawa Kyoto 619-0215, Japan

4. Department of Applied Quantum Physics and Nuclear Engineering, Kyushu University, Fukuoka 819-0395, Japan

5. Department of Advanced Energy Engineering Science, Kyushu University, Fukuoka 816-8580, Japan

6. Department of Physics, Kyushu University, Fukuoka 812-8581, Japan

*E-mail: takahashi.hiroki@jaea.go.jp

The Engineering Validation of the IFMIF/EVEDA accelerator prototype, up to 9MeV by employing the deuteron beam of 125mA, is planning at the BA site in Rokkasho. The design of this area monitoring system, comprising of Si semiconductors and ionization chambers for covering wide energy spectrum of gamma-rays and ^{3}He counters for neutrons, is now in progress. To establish the applicability, photon and neutron energy has to be suppressed to the detector ranges of 1.5MeV and 15MeV, respectively. For this purpose, the reduction of neutron and photon energies throughout shield of water and concrete layer is evaluated by PHITS code, using the experimental data of neutron source spectra. As the first step, simple sphere model is used and it is found that the photon energy range exceeded over 10MeV by water and concrete shielding material only.

In this article, in order to decrease the maximum photon energy, a model with iron layer is evaluated.

1. Introduction

International Fusion Materials Irradiation Facility (IFMIF) [1-3] is an accelerator-based neutron irradiation facility to develop materials for a demonstration fusion reactor next to ITER. For preparing the necessary information to make a decision of the IFMIF construction, Engineering Validation and Engineering Design Activities (EVEDA) have been started.

IFMIF/EVEDA prototype accelerator consists of an injector (output energy;100keV), a 175MHz RFQ linac (0.1-5.0MeV), a medium energy beam transport, the first section of Superconducting RF linac

(5.0-9.0MeV), a high energy beam transport line and a beam dump (9MeV-125mA CW) [4]. In the accelerator building, an accelerator vault is surrounded by the concrete wall with thickness of 1.5m. For the radiation controlled area (with no possibility of RI contamination), the effective dose rate has to be suppressed to less than 12.5 micro Sv/h with no neutron leakage. For Personal Protection System [PPS] in the prototype accelerator, a design study of the area monitoring system, comprising of Si semiconductors and ionization chambers for covering wide energy spectrum of gamma-rays and ^{3}He counters for neutrons, is now in progress. In this system, the upper limits of detectable photon and neutron energies are set to be 1.5MeV and 15MeV, respectively. In the previous works, the reduction of neutron and photon energies penetrating through shield of water and concrete layers were evaluated by using PHITS code, and it was found that the highest photon energy exceeded over 10MeV when the shield consists of water and concrete layers only [5]. In order to fulfill the requirement of the maximum photon energy, a model with iron layer is evaluated.

2. IFMIF/EVEDA Accelerator

2.1 Accelerator Building

A schematic drawing of the prototype accelerator is shown in Fig.1. The IFMIF/EVEDA accelerator building in Rokkasho site has the total area of 2019.5m^2, and the accelerator vault has the inside area of W: 8.0m x D: 41.5m x H: 7.0m. The vault is surrounded by concrete walls of 1.5m thickness. Additional local concrete shield of 0.5m thickness around the beam dump is also planned.

2.2 Beam Dump

A beam dump is required stopping the deuteron beam with maximum power of 1.125 MW in the CW

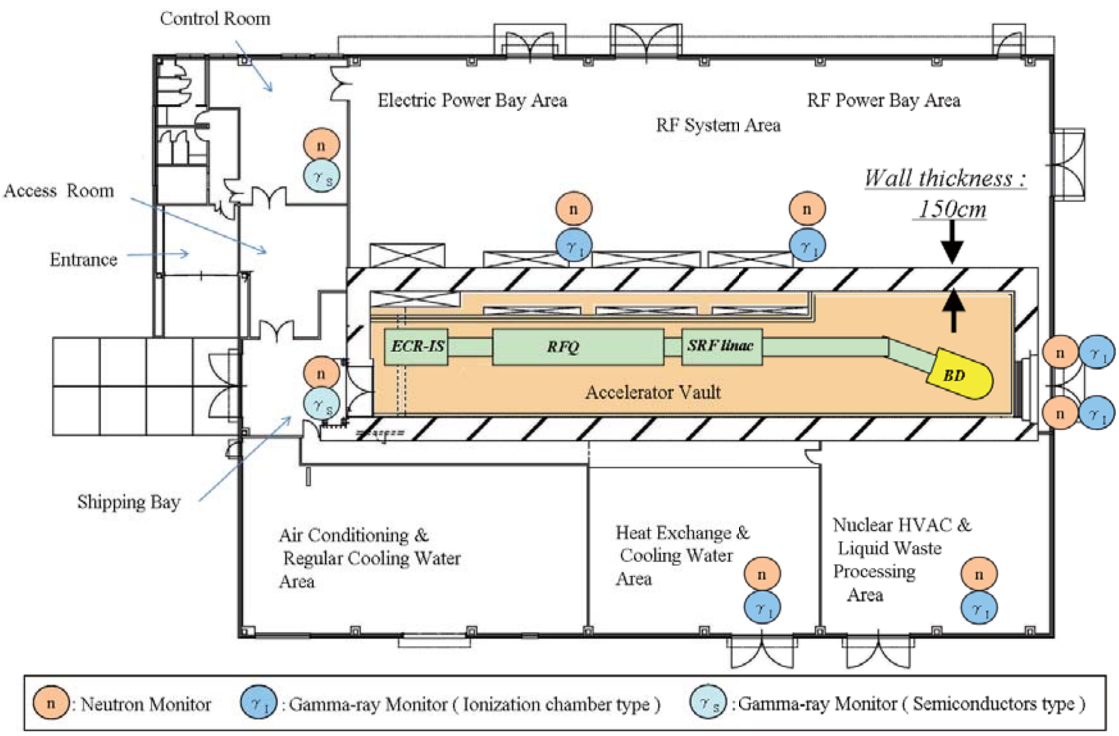

Figure 1: IFMIF/EVEDA accelerator building and area monitor layout

operation mode. A selection of the beam facing materials has to take into account the neutron production and the activation level as well as the thermal stresses. In the present design, a cone shaped copper with 0.005m thickness is used, and it is surrounded by water tank of a 0.75m-radius.

2.3 Area Monitoring System

Area monitoring system consists of two types; gamma-ray monitors and neutron monitor. The specifications of these monitors are shown in Table 1, and the location is shown in Fig.1. As shown in Table 1, the detectable energy range of the neutron monitor is from 0.025eV to 15MeV and the directional characteristics is -60 to +240° for a vertical direction, and that of the gamma-ray monitor is from 80keV to 1.5MeV and ±90° for a horizontal direction, -60 to +240° for a vertical direction. As shown in Fig.1, the area monitors are installed the external side of accelerator vault.

Table 1: The kinds of area monitor

Monitor	Specification	
Neutron monitor	Type	helium-3 counter
	Energy range	0.025eV to 15MeV
	Dose rate characteristic	dose equivalent rate: 10^{-2} to 10^{4} μSv/h
	Directional characteristics	vertical direction: -60 to +240°
Gamma-ray monitor	Type	semiconductors type
	Energy range	photon: 80keV to 1.5MeV
	Dose rate characteristic	dose equivalent rate: 10^{-1} to 10^{4} μSv/h
	Directional characteristics	horizontal direction: ±90°, vertical direction: -60 to + 90
	Type	ionization chamber type
	Energy range	photon: 80keV to 1.5MeV
	Dose rate characteristic	dose equivalent rate: 10^{-1} to 10^{5} μSv/h
	Directional characteristics	horizontal direction: ±90°, vertical direction: -60 to +90

3. Analysis

3.1 Nuclear data

Deuteron induced thick target neutron yield at 9MeV was measured in collaboration with Kyushu University because there was no experimental data for Cu(d,nx) reaction in the range of 5-9MeV[6]. The experimental data which is neutron generation in case of 1 μC irradiated to cupper is used as a source term in neutron transportation, and the energy reduction of photon are evaluated by PHITS code. The JENDL 4.0 is used for nuclear cross-section library.

3.2 Model

A point source which has the neutron angular distribution is used for this analysis as shown in Fig.2. The neutron point source is located in the center, and the total number of 1.35 $\times 10^{10}$ [n] by a 9MeV-1μC deuteron beam, is emitted. The 0.005m thickness copper is set around the point source. As for concrete components, the 0.56Wt% for hydrogen concentration adopted in ITER design is employed, and the concrete density of 2.1g/cm^3 (instead of 2.3 for ITER) is used to consider a safety margin for required environmental assessment.

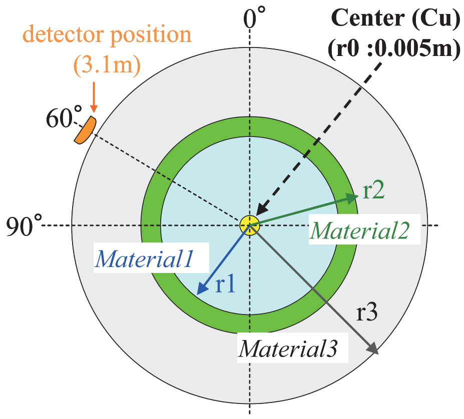

Figure 2: Analysis model

3.3 Calculations

Fig.3 shows the neutron number in void at the angle of 60º with respect to beam direction and the position of the 3.1m-radius. The gamma-ray and neutron are generated in central Cu with 0.005m radius. For the neutron number, the maximum of 5x10^8[n] is obtained and the energy range extends to 15MeV. For photon, the maximum number is 5x10^7[n] and the maximum energy is 14MeV.

In Fig.4, neutron and photon numbers at the same detector position with additional 0.75m radius water layer is indicated. This geometry corresponds to Material0 (Copper) radius r0=0.005, Material1 (water) layer r1=0.755m (0.005m+0.75m) and no Material2 and Material3 layer, in Fig.2. The neutron number is reduced to the 10^4-order level.

Fig.5 indicates neutron and photons throughout the combined geometry with water layer of 0.75m and the concrete layer of 2.0m (local concrete: 0.5m + concrete wall: 1.5m) at the same detector position. The numbers of neutron and photon is reduced to 10^2-order level, and it is found that these energy ranges extend to 6MeV (neutron) and 8MeV (photon).

As shown in Fig.6, for geometry with the water layer of 0.75m and the iron layer of 0.25m the maximum neutron number is the same level as

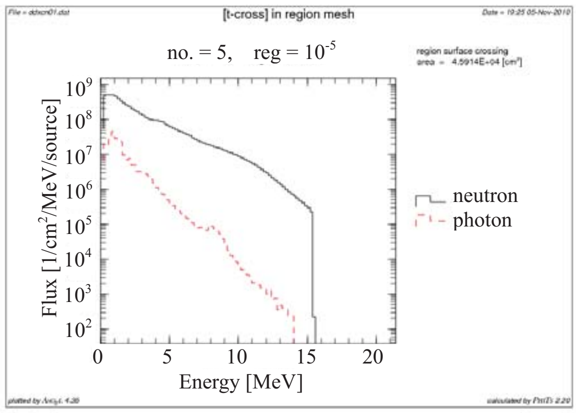

Figure 3: No shield (Vacuum status)
(M1, M2 and M3 are in vacuum)

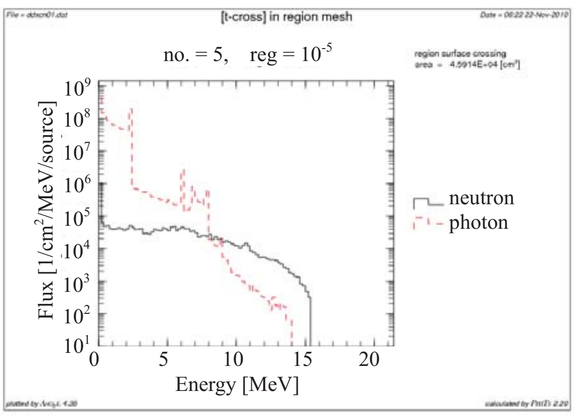

Figure 4: Water
(M1 is water, r1=0.755m without M2 and M3)

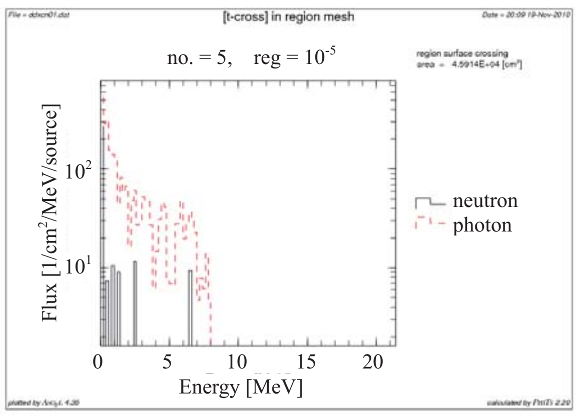

Figure 5: Water & Concrete
(M1 is water, r1=0.755m and M2 is concrete, r2=2.755m, without M3)

water only case (Fig.4.), however the number of photon is drastically reduced to less than 10^5 level, and the maximum energy is also decreased to the 10MeV from 14MeV.

In Fig.7, the case of the water layer of 0.75m, the iron layer of 0.25m and the concrete layer of 2.0m at the same detector position is indicated. While the numbers of neutron and photon fall below the 10^1-order level, the photon energy extends to 8MeV. The maximum neutron energy is less than 5MeV, to be covered by the specification of selected neutron monitor.

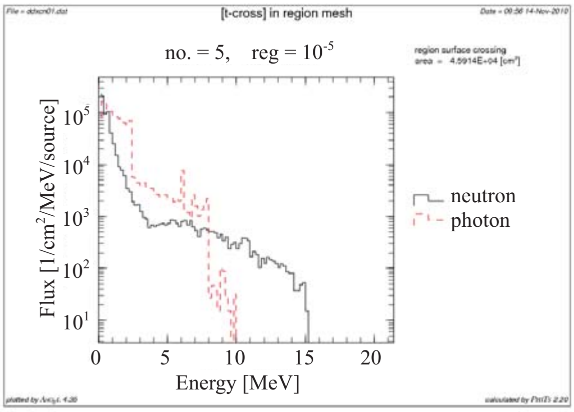

Figure 6: Water & Iron
(M1 is water, r1=0.755m and M2 is iron, r2=1.005m, without M3)

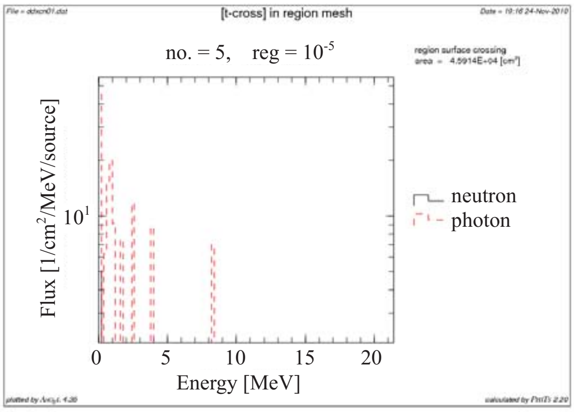

Figure 7: Water & Iron & Concrete
(M1 is water, r1=0.755m, M2 is iron, r2=1.005m and M3 is concrete, r3=3.005m)

4. Conclusion

For an iron layer, the energy reductions of photon are evaluated by using PHITS code. In the case of "water: 0.75m, iron: 0.25m, concrete: 2.0m", the numbers of neutron and photon fall below the 10^1-order level, and the photon energy range extends to 8MeV. This range exceeds the detectable limit of monitors, and it is not enough for required shielding of gamma-ray. On the other hand, the neutron energy range, of which maximum is less than 5MeV, is covered by the specification of detectors. However, dozens of neutrons are counted at the outside of concrete, and it is not completely zero. For both neutron and gamma-ray, therefore, an improvement of shielding components is furthermore necessary.

In the next step, the improved shielding components, a realistic model using beam dump structure and the position with a degree of leaning for concrete wall in the accelerator vault will be used, and their energy reduction including Air will be evaluated.

References

[1] IFMIF-CDA Team (Ed.) M. Martone, ENEA Frascati Report, RT/ERG/FUS/96/17 (1996).
[2] T. Kondo et al., J.of Nuc. Mater., 258-263,47(1998).
[3] T. E. Shannon et.all., J. of Nucl. Mater., 106(1998)
[4] A. Mosnier et al., MOPEC056, Proceedings of 1st International Particle Accelerator Conference (2010)
[5] H. Takahashi et al., P4-94, Symposium on Fusion Technology 2010, Porto, Portugal,
[6] N. Shigyo et.al., Proc. Int. Conf. on Nucler Data for Science and Technology 2010, will be published.

37. Sensitivity Analysis for Curium Isotope Concentrations of Light Water Reactor Mixed-Oxide Burned Fuel

Go CHIBA and Makoto ISHIKAWA
Research Group for Reactor Physics, Japan Atomic Energy Agency
Tokai-mura, Naka-gun, Ibaraki-ken 319-1195
e-mail: chiba.go@jaea.go.jp

With a help of the depletion perturbation theory, sensitivities of curium isotope concentrations to nuclear data are calculated for a light water reactor mixed-oxide burned fuel. Through the sensitivity analysis, phenomenon of the curium isotope generations during a reactor operation is well understood. In addition, important nuclear data for accurate prediction of the curium isotope concentrations are successfully specified. These information are helpful to investigate a cause of discrepancy between experimental and calculation values for the curium isotope concentrations.

1. Introduction

In order to validate prediction calculation methods for fuel depletion of light water reactors, some experimental programs focusing on fuel depletion, such as the MALIBU program [1], have been conducted, and the experimental data obtained through these programs have been analyzed by calculation methods used for core design of light water reactors. As shown in Ref. [2], there are still some discrepancies between experimental and calculation values even if modern nuclear data files are employed, and some differences are observed among results obtained with different nuclear data files.

A sensitivity analysis, which is performed with sensitivity coefficients of nuclide concentrations (number densities) to nuclear data, is quite a useful technique to investigate causes of the discrepancies and the differences between different nuclear data files. Moreover, sensitivity coefficients can be utilized also to quantify uncertainties associated with nuclear data if uncertainty data for the nuclear data are available.

Sensitivity coefficients of nuclide concentrations to nuclear data can be easily calculated by the depletion perturbation theory. The depletion perturbation theory for the zero-dimensional nuclide field equation has been initially proposed by Gandini [3], and has been extended to the nuclide/neutron coupled field by Williams [4]. Application of the depletion perturbation theory can be found in some literatures. For example, we can see some examples of the application of this theory to sensitivity studies for fission product concentrations [5][6].

In a light water reactor mixed-oxide fuel, curium isotopes are generated and are accumulated through a reactor operation. The accurate prediction for the curium isotope concentrations after burn-up is not easy since the many ancestor nuclides contribute to the curium isotope generations. In the present study, we perform a sensitivity analysis focusing on curium isotope concentrations of a light water reactor mixed-oxide burned fuel with the depletion perturbation theory.

Sensitivities of curium isotope concentrations to nuclear data of major and minor actinides are calculated in order to specify the important nuclear data for accurate prediction of the curium isotope concentrations after burn-up.

2. Brief description of the depletion perturbation theory

In the present section, the depletion perturbation theory for the nuclide field is briefly described. Its detail can be found in the literatures [3][4][6].

The nuclide densities of a reactor are expressed using the following nuclide density vector:

$$\mathbf{N}(t) = \left[N_1(t), N_2(t), \ldots, N_n(t)\right],$$

where $N_i(t)$ is the number density of nuclide i at time t. We denote the initial time as $t = 0$ and the final time as $t = T$. The number density vector satisfies the following burn-up equation:

$$\frac{d}{dt}\mathbf{N}(t) = \mathbf{MN}(t),$$

where $\mathbf{M}$ is the so-called burn-up matrix.

In the present study, we calculate the sensitivity of the nuclide concentrations after burn-up to nuclear data. The sensitivity is defined as

$$S^i = \frac{dN_i(t)/N_i(t)}{d\sigma/\sigma} = \frac{\sigma}{N_i(t)} \cdot \frac{dN_i(t)}{d\sigma},$$

where σ denotes nuclear data such as reaction cross sections and half-lives Using the depletion perturbation theory, the derivative term in the above equation can be calculated as

$$\frac{dN_i(t)}{d\sigma} = \int_0^T dt\left(\mathbf{N}^*(t)\frac{d\mathbf{M}}{\mathbf{d}\sigma}\mathbf{N}(t)\right),$$

where $\mathbf{N}^*$ is the adjoint number density vector which satisfies the following equation:

$$-\frac{d}{dt}\mathbf{N}^*(t) = \mathbf{M}^*\mathbf{N}^*(t),$$

where $\mathbf{M}^*$ is a transposed matrix of $\mathbf{M}$. In this adjoint burn-up equation, an appropriate initial vector is given at $t = T$ according to the target nuclide for which the sensitivity is calculated.

In the depletion perturbation theory for the neutron flux and nuclide density coupled field, the generalized adjoint flux and the adjoint power are introduced in order to consider a neutron flux spatial/energetical distribution effect and a power normalization effect.

3. Numerical procedure

The present study treats a light water mixed-oxide fuel pin cell model, which is made to represent a 17×17 pressurized water reactor fuel assembly [7]. This model and a calculation condition are almost same as those used in the previous sensitivity study for fission product concentrations [6]. The uranium-235 concentration and the plutonium content of the fuel are 0.2 wt% and 10.0 wt%, respectively. The initial number densities of the fuel are shown in **Table 1**.

The geometrical parameters of this pin cell are:

- pin pitch : 1.265 cm,
- fuel pellet radius : 0.412 cm,
- outer radius of cladding region : 0.476 cm.

Fuel depletion calculations are performed with a linear heat rating of 179 W/cm till 45 GWd/t and are followed by a cooling time of five years.

Resonance self-shielded cross sections are generated with the equivalence theory using a 107-group library based on JENDL-4.0. With the region-wise 107-group cross sections, eigenvalue calculations are performed with the collision probability method. White boundary conditions are assigned to reduce a computational cost. The above resonance and eigenvalue calculations are performed at depletion steps, 0, 0.1, 1, 2.5, 5, 7.5, 10, 12.5, 15, 17.5, 20, 22.5, 25, 27.5, 30, 32.5, 35, 37.5, 40, 42.5 and 45 GWd/t. Depletion calculations are carried out by the Pade method with twenty depletion sub-steps for each depletion step. **Figure 1** shows a burn-up chain for heavy nuclides utilized in the present study. This chain is almost the same as that of the SRAC code.

Table 1 Initial number densities of fuel

Nuclide	Number density ($10^{24}/cm^3$)
U−235	4.104E−5
U−238	2.022E−2
Pu−238	4.731E−5
Pu−239	1.223E−3
Pu−240	5.586E−4
Pu−241	2.069E−4
Pu−242	1.418E−4
Am−241	6.007E−5
O−16	4.500E−2

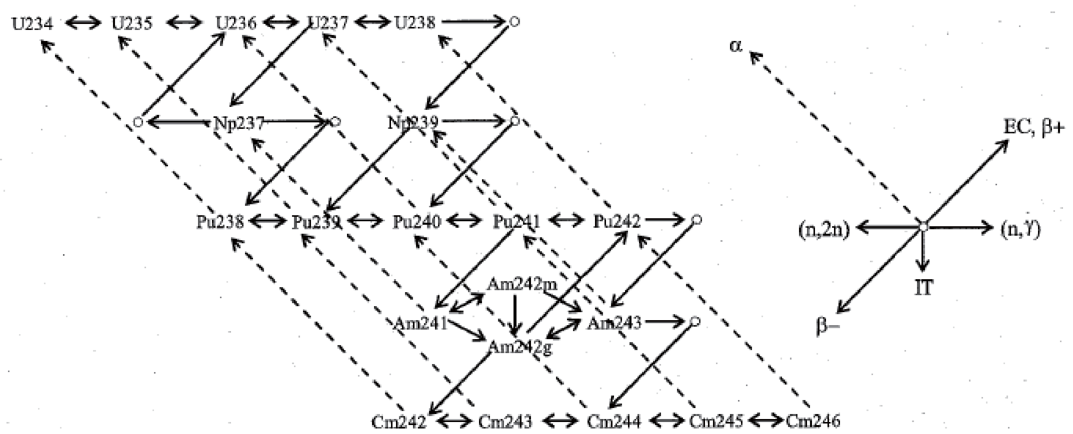

Fig. 1 Burn-up chain for heavy nuclides

Sensitivity calculations are performed with the depletion perturbation theory for the neutron flux and nuclide density coupled field. The target of the sensitivity calculations is concentrations of curium isotopes after 45 GWd/t burn-up and 5-year cooling time. The sensitivities of the concentrations are calculated to fission and capture cross sections and half-lives of heavy nuclides. While we obtain energy group-wise sensitivities, we show one-group-integrated sensitivities in order to ease a comparison.

4. Numerical results

Figure 2 shows one-group sensitivities to fission and capture cross sections of major actinides. The following are observed in this figure:

- Negative sensitivities to fission cross sections are observed. When a fission cross section increases, the neutron flux level decreases since the heat rating is constant. That results in decreases of (n,g) reaction rates, and then generations of curium isotopes are restricted. That is why the sensitivities to fission cross sections are negative.

- The negative sensitivities to fission cross sections are large for concentrations of high order curium isotopes such as Cm-245 and -246 since such nuclides are generated via a large number of (n,g) reactions.
- As mentioned above, an increase of fission cross sections results in decreases of reaction rates. It relatively increases contribution of the nuclide decay to concentration changes. For example, the increase of fission cross sections promotes the Pu-241 decay and the Am-241 generation. Since Am-241 is a parent nuclide of Am-242m, which is a parent nuclide of Cm-242, that results in an increase of the Cm-242 concentration. This means that there is a positive component in the Cm-242 concentration sensitivity to fission cross sections. Note that the Cm-242 concentration after 5-year cooling is quite small since Cm-242 is transformed to Pu-238 during the cooling time.
- The sensitivity of the Cm-242 concentration to the Pu-239 fission cross section is positive. Additional calculations show that this sensitivity is dependent on the cooling time. The sensitivity changes to -0.09 without cooling time, and to +0.52 with 10-year cooling. That is because contribution of the Am-242m decay during the cooling time to the Cm-242 concentration becomes larger as cooling time increases.
- Sensitivities to the U-238 capture cross sections are negative. If the U-238 capture cross section increases, the Pu-239 concentration also increases. That results in a decrease of the neutron flux level and restrict (n,g) reactions since the heating rate is constant.
- The concentrations of Cm-244, -245 and -246 have sensitivities to the Pu-242 capture cross section since these nuclides are generated mainly via Am-243, which is a daughter nuclide of Pu-242. On the other hand, the concentrations of Cm-242 and -243 have no sensitivities to this cross section since these nuclides are generated mainly via Am-241.
-

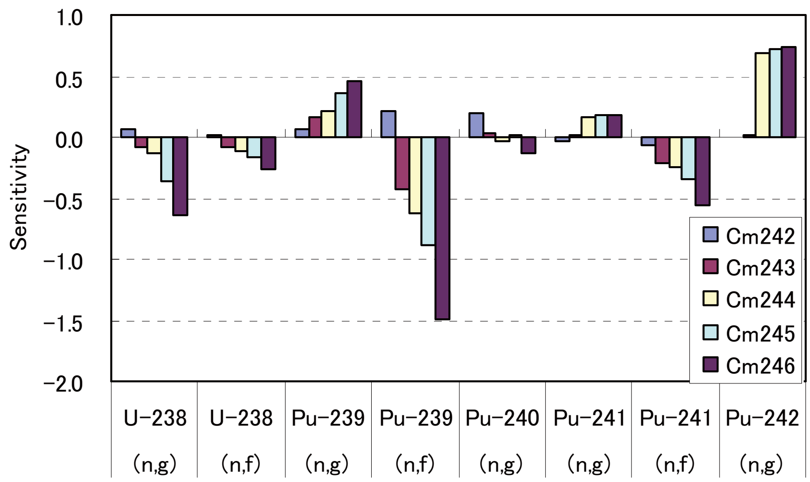

Fig. 2 One-group sensitivities of the curium concentrations to major actinide cross sections

Figure 3 shows one-group sensitivities to fission and capture cross sections of minor actinides, and **Fig. 4** shows sensitivities to half-lives. The following are observed in these figures:

- As already described, Cm-242 and -243 are generated mainly via Am-241 while Cm-244, -245 and -246 are generated mainly via Am-243. Since the Cm-244 concentration has no sensitivity to the Cm-243 capture cross section, the link between Cm-243 and -244 in the burn-up chain is quite weak.
- Except for Cm-242, all the curium isotopes have no sensitivities to the capture cross sections and half lives of themselves. Thus, the concentrations of these nuclides are far from an equilibrium state; the generation is much larger than the loss for these nuclides.
- The concentrations of both Cm-245 and -246 are sensitive to the Am-243 and Cm-244 capture cross sections. On the other hand, the Cm-246 concentration is sensitive to the Cm-245 capture cross section while the Cm-245 concentration is not sensitive to that. The similar trend can be observed in the concentration sensitivities of Cm-244 and -245. These similarities and differences in the sensitivities are beneficial to investigate a difference in the prediction accuracy for concentrations of these nuclides.

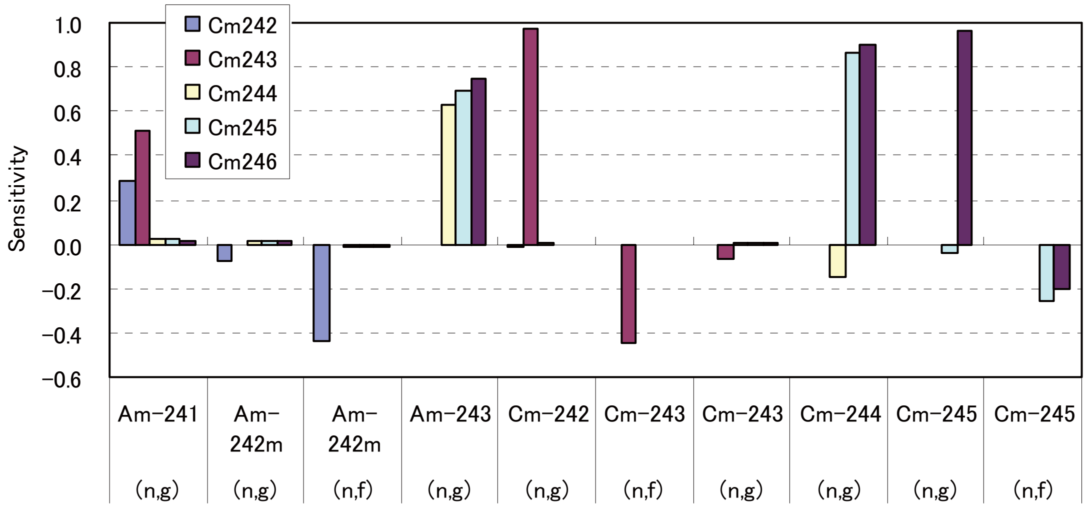

Fig. 3 One-group sensitivities of the curium concentrations to minor actinide cross sections

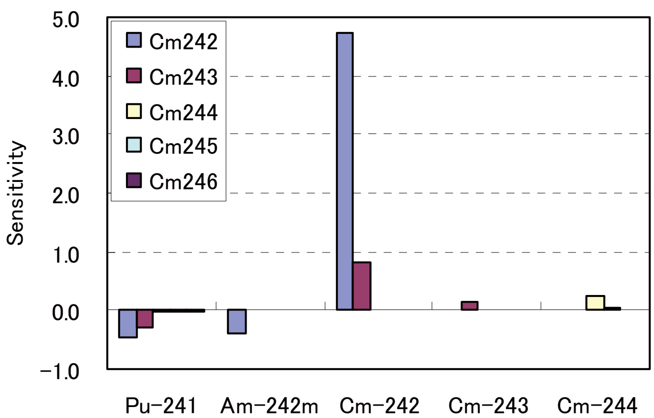

Fig. 4 Sensitivities of the curium concentrations to minor actinide half-lives

5. Conclusion

With the help of the depletion perturbation theory, sensitivities of the curium isotope concentrations to nuclear data have been calculated for a light water reactor mixed-oxide burned fuel. Through the sensitivity analysis, phenomenon of the curium isotope generations during a reactor operation has been well understood. In addition, important nuclear data for accurate prediction of the curium isotope concentrations have been successfully specified. These information are helpful to investigate a cause of discrepancy between experimental and calculation values for the curium isotope concentrations.

References

[1] D. Boulanger, M. Lippens, J. Basselier, "High Burnup PWR and BWR MOX fuel performance: A review of BELGONUCLEAIRE Recent Experimental Programs," *Proceeding of the 2004 International Meeting on LWR Fuel Performance*, Orland, Florida, September 19-22, paper1109(2004).

[2] S. Matsuoka, T. Ito, "Impact of difference of neutron cross section libraries to isotopic concentration of actinides," Proc. of Int. Conf. on Physics of Reactor, Physor2010, Pittsburgh, (2010).

[3] A. Gandini, "Time-dependent generalized perturbation theory for burn-up analysis," CNEN RT/FI(75)4, Comitato Nazionale per l'Energia Nucleare, Rome (1975).

[4] M.L.Williams, "Development of depletion perturbation theory for coupled neutron/nuclide fields," Nucl. Sci. Eng., 70, p.20-36 (1979).

[5] I.C.Gauld, D.E.Mueller, Evaluation of cross-section sensitivities in computing burnup credit fission product concentrations, ORNL/TM-2005/48, Oak Ridge National Laboratory (2005).

[6] G.Chiba, et al., "Sensitivity analysis of fission product concentrations for light water reactor burned fuel," J. Nucl. Sci. Technol., 47[7], p.652-660 (2010).

[7] J. Katakura, et al., A set of ORIGEN2 cross section libraries based on JENDL-3.3 library: ORLIBJ33, JAERI-Data/Code 2004-015, Japan Atomic Energy Research Institute (2004).[in Japanese]

38. Sensitivity Analysis for Higher Order Legendre Coefficients of Elastic Scattering Matrices

Go CHIBA
Research Group for Reactor Physics, Japan Atomic Energy Agency
Tokai-mura, Naka-gun, Ibaraki-ken 319-1195
e-mail: chiba.go@jaea.go.jp

A sensitivity analysis is carried out focusing on higher order Legendre coefficients of elastic scattering matrices. Non-negligible library effects, which are defined as differences in criticalities caused by differences in nuclear data of different libraries, are observed in higher order Legendre coefficients of elastic scattering matrices of uranium-238 and iron-56 between JENDL-4.0 and the other modern nuclear data files. It is also found that an attention should be paid to the type of multi-group cross sections used for library effect calculations. It is concluded that higher order Legendre coefficients should be accounted for if accurate library effect evaluation is required.

1. Introduction

The nuclear data is usually stored in the evaluated nuclear data files with the so-called ENDF format. There are several evaluated nuclear data files such as JENDL, ENDF and JEFF in the world. These libraries have been updated along with the improvement on the nuclear reaction models, the evaluation codes and the experimental data used for nuclear data evaluations. Since the nuclear data is the physical quantity, the evaluated nuclear data may converge to the true values by their improvement. While the latest evaluated nuclear data files such as JENDL-4.0, ENDF/B-VII.0 and JEFF-3.1 have quite high qualities, there are still large differences among them, and these differences significantly affect integral parameters calculated with these nuclear data files.

Sensitivity analyses are useful to investigate causes of differences in integral parameters among different nuclear data files, and they have been effectively carried out in order to improve the qualities of the nuclear data files. In the usual sensitivity analyses, various kinds of the nuclear data have been accounted for. Scattering matrices and the first order Legendre coefficients of them have been also treated. Higher order Legendre coefficients of scattering matrices however have been ignored since the contributions of these data are supposed to be negligibly small.

In the present paper, a sensitivity analysis is carried out focusing on higher order Legendre coefficients of elastic scattering matrices. Criticalities of various fast neutron systems are calculated with the modern nuclear data files, JENDL-4.0, -3.3, ENDF/B-VII.0 and JEFF-3.1, and differences in the calculated values are investigated from a view point of a difference in higher order Legendre coefficients of elastic scattering matrices.

2. Foundation of sensitivity analyses

In the present study, only criticality k is treated as an integral parameter. Sensitivity coefficients of k to the nuclear data σ, S_σ^k, can be easily calculated by the first order perturbation theory with forward and adjoint neutron fluxes. Usually S_σ^k is interpreted as a relative change in k due to a relative change in σ, and is defined as $S_\sigma^k = (dk/k)/(d\sigma/\sigma)$. This definition is however inappropriate to describe sensitivities to higher order Legendre coefficients of scattering matrices a_l since a_l can take both positive and negative values, and a value close to zero. Thus the definition of sensitivity coefficients is modified as $S_\sigma^k = (dk/k)/d\sigma$ in the present study.

The so-called library effect is calculated as follows. Let us consider two multi-group libraries, LIB1 and LIB2. Here criticalities calculated with these two libraries are written as k^{LIB1} and k^{LIB2}. A difference in these criticalities $\Delta k = k^{LIB2} - k^{LIB1}$ due to differences in Legendre coefficients of elastic scattering matrices are calculated as

$$\Delta k = \sum_n \sum_{l=1} \sum_g \sum_{g'} S_{\sigma_{l,g\to g'}}^{k,LIB1} \left(a_{l,g\to g'}^{LIB2} - a_{l,g\to g'}^{LIB1} \right) \sigma_{0,g\to g'}^{LIB1} , \qquad (1)$$

where n denotes nuclides, l denotes the Legendre order, g and g' denote energy groups, respectively. This Δk corresponds to the library effect of higher order Legendre coefficients. Usually, higher order Legendre components of scattering matrices $\sigma_{l,g\to g'}$ are stored in multi-group cross section libraries. Thus Legendre coefficients of scattering matrices $a_{l,g\to g'}$ are derived from scattering matrices stored in multi-group libraries as $a_{l,g\to g'} = \sigma_{l,g\to g'} / \sigma_{0,g\to g'}$. Note that infinite dilution cross sections are used for the present library effect calculations as usual.

If we focus on a difference in Legendre components (cross sections), not in Legendre coefficients, of scattering matrices, a library effect is calculated with the following equation:

$$\Delta k = \sum_n \sum_{l=1} \sum_g \sum_{g'} S_{\sigma_{l,g\to g'}}^{k,LIB1} \left(a_{l,g\to g'}^{LIB2} \sigma_{0,g\to g'}^{LIB2} - a_{l,g\to g'}^{LIB1} \sigma_{0,g\to g'}^{LIB1} \right).$$

3. Numerical procedure

The following are fast neutron systems for which sensitivity analyses are carried out in the present study. The specifications of these systems are derived from the ICSBEP handbook [1]:

- HEU-MET-FAST-001 (Godiva): a bare sphere of highly enriched uranium.

- PU-MET-FAST-001 (Jezebel): a bare sphere of plutonium-239 metal.
- U233-MET-FAST-001 (Jezebel-233): a bare sphere of uranium-233 metal.
- HEU-MET-FAST-028 (Flattop-U): a highly enriched uranium sphere reflected by normal uranium.
- PU-MET-FAST-006 (Flattop-Pu): a plutonium sphere reflected by normal uranium.
- U233-MET-FAST-006 (Flattop-233): a uranium-233 sphere reflected by normal uranium.
- HEU-MET-FAST-003-011: a highly enriched uranium sphere reflected by tungsten-carbide.
- HEU-MET-FAST-021: a highly enriched uranium sphere reflected by iron.
- PU-MET-FAST-040: a plutonium sphere reflected by copper.
- HEU-MET-FAST-027: a highly enriched uranium sphere reflected by lead.

70-group sensitivity coefficients are derived with forward and adjoint neutron fluxes calculated by using an in-house discrete ordinates neutron transport code. In the discrete ordinates neutron transport calculations, Legendre coefficients of scattering matrices are accounted for up to the fifth order, and the 32-point double Gaussian angular quadrature set is used. Effective cross sections used for the neutron transport calculations are obtained by using the SLAROM-UF code [2] and UFLIB-J4.0 based on JENDL-4.0. **Figure 1** shows a sensitivity of the HEU-MET-FAST-028 criticality to Legendre coefficients of elastic scattering cross sections of uranium-238.

Library effects are calculated according to Eq.(1) with the sensitivity coefficients and the infinite dilution cross sections stored in UFLIB. JENDL-4.0 is treated as a base library, and differences of the other libraries to JENDL-4.0 are evaluated.

4. Result of sensitivity analysis

Table 1 shows differences in criticalities due to differences in each order of Legendre coefficient of elastic scattering matrices. Large effects over 0.001 are written in a bold style.

While library effects due to differences in higher order Legendre coefficients are generally small, non-negligible effects are observed in PU-MET-FAST-006 with JENDL-3.3 and ENDF/B-VII.0, and HEU-MET-FAST-021 with all the libraries. The former is due to the difference in the uranium-238 data and the latter is due to the difference in the iron-56 data.

Please remember that the above library effect calculations are carried out by using infinite dilution cross sections. Since medium-heavy nuclides such as iron-56 have resonance cross sections in the energy range above 0.1MeV, which is a dominant range in the present benchmark systems, the resonance self-shielding effect should be considered for accurate evaluation of library effects. Thus, a library effect calculation is again carried out for HEU-MET-FAST-021 with shielded cross sections. In the resonance self-shielding factor calculation, background cross sections for iron isotopes are set at 50, 0.5, 150 and 1,000 barns for iron-54, -56, -57 and -58, respectively. These values are evaluated for the reflector medium of HEU-MET-FAST-021. In this case, a library effect is calculated with the following equation:

$$\Delta k = \sum_n \sum_{l=1} \sum_g \sum_{g'} S^{k,LIB1}_{\sigma_{l,g\to g'}} \left(a^{LIB2}_{l,g\to g'} - a^{LIB1}_{l,g\to g'} \right) f^{LIB1}_g \sigma^{LIB1}_{0,g\to g'}$$

$$= \sum_n \sum_{l=1} \sum_g \sum_{g'} S^{k,LIB1}_{\sigma_{l,g\to g'}} \left(f^{LIB2}_{t1,g} \sigma^{LIB2}_{l,g\to g'} \Big/ f^{LIB2}_g \sigma^{LIB2}_{0,g\to g'} - f^{LIB1}_{t1,g} \sigma^{LIB1}_{l,g\to g'} \Big/ f^{LIB1}_g \sigma^{LIB1}_{0,g\to g'} \right) f^{LIB1}_g \sigma^{LIB1}_{0,g\to g'} ,$$

where f_g and $f_{t1,g}$ are self-shielding factors for elastic scattering cross sections and current-weighted total cross sections, respectively. Since a multi-group library does not include self-shielding factors for higher order Legendre components of elastic scattering cross sections, self-shielding factors for current-weighted total cross sections are used instead.

The revised library effect for HEU-MET-FAST-021 is shown in **Table 2**. In comparison with the results before the revision, library effects become much smaller since shielded cross sections are generally smaller than infinite dilution cross sections. Even after the revision, however, non-negligible library effects due to the difference in higher order Legendre coefficients are still observed. **Figure 2** shows an energy group-wise library effect of iron-56 to the criticality of HEU-MET-FAST-021 between JENDL-4.0 and JEFF-3.1.

In order to confirm the validity of the above treatment, a difference in the criticality of HEU-MET-FAST-021 between JENDL-4.0 and JEFF-3.1 is directly calculated by the perturbation theory. This perturbation calculation shows that differences in criticality due to the difference in the first and second Legendre components of elastic scattering matrices are -0.0058 and +0.0025, respectively. Since this perturbation calculation focuses on differences in the Legendre scattering cross sections, not in the Legendre coefficients, library effects of the Legendre components of elastic scattering matrices between JEFF-3.1 and JENDL-4.0 are also calculated. The library effects due to the first and second Legendre scattering cross section differences are evaluated at -0.0047 and +0.0023, respectively. This result is consistent with the former direct perturbation calculation.

5. Conclusion

A sensitivity analysis has been carried out focusing on higher order Legendre coefficients of elastic scattering matrices. Non-negligible library effects have been observed in higher order Legendre coefficients of elastic scattering matrices of uranium-238 and iron-56 between JENDL-4.0 and the other modern nuclear data files. It has been also found that an attention should be paid to the type of multi-group cross sections used for the library effect calculations. It is concluded that the higher order Legendre coefficients should be accounted for if accurate library effect evaluation is required.

Acknowledgment

The author wishes to express his deep gratitude to M. Ishikawa of Japan Atomic Energy Agency for providing useful comments on this manuscript.

References

[1] J. Blair Briggs (ed.): International handbook of evaluated criticality safety benchmark experiments, NEA/NSC/DOC(95)03/I, Nuclear Energy Agency, Paris (2009 Edition).

[2] T. Hazama, et al.: "Development of SLAROM-UF : a lattice calculation code with fine and ultra-fine energy group cross sections," J. Nucl. Sci. Technol., 43, p.908 (2006).

Table 1 Library effects due to Legendre coefficients of elastic scattering matrices
(Base library: JENDL-4.0, infinite dilution cross section is used)

System	Nuclide	Legendre order	Nuclear data files		
			JENDL-3.3	ENDF/B-VII.0	JEFF-3.1
HEU-MET-FAST-001	U-235	1	**-0.0042**	**-0.0032**	**-0.0032**
		2	0.0002	0.0001	0.0001
	U-238	1	-0.0005	-0.0001	-0.0001
PU-MET-FAST-001	Pu-239	1	**0.0011**	-0.0007	**0.0029**
		2	-0.0002	-0.0001	-0.0003
	Pu-240	1	0.0007	-0.0001	0.0001
U233-MET-FAST-001	U-233	1	**-0.0015**	-0.0001	**-0.0015**
		2	0.0001		0.0001
HEU-MET-FAST-028	U-235	1	**-0.0015**	**-0.0012**	**-0.0012**
	U-238	1	**-0.0106**	**-0.0014**	**-0.0021**
		2	0.0009	-0.0009	-0.0006
PU-MET-FAST-006	Pu-239	1	0.0004	-0.0002	0.0009
	Pu-240	1	0.0003	-0.0001	
	U-238	1	**-0.0112**	**-0.0012**	**-0.0026**
		2	**0.0013**	**-0.0013**	-0.0007
U233-MET-FAST-006	U-233	1	**-0.0005**	0.0001	-0.0005
	U-238	1	**-0.0107**	**-0.0012**	**-0.0024**
		2	0.0012	**-0.0012**	-0.0007
HEU-MET-FAST-003.11	W-182	1	0.0003	0.0003	0.0003
	W-184	1	**0.0013**	**0.0013**	**0.0013**
	W-186	1	0.0009	**0.0010**	0.0009
HEU-MET-FAST-021	Fe-54	1		-0.0003	0.0006
	Fe-56	1	**0.0028**	**0.0019**	**-0.0091**
		2	**0.0023**	**0.0036**	**0.0054**
		3	-0.0001	-0.0003	-0.0002
	Fe-57	1		0.0003	0.0002
PU-MET-FAST-020	Cu-63	1	**0.0025**	**0.0012**	**0.0012**
		2	-0.0004	-0.0001	-0.0001
	Cu-65	1	**0.0025**	**-0.0012**	**-0.0012**
		2	-0.0005		
HEU-MET-FAST-027	Pb-206	1	0.0003		
	Pb-207	1	0.0002		
	Pb-208	1	0.0002	**-0.0038**	0.0001
		2	-0.0002	-0.0002	
		3		-0.0002	

Table 2 Library effects due to Legendre coefficients of elastic scattering matrices
(Base library: JENDL-4.0, shielded cross section is used)

Nuclide	Legendre order	Nuclear data files		
		JENDL-3.3	ENDF/B-VII.0	JEFF-3.1
Fe-56	1	0.0034 (0.0028*)	0.0012 (0.0019)	-0.0026 (-0.0091)
	2	0.0012 (0.0023)	0.0017 (0.0036)	0.0019 (0.0054)
	3	-0.0001 (-0.0001)	-0.0001 (-0.0003)	0.0000 (-0.0002)

* Results obtained with infinite dilution cross sections

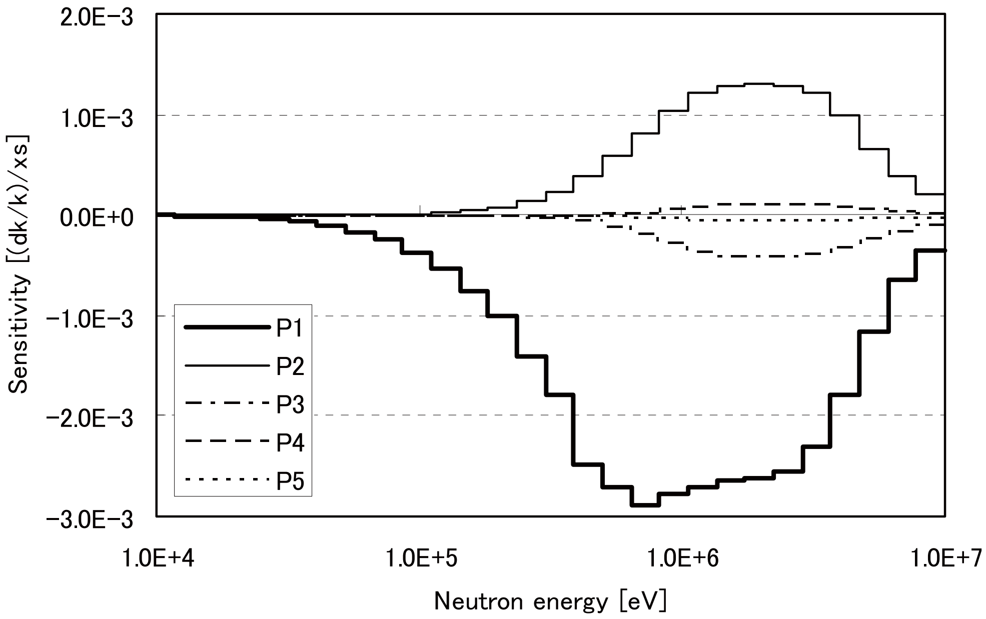

Fig.1 Sensitivity coefficient of the HEU-MET-FAST-028 criticality to Legendre coefficients of uranium-238 elastic scattering cross sections

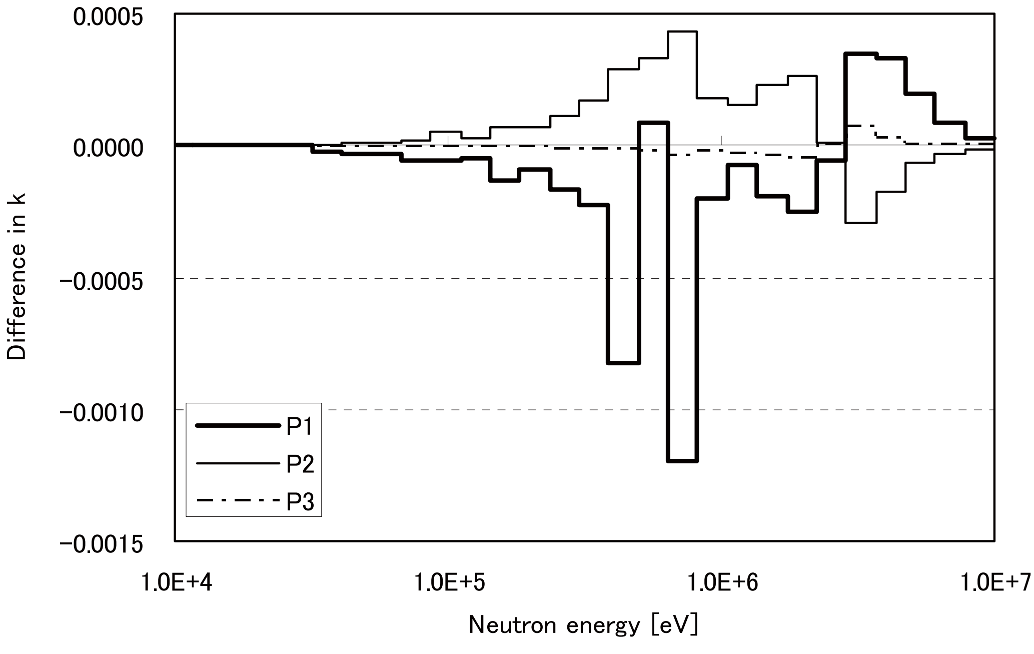

Fig.2 Energy group-wise library effect of Legendre coefficients of iron-56 elastic scattering matrices to the HEU-MET-FAST-021 criticality between JENDL-4.0 and JEFF-3.1 (Base library: JENDL-4.0)

39. Detailed Evaluation of Criticality Change of MOX Cores Based on Sensitivity Analysis

Masahiro KIMURA, Takanori KITADA, and Yosuke INOUE

Osaka University, 2-1Yamada-oka, Suita-shi, Osaka, Japan, 565-0871

E-mail: m-kimura@ne.see.eng.osaka-u.ac.jp

Detailed evaluation of the criticality change observed in MOX core was performed based on sensitivity analysis to clarify what is main cause of the difference in the criticality change between JENDL-3.3 and JENDL-4.0. It is found that the difference in the criticality change between two libraries is mainly caused by the change of ^{241}Am capture cross section, and the difference in the criticality change caused by the change of ^{239}Pu cross sections cancels among reaction types, although the change of ^{239}Pu cross sections brings a relatively large impact on the difference in the criticality change for each reaction type.

1. Introduction

NUPEC has been performing conceptual design studies of high moderation full MOX LWR cores. In a series of experimental analyses, the overestimation of multiplication factor (k_{eff}) slightly increases as shown in Fig. 1.

The target cores in this study are EPICURE MH1.2 (1993) and MISTRAL core4 (1999) [1]. The difference of overestimation in "k_{eff}" (diff-k) between EPICURE MH1.2 ("k_{eff}"=k_1) and MISTRAL core4 ("k_{eff}"=k_2) is about 0.6%Δk/k by using the 107-group cross section data based on JENDL-3.3 [2]. But it was reported that "diff-k" between two cores is reduced to about 0.4%Δk/k by using the data based on JENDL-4.0 [3]. To clarify what nuclides and reaction types are dominant to "the difference in diff-k" (about -0.2%Δk/k) between JENDL-3.3 and JENDL-4.0, sensitivity analysis was performed in this study.

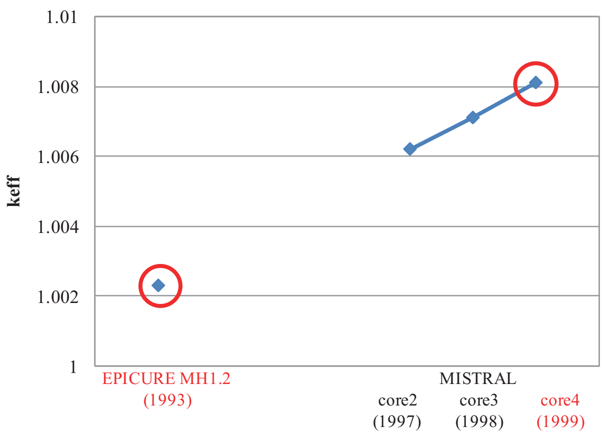

Fig. 1 Criticality of MOX cores (JENDL-3.3)

2. Core Configurations

An outline of core configurations of EPICURE MH1.2 and MISTRAL core4 is shown in Table 1 and Fig. 2.

Table 1 Core parameters

Program	EPICURE MH1.2	MISTRAL core4
Core Configuration	Partial MOX Homogeneous	Full MOX 17×17 Mockup
Vm/Vf	1.3	2.0
H/HM	3.7	5.8
Fuel pitch [cm]	1.26	1.32
Fuel rod type	MOX-7.0% UO_2-3.7%	MOX-7.0%
Core size [cm]	69	62

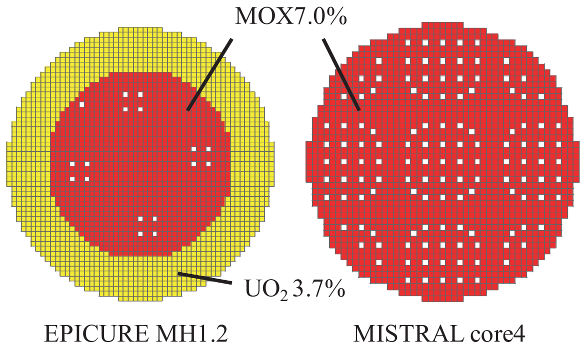

Fig. 2 Core configurations

3. Calculation Procedure

All calculations were performed in 107 energy groups: SRAC2006 [4] was used to obtain the group-wise cross sections for both JENDL-3.3 and JENDL-4.0. The group-wise cross sections were used in the generalized perturbation theory code SAGEP [5] to obtain the sensitivity coefficients for “diff-k” between EPICURE and MISTRAL. “The difference in diff-k” between JENDL-3.3 and JENDL-4.0 denoted as $\delta(\delta k_{4.0}\text{-}\delta k_{3.3})$ was evaluated by the following equation to obtain detailed information for the difference.

$$\langle S \rangle_{l,r,g} \equiv \frac{\delta(k_2 - k_1)}{\langle \delta\sigma / \sigma \rangle_{l,r,g}} = k_2 S_2 - k_1 S_1 \tag{1}$$

$$\delta(\delta k_{4.0} - \delta k_{3.3}) = \left\langle S_{3.3} \times \frac{(\sigma_{4.0} - \sigma_{3.3})}{\sigma_{3.3}} \right\rangle_{l,r,g} , \tag{2}$$

where < > represents integration over nuclide, reaction type and energy group, k_1 and k_2 are “k_{eff}” in EPICURE MH1.2 and MISTRAL core4, S_1 and S_2 are the sensitivity coefficient for “k_{eff}” in EPICURE MH1.2 and MISTRAL core4, $\delta k_{3.3}$ and $\delta k_{4.0}$ are “diff-k” based on JENDL-3.3 and JENDL-4.0, $S_{3.3}$ is the sensitivity coefficient for “diff-k” based on JENDL-3.3, $\sigma_{3.3}$ and $\sigma_{4.0}$ are the cross section based on JENDL-3.3 and JENDL-4.0, respectively.

4. Results

4.1 Contribution to "the difference in diff-k"

Summary of the breakdown of the contribution to "the difference in diff-k" of nuclide and reaction type is summarized in Table 2. "The difference in diff-k" is mainly caused by the change of ^{241}Am capture cross section, as shown Table 2. "The difference in diff-k" by the change of ^{239}Pu cross sections cancels among reaction types, although the change of ^{239}Pu cross sections brings relatively large impact on "the difference in diff-k" for each reaction type.

The change of ^{238}Pu capture cross section also causes "the difference in diff-k" of about +0.08%Δk/k, and the value of ^{238}U capture cross section is about -0.05%Δk/k. "The difference in diff-k" of about -0.33%Δk/k does not match the value of about -0.2%Δk/k, because there are many positive and negative portions and those cancel each other.

Table 2 Contribution to "the difference in diff-k" of each nuclide and reaction type

	Fission	ν	Capture	Elastic	Total
			[%Δk/k]		
^{235}U	0.005	-0.006	-0.020	0.000	-0.022
^{238}U	0.006	-0.008	-0.049	0.004	-0.043
^{238}Pu	0.000	0.000	0.084	0.000	0.084
^{239}Pu	0.062	-0.101	0.035	0.000	-0.002
^{240}Pu	0.000	0.000	-0.001	0.000	-0.001
^{241}Pu	0.003	0.015	-0.011	0.001	0.008
^{242}Pu	0.000	0.000	-0.005	0.000	-0.005
^{241}Am	-0.001	0.002	-0.334	0.000	-0.333
^{1}H	-	-	0.000	-0.015	-0.015
^{16}O	-	-	0.000	0.014	0.014
Zr	-	-	0.000	-0.004	-0.020
					-0.333

4.2 Detailed Analysis of ^{241}Am

The main contribution to "the difference in diff-k" comes from the ^{241}Am capture reaction in the following energy ranges; 1.13eV~1.45eV, 0.47eV~0.62eV and 0.25eV~0.32eV (Fig. 3). This comes from the fact that there are large positive difference in the cross sections between JENDL-3.3 and JENDL-4.0, and comparatively large negative sensitivity coefficients in such energy ranges as shown in Fig. 4. Sensitivity coefficients for "diff-k" of ^{241}Am capture cross section is always negative caused by the fact that the number density of ^{241}Am in MISTRAL core4 is larger than that in EPICURE MH1.2. It should be noted that ^{241}Am capture cross section based on JENDL-4.0 is out of one standard deviation of JENDL-3.3 in above energy ranges.

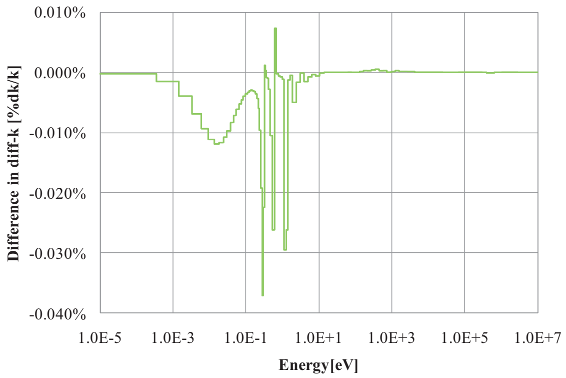

Fig. 3 "The difference in diff-k" from ^{241}Am

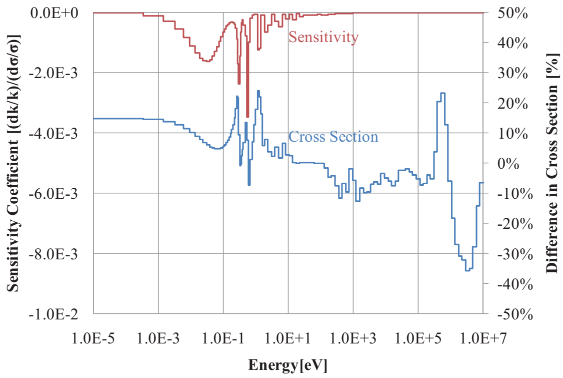

Fig. 4 Sensitivity coefficients and the difference in ^{241}Am capture cross section $((\sigma_{4.0}-\sigma_{3.3})/\sigma_{3.3})$

4.3 Detailed Analysis of ^{239}Pu

"The difference in diff-k" from ^{239}Pu for each reaction type is shown in Fig. 5. Sensitivity coefficients for "diff-k" and the difference in the cross sections between JENDL-3.3 and JENDL-4.0 are shown in Fig. 6 and Fig. 7, respectively.

① Fission and Capture

There are relatively large sensitivity coefficients especially in thermal groups. However the sign of the difference in cross sections depend on energy groups, this fact brings cancellations in "the difference in diff-k" among energy groups.

② ν-value

There are large sensitivity coefficients in thermal groups and about 0.1% difference in the cross sections between two libraries. "The difference in diff-k" does not cancel among energy groups because the difference in the cross sections is always negative in such groups. Therefore ν-value has relatively large impact on "the difference in diff-k" compared to fission and capture cross sections.

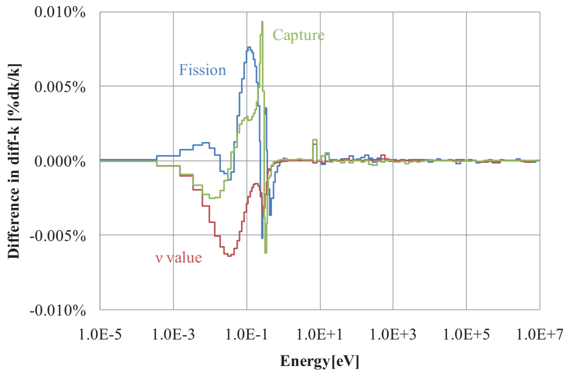

Fig. 5 "The difference in diff-k" from ^{239}Pu

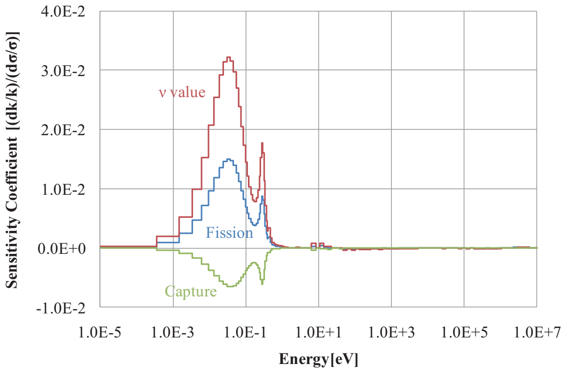

Fig. 6 Sensitivity coefficients of ^{239}Pu

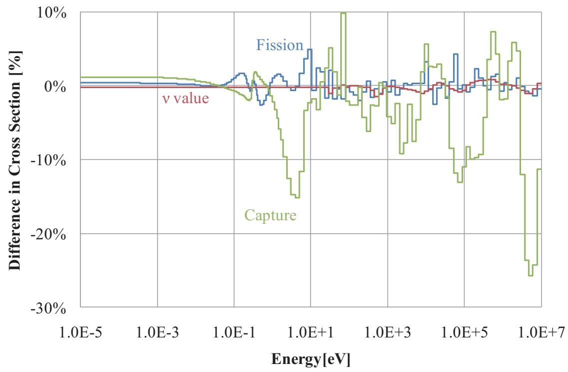

Fig. 7 The difference in cross section of ^{239}Pu

$((\sigma_{4.0}-\sigma_{3.3})/\sigma_{3.3})$

4.4 Detailed Analysis of Several Other Nuclides

"The difference in diff-k" from other nuclides such as ^{241}Am and ^{239}Pu are shown in Fig. 8 and Fig. 9.

Except for ^{241}Am and ^{239}Pu, the change of ^{238}Pu capture cross section has relatively large impact on "the difference in diff-k" about +0.84%Δk/k, and this is caused by the fact that the difference in the cross sections is about -20% in thermal groups and relatively large sensitivity coefficients in such energy groups as shown in Fig. 10.

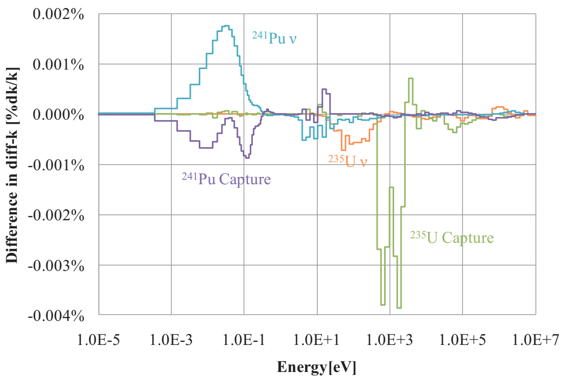

Fig. 8 "The difference in diff-k" from

^{235}U capture, ν and ^{241}Pu capture, ν

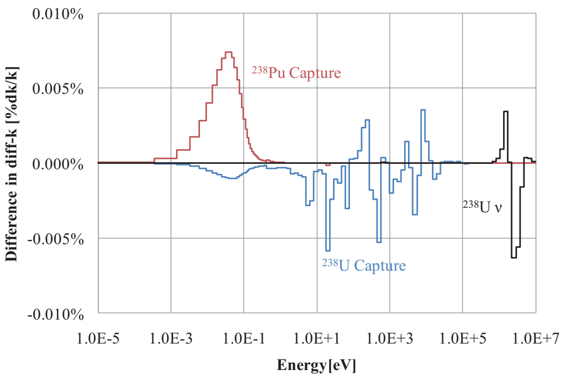

Fig. 9 "The difference in diff-k" from

^{238}U capture, ν and ^{238}Pu capture

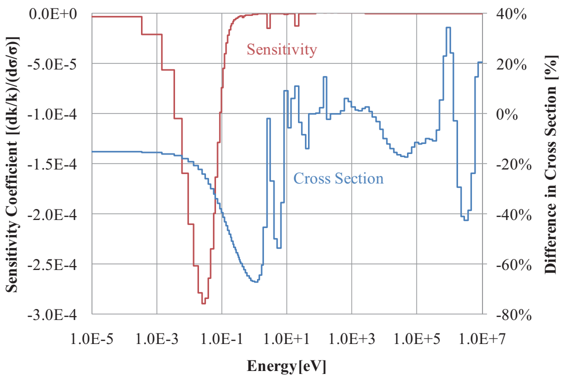

Fig. 10 Sensitivity coefficients and the difference in ^{238}Pu capture cross section

$((\sigma_{4.0}-\sigma_{3.3})/\sigma_{3.3})$

5. Conclusion

To clarify what nuclides and reaction types are dominant to “the difference in diff-k” about -0.2%Δk/k between JENDL-3.3 and JENDL-4.0, sensitivity analysis was performed. The followings were found in this investigation. The main contribution to “the difference in diff-k” comes from ^{241}Am capture reaction, and the value is about -0.3%Δk/k. “The difference in diff-k” caused by the change of ^{239}Pu cross sections cancels among reaction types, although the change of ^{239}Pu cross sections for each reaction type brings relatively large impact on “the difference in diff-k”. It is also noted that the change of ^{238}Pu capture cross section has relatively large impact on “the difference in diff-k” about +0.8%Δk/k.

Acknowledgements

The author wishes to express his gratitude to T. Nakagawa of Japan Atomic Energy Agency for providing the covariance data of ^{241}Am.

References

[1] K. Ishii, M. Tatsumi, T. Kan et al., “Analysis of MOX corephysics experiments MISTRAL,” Trans. At. Energy Soc. Jpn.,2, 39–54 (2003), [in Japanese].

[2] K. Shibata,"Japanese Evaluated Nuclear Data Library Version 3 Revision-3: JENDL-3.3," *J. Nucl. Sci. Technol*. **39**, 1125 (2002).

[3] K. Shibata,"JENDL-4.0: A New Library for Nuclear Science and Engineering" (to be published to *J. Nucl. Sci. Technol.*).

[4] Keisuke OKUMURA, "SRAC2006: A Comprehensive Neutronics Calculation Code System, " JAEA-Data/Code 2007-004 (2007).

[5] A. Hara, T. Takeda and Y. Kikuchi ”SAGEP:Two-Dimensional Sensitivity Analysis Code Based on Generalized Perturbation Theory” JAERI-M 84-027 (Jan. 1984) [in Japanese].

40. Analysis of Sample Worth for Dy_2O_3, Ho_2O_3, Er_2O_3 and Tm_2O_3 Measured at KUCA by MVP with Recent Version of JENDL, ENDF and JEFF

Koichi IEYAMA, Kosuke SHIMOZATO, Takanori KITADA

Osaka University, 2-1Yamada-oka, Suita-shi, Osaka, Japan, 565-0871

k-ieyama@ne.see.eng.osaka-u.ac.jp

Analyses were performed to verify nuclear data of some rare-earth elements (Dy, Ho, Er and Tm) by using the continuous energy Monte-Carlo code: MVP, and to evaluate the validity of the cross section libraries (JENDL-4.0, JENDL-3.3, ENDF/B-VII.0 and JEFF-3.1) by comparing infinite dilution cross section in SRAC library 107 energy groups. The difference of energy-integrated capture rate among these libraries is about 0.1% for Dy and 0.2% for Er at both E3 and EE1 cores, and the influence on energy-integrated capture rate by the difference of the cross section libraries is small at these cores. Though there is a relatively large difference in the C/E value of Ho_2O_3 at EE1 core between ENDF/B-VII.0 and JEFF-3.1, the difference of energy-integrated capture rate between these libraries is about 0.8% at EE1 core.

1. Introduction

The rare-earth elements would be useful as an advanced burnable poison. However, only a few critical experiments with rare-earth element have been carried out so far to validate the accuracy of their nuclear data. Critical experiments with four rare-earth elements (Dy, Ho, Er and Tm) at Kyoto University Critical Assembly (KUCA) were performed in two kinds of cores (E3 and EE1 core) with different neutron spectra shown in Fig. 1. The validity of cross section of rare-earth elements was estimated from the analysis of measured data by the continuous energy Monte-Carlo code; MVP and infinite dilution cross section in SRAC library 107 energy groups.

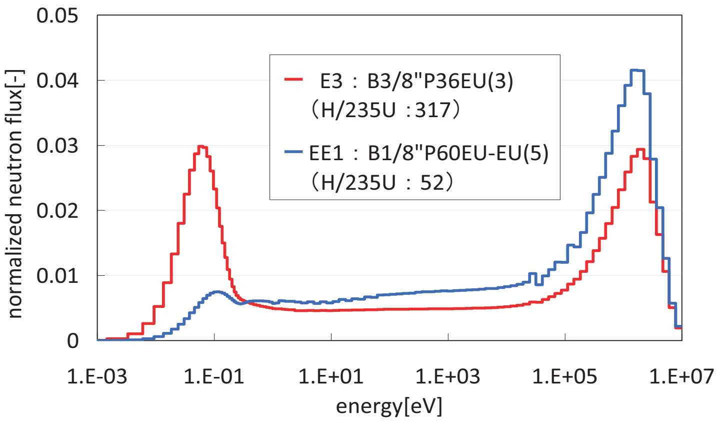

Fig. 1 Neutron Spectrum for each unit cell

2. Comparison of Calculation and Experimental Results

Calculation was performed by the MVP with rigorous treatment of the core geometries and material compositions as much as possible. The nuclear data libraries used in the MVP analyses were JENDL-4.0, JENDL-3.3, ENDF/B-VII.0 and JEFF-3.1. These nuclear data were used to evaluate sample worth of rare-earth elements (Dy_2O_3, Ho_2O_3, Er_2O_3 and Tm_2O_3), and the results were compared to evaluate the difference among nuclear data libraries. A sample worth was evaluated as the multiplication factors between the cores with a sample and without a sample. Neutron multiplication factor for each core was evaluated with 2.5 billion histories. C/E value of sample worth is shown in Table 1 and Fig. 2.

Table 1 C/E value of sample worth

E3 : B3/8″P36EU(3) core

element	C/E value			
	JENDL-4.0	JENDL-3.3	ENDF/B-VII.0	JEFF-3.1
Dy_2O_3	1.062 (±0.021)	–	1.082 (±0.021)	1.091 (±0.021)
Ho_2O_3	–	–	1.065 (±0.022)	1.089 (±0.022)
Er_2O_3	1.056 (±0.018)	1.033 (±0.018)	1.040 (±0.018)	1.054 (±0.018)
Tm_2O_3	1.017 (±0.021)	–	–	–

EE1 : B1/8″P60EUEU(5) core

element	C/E value			
	JENDL-4.0	JENDL-3.3	ENDF/B-VII.0	JEFF-3.1
Dy_2O_3	1.033 (±0.020)	–	1.024 (±0.020)	1.028 (±0.020)
Ho_2O_3	–	–	1.013 (±0.024)	1.101 (±0.025)
Er_2O_3	1.008 (±0.019)	0.993 (±0.019)	0.975 (±0.019)	0.979 (±0.019)
Tm_2O_3	0.987 (±0.021)	–	–	–

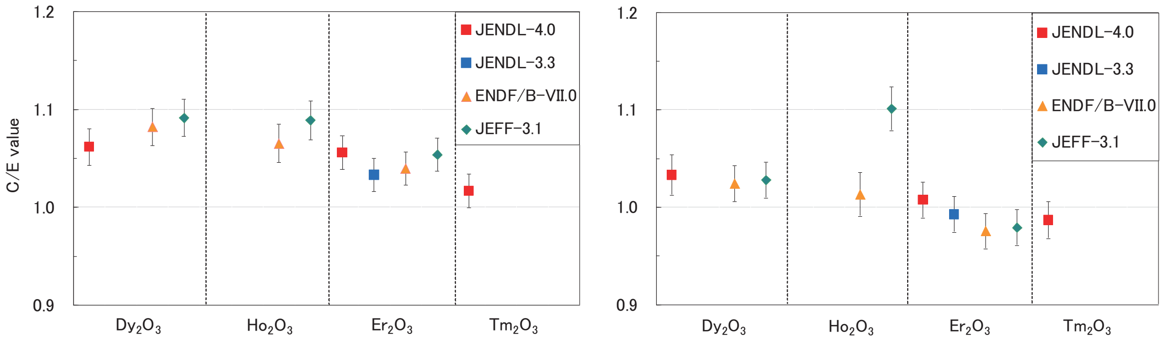

Fig. 2 C/E value of sample worth

As shown in Table 1 and Fig. 2, remarkable difference in C/E values among nuclear data libraries could not be observed for all elements and cores. However there is a relatively large difference in the C/E value of Ho_2O_3 at EE1 core between ENDF/B-VII.0 and JEFF-3.1. The spectrum dependency on C/E values would be in the case of Dy_2O_3 calculated with ENDF/B-VII.0 and JEFF-3.1. A spectrum dependency on C/E values can be evaluated by the comparison of C/E values at between E3 and EE1 cores. However all C/E values are roughly around 1.0 (from 0.98 to 1.11) by considering a standard deviation of about 0.03 depicted as error bars in Fig. 2. This fact indicates the validity of cross section data for Dy, Er, Ho and Tm in the libraries (JENDL-3.3, JENDL-4.0, ENDF/B-VII.0 and JEFF-3.1). The next chapter describes the difference of the C/E values between these libraries in detail by considering infinite dilution cross section for each nuclide.

3. Analysis

3.1 Detailed Analysis of Dysprosium

We evaluated the validity of the cross section libraries (JENDL-4.0, ENDF/B-VII.0 and JEFF-3.1) by comparing infinite dilution ^{164}Dy cross section in SRAC library 107 energy groups. Dy capture rates of each nuclide at E3 core are shown in Fig. 3. ^{164}Dy has the largest capture rate in Dy at E3 core, and it is also similar to that at EE1 core. And ^{164}Dy capture cross section has the difference at higher energy range among these libraries as shown in Fig. 4. However, the energy range is different from the energy range where capture rate is significant. Also Fig. 5 shows ^{164}Dy capture rate difference among these libraries, and the difference of energy-integrated capture rate among these libraries is negligibly small by considering the magnitude of the capture rate shown in Fig. 3. Therefore the influence on capture rate by the difference of the cross section libraries is small at both E3 and EE1 cores, and the tendency is consistent to the results of C/E value shown in Fig. 2.

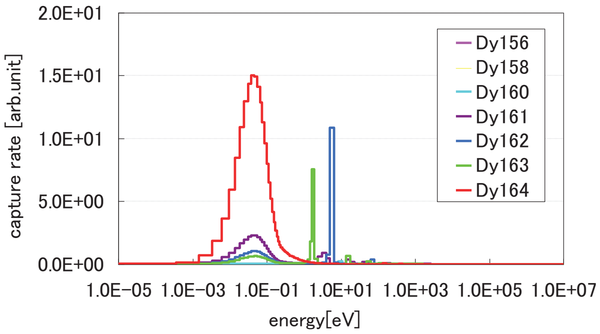

Fig. 3 Dy capture rate in each nuclide at E3

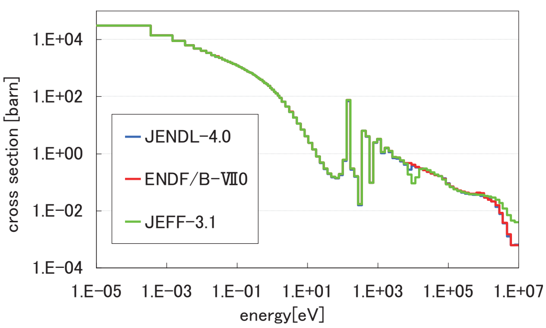

Fig. 4 ^{164}Dy capture cross section

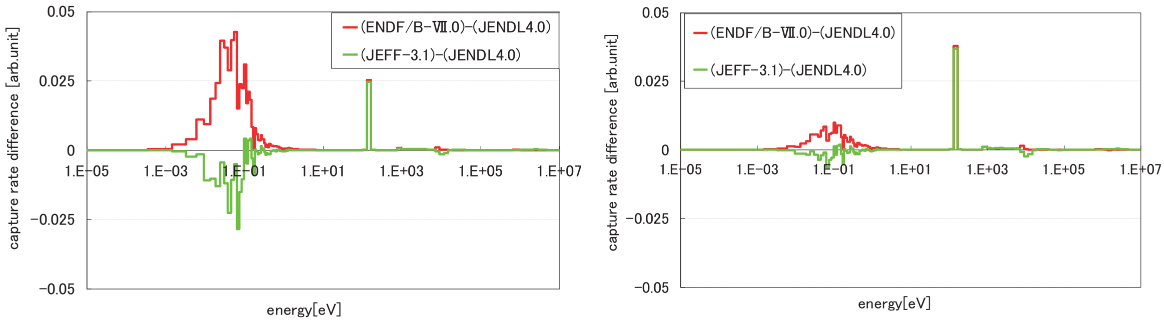

Fig. 5 ^{164}Dy capture rate difference at E3 core (left) and EE1 core (right)

3.2 Detailed Analysis of Erbium

Er capture rates of each nuclide at E3 core are shown in Fig. 6. ^{167}Er has the largest capture rate in Er at E3 core, and it is also similar to that at EE1 core. And ^{167}Er capture cross section has the difference in resonance region among libraries (JENDL-4.0, ENDF/B-VII.0 and JEFF-3.1) shown in Fig. 7. However, the energy range is not dominant on energy-integrated capture rate. Fig. 8 shows ^{167}Er capture rate difference among these libraries, and the difference in energy-integrated capture rate among these libraries can be seen at some range. However the magnitude of the difference is also small enough not to affect remarkably on the difference in energy-integrated capture rate among these libraries.

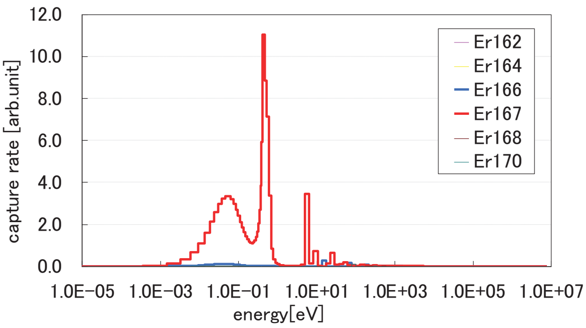

Fig. 6 Er capture rate in each nuclide at E3 core

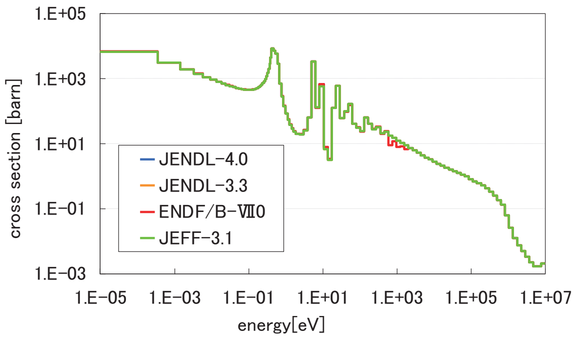

Fig. 7 ^{167}Er capture cross

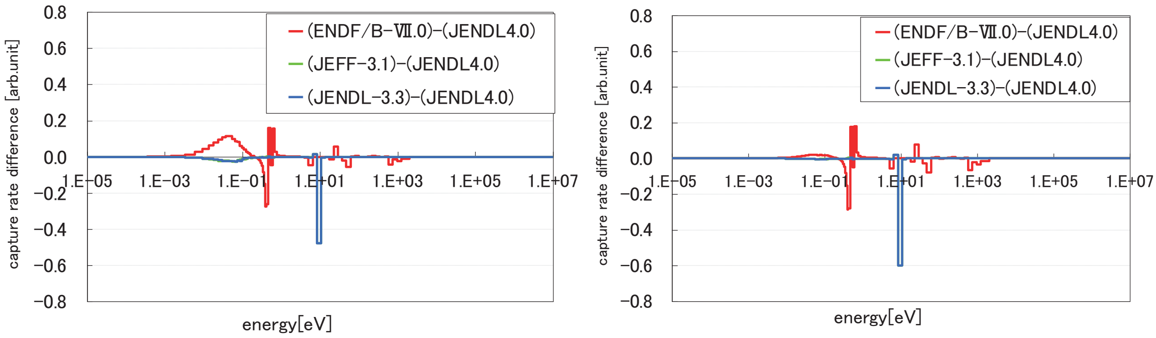

Fig. 8 ^{167}Er capture rate difference at E3 core (left) and EE1 core (right)

3.3 Detailed Analysis of Holmium

There is a difference in C/E value of Ho_2O_3 between ENDF/B-VII.0 (~1.01) and JEFF-3.1 (~1.10) at EE1 core as shown in Fig. 2. The infinite dilution ^{165}Ho cross section in SRAC library 107 energy groups is shown in Fig.9. Figure 9 shows a slight difference of ^{165}Ho capture cross section in some energy ranges between ENDF/B-VII.0 and JEFF-3.1. Also the capture rate of ^{165}Ho shows the difference in some energy ranges at EE1 core as shown in Fig. 10. However the energy-integrated capture rate is almost the same between ENDF/B-VII.0 and JEFF-3.1 by the cancellation among energy groups. The difference in capture rate is about 0.8% at EE1 core, and the magnitude of the difference is not enough to explain the difference in C/E value. The cause of the C/E difference in Ho_2O_3 worth between ENDF/B-VII.0 and JEFF-3.1 at EE1 core could not be clarified by considering the capture rate obtained by infinite dilution cross section, and the further investigation is necessary to explain the difference in C/E value ENDF/B-VII.0 and JEFF-3.1.

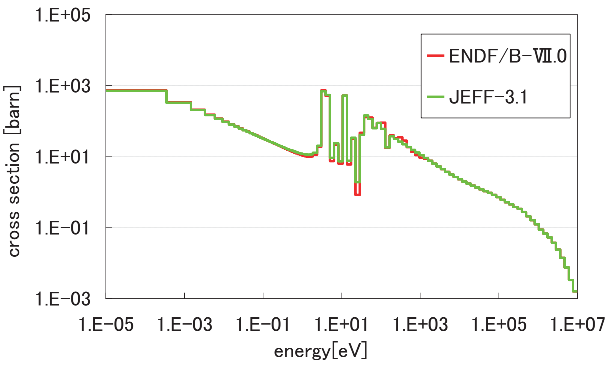

Fig.9 ^{165}Ho capture cross section

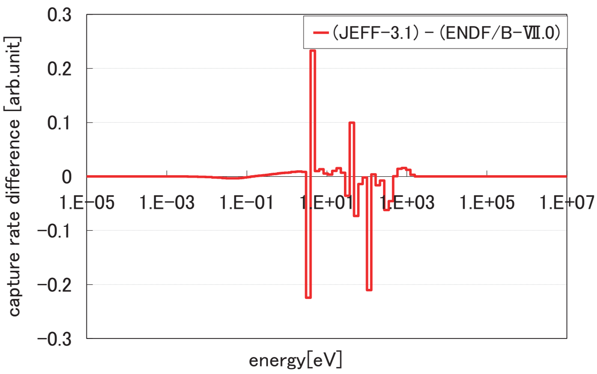

Fig.10 ^{165}Ho capture rate difference at EE1 core

3. Conclusions

Analyses were performed to verify nuclear data of some rare-earth elements (Dy, Ho, Er and Tm) in the cross section libraries (JENDL-4.0, JENDL-3.3, ENDF/B-VII.0 and JEFF-3.1) by using MVP calculation. The remarkable discrepancy of C/E value from 1.0 is not obtained for all elements and cores, although there is a relatively large discrepancy in the C/E value of Ho_2O_3 at EE1 core between ENDF/B-VII.0 and JEFF-3.1.

To be clear the discrepancy of C/E value by considering the difference in cross section among these libraries, infinite dilution cross section in SRAC library 107 energy groups are used for energy-integrated capture rate. The difference in the cross section can be seen in some energy ranges, however the difference of energy-integrated capture rate among these libraries is small within 0.1% for Dy and 0.2% for Er at both cores. The magnitude of the difference is small and is consistent to the tendency of the C/E value among libraries. The largest difference in C/E value is obtained in the case of Ho at EE1 core between ENDF/B-VII.0 and JEFF-3.1, however this difference could not be explained from the comparison of infinite dilution cross section in 107 energy-groups, therefore the further investigation is planning to be clear the cause of the difference.

Acknowledgements

This work has been carried out in partly under the Visiting Researcher's Program of the Research Reactor Institute, Kyoto University. The authors are deeply grateful to the staffs of KUCA, including Dr. Tsuyoshi Misawa, Dr. Choel-Ho Pyeon, Dr. Lim Jaeyong, Mr. Hiroshi Nakamura, Mr. Hiroshi Yamamoto, Dr. Tadafumi Sano, Mr. Tomoyoshi Takeshita and Mr. Yoshiaki Tanaka for their generous help and cooperation during the experiments.

Reference

[1] K.Shimozato, K.Ieyama, T.Kitada et al., "Measurements and Analysis of Reactivity Worth of Rare-Earth Elements at Kyoto University Critical Assembly," Proc. Int. Conf. on the Physics of Reactors (PHYSOR2010), May 9-14, 2010, Pittsburgh, Pennsylvania, USA.

41. Renewal of JENDL photonuclear data file 2004
(I) Elements of atomic number below 20

T. Murata[1)], K. Kosako[2)] and T. Fukahori[3)]
1) former NAIG Nuclear Research Lab.
2) Shimizu Institute of Technology
3) Nuclear Data Center, JAEA
E-mail t.murata@ma.point.ne.jp, k.kasako@shimz.co.jp, fukahori.tokio@jaea.go.jp

Revision of JENDL photonuclear data file released in 2004 has been made for target nuclides ; ^{12}C, ^{14}N, ^{16}O, ^{19}F, ^{23}Na, $^{24, 26, 26}$Mg, ^{27}Al, $^{28\ 29,\ 30}$Si, ^{31}P and $^{40,\ 48}$Ca and new evaluations of photonuclear data have been made for target nuclides; ^{13}C, ^{15}N, $^{17,\ 18}$O, $^{20,\ 21,\ 22}$Ne, $^{32,\ 33,\ 34,\ 36}$S, $^{35,\ 37}$Cl, $^{36,\ 38,\ 40}$Ar, $^{39,\ 42}$ and $^{42,\ 43,\ 44,\ 46}$Ca.

1. Introduction

For some nuclides, the first version of JENDL photonuclear data file (2004) was enable to reproduce experimental cross sections and may carelessly gave some production cross sections of nuclides which can not be allowed physically. Now we are revising the data file to reproduce the experimental data of neutron production and photo-absorption cross sections. High resolution measurements made after the previous evaluation are also included for the renewal.

Formula of resonance plus quasi-deuteron model is applied for analysis of experimental cross sections of the (γ,xn) reactions compiled by Dietrich and Berman[1)] and the (γ,abs) reactions[2)]. For nuclides, no experimental data are available, relative resonance absorption cross sections are calculated using the parameters given in the RIPL-2 theoretical giant dipole resonances[3)]. For light nuclides, no Giant Dipole Resonance (GDR) parameters are given in the RIPL-2, and the GDR structures were estimated using the level scheme given in the ENSDF and neutron resonance parameters. The estimated relative cross sections are normalized to satisfy the sum rule of the giant dipole plus quasi deuteron cross sections. Cross sections other than obtained by analyses of experimental data are estimated using the branching ratios calculated with the ALICE-F code[4)].

2. Method of analysis and evaluation

<u>Resonance formula for the experimental cross section analysis</u>

Experimental cross sections of the photo absorption reaction are analyzed with sum of the resonance and the quasi-deuteron model terms. The resonance cross sections are calculated with the following formula[5)].

$$\sigma_{abs}(E) = \frac{2\pi}{k^2}\sum_i \frac{2J_i+1}{2I_0+1}B_{i0}\frac{(E\Gamma_i)^2}{\left(E_i^{\,2}-E^2\right)^2+(E\Gamma_i)^2} \tag{1}$$

where E is incident photon energy, k its wave number, I_0 spin of the target nucleus, J_i, E_i, Γ_i and B_{i0} are spin, energy, total width and the gamma transition branching ratio to the ground state of the i-th resonance level, respectively. Gamma-ray emission widths are quite small comparing with particle emission width, so the (γ,γ') reactions were ignored and assumed σ_{abs}=0 below particle emission threshold energy.

. Resonance cross section for the reaction j are given by

$$\sigma_J(E)=\frac{2\pi}{k^2}\sum_i\frac{2J_i+1}{2I_0+1}B_{ij}(E)B_{i0}\frac{(E\Gamma_i)^2}{\left(E_i^{\,2}-E^2\right)^2+(E\Gamma_i)^2} \tag{2}$$

where B_{ij} is the i-th resonance branching ratio to the j reaction. Incident energy dependence of Γ_i and B_{ij} are given by barrier penetration factors $\left\langle p_j(E_j)\right\rangle_l$ of the emission particle j averaged over the angular momentum ℓ determined using the impact parameter with the weight of nuclear volume.

$$\Gamma_i(E)=\sum_j\Gamma_{ij}(E_i)\cdot\frac{\left\langle p_j(E_j)\right\rangle_l}{\left\langle p_j(E_{ij})\right\rangle_l},\quad B_{ij}(E)=B_{ij}(E_i)\cdot\frac{\left\langle p_j(E_j)\right\rangle_l}{\left\langle p_j(E_{ij})\right\rangle_l} \tag{3}$$

In the whole mass region of the present target nuclides, the averaged penetration factors of neutrons were well approximated as a function of emission neutron energy, and for protons and alpha particles, the factors are well described by a function of the emission energy divided by the Coulomb barrier height.

Resonance formula for RIPL-2 parameters

$$\sigma_{abs}(E)=\sigma_0\sum_{i=1}^{i=2}\frac{a_iE^2\Gamma_i^2}{(E^2-E_i^2)^2+E^2\Gamma_i^2} \tag{4}$$

where σ_0 is the normalization constant to satisfy the GDR sum-rule described below and $a_1=\eta$ (deformation=ratio of the long axis to the short axis of nuclide) , $a_2=1$.

Quasi Deuteron model[6)]

Photo absorption cross section is given by

$$\sigma_{abs}(E)=\sigma_{qd}\,\frac{NZ}{A}\cdot(E-E_b)^{3/2}E^3P(E) \tag{5}$$

and cross section of the reaction j is

$$\sigma_j(E)=B_j(E)\cdot\sigma_{abs}(E) \tag{6}$$

where N,Z,A are target nucleus neutron, proton and mass number, σ_{qd}, constant to reproduce the experimental cross section in the QDM region (say, E>80MeV; σ_{qd}=133 mb)、E_b n-p binding energy of deuteron (2.223MeV) , P(E) : Pauli blocking factor[7)] and B_j branching ratio to the reaction j.

GDR sum-rule[8)]

Photo absorption cross sections are approximately satisfy the following sum rule relationship including quasi deuteron term Eq. (5),

$$\int_0^{140} \sigma_{abs}(E)dE = C_s \frac{NZ}{A} \quad , \quad C_s=105\backsim110 \quad (\text{mb} \cdot \text{MeV}) \qquad (7)$$

With the above formula, photo absorption cross section and experimental cross sections such as the (g,x1n) reaction and the (g,x2n) reactions are analyzed and the evaluated cross sections are determined. The other cross sections are obtained using the branching ratios calculated with the ALICE-F code by the following formula.

$$\sigma_j = (\sigma_{abs} - \sum_x \sigma_x) \times B_j / (1 - \sum_x B_x) \qquad (8)$$

where σ_x is cross section determined experimentally, B_x it's calculated branching ratio and Bj calculated other branching ratios.

3．Results of resonance analysis

Some examples of the present resonance analysis are shown in Fig.1 to Fig.6 compared with experimental cross sections. Resonance parameters for the analysis are summarized in Table 1 to Table 6. These parameters are fitting parameters to reproduce experimental data and may not have physical meaning. Photo absorption cross sections of which experimental data were not available are calculated with resonance parameters determined to reproduce experimental cross sections of the (g,x1n) and / or the (g,x2n) reactions and in cases of charged particle emission threshold energy is less than that of neutron emission, correction of the cross sections were made using the penetration factors in the energy region from the threshold energy to 1.5・Coulomb barrier height energy.

Resonance parameters of the RIPL-2 were adopted for target nuclides; ^{33}S, ^{34}S, ^{36}S, ^{36}Ar, ^{38}Ar, ^{41}K, ^{42}Ca, ^{43}Ca, ^{44}Ca, ^{46}Ca and ^{48}Ca to obtain photo absorption cross sections.

All other nuclear data, such as emitted particle spectrum, angular distributions and production cross sections of the radio isotopes which have half lives almost longer than one second were calculated with the ALICE-F code.

References

1) S. S. Dietrich, B. L. Berman, Atomic Data and Nuclear Data Tables, 38, 199(1988).
2) J. Ahrens et al., Nucl. Physics A251, 479 (1975), J. Ahrens, Nucl. Physics A446, 229c (1985), H. Harada et al., Phys. Rev. Lett. 80, 33 (1998), H. Harada et al., J. Nucl. Sci. Eng. 35, 783 (1998), H. Harada et al., J. Nucl. Sci. Eng. 38, 465 (2001).
3) T. Fukahori et al., IAEA TECDOC 1506 (IAEA,2006); "Gamma-ray Segment, Theoretical GDR Parameters".
4) T. Fukahori, JAERI-M 92-039(1992), p.114.
5) P. M. Endt, P. B. Smith (eds.), "Nuclear Reactions II", North-Holland (1962) Chap. 3 "The Giant Resonance of the Nuclear Photoeffect".
6) J. S. Levinger, Phys. Rev. 84, 43 (1951).
7) M. B. Chadwick et al., Phys. Rev. C44, 814 (1991).
8) A. deShalit, H. Feshbach, "Theoretical Nuclear Physics I", John Wiley (1974), Chap.VIII "Electromagnetic Transitions".

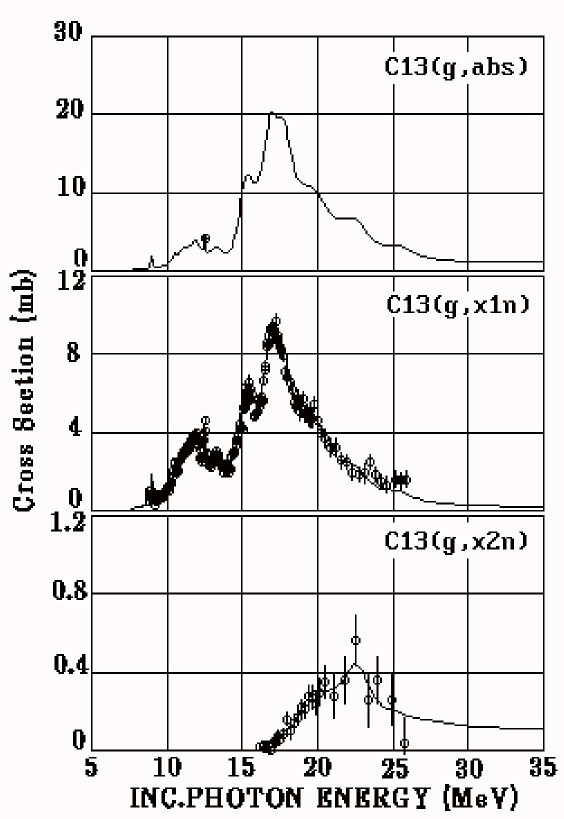

Fig.1 ^{13}C Photo reaction cross sections.

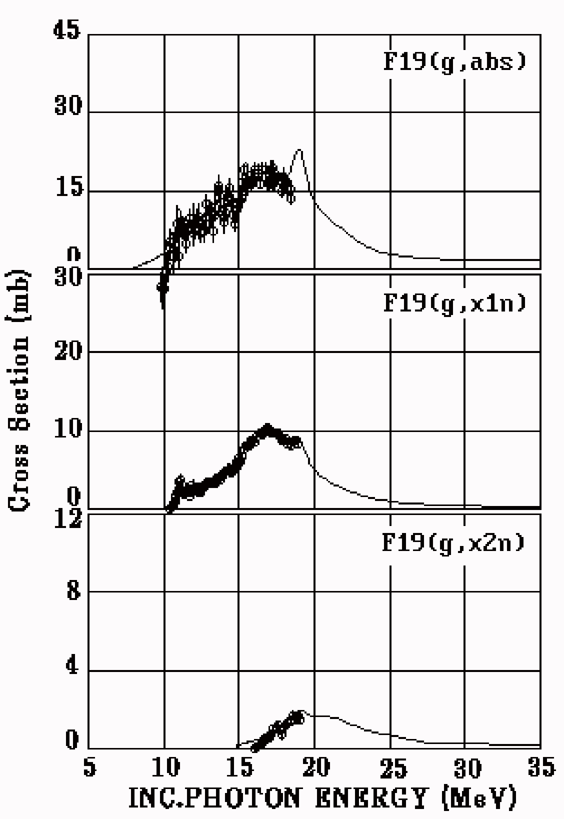

Fig.2 ^{19}F Photo reaction cross sections.

Table 1 Resonance parameters of ^{13}C
(sum rule　Cs=105.1 mb・MeV)

E_i (MeV)	J_i^{π}	Γ_i (MeV)	B_{i0}	B_{i1n}	B_{i2n}
8.0	1/2+	0.2	4.0E−5	1.0	0.0
11.0	1/2+	0.5	5.0E−5	1.0	0.0
12	1/2+	2.0	1.2E−4	1.0	0.0
14	1/2+	1.5	2.0E−4	1.0	0.0
15.0	1/2+	0.2	2.0E−4	1.0	0.0
17	1/2+	2.0	2.0E−4	1.0	0.0
21	1/2+	2.5	1.3E−3	0.6	0.0
24	3/2+	2.5	1.3E−3	0.5	0.0
26	3/2+	3.0	1.5E−3	0.4	0.0
30	3/2+	6.0	1.3E−3	0.5	0.03
35.0	3/2+	5.0	1.0E−3	0.3	0.08
41.0	3/2+	5.0	5.0E−4	0.3	0.02

Table 2　Resonance parameters of ^{19}F
(sum rule　Cs=105.4 mb・MeV)

E_i (MeV)	J_i^{π}	Γ_i (MeV)	B_{i0}	B_{i1n}	B_{i2n}
10.9	3/2−	0.5	1.0E−4	0.1	0.0
11.8	1/2−	0.1	3.0E−4	0.4	0.0
12.1	3/2−	0.3	3.0E−4	0.5	0.0
12.5	1/2−	0.1	2.0E−5	0.4	0.0
12.6	1/2−	0.3	6.0E−5	0.5	0.0
13.0	3/2−	0.3	8.0E−5	0.6	0.0
13.8	3/2−	0.4	2.8E−4	0.3	0.0
14.5	1/2−	0.4	2.0E−4	0.4	0.0
15.7	3/2−	1.5	3.0E−4	0.35	0.0
17.3	1/2−	1.0	4.0E−4	0.3	0.0
18.5	1/2−	1.0	1.0E−3	0.3	0.0
20.7	3/2−	1.0	7.0E−4	0.25	0.0
24.0	3/2−	7.0	1.7E−3	0.65	0.01
28.0	3/2−	2.5	2.0E−3	0.3	0.07
32.0	3/2−	10.0	1.3E−3	0.28	0.20

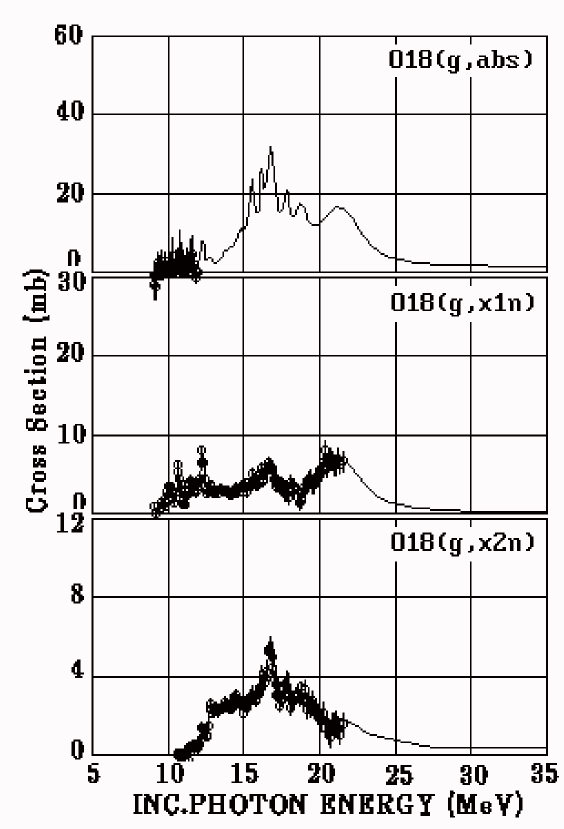

Fig.3 ^{18}O Photo reaction cross sections.

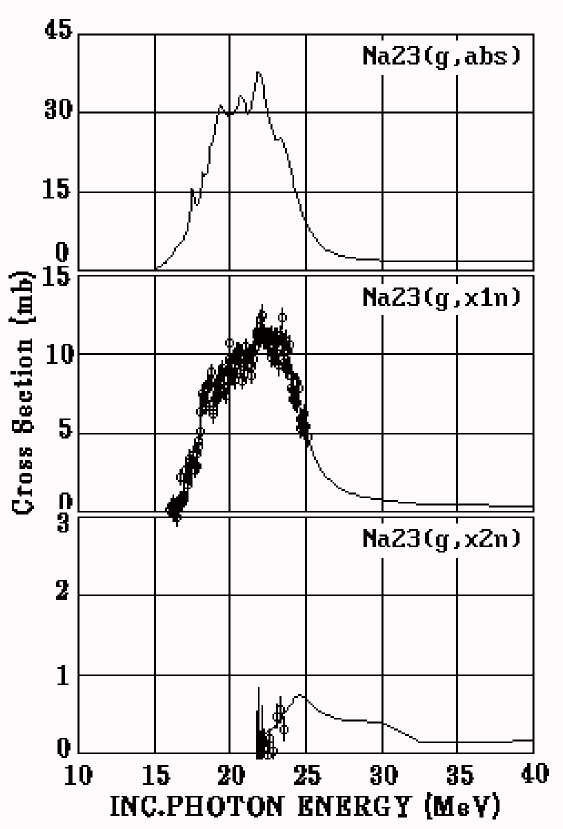

Fig.4 ^{23}Na Photo reaction cross sections.

Table 3. Resonance parameters of ^{18}O.
(sum rule Cs=105.3 mb・MeV)

E_i (MeV)	J_i^{π}	Γ_i (MeV)	B_{i0}	B_{i1n}	B_{i2n}
10.3	1−	0.3	5.0E−5	1.0	0.0
11.22	1−	0.3	9.0E−5	1.0	0.0
13.0	1−	0.5	1.0E−4	0.9	0.01
14.5	1−	0.6	3.0E−4	0.7	0.08
15.5	1−	0.5	3.0E−4	0.2	0.12
17.3	1−	3.0	3.0E−4	0.3	0.32
19.5	1−	1.0	2.0E−4	0.3	0.35
21.0	1−	1.0	1.0E−3	0.2	0.12
22.3	1−	0.4	1.0E−3	0.16	0.15
23.5	1−	1.5	2.0E−3	0.2	0.18
25.6	1−	1.0	1.0E−3	0.05	0.20
27.5	1−	2.0	1.0E−3	0.07	0.25
33.0	1−	7.0	2.2E−3	0.44	0.08

Table 4 Resonance parameters of ^{23}Na.
(sum rule Cs=105.0 mb・MeV)

E_i (MeV)	J_i^{π}	Γ_i (MeV)	B_{i0}	B_{i1n}	B_{i2n}
15.0	1/2−	0.8	1.5E−3	0.2	0.0
16.3	1/2−	0.8	1.5E−3	0.7	0.0
17.3	1/2−	1.0	1.3E−3	0.7	0.0
18.5	5/2−	2.0	1.3E−3	0.2	0.0
20.0	5/2−	4.0	1.7E−3	0.4	0.0
21.5	5/2−	2.0	1.7E−3	0.2	0.0
23.5	5/2−	2.0	2.2E−3	0.3	0.0
24.5	5/2−	3.0	2.8E−3	0.3	0.0
27.0	5/2−	3.0	2.8E−3	0.45	0.0
29.0	1/2−	5.0	3.3E−3	0.6	0.1

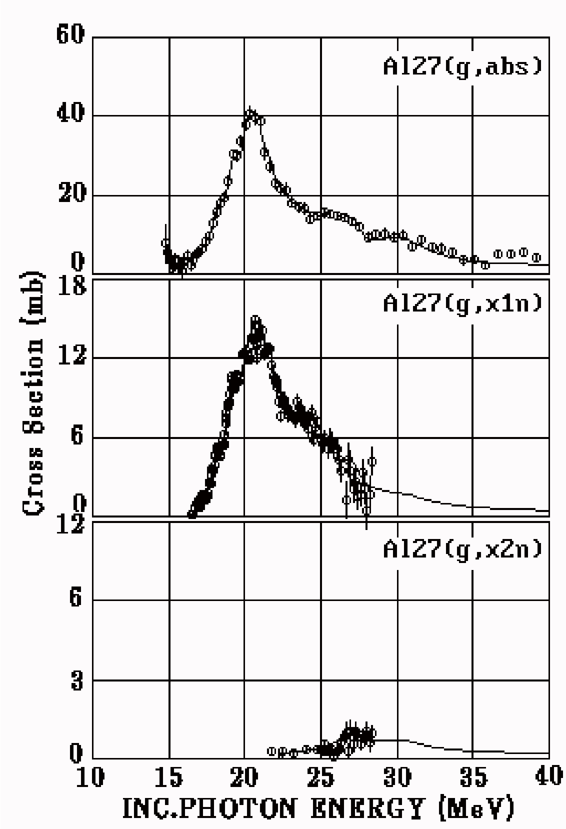

Fig.3 ^{27}Al Photo reaction cross sections.

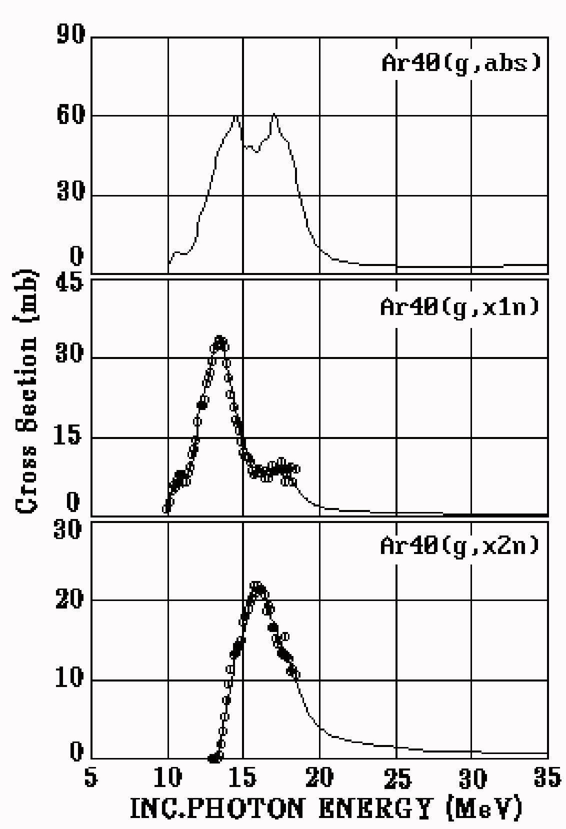

Fig.4 ^{40}Ar Photo reaction cross sections.

Table 3 Resonance parameters of ^{27}Al.
(sum rule Cs=110.0 mb・MeV)

E_i (MeV)	J_i^{π}	Γ_i (MeV)	B_{i0}	B_{i1n}	B_{2n}
16.3	3/2−	1.5	1.4E−3	0.3	0.0
18,5	7/2−	2.0	1.8E−3	0.4	0.0
20.5	7/2−	2.5	2.8E−3	0.3	0.0
21.8	7/2−	2.5	3.0E−3	0.4	0.0
23.3	7/2−	2.0	1.5E−3	0.5	0.0
25.0	3/2−	3.0	3.5E−3	0.45	0.005
27.0	3/2−	3.0	3.0E−3	0.45	0.01
29.0	7/2−	3.0	1.5E−3	0.5	0.01
31.5	7/2−	3.0	2.5E−3	0.3	0.012
34.0	7/2−	3.0	2.5E−3	0.25	0.12
41.0	7/2−	10.0	3.5E−3	0.15	0.08

Table 4 Resonance parameters of ^{40}Ar.
(sum rule Cs=105.3 mb・MeV)

E_i (MeV)	J_i^{π}	Γ_i (MeV)	B_{i0}	B_{i1n}	B_{i2n}
11.0	1−	2.0	1.0E−4	1.0	0.0
14.3	1−	1.5	3.0E−4	0.9	0.0
16.0	1−	3.0	7.0E−4	0.8	0.0
17.2	1−	3.0	1.0E−3	0.75	0.02
19.0	1−	3.0	1.8E−3	0.2	0.25
21.0	1−	2.0	1.0E−3	0.15	0.74
22.5	1−	2.0	1.2E−3	0.12	0.62
24.0	1−	2.0	2.2E−3	0.13	0.23
26.0	1−	4.0	3.5E−3	0.13	0.20

国際単位系（SI）

表１．SI 基本単位

基本量	SI 基本単位	
	名称	記号
長さ	メートル	m
質量	キログラム	kg
時間	秒	s
電流	アンペア	A
熱力学温度	ケルビン	K
物質量	モル	mol
光度	カンデラ	cd

表２．基本単位を用いて表されるSI組立単位の例

組立量	SI 基本単位	
	名称	記号
面積	平方メートル	m^2
体積	立法メートル	m^3
速さ，速度	メートル毎秒	m/s
加速度	メートル毎秒毎秒	m/s^2
波数	毎メートル	m^{-1}
密度，質量密度	キログラム毎立方メートル	kg/m^3
面積密度	キログラム毎平方メートル	kg/m^2
比体積	立方メートル毎キログラム	m^3/kg
電流密度	アンペア毎平方メートル	A/m^2
磁界の強さ	アンペア毎メートル	A/m
量濃度 (a)，濃度	モル毎立方メートル	mol/m^3
質量濃度	キログラム毎立法メートル	kg/m^3
輝度	カンデラ毎平方メートル	cd/m^2
屈折率 (b)	（数字の）　1	1
比透磁率 (b)	（数字の）　1	1

(a) 量濃度（amount concentration）は臨床化学の分野では物質濃度（substance concentration）ともよばれる。
(b) これらは無次元量あるいは次元１をもつ量であるが、そのことを表す単位記号である数字の１は通常は表記しない。

表３．固有の名称と記号で表されるSI組立単位

組立量	SI 組立単位			
	名称	記号	他のSI単位による表し方	SI基本単位による表し方
平面角	ラジアン(b)	rad	1 (b)	m/m
立体角	ステラジアン(b)	sr(c)	1 (b)	m^2/m^2
周波数	ヘルツ (d)	Hz		s^{-1}
力	ニュートン	N		$m\ kg\ s^{-2}$
圧力，応力	パスカル	Pa	N/m^2	$m^{-1}\ kg\ s^{-2}$
エネルギー，仕事，熱量	ジュール	J	N m	$m^2\ kg\ s^{-2}$
仕事率，工率，放射束	ワット	W	J/s	$m^2\ kg\ s^{-3}$
電荷，電気量	クーロン	C		s A
電位差（電圧），起電力	ボルト	V	W/A	$m^2\ kg\ s^{-3}\ A^{-1}$
静電容量	ファラド	F	C/V	$m^{-2}\ kg^{-1}\ s^4\ A^2$
電気抵抗	オーム	Ω	V/A	$m^2\ kg\ s^{-3}\ A^{-2}$
コンダクタンス	ジーメンス	S	A/V	$m^{-2}\ kg^{-1}\ s^3\ A^2$
磁束	ウエーバ	Wb	Vs	$m^2\ kg\ s^{-2}\ A^{-1}$
磁束密度	テスラ	T	Wb/m^2	$kg\ s^{-2}\ A^{-1}$
インダクタンス	ヘンリー	H	Wb/A	$m^2\ kg\ s^{-2}\ A^{-2}$
セルシウス温度	セルシウス度(e)	℃		K
光束	ルーメン	lm	cd sr(c)	cd
照度	ルクス	lx	lm/m^2	$m^{-2}\ cd$
放射性核種の放射能 (f)	ベクレル (d)	Bq		s^{-1}
吸収線量, 比エネルギー分与, カーマ	グレイ	Gy	J/kg	$m^2\ s^{-2}$
線量当量, 周辺線量当量, 方向性線量当量, 個人線量当量	シーベルト (g)	Sv	J/kg	$m^2\ s^{-2}$
酸素活性	カタール	kat		$s^{-1}\ mol$

(a)SI接頭語は固有の名称と記号を持つ組立単位と組み合わせても使用できる。しかし接頭語を付した単位はもはやコヒーレントではない。
(b)ラジアンとステラジアンは数字の１に対する単位の特別な名称で、量についての情報をつたえるために使われる。実際には、使用する時には記号rad及びsrが用いられるが、習慣として組立単位としての記号である数字の１は明示されない。
(c)測光学ではステラジアンという名称と記号srを単位の表し方の中に、そのまま維持している。
(d)ヘルツは周期現象についてのみ、ベクレルは放射性核種の統計的過程についてのみ使用される。
(e)セルシウス度はケルビンの特別な名称で、セルシウス温度を表すために使用される。セルシウス度とケルビンの単位の大きさは同一である。したがって、温度差や温度間隔を表す数値はどちらの単位で表しても同じである。
(f)放射性核種の放射能（activity referred to a radionuclide）は、しばしば誤った用語で”radioactivity”と記される。
(g)単位シーベルト（PV,2002,70,205）についてはCIPM勧告2（CI-2002）を参照。

表４．単位の中に固有の名称と記号を含むSI組立単位の例

組立量	SI 組立単位		
	名称	記号	SI 基本単位による表し方
粘度	パスカル秒	Pa s	$m^{-1}\ kg\ s^{-1}$
力のモーメント	ニュートンメートル	N m	$m^2\ kg\ s^{-2}$
表面張力	ニュートン毎メートル	N/m	$kg\ s^{-2}$
角速度	ラジアン毎秒	rad/s	$m\ m^{-1}\ s^{-1}=s^{-1}$
角加速度	ラジアン毎秒毎秒	rad/s^2	$m\ m^{-1}\ s^{-2}=s^{-2}$
熱流密度，放射照度	ワット毎平方メートル	W/m^2	$kg\ s^{-3}$
熱容量，エントロピー	ジュール毎ケルビン	J/K	$m^2\ kg\ s^{-2}\ K^{-1}$
比熱容量，比エントロピー	ジュール毎キログラム毎ケルビン	J/(kg K)	$m^2\ s^{-2}\ K^{-1}$
比エネルギー	ジュール毎キログラム	J/kg	$m^2\ s^{-2}$
熱伝導率	ワット毎メートル毎ケルビン	W/(m K)	$m\ kg\ s^{-3}\ K^{-1}$
体積エネルギー	ジュール毎立方メートル	J/m^3	$m^{-1}\ kg\ s^{-2}$
電界の強さ	ボルト毎メートル	V/m	$m\ kg\ s^{-3}\ A^{-1}$
電荷密度	クーロン毎立方メートル	C/m^3	$m^{-3}\ sA$
表面電荷	クーロン毎平方メートル	C/m^2	$m^{-2}\ sA$
電束密度，電気変位	クーロン毎平方メートル	C/m^2	$m^{-2}\ sA$
誘電率	ファラド毎メートル	F/m	$m^{-3}\ kg^{-1}\ s^4\ A^2$
透磁率	ヘンリー毎メートル	H/m	$m\ kg\ s^{-2}\ A^{-2}$
モルエネルギー	ジュール毎モル	J/mol	$m^2\ kg\ s^{-2}\ mol^{-1}$
モルエントロピー, モル熱容量	ジュール毎モル毎ケルビン	J/(mol K)	$m^2\ kg\ s^{-2}\ K^{-1}\ mol^{-1}$
照射線量（X線及びγ線）	クーロン毎キログラム	C/kg	$kg^{-1}\ sA$
吸収線量率	グレイ毎秒	Gy/s	$m^2\ s^{-3}$
放射強度	ワット毎ステラジアン	W/sr	$m^4\ m^{-2}\ kg\ s^{-3}=m^2\ kg\ s^{-3}$
放射輝度	ワット毎平方メートル毎ステラジアン	$W/(m^2\ sr)$	$m^2\ m^{-2}\ kg\ s^{-3}=kg\ s^{-3}$
酵素活性濃度	カタール毎立方メートル	kat/m^3	$m^{-3}\ s^{-1}\ mol$

表５．SI 接頭語

乗数	接頭語	記号	乗数	接頭語	記号
10^{24}	ヨタ	Y	10^{-1}	デシ	d
10^{21}	ゼタ	Z	10^{-2}	センチ	c
10^{18}	エクサ	E	10^{-3}	ミリ	m
10^{15}	ペタ	P	10^{-6}	マイクロ	µ
10^{12}	テラ	T	10^{-9}	ナノ	n
10^{9}	ギガ	G	10^{-12}	ピコ	p
10^{6}	メガ	M	10^{-15}	フェムト	f
10^{3}	キロ	k	10^{-18}	アト	a
10^{2}	ヘクト	h	10^{-21}	ゼプト	z
10^{1}	デカ	da	10^{-24}	ヨクト	y

表６．SIに属さないが、SIと併用される単位

名称	記号	SI 単位による値
分	min	1 min=60s
時	h	1h =60 min=3600 s
日	d	1 d=24 h=86 400 s
度	°	1°=(π/180) rad
分	’	1’=(1/60)°=(π/10800) rad
秒	”	1”=(1/60)’=(π/648000) rad
ヘクタール	ha	$1ha=1hm^2=10^4m^2$
リットル	L，l	$1L=1l=1dm^3=10^3cm^3=10^{-3}m^3$
トン	t	$1t=10^3\ kg$

表７．SIに属さないが、SIと併用される単位で、SI単位で表される数値が実験的に得られるもの

名称	記号	SI 単位で表される数値
電子ボルト	eV	$1eV=1.602\ 176\ 53(14)\times10^{-19}J$
ダルトン	Da	$1Da=1.660\ 538\ 86(28)\times10^{-27}kg$
統一原子質量単位	u	1u=1 Da
天文単位	ua	$1ua=1.495\ 978\ 706\ 91(6)\times10^{11}m$

表８．SIに属さないが、SIと併用されるその他の単位

名称	記号	SI 単位で表される数値
バール	bar	$1\ bar=0.1MPa=100kPa=10^5Pa$
水銀柱ミリメートル	mmHg	1mmHg=133.322Pa
オングストローム	Å	$1\ Å=0.1nm=100pm=10^{-10}m$
海里	M	1 M=1852m
バーン	b	$1\ b=100fm^2=(10^{-12}cm)2=10^{-28}m^2$
ノット	kn	1 kn=(1852/3600)m/s
ネーパ	Np	SI単位との数値的な関係は、対数量の定義に依存。
ベル	B	
デジベル	dB	

表９．固有の名称をもつCGS組立単位

名称	記号	SI 単位で表される数値
エルグ	erg	$1\ erg=10^{-7}\ J$
ダイン	dyn	$1\ dyn=10^{-5}N$
ポアズ	P	$1\ P=1\ dyn\ s\ cm^{-2}=0.1Pa\ s$
ストークス	St	$1\ St=1cm^2\ s^{-1}=10^{-4}m^2\ s^{-1}$
スチルブ	sb	$1\ sb=1cd\ cm^{-2}=10^4cd\ m^{-2}$
フォト	ph	$1\ ph=1cd\ sr\ cm^{-2}\ 10^4lx$
ガル	Gal	$1\ Gal=1cm\ s^{-2}=10^{-2}ms^{-2}$
マクスウェル	Mx	$1\ Mx = 1G\ cm^2=10^{-8}Wb$
ガウス	G	$1\ G=1Mx\ cm^{-2}=10^{-4}T$
エルステッド (c)	Oe	$1\ Oe \triangleq (10^3/4\pi)A\ m^{-1}$

(c) ３元系のCGS単位系とSIでは直接比較できないため、等号「 ≙ 」は対応関係を示すものである。

表10．SIに属さないその他の単位の例

名称	記号	SI 単位で表される数値
キュリー	Ci	$1\ Ci=3.7\times10^{10}Bq$
レントゲン	R	$1\ R = 2.58\times10^{-4}C/kg$
ラド	rad	$1\ rad=1cGy=10^{-2}Gy$
レム	rem	$1\ rem=1\ cSv=10^{-2}Sv$
ガンマ	γ	1 γ =1 nT=10-9T
フェルミ		1フェルミ=1 fm=10-15m
メートル系カラット		1メートル系カラット = 200 mg = 2×10-4kg
トル	Torr	1 Torr = (101 325/760) Pa
標準大気圧	atm	1 atm = 101 325 Pa
カロリー	cal	1cal=4.1858J（「15℃」カロリー），4.1868J（「IT」カロリー）4.184J（「熱化学」カロリー）
ミクロン	µ	$1\ \mu=1\mu m=10^{-6}m$

（第8版，2006年改訂）